There must be order: Structure-transport correlations in self-assembled nanocrystal superlattices

Dissertation

der Mathematisch-Naturwissenschaftlichen Fakultät
der Eberhard Karls Universität Tübingen
zur Erlangung des Grades eines
Doktors der Naturwissenschaften
(Dr. rer. nat.)

vorgelegt von
Andre Maier
aus Lahr/Schwarzwald

Tübingen
2021

Gedruckt mit Genehmigung der Mathematisch-Naturwissenschaftlichen Fakultät der Eberhard Karls Universität Tübingen.

Tag der mündlichen Qualifikation:	15.07.2021
Dekan:	Prof. Dr. Thilo Stehle
1. Berichterstatter:	Prof. Dr. Marcus Scheele
2. Berichterstatter:	Prof. Dr. Reinhold Fink
3. Berichterstatter:	Prof. Dr. Alexander Eychmüller

This dissertation has been completed in the group of Prof. Dr. Marcus Scheele at the Institute of Physical and Theoretical Chemistry of the Eberhard Karls University of Tübingen between March 2018 and February 2021.

Abstract

In recent years, nanocrystal building blocks and their controlled self-assembly into highly ordered superlattices have created new opportunities for scientists and engineers to build novel materials with structure-related optoelectronic properties by design. However, sufficient experimental evidence for such theoretically predicted structure-property relationships is still lacking until now.

This cumulative dissertation is based on three publications and addresses the question whether structural order has a significant effect on the electronic properties of nanocrystal ensembles, focussing on π-system functionalized lead sulfide (PbS) nanocrystals and atom-precise gold (Au_{32}) nanoclusters as model systems.

First, a soft-lithography technique is developed to fabricate micrometer-sized channels of long-range ordered PbS nanocrystal superlattices with dimensions approaching the size of typical single-crystalline domains of only a few μm^2. By means of microcontact printing, hundreds of superlattice microchannels can be realized, enabling a statistically meaningful investigation of charge transport in single-crystalline superlattice domains. Indicated by conductivity and field-effect transistor measurements, charge transport within those superlattice microchannels is found to be orders of magnitude more efficient compared to state-of-the art channels where transport is averaged over large scales. This clearly emphasizes the advantage of the near single-crystalline superlattice microchannels for the characterization of intrinsic charge transport properties.

Then, the developed microcontact printing process is applied to fabricate superlattice microchannels on X-ray transparent devices, enabling a correlative investigation of the structural and the electronic properties of the same PbS superlattice domains. A full structural characterization of the superlattice symmetry and nanocrystal orientation within is achieved by synchrotron-based X-ray nano-diffraction in combination with angular X-ray cross-correlation analysis. The direct correlation of structural properties, such as superlattice type and particle spacing, with the conductivity of hundreds of superlattice channels provides meaningful evidence for structure-transport relationships. It is shown that the conductivity decreases with the interparticle spacing and that the crystallinity of the superlattices has a beneficial effect on charge transport. Further, an anisotropy of charge transport in long-range ordered monocrystalline superlattices is revealed, based on the dominant effect of shortest interparticle hopping distances. Thus, anisotropic charge transport could be considered an inherent feature of weakly coupled superlattices.

Finally, atom-precise Au_{32} nanoclusters are self-assembled into well-defined microcrystals, which are investigated by grazing-incident small-angle X-ray scattering, absorption spectroscopy as well as conductivity and field-effect transistor measurements. It is demonstrated that the conductivity and charge carrier mobility of these long-range ordered crystalline domains exceed that of glassy assemblies of the same nanoclusters by two orders of magnitude. Along with additionally emerging optical transitions, this effect indicates an enhanced electronic coupling in highly ordered superstructures, attributed to a vanishing degree of structural and energetic disorder and a significantly reduced activation energy to charge transport.

This thesis provides experimental evidence for structure-related electronic properties of self-assembled nanocrystal superlattices and illustrates the advantageous effect of long-range structural order on charge transport.

Deutsche Zusammenfassung

In den letzten Jahren hat die Verwendung von Nanokristallen als Bausteine neue Möglichkeiten für Wissenschaft und Technik eröffnet. Durch ihre kontrollierte Selbstassemblierung zu hochgeordneten Übergittern lassen sich neuartige und maßgeschneiderte Materialien herstellen, deren optoelektronischen Eigenschaften als strukturabhängig gelten. Experimentelle Nachweise entsprechender theoretisch vorhergesagten Struktur-Eigenschafts-Beziehungen sind jedoch bisher nur spärlich vorhanden. Die vorliegende kumulative Dissertation basiert auf drei Publikationen und geht der Frage nach, ob strukturelle Ordnung einen signifikanten Einfluss auf die elektronischen Eigenschaften von Nanokristall-Ensembles hat. Hierfür werden π-funktionalisierte Bleisulfid (PbS) Nanokristalle und atompräzise Gold (Au_{32}) Nanocluster als Modellsysteme verwendet.

Zunächst wird eine Stempel-Lithographie-Technik entwickelt, um mikrometergroße Kanäle aus langreichweitig geordneten PbS Nanokristallübergittern herzustellen, deren Abmessungen der Größe typischer einkristalliner Domänen von nur wenigen μm^2 entsprechen. Mittels Mikrokontaktdruck können so hunderte Übergitter-Mikrokanäle hergestellt werden, was eine statistisch aussagekräftige Untersuchung des Ladungstransports in einkristallinen Übergitterdomänen ermöglicht. Anhand von Leitfähigkeits- und Feldeffekttransistormessungen kann gezeigt werden, dass der Ladungstransport in diesen Übergitter-Mikrokanälen um Größenordnungen effizienter ist als in konventionellen Kanälen, bei denen der Ladungstransport über weitaus größere Bereiche gemittelt wird. Dies ist ein deutlicher Hinweis auf den Vorteil einkristalliner Übergitter-Mikrokanäle für die Charakterisierung von intrinsischen Transporteigenschaften.

Anschließend wird der im Rahmen dieser Arbeit entwickelte Mikrokontaktdruck-Prozess angewandt, um Übergitter-Mikrokanäle auf röntgentransparenten Substraten herzustellen. Dies ermöglicht eine korrelative Untersuchung der strukturellen und der elektronischen Eigenschaften derselben PbS-Übergitterdomänen. Eine vollständige strukturelle Charakterisierung der Übergitter-Symmetrie und der Nanokristall-Orientierung wird durch synchrotronbasierte Röntgenstreuung mit einem nanofokussiertem Strahl in Kombination mit winkelabhängiger Röntgendiffraktions-Kreuzkorrelationsanalyse erreicht. Die direkte Korrelation der strukturellen Eigenschaften, wie z.B. Übergitter-Typ und Partikelabstand, mit der Leitfähigkeit von Hunderten von Übergitter-Kanälen liefert aussagekräftige Hinweise auf die Existenz von Struktur-Transport-Beziehungen. Es wird gezeigt, dass mit zunehmendem interpartikulärem Abstand die Leitfähigkeit sinkt und dass die Kristallinität der Übergitter einen positiven Effekt auf den Ladungstransport hat. Außerdem wird eine Anisotropie des Ladungstransports in langreichweitig geord-

neten monokristallinen Übergittern aufgezeigt, die auf den dominierenden Effekt der kürzesten interpartikulären Sprungdistanzen zurückzuführen ist. Somit kann angenommen werden, dass anisotroper Ladungstransport generell eine intrinsische Eigenschaft von schwach gekoppelten Übergittern ist.

Schließlich werden atompräsize Au_{32} Nanocluster zu definierten Mikrokristallen selbstassembliert, die mittels Kleinwinkel-Röntgenstreuung im streifenden Einfall, Absorptionsspektroskopie sowie Leitfähigkeits- und Feldeffekttransistormessungen untersucht werden. Für dieses neuartige halbleitende Material wird gezeigt, dass die Leitfähigkeit und Ladungsträgerbeweglichkeit von langreichweitig geordneten kristallinen Domänen die von polykristallinen/glasartigen Anordnungen der gleichen Nanocluster um zwei Größenordnungen übersteigt. Zusammen mit zusätzlich auftretenden optischen Übergängen deutet dieser Effekt auf eine verstärkte elektronische Kopplung in hochgeordneten Überstrukturen hin. Diese lässt sich auf einen verschwindend geringen Grad an struktureller und energetischer Unordnung und somit auf eine drastisch reduzierte Aktivierungsenergie für den Ladungstransport zurückführen.

Diese Arbeit liefert somit experimentelle Hinweise auf strukturabhängige elektronische Eigenschaften von selbstorganisierten Nanokristall-Übergittern und veranschaulicht die Auswirkungen von langreichweitiger struktureller Ordnung auf den Ladungstransport.

Contents

1. Introduction

In recent decades, semiconductors have dramatically changed the world and our society. This was particularly evident in the global health crisis of 2020/2021, when the coronavirus nearly paralyzed the entire world. However, a material often overlooked in this context has kept life going by bringing many aspects of life online: Semiconductor technology has allowed businesses to move their operations online and enabled employees to work remotely, families have enjoyed video calls with loved ones, teachers have taught lessons remotely and chains of infections were traced and interrupted using smartphone apps.[1] This is all owed to the microchips in our computers, datacenters and smartphones, which are based on semiconductor transistors. Moreover, semiconductors are the fundamental components in solar cells, a key player in managing the climate crisis, and in many other components of everyday life. Initially, these devices were based on silicon, but in the last years many other materials have been explored to achieve tailored properties and further improve the device performances.

1.1. Motivation

Promising candidates for novel semiconducting materials with properties by design are colloidal nanoparticles, such as semiconducting nanocrystals (NCRs) or atomically precise metallic nanoclusters (NCLs), which are capped with ligand molecules and can thus be dispersed in solution. Their strongly size-dependent optoelectronic properties in combination with a solution-processed fabrication offer a powerful platform for the development of tunable and low-cost next-generation devices[2–4], such as transistors[5,6], solar cells[7,8], light emitting devices[9,10], photodetectors[11,12] and thermoelectrics[13].

Due to recent advances in physical and chemical nanoscience, the precise fabrication of NCRs of various materials, sizes, shapes and ligand passivation with atomic-scale control has become possible.[14–19] However, to apply these novel materials in next-generation devices, it is necessary to assemble them into structures with sizes that can easily be handled and implemented.[20,21] Thus, using NCRs and NCLs as building blocks to self-assemble artificial solids to create functional materials by design has become an increasingly popular field of research.[22,23]

Since the seminal work of Murray et al. in 1995[24], the focus of current research on NCRs self-assembly is to achieve highly ordered superlattices (SLs) with electronically coupled building blocks, resulting in electronic conductivity, high carrier mobilities, long carrier lifetimes and diffusion lengths.[25] In analogy to classical crystals consisting of ordered atoms, SLs are referred to as artificial solids, where the NCRs can be considered as quasi-atoms.[26,27] The resulting properties are dictated by the building blocks themselves and their interplay.[2,28] There is a wide variety of studies on the self-assembly process and structural properties of NCR SLs[29–37] and on their charge transport properties, including the effect of NCR size, composition and interparticle distance[5,25,38–42]. Nevertheless, there is a considerable lack of the fundamental understanding of the relationship between structural order and the corresponding (opto-)electronic properties of NCR SLs.

Up to date, it is not clear to what degree the structural order and symmetry of the SL plays a role in determining the charge transport.[26,28] Indeed, computational studies have predicted that the degree of organization and structure of the individual nanocrystals determine the SL properties such as electronic coupling or charge transport.[28,43–48] Additionally, there are a few first experimental attempts addressing these questions[25,49–52], which hint towards a possible effect of structural order on charge transport. A more comprehensive discussion of previous studies on structure-dependent properties of NCR assemblies is given in Section 2.4.2.2. Nevertheless, a holistic explanation of the relation between structural order and charge transport in self-assembled SLs has not yet been achieved experimentally, as this has proven to be challenging.[47,49,51,53]

The growing technological and scientific appeal of these NCR SLs requires an understanding of such fundamental properties, which are extremely important for developing new materials and devices.

1.2. Objective of this thesis

In order to understand the overall picture of charge transport in NCR SLs, a correlative investigation of electronic transport and structural properties is required, which has not yet been established. Thus, fundamental questions are still pending: What is the effect of long-range order on the electronic properties? Does the degree of structural order influence the electronic coupling within SLs? Do polycrystalline and monocrystalline NCR assemblies differ in conductivity? Are the (opto-)electronic properties of NCR SLs influenced by the SL size, type and orientation? Is charge transport within NCR SLs isotropic?

Accordingly, this thesis addresses the question *"Does structural order have a significant effect on the (opto-)electronic properties of nanocrystal assemblies?"* by correlatively investigating structural and electronic properties of two model systems, namely assemblies of lead(II) sulfide (PbS) NCRs and atom-precise gold NCLs $Au_{32}(^{n}Bu_3P)_{12}Cl_8$ (Au_{32}).

PbS NCRs were chosen as a model system, as they are among the best understood systems.[54–56] The use of PbS NCRs functionalized with organic semiconductor molecules provides a great platform for the investigation of structure-transport correlations, as these self-assembled SLs offer an ideal compromise between long-range order and electronic coupling.[36,57–60]

However, the influence of the inherent NCR size distribution and thus energy fluctuations on the electronic coupling in NCR assemblies is still unknown.[45,61] To eliminate these energy fluctuations, atom-precise Au_{32} NCLs were chosen as another model system, being extremely promising building blocks with perfect size and shape uniformity.[26,62] Although there exists a plethora of atom-precise NCLs with well-established synthesis and characterization routes, only few have been used as building-blocks to fabricate functional devices.[63–66] In the present thesis, these nanoclusters (NCLs) are also included under the term "nanocrystals" (NCRs) for the sake of consistency.

Unravelling fundamental correlations between structural order and electronic transport properties in self-assembled NCR SLs would provide a deeper understanding of the charge transport mechanisms and paves the way towards specifically controlling the (opto-)electronic properties of NCR assemblies.

1.3. Outline of this thesis

This cumulative thesis is organized as follows and graphically outlined in Figure 1.1:

Chapter 2 introduces the relevant fundamentals of colloidal NCRs and atom-precise NCLs as well as the concepts of self-assembly and SLs. Further, the theoretical basics of charge transport in NCR ensembles are given, followed by a comprehensive discussion of the current state of research on this field. Then, the experimental approaches to study the properties of self-assembled SLs are introduced, including structural as well as electronic properties. Finally, some basic microfabrication techniques are briefly introduced.

Chapter 3 deals with the development of a soft-lithography technique to fabricate devices with micro-patterned PbS NCR SLs on microelectrodes, forming microchannels with dimensions of the size of SL single domains. The Chapter is based on the publication *"Fabrication of nanocrystal superlattice microchannels by soft-lithography for electronic measurements of single crystalline domains"*, published in Nanotechnology.

In Chapter 4, the technique developed in Chapter 3 is applied to fabricate microchannels on X-ray transparent devices. This allows to correlatively investigate the structural and electronic properties of the same SL domains, finally revealing anisotropic charge transport in coupled PbS NCR SLs. This Chapter is based on the publication *"Structure-transport correlation reveals anisotropic charge transport in coupled PbS nanocrystal superlattices"*, published in Advanced Materials.

In Chapter 5, self-assembled micro-crystals of Au_{32} NCLs are investigated and compared to glassy, polycrystalline thin films of the same NCLs. It is demonstrated that the micro-crystals exhibit enhanced charge carrier transport together with additionally emerged optical transitions due to structural long-range order. This Chapter is based on the publication *"Structural order enhances charge carrier transport in self-assembled Au nanoclusters"*, published in Nature Communications.

Chapter 6 provides a comprehensive summary of the results and the conclusion of this thesis, along with an outlook, how this research could be continued.

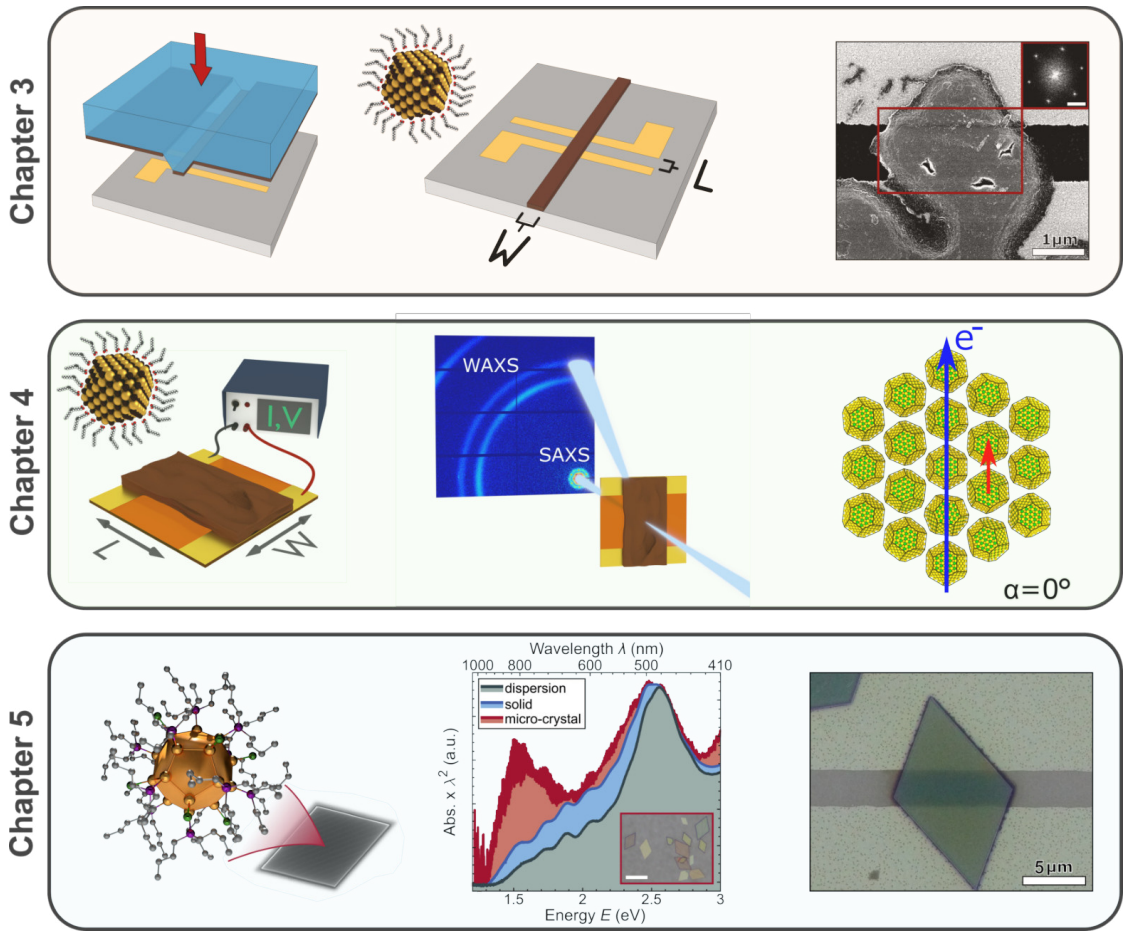

Figure 1.1: Graphical outline of this cumulative thesis, based on peer-reviewed publications. **Chapter 3:** Fabrication of nanocrystal superlattice microchannels by soft-lithography for electronic measurements of single crystalline domains (published in Nanotechnology). **Chapter 4:** Structure-transport correlation reveals anisotropic charge transport in coupled PbS nanocrystal superlattices (published in Advanced Materials). **Chapter 5:** Structural order enhances charge carrier transport in self-assembled Au nanoclusters (published in Nature Communications).

2. Theoretical & scientific fundamentals

In this Chapter, the fundamental theoretical and scientific background and the experimental approaches are provided. First, nanoparticles, NCRs and NCLs are introduced, together with the concepts of self-assembly and SLs as well as the basics of charge transport in NCR ensembles. Then, characterization techniques to study the structural and electronic properties of NCR assemblies are provided, followed by the basics of common microfabrication techniques and an introduction to soft-lithography and microcontact printing.

This Chapter is intended to enable a reader who is not familiar with the theoretical and experimental concepts to understand the basis of this thesis. A detailed discussion of the presented fundamentals is beyond the scope of this work, but references to further literature are given throughout the Chapter.

2.1. Nanoparticle building blocks

Nanoparticles are nanometer-sized fragments of metals, semiconductors, dielectric or organic materials and are extensively researched for applications in diverse fields such as biology, medicine and optoelectronics.[16] Nanoparticles have significantly different properties than the respective bulk materials. The surface area to volume ratio becomes larger the smaller the solid under consideration, which leads to significantly increased surface energies and reactivities.[30] The tremendous developments of the past decades have enabled finely tuned syntheses for the realization of nanoparticles of various materials, sizes and shapes.[16,18] One growing field of research is the use of nanoparticles as versatile building blocks for the self-assembly of novel materials with properties by design, which is also the focus of this thesis.

The following Section introduces semiconductor NCRs and their size-tunable properties as well as atom-precise NCLs. Details are provided for the model systems used in this thesis, PbS NCRs and Au_{32} NCLs.

2.1.1. Semiconductor nanocrystals

Colloidal NCRs in particular are crystalline fragments of inorganic materials with diameters of $\sim$ 2–20 nm and consist of approximately $\sim 10^2$–10^4 atoms.[18,67–69] Typically, long-chain hydrocarbons are used as ligand molecules whose functional head groups bind to the surface of the NCR.[70] This passivation prevents agglomeration of the NCRs due to steric stabilization and allows stable dispersion in nonpolar solvent.[71]

Semiconductor NCRs are a subset of NCRs and commonly consist of II-VI, III-V, and IV-VI semiconductors, prepared by means of inexpensive and scalable solution-processed synthesis.[4,67,72] In macroscopic semiconductor materials, a small band gap E_{gap} separates the conduction band (CB) from the valence band (VB). An electron (e^-) can be excited, by e.g. absorption of light, from the VB into the CB, leaving behind a positively charged defect electron or hole (h^+).[73] Due to electrostatic Coulomb interaction, this electron-hole pair, referred to as exciton, can be described as a quasiparticle, featuring a characteristic spatial delocalization length. This is quantified by a material specific parameter, the exciton Bohr radius. Semiconductor NCRs are often referred to as quantum dots, indicating the occurrence of size-dependent quantum effects, which dramatically alter their optical and electronic properties.[2,27]

2.1.1.1. Quantum confinement

In NCRs with sizes smaller than its exciton Bohr radius, the excitons are spatially constricted in three dimensions, which is called quantum confinement.[67] Consequently, the band gaps of NCRs increase with decreasing particle size due to strong confinement and the electronic states become more discrete.[69,74] The emerged CB and VB band edges are termed $1S_e$ and $1S_h$ for electrons and holes, respectively.[67] This is schematically illustrated in Figure 2.1. The effect of quantum confinement gives rise to unique optical and electronic properties of colloidal semiconductor NCRs, as the energetic levels and thus both the absorption and emission wavelength can be tuned by changing the size of the NCRs.

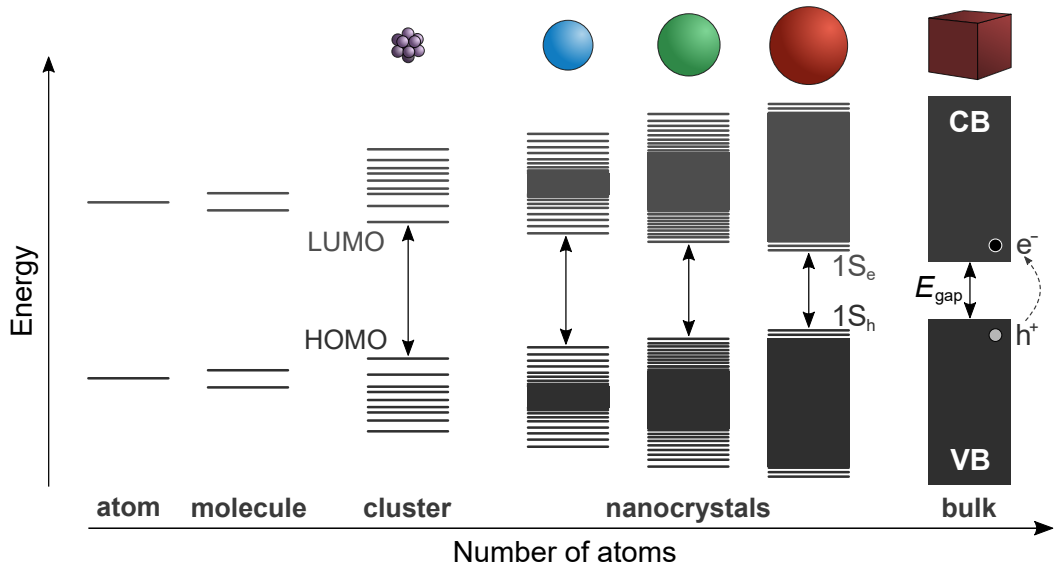

Figure 2.1: Illustration of the quantum confinement effect of nanocrystals and nanoclusters. The bandgap E_{gap} separates the CB and VB of a semiconductor. Excitation results in the formation of excitons (e^--h^+ pairs). For NCRs, E_{gap} increases with decreasing particle size. $1S_e$ and $1S_h$ correspond to the CB and VB edges. For metal NCLs with a limited number of atoms, a band gap occurs, separating the HOMO and LUMO, such as in molecular compounds.

2.1.1.2. Lead(II) sulfide nanocrystals

One of the most extensively investigated NCR systems are lead(II)sulfide (PbS) NCRs, as their bandgap can be tuned throughout the near-infrared region of $\sim$ 600–3000 nm (2.1 eV $< E_{gap} <$ 0.41 eV).[17,54,55,74–78] The band gap of bulk PbS with $E_{gap} = 0.41$ eV and the exciton Bohr radius of 18 nm lead to strong quantum confinement in PbS NCRs.[54] PbS NCRs consist of an ionic crystal featuring a rock salt structure and typically exhibit a cuboctahedron shape, which is composed of eight {111} and six {100} facets.[34,56] Commonly, PbS NCRs are capped with oleic acid (OA) ligands.[70] Due to the difference in the surface termination, the OA ligand binding is much stronger on the Pb^{2+}-terminated {111} facets than on the nonpolar {100} facets.[15,56,79] Figure 2.2 displays a typical $\sim$ 5 nm PbS NCR.

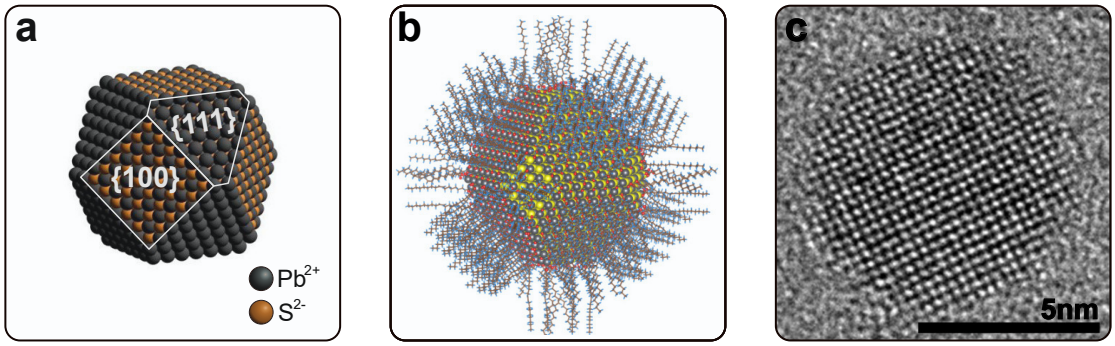

Figure 2.2: Model of a colloidal PbS NCR. (**a**) Illustration of a cuboctahedron-shaped PbS NCR exhibiting a rock salt atomic structure and differently terminated {111} and {100} facets. (**b**) Calculated atomic structure of a 5 nm sized PbS NCR passivated with OA ligands. (**c**) High-resolution transmission electron micrograph of an individual PbS NCR capped with OA ligands. A cubic atomic structure can be identified. [(a) Adapted with permission from Boles et al.[70] (Copyright 2016, Springer Nature). (b) Adapted with permission from Zherebetskyy et al.[56] (Copyright 2014, The American Association for the Advancement of Science). (c) Adapted from Weidman et al.[55] (Copyright 2014, America Chemical Society).]

Contrary to molecular species, NCRs exhibit an inherent size distribution, meaning that they are never exactly identical in size, i.e. number of atoms, and structure. The most homogeneous semiconductor NCRs today still feature a size distribution of $\sim 4\%$.[55,72,80,81] Due to their strong size-dependent quantum confinement, a distribution of NCR sizes results in a distribution of energy levels. Thus, this size inhomogeneity is a distinct disadvantage in terms of a fundamental understanding of NCRs and their technological application.

2.1.2. Atom-precise metal nanoclusters

In contrast to colloidal NCRs, ligand-stabilized atom-precise metal NCLs feature uniformity in size, composition and ligand coverage and are typically sized in the range of $\sim$ 1–3 nm.[62,82] While bulk metals and large metal nanoparticles have a continuous band of energy levels resulting in plasmonic states, the finite number of atoms in metal NCLs causes discrete energy levels due to quantum confinement, as illustrated in Figure 2.1.[3,83] For metals, the quantum size effect can be explained by considering the de Broglie wavelength of an electron at the Fermi energy, which is material specific and is ~ 0.5 nm for gold.[84] Thus, reducing the size of metal nanoparticles approaching the de Broglie wavelength, an evolution from plasmonic to excitonic states occurs.[85] This is manifested by discrete energy levels and the existence of highest occupied molecular orbitals (HOMO) and lowest unoccupied molecular orbitals (LUMO), separated by

a band gap E_{gap}.[19,82] Accordingly, NCLs bridge the gap between semiconducting molecules and NCRs.[19]

2.1.2.1. Gold nanocluster

In recent years, a wealth of atomically precise NCLs has been synthesized from various materials, with gold NCLs being established as very promising model systems.[86] One of the first and most prominent representatives of this material class is the Au_{55} NCL ($Au_{55}(Ph_3P)_{12}Cl_6$), synthesized by Schmid et al. in 1981.[87] Due to geometric considerations, the structure is assumed to feature a closest packing of 55 Au atoms, forming a cuboctahedron core of $\sim$ 1.4 nm.[3,87] However, this structure could not be verified experimentally yet. Another prominent gold NCL is the structurally fully characterized Au_{25} NCL ($Au_{25}(SR)_{18}$, R = 2-phenylethanethiole).[19,88–90] This consists of a central Au atom surrounded by an Au_{12} icosahedron plus an outer shell of 12 Au atoms. The Au-Au bond lengths differ from that of bulk gold. This clearly shows that NCLs are not just a fraction of the bulk material, but rather have their unique structural features determining their physicochemical properties.[82,83,86] There are numerous gold NCLs with different ligand protection, ranging from Au_{13}[91], Au_{21}[64], Au_{108}[92] to Au_{246}[93] or Au_{279}[94], just to name a few examples.[82,86]

In general, many NCLs, not only gold NCLs, exhibit a "magic number" behavior, meaning that clusters with certain characteristic numbers of atoms are more stable.[19,95–97] The category of metalloid clusters defines clusters that have more direct metal-metal contacts than metal-ligand contacts, and contain metal atoms that participate exclusively in metal-metal interactions.[98,99]

2.1.2.2. $Au_{32}(^nBu_3P)_{12}Cl_8$ nanocluster

A recently investigated atom-precise NCL is $Au_{32}(^nBu_3P)_{12}Cl_8$ (Au_{32}).[100] Its structure is displayed in Figure 2.3a. Here, the core consists of a hollow Au_{12} icosahedron, surrounded by a shell of 20 Au atoms arranged in a pentagon dodecahedron. This Au_{32} core is $\sim$ 0.9 nm large and slightly distorted due to electronic reasons.[100] The third shell consists of eight chlorine atoms in a cubic arrangement and 12 tri-butylphosphine ligands, where the phosphorous atoms bound to the outer Au shell form an icosahedron.[100] Including the ligand shell, this building block has a full size of $\sim$ 1.4 nm (Figure 2.3b). Due to its stability, good solubility, easily reproducible synthesis and high yield, this atom-precise NCL is an ideally suited model system for this thesis.

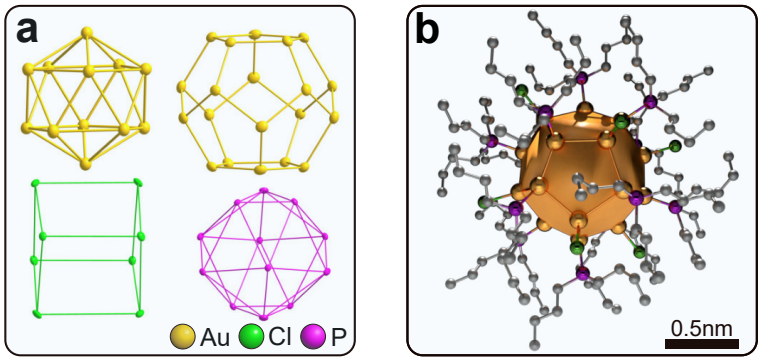

Figure 2.3: Model of the atomically precise Au_{32} NCL. (**a**) Structure of the Au_{32} core (yellow), consisting of an inner hollow Au_{12} icosahedron (left) and an outer Au_{20} pentagon dodecahedron. The eight chlorine atoms (green) form a cubic arrangement and the phosphor atoms (purple) of the 12 phosphine ligands form an icosahedral arrangement. Carbon and hydrogen atoms of the ligands are omitted for clarity. (**b**) Structural drawing of the atom-precise $Au_{32}(^{n}Bu_3P)_{12}Cl_8$ NCL with a core size of ~ 0.9 nm. The different colors represent the Au- (gold), Cl- (green), P- (purple) and C- (grey) atoms. Hydrogens are omitted for clarity. [(a) Adapted with permission from Kenzler et al.[100] (Copyright 2019, Wiley).]

The building blocks used in this thesis were kindly provided. PbS NCRs were synthesized according to Weidman et al.[55] by Dr. Michelle Weber, former member of the research group of Marcus Scheele. Au_{32} NCLs were synthesized by Florian Fetzer, collaboration partner and member of the research group of Andreas Schnepf (University of Tübingen), according to their developed synthesis route.[100] A detailed description of the general concepts and experimental approaches on the synthesis of (PbS) NCRs and (Au) NCLs is beyond the scope of this thesis and given elsewhere.[19,55,72,76,82,83,100–102]

In summary, the size-dependent properties of semiconducting NCRs and metal NCLs can be used to generate a wide variety of building blocks. Especially the versatile PbS NCRs are of particular interest as one of the best investigated model systems. However, NCRs in general feature an inherent size distribution, which is a distinct disadvantage. This can be circumvented by using atom-precise NCLs featuring size uniformity, such as Au_{32} NCLs. Together with their discrete energy levels due to the quantum size effect, they represent the transition from semiconducting molecules to semiconducting NCRs.

2.2. The concept of self-assembly

NCRs can be used as building block to form larger complex ensembles or superstructures, expected to exhibit novel collective properties. Such structures are usually obtained by the spontaneous self-assembly of the building blocks.[103,104] Self-assembly is a bottom-up process where individual components organize themselves into an ordered structure.[105]

The following Section aims to provide a rough theoretical overview of the process of self-assembly and the underlying mechanisms and is based on the comprehensive articles of Pileni[22], Vanmaekelbergh[103], Boles et al.[71], Min et al.[106] and Bishop et al.[23]

2.2.1. Theoretical considerations

The driving force of self-assembly, regardless of the NCRs and the preparation method, is the minimization of the Gibbs free energy ΔG. The difference in Gibbs free energy between the assembled state and the initial state has to be $\Delta G < 0$. According to Equation (2.2.1), either a decrease in enthalpy ΔH and/or an increase in entropy ΔS can accomplish the lowering of ΔG (for constant temperature T).

$$\Delta G = \Delta H - T\Delta S \tag{2.2.1}$$

Considering NCRs as hard spheres, no interparticular interactions are present and thus, self-assembly occurs solely due to an increase of ΔS. This somewhat counter-intuitive phenomenon can be explained by a gain in accessible free volume available to each particle through the formation of a crystalline state compared to a jammed state, as depicted in Figure 2.4a.[71,103] Due to the more efficient packing in the ordered state, each particle has a larger volume to wiggle and thus, the total number of possible configurations is enhanced, resulting in $\Delta S > 0$.

Additionally, interparticle interactions need to be taken into account for colloidal NCRs with ligand-stabilization. A decrease in enthalpy by interparticular interactions in the NCR assembly compared to diluted NCRs represent the enthalpic contribution. The interactions can be of different kind depending on the NCR core, the ligand shell and the self-assembly conditions. Some of the typical interparticle forces are van der Waals forces, steric repulsion, electrostatic interaction and capillary forces, illustrated in Figure 2.4b–d. The magnitude of the interparticle interactions do not greatly exceed the thermal energy $k_{\mathrm{B}}T$.

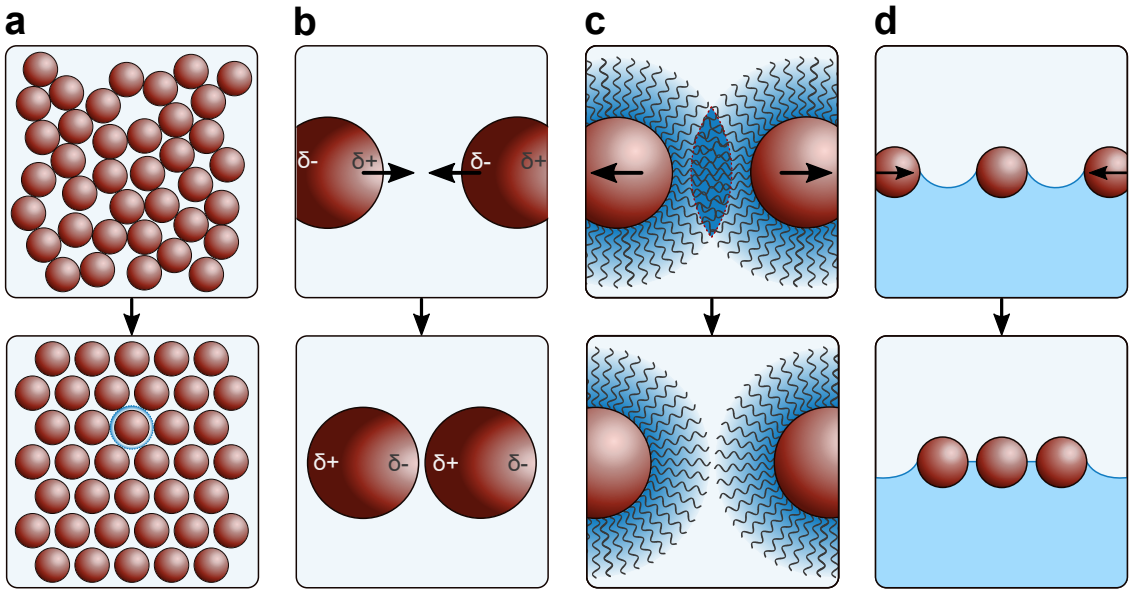

Figure 2.4: Schematic illustration of different interparticle interactions. (**a**) Entropic forces: For hard spheres the entropy is increased ($\Delta S > 0$) by assembling into crystalline state, caused by a gain in accessible free volume, indicated for one sphere in blue. (**b**) Van der Waals attraction: Charge density fluctuations create induced dipoles (δ^+ and δ^-), resulting in an attractive force of NCR cores. (**c**) Steric repulsion: Overlapping ligand shells of adjacent NCRs result in a repulsive force, preventing NCR agglomeration. (**d**) Capillary forces: Adsorption of NCRs at an interface cause distortion, resulting in an induced attractive force.

Van der Waals forces arise between all atoms due to interactions between electric dipoles, including induced dipoles originating from charge density fluctuations, which lead to attractive forces between identical NCRs. Thus, uncoated NCR tend to agglomerate caused by attractive van der Waals forces.

To prevent agglomeration, counteracting repulsive forces are required, which are generally obtained by modifying the particle surface. Shells formed by soft capping ligands can interact with one another through deformation. This results in repulsive forces in good solvents, which keep the NCR cores at a considerable distance so that core-core attraction remains weak. During self-assembly, the steric interaction energy can be reduced by close packing, deformation of the ligand shells and interdigitation of the ligands from adjacent NCRs. Besides, colloidal NCRs can also be electrostatically stabilized by adsorption of charged species, which balance the oppositely charged NCR surface.

Additionally, other forces related to the environment of the self-assembly process may be present. For instance, capillary forces come into play when the NCR dispersion is spread onto a liquid surface/interface.[107] The adsorption of the NCRs cause a distortion

of the interface due to preferred adsorption depths and wetting angles, which in turn can induce attractive capillary forces on neighboring NCRs. Further possible interactions (e.g. convective, shear or electromagnetic forces, as well as NCR-substrate interactions) and their complex interplay during self-assembly can be found detailed in the above mentioned reviews.[22,23,71,103,106] By considering additional chemical interactions, such as cross-linking ligands, the problem becomes even more complex.

Generally, both a maximization of entropy ($\Delta S > 0$) and a minimization of the enthalpic contribution ($\Delta H < 0$) drive the spontaneous process of NCR self-assembly.

2.2.2. Degree of structural order

Regardless of the symmetry of the resulting assemblies, different degrees of structural order can be theoretically classified, which are schematically illustrated in Figure 2.5 for hard spheres.

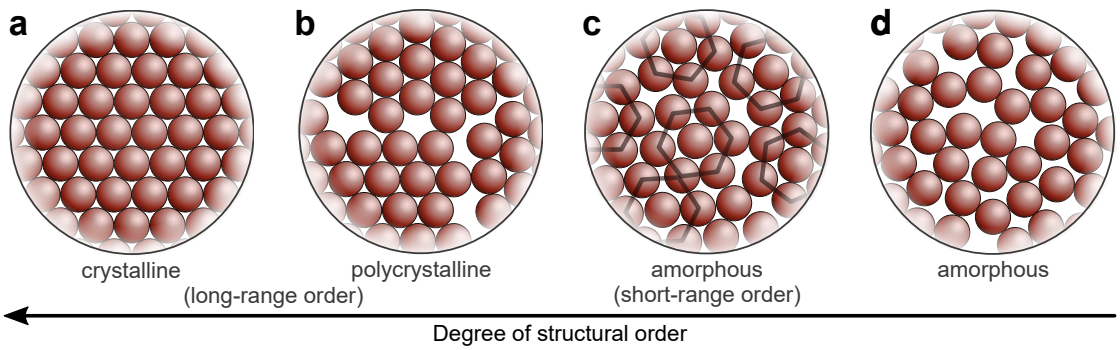

Figure 2.5: Illustration of different degrees of structural order: (**a**) (Mono-) crystalline and (**b**) polycrystalline ensemble with long-range order, (**c**) amorphous/glassy ensemble with short-range order and (**d**) fully amorphous ensemble of hard spheres. The degree of structural order is increasing from right to left.

Here, the degree of structural order is increasing from right to left, starting from a fully amorphous state, where no order is present. If the building blocks exhibit some preferential local order over spatial dimensions that are typically on the order of the nearest neighbor spacing, short-range order is achieved.[108] Thus, each building block is surrounded by the same number of the nearest neighbors and the distribution of nearest-neighbor spacings is narrow, meaning the assembly is close-packed.[67,69]

If order over distances much larger than the unit cell is present, the structure is long-range ordered and features translational periodicity.[67,109] An assembly consisting of several domains which are separated by disruptions in the crystalline packing, so-

called grain boundaries, is referred to as polycrystalline. The domains can have different expansions and orientations.[68,71] However, if the assembly consists of a single periodic lattice of long-range ordered building blocks, it is called a monocrystalline material.

For NCR SLs, the degree of structural order can additionally be determined by the orientation of the non-spherical individual building blocks within the crystalline assembly. In mesocrystalline materials, the individual NCRs are iso-oriented, so the degree of structural order is considered higher than in a similar SL with randomly oriented NCRs (orientational order).[36,110,111]

2.2.3. Practical implementations

Several experimental techniques are reported in literature for the self-assembly of NCRs.[20,112] To investigate the (opto-)electronic properties of NCR assemblies, they are commonly fabricated in the form of thin films.[4,20] For this purpose, the solvent evaporation-induced self-assembly is the most appropriate method, comprising the techniques of drop-casting, spin-coating, dip-coating and the assembly at the liquid/air interface, as illustrated in Figure 2.6.[71]

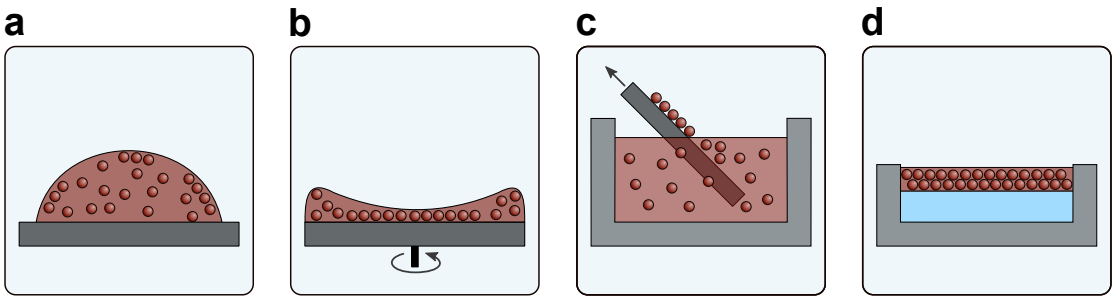

Figure 2.6: Schematic illustration of evaporation-based self-assembly methods: (**a**) drop-casting, (**b**) spin-coating, (**c**) dip-coating, (**d**) self-assembly at the liquid/air interface.

Besides predominantly attractive interactions (e.g. due to a lack of ligand passivation), several other factors – such as a large NCR size dispersity, a fast solvent evaporation rate or a poor NCR solubility in a given solvent – favor the formation of glassy assemblies with short-range order or fully disordered structures.[23,67,72]

Usually, densely packed NCR thin films with short-range order can be easily obtained by drop-casting, where the NCR dispersion is placed on a solid substrate and the solvent evaporates, by spin-coating, where the sample is rotated to spin off the excess solvent, and by dip-coating, where the substrate is dipped in a NCR dispersion.[67,113] The film thickness can be controlled by the properties of the dispersion, such as the

NCR concentration, the rotation speed (in case of spin-coating) and by the number of dips (in case of dip-coating).

Obtaining long-range ordered assemblies requires the system to reach its thermodynamically favourable state ($\Delta G < 0$) instead of a potential kinetically (disordered) state.[68,69,72] A common technique to fabricate long-range ordered NCR SL films is the assembly at the liquid/air interface,[35,59,60,114–118] as the formation of long-range ordered assemblies and an increase in domain size seems to require conditions that minimize the interaction between NCRs and the substrate during self-assembly.[22,37,69,71,106] Here, a small volume of NCR dispersion is drop-cast on top of an immiscible liquid allowing a dynamic self-assembly process during solvent evaporation.[69,114] The free-floating film can readily be transferred onto arbitrary substrates via scooping,[119] the Langmuir-Blodgett technique[120], contact printing, the Langmuir-Schaefer technique[112,121,122] or the retraction of the liquid subphase to deposit the thin film on an immersed substrate[123–125]. Further, the liquid/air interface method is well suited to perform an *in situ* ligand exchange of the free-floating thin film by introducing the ligand into the liquid subphase.[60,119,122,126]

This Section has introduced the theoretical framework of NCR self-assembly, which is driven by a minimization of the Gibbs free energy. This can be achieved by both an increase in entropy and a lowering of enthalpy. The enthalpic contribution mainly arises from interparticle interactions, as described above. Further, the degree of structural order – ranging from fully amorphous to highly ordered crystalline structures – can be tuned, which was experimentally shown in literature. However, controlling the self-assembly processes is far from trivial, which renders the targeted production of NCR assemblies with specific properties considerably tricky.[23,67] In the next Section, a concept of describing highly ordered NCR assemblies is provided.

2.3. Self-assembled superlattices

As shown above, building blocks, ranging from atomically precise NCLs with diameters on the order of 1–3 nm to larger inorganic NCRs with diameters of up to tens of nanometers, can be self-assembled into solid ensembles.[62,72,96] If such an assembly consists of a regular crystal-like (three-dimensional) arrangement of the NCRs, it is called a "SL".[24,26] One prerequisite for the self-assembly into ordered SL is a sufficiently narrow size distribution of the NCRs of $< 10\%$.[24,67,115,127] Once assembled, SLs are expected to exhibit emergent collective properties, differing from those of the individual building blocks, caused by quantum mechanical and dipolar coupling between the individual NCRs.[2,29,30,69,128,129]

2.3.1. Colloidal nanocrystals as building blocks

There is a variety of reports of SLs from colloidal NCRs adopting three-dimensional arrangements with standard crystal structures, such as body-centred cubic (bcc), face-centred cubic (fcc) and hexagonal close-packed (hcp) lattices.[81,116,130–135] Here, the NCR SLs can be described by a single unit cell and the nearest-neighbor distance of the respective unit cell defines the center-center distance of the NCRs.

The following takes a closer look at PbS NCRs, which are used in this thesis as a model system and are unarguably among the best understood systems.[33,34,36,37,81,136–144] Whereas the thermodynamically preferred structures are those of hcp and fcc SLs, bcc SLs are also observed.[31,130,134,136,141,145–147] PbS NCRs passivated by a ligand shell of oleic acid (OA) behave as hard spheres with short-range attraction and form a close-packed SL with fcc symmetry, together with a random orientation of the NCR cores. In contrast, the same NCRs with an incomplete passivating ligand shell form a bcc SL, where the NCRs are orientally aligned,[130] as displayed in Figure 2.7a,b. This is attributed to a preferred ligand coverage on the {111} NCR facets, resulting in a better ligand interaction between adjacent NCRs in the bcc lattice together with an increased NCR core interaction.[34,77,130,134,136,139–141,143,148] This transition from fcc to bcc is very well known from atomic lattices as the Bain path.[130] The fcc lattice is transformed to the bcc lattice by an uniaxial contraction (also called Bain distortion), with the intermediate state of the body-centred tetragonal (bct) lattice, as illustrated in Figure 2.7c. The transformation along the Bain path can be tuned to arrest the PbS NCR SL in the intermediate bct lattice by tuning the solvent evaporation rate, changing the interparticle distance or by functionalization with π-conjugated ligands.[33,34,36,130,138]

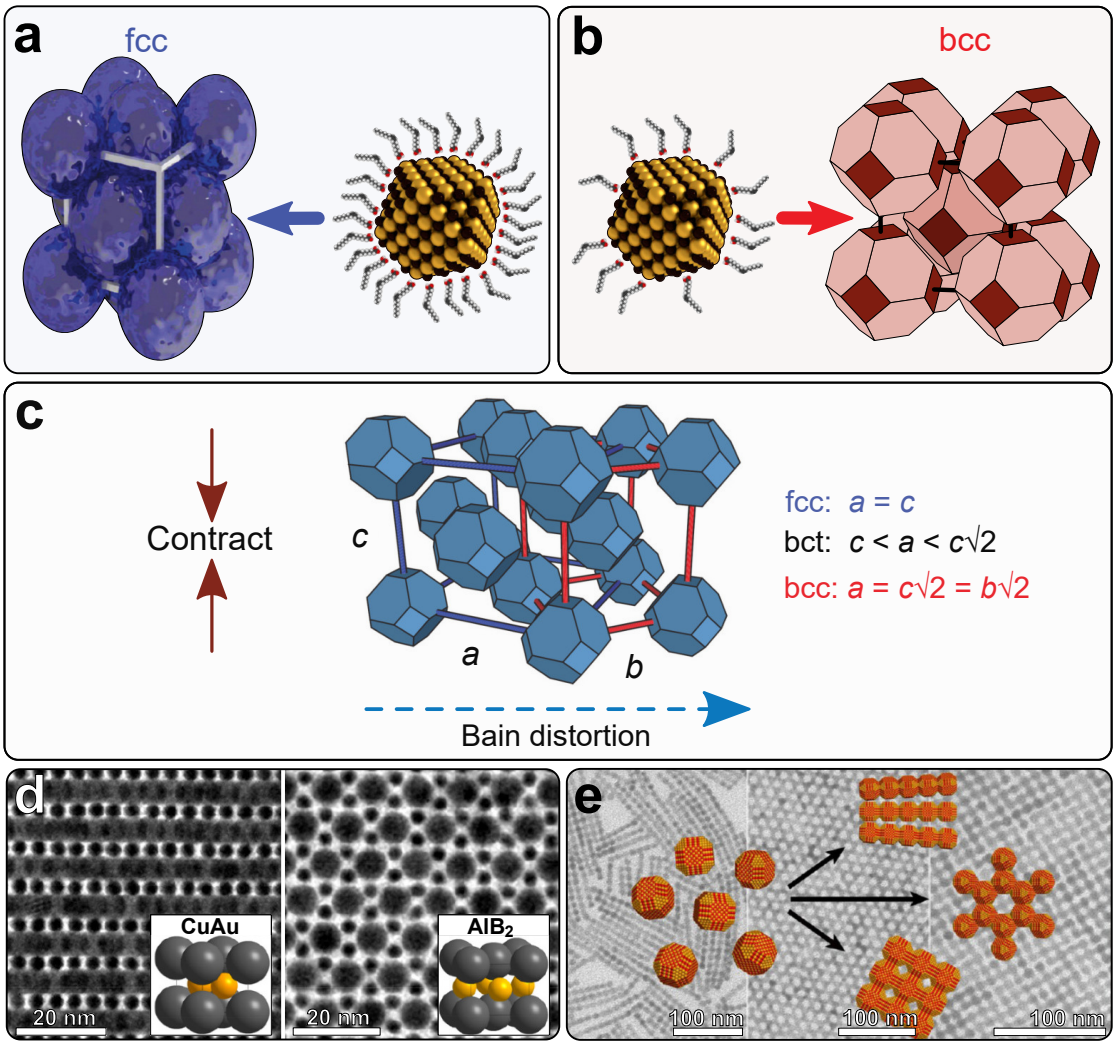

Figure 2.7: Illustration of different SLs formed by colloidal NCRs. (**a**) Completely passivated PbS NCRs behave as hard spheres, forming a close-packed fcc SL with random orientation of the NCR cores, (**b**) whereas incomplete ligand passivation results in a bcc SL with coherently oriented NCR cores, caused by improved core-core interactions. (**c**) Model of the fcc (blue) and bcc (red) unit cells related via the Bain distortion. The uniaxial contraction along axis c transforms a fcc lattice to a bcc lattice through bct intermediate states. The corresponding ratios of unit cell axes are given. (**d**) Structure of binary NCR SLs formed from 7.5 nm PbS and 3.1 nm Au NCRs. Transmission electron micrographs of a CuAu-type binary SL with (100)-orientation (left) and a AlB_2-type binary SL with (001)-orientation, where the PbS NCR have a higher ligand passivation (right). Insets depict the respective unit cells (grey: PbS, yellow: Au). (**e**) Transmission electron micrographs of atomically attached PbSe NCR SLs. Oriented attachment along specific crystal facets results in linear (left), square (middle) or honeycomb (right) lattices. [(a,b) Adapted with permission from Choi et al.[136] (Copyright 2011, American Chemical Society). (c) Adapted with permission from Zhang et al.[149] (Copyright 2016, Nature Publishing Group). (d) Adapted with permission from Boles et al.[150] (Copyright 2019, American Chemical Society). (e) Adapted with permission from Evers et al.[117] (Copyright 2013, American Chemical Society).]

SLs can not only differ by their SL symmetry and axes lengths, but also by the orientation of the individual NCRs. As described above, in the reported bcc and bct SLs, the PbS NCRs are iso-oriented. This means that the atomic lattices of the individual PbS NCR core are oriented the same (at least to a certain degree of misalignment).[34,36] Such SLs containing iso-oriented NCRs are referred to as mesocrystals.[59,110,151,152]

Next to SLs with classical symmetry, binary SLs with more sophisticated structures were also reported, as depicted in Figure 2.7d. Here, two sizes of different NCRs self-assemble into a SL, where the packing symmetry depends on the size ratio of the NCRs, as well as the NCR and ligand interactions.[127,150,153–155]

Additionally to three-dimensional SLs, highly ordered monolayers of NCRs could also be counted as a subclass of SLs.[123,156–158] Recently, two-dimensional SLs were reported, where the individual PbS or PbSe NCRs are atomically connected along specific crystal facets by oriented attachment. Here, the controlled ligand displacement on certain facets yields fused NCRs by atomic bondings. This creates highly ordered low-dimensional SLs of various geometries, such as square and honeycomb lattices or one-dimensional linear and zigzag structures or even dimers, as illustrated in Figure 2.7e.[111,117,159–163] These are very promising candidates for materials with emergent optoelectronic properties.

2.3.2. Atom-precise nanoclusters as building blocks

The SLs of colloidal NCRs intrinsically lack atomic precision and exhibit a complex surface chemistry, which renders them challenging for a controlled design and fabrication.[68,164] Thus, atom-precise NCLs are an attractive subset of building blocks, sometimes referred to as superatoms and the corresponding SLs as superatomic crystals.[62,165]

The great advantage of NCL SLs over colloidal NCR SLs is their precisely known composition and symmetry, achieved by crystallization.[166,167] Commonly, the total structure of the NCL core and ligand shell as well as the three-dimensional arrangement is determined by single crystal X-ray crystallography.[19,167] Due to the atomic precision, SLs of NCLs are essentially molecular crystals, albeit with large unit cells.[26] Here it should be noted that in this thesis “nanocrystal superlattice” is used synonymously for the terms “nanocluster crystal” and “superatomic crystal” found in literature.
In a seminal work by Schmid et al., highly ordered SLs of Au_{55} NCLs featuring a fcc

structure were obtained[168], followed by the preparation of highly ordered monolayers.[169] Further, a structure formation similar to the oriented attachment process of NCRs was observed for Au_{55} NCLs upon ligand removal.[170]

In contrast to larger NCRs, which are typically packed in SLs with simple translational symmetry (e.g. hcp, fcc, bcc), atomically precise NCLs can pack into more complex lattices, such as monoclinic or triclinic, which are driven by specific interparticle interactions.[88,167,171] Further examples and a detailed description of the assembly of atom-precise NCLs into solid structures can be found in literature.[21,64,66,96,97,129,167,171–173]

This Section clearly illustrates how structural order and the symmetry of the SLs can be varied by adjusting various parameters, such as NCR size and shape, ligand shell, solvent, evaporation time, preparation method and many more. Further it is shown that the assembly of atom-precise NCLs bears the potential of SL formation with atomic precision.

2.4. Charge transport in nanocrystal ensembles

In this Section, first a brief theoretical description of charge transport is given. Then, experimental implementations and strategies reported in literature to control the interparticle electronic coupling are provided, followed by a comprehensive discussion of previous studies about the influence of structural order on the electronic properties of NCR ensembles.

2.4.1. Theoretical description

The brief introduction to the theoretical description of charge transport is based on several references, in which further details can be found, that have been omitted in this thesis for the sake of clarity. [27,28,45,58,67,69,174–179]

2.4.1.1. The interplay of energetic parameters

From an energetic point of view, the charge transport in NCR ensembles is determined by the interplay of three parameters: the transfer integral β, the charging energy E_C and the energetic disorder $\Delta\alpha$.

Simplified, the electronic structure of an individual NCR can be described by a discrete quantum confined wave function localized within the particle. The wave functions of two adjacent NCRs may overlap when the NCRs are in close proximity, allowing the electrons to tunnel. This quantum mechanical coupling can be expressed by the transfer integral β, given in Equation (2.4.1):

$$\beta \approx h\Gamma \quad , \tag{2.4.1}$$

where h is the Planck's constant and Γ the tunneling rate between two adjacent NCRs. The tunneling rate Γ depends exponentially on the tunneling width Δx, being the interparticle distance, and the square root of the tunneling barrier height ΔE, defined by the interparticular medium, as given in Equation (2.4.2):

$$\Gamma \approx \frac{2E_A}{h} \cdot \exp\left(-2\sqrt{\frac{2m^*\Delta E}{\hbar^2}}\Delta x\right) \quad , \tag{2.4.2}$$

with the activation energy E_A, the charge carrier effective mass m^* and $\hbar = h/2\pi$.

The energy required for an actual charge transfer process, described by the charging energy E_C, is referred to as the self-capacitance of the NCR. In a simplified form, E_C can be approximated as given in Equation (2.4.3):

$$E_C \approx \frac{e^2}{4\pi\varepsilon_0\varepsilon_r r} \quad , \tag{2.4.3}$$

with the NCR radius r and the dielectric constant of the environment $\varepsilon_0\varepsilon_r$. Thus, the NCR size and the dielectric constant of the interparticular medium inversely affect the charging energy. A formula describing E_C of a NCR assembly more realistically is given in Chapter 5, Equation (S5.13,S5.14). In order to transfer a charge carrier from one NCR to another, the Coulomb or Hubbard gap $E \approx 2E_C$ must be overcome, as illustrated in Figure 2.8a. This suppresses charge transport at low biases, referred to as the Coulomb blockade, which can be overcome at higher biases.[180]

As the third parameter, the energetic disorder $\Delta\alpha$ is introduced, representing a measurement of the dissimilarity of adjacent NCRs, acting against a collective behavior.[174] These inhomogeneities are introduced by the NCRs themselves via variations in size, shape and composition, and by the ensemble via variations in interparticle distances and structural order.

To understand how disorder or order, affects the electronic structure and thus charge transport within NCR ensembles, the interplay of the three energetic parameter $\Delta\alpha$, β and E_C needs to be evaluated. This creates two limiting cases: the Mott regime, where $E_C > \Delta\alpha$, and the Anderson regime, where $E_C < \Delta\alpha$.

In the regime of very low disorder, where $E_C > \Delta\alpha$, the Mott metal-insulator transition can occur, caused by electrostatic effects. For large interparticle spacings Δx, the transfer integral β cannot overcome the charging energy E_C ($\beta << E_C$), resulting in an insulating NCR ensemble due to only weak interparticle coupling (Mott insulator). Here, sequential tunneling and temperature activated hopping occurs. As the interparticle separation decreases, electronic coupling becomes significant due to the increasing transfer integral. If $\beta > E_C$, the coupling overcomes the carrier localization, the Coulomb gap disappears and the wave functions of individual NCRs extend throughout the ensemble and form a delocalized electronic state. This is known as the Mott metal-insulator transition. A schematic illustration is given in Figure 2.8a.

In the Anderson regime, where $E_C < \Delta\alpha$, the Anderson metal-insulator or localized-to-delocalized transition can occur, caused by disorder effects. This depends on the relative strength of the transfer integral with respect to the disorder of the system.

For $\Delta\alpha > \beta$, Anderson localized states are formed, as the transfer integral cannot overcome the energetic fluctuations caused by disorder. However, these can be overcome if $\Delta\alpha < \beta$, causing the spreading of extended wave function over the NCR ensemble (Anderson delocalization). In addition, an intermediate domain-localized state between a fully localized ($\Delta\alpha > \beta$) and delocalized ($\Delta\alpha < \beta$) state can occur. Here, the system breaks into small isolated domains of strong coupling, separated by weakly coupled regions. The extension of the domain is determined by the amount of $\Delta\alpha$ and charge transfer between domains is thermally assisted.

The different regimes of electronic coupling within a NCR ensemble can be described in a simplified way by the phase diagram visualized in Figure 2.8b. Here, the interplay between the dimensionless parameter of the effective coupling strength $E_C(E_C+\beta)^{-1}$ and the disorder $\Delta\alpha$ is described. The weak coupling regime corresponds to $E_C(E_C+\beta)^{-1} \rightarrow 1$, whereas $E_C(E_C+\beta)^{-1} \rightarrow 0$ is the limit of strong coupling.

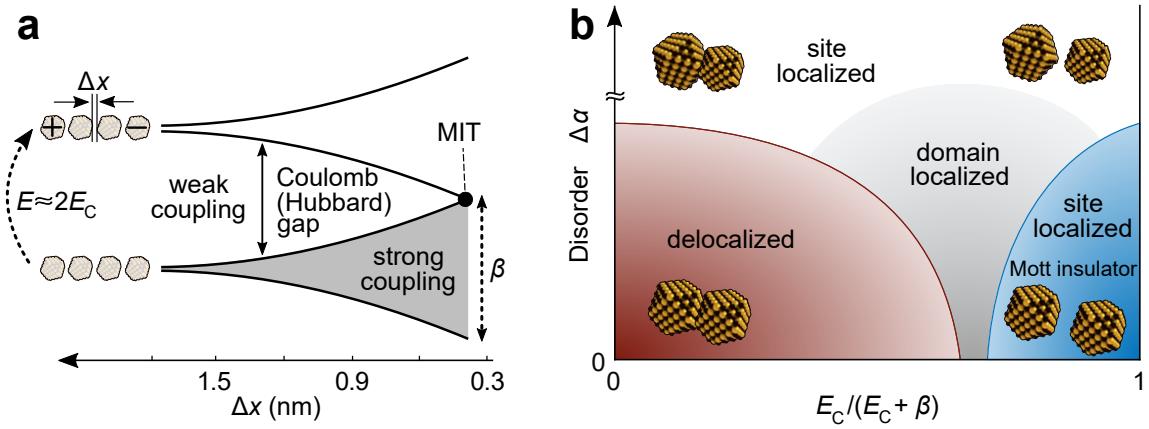

Figure 2.8: (**a**) Schematic of the electronic structure and interparticle interactions in NCR assemblies. At large interparticle distances Δx, where the transfer integral β cannot overcome the charging energy E_C (Coulomb gap), the NCRs are only weakly coupled, resulting in an insulating ensemble (Mott insulator). With diminishing Δx, β increases. At the metal-insulator transition (MIT) point, delocalized states are formed throughout the entire assembly. (**b**) Schematic phase diagram of electronic states as a function of coupling strength $E_C(E_C+\beta)^{-1}$ and disorder $\Delta\alpha$. The limits of strong and weak coupling correspond to $E_C(E_C+\beta)^{-1} \rightarrow 0$ and $E_C(E_C+\beta)^{-1} \rightarrow 1$, respectively. The interplay of the energetic parameters transfer integral β, charging energy E_C and disorder $\Delta\alpha$ define different regions of electronic states. The two NCRs in each corner sketch the structural arrangement within the ensemble. Ligand spheres are omitted for clarity. [(a) Adapted with permission from Murray et al.[72] (Copyright 2000, Annual Reviews.) (b) Adapted with permission from Remacle et al.[28] (Copyright 2001, Wiley).]

In case of very high disorder $\Delta\alpha$, the electronic states are fully Anderson localized, whereas for reduced $\Delta\alpha$, interparticle coupling and delocalization can occur. The Anderson metal-insulator transition therefore proceeds along the vertical direction. In contrast, for very low $\Delta\alpha$, Coulomb charging effects can cause the Mott metal-insulator transition from a delocalized to a site-localized state along the horizontal direction. However, the two extremes of fully delocalized and site-localized states are separated by an intermediate region, where the wave function is localized over single domains of finite size.

2.4.1.2. Band-like transport

Theoretically, in the regime of strongly coupled NCRs, band-like transport may occur. In this regime, the coupling between adjacent NCRs through delocalized states could be comparable to the coupling of individual atoms within a solid, forming an energy continuum or band.[27] For this reason, NCRs are often referred to as artificial atoms, whose strongly coupled ensembles form artificial solids.[26] Characteristic for band-like transport is a high charge carrier mobility of $\mu > 10$ cm^2 V^{-1} s^{-1} (in comparison to $\mu < 1$ cm^2 V^{-1} s^{-1} for hopping transport), together with a conductivity σ and mobility μ inversely scaling with temperature (σ, $\mu \propto T^{-1}$).[45,67,179] Details on the measurement techniques of electronic properties are given below in Section 2.6. Completely expanded band-like structures are not to be expected, however, as even the smallest amount of $\Delta\alpha$ could prevent a full delocalization. Nevertheless, it is assumed that so called mini-bands could exist in highly ordered domains of finite size.[43]

2.4.1.3. Activated hopping transport

Thermally activated hopping dominates charge transport in NCR ensembles when the interparticular coupling is weak, caused by relatively far interparticle distances of $\gtrsim 1$ nm.[26] The charge carriers hop from one NCR to its nearest neighbor along the current path.[67] Characteristically, the conductivity σ of the NCR ensemble exponentially increases with increasing temperature T since the hopping process requires phonon-assisted transitions between the localized states with different energies.[178] This can be described as an Arrhenius-type behavior, expressed in Equation (2.4.4):[181,182]

$$\sigma = \sigma_0 \cdot \exp\left(\frac{-E_\mathrm{A}}{k_\mathrm{B}T}\right) \quad , \tag{2.4.4}$$

with the activation energy E_A, the Boltzmann constant k_B and a material specific constant σ_0. Thus, E_A can be obtained from the slope of $\ln(\sigma)$ as a function of T^{-1}.

However, dependent on the complex interplay of β, E_C and $\Delta\alpha$, hopping to a site not localized at the nearest neighbor NCR may be energetically more favorable although the hopping distance is larger.[27] Different types of variable range hopping can occur, where the transport depends on the interparticle distances and the energy difference between hopping sites. Here, a non-Arrhenius behavior is present, as the conductivity σ of the NCR ensemble increases with $\ln(\sigma) \sim T^{-\kappa}$, where the constant κ is specific for the type of hopping mechanism with e.g. $\kappa = \frac{1}{2}$ or $\kappa = \frac{1}{4}$. A detailed discussion of the different variable range hopping mechanisms can be found elsewhere.[5,54,183,184]

2.4.1.4. Small polaron hopping

A mechanism of hopping transport in polar semiconductors, such as PbS or CdSe, that has recently been investigated in depth is the small polaron hopping.[48,58,185] This model has been used for years to describe charge transport in organic semiconductors and molecular crystals.[186,187]

Polarons are quasiparticles formed by a strong interaction between charge carriers and optical phonons,[188,189] causing a local deformation/polarization of the atomic lattice, as schematically illustrated in Figure 2.9a.[58,186] In case the radius of this polarization is small compared to the atomic lattice, the polaron is referred to as small. The binding energy of a polaron is given by the reorganization energy Λ.[48,58] When Λ is much stronger than the interparticle electronic coupling, the charge carrier is trapped by the phonon and charge transport occurs via hopping of small polarons between adjacent NCRs with the polaronic hopping rate ξ given in Equation (2.4.5):[48,58,61,185]

$$\xi \approx \frac{\beta^2}{\hbar} \cdot \sqrt{\frac{\pi}{\Lambda k_B T}} \cdot \exp\left(- \frac{(\Lambda + \Delta E)^2}{4 \Lambda k_B T} \right) \quad , \tag{2.4.5}$$

where ΔE is the potential barrier height.

For PbS NCRs, the polaron formation takes place at the ligand-functionalized NCR surface.[48] Thus, charge transfer between NCRs implies a rearrangement of surface atoms, where the bond length between the ligands and surface atoms are slightly elongated/shortened to stabilize the polarons of electrons/holes.[48,61] This is schematically depicted in Figure 2.9b. Since the surface ligands are typically anionic, they affect the polaron propagation within the NCR ensemble by electrostatic interactions.[190] Due to differing ligand densities for distinct facets – such as for PbS NCRs, where

oleic acid is significantly stronger bound to the {111} than to the {100} facets[56,162,191] – a facet-specific interaction potential is created.[48,61,189] In accordance, the calculated coupling energy for a bcc PbS NCR SL along the [100] directions is about one order of magnitude larger than along [111]. Hence, a direction-dependent anisotropic charge transport can be predicted for long-range ordered SLs.[48,61]

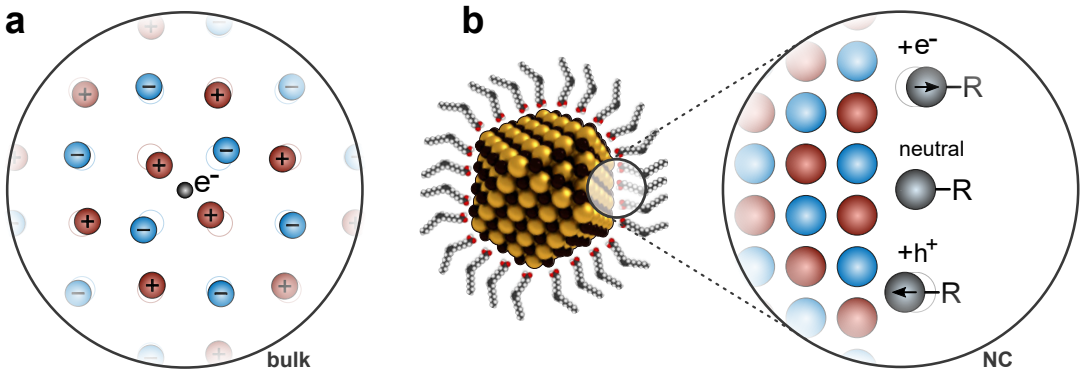

Figure 2.9: Schematic of polarons. (**a**) In bulk, the strong interaction between charge carriers and phonons create a deformation of the atomic lattice, referred to as polaron. (**b**) In polar NCRs, the polaron consists of a surface atom rearrangement, specifically an adjustment of the bond length between the (anionic) ligand and the NCR surface. Polarons of electrons (e^-) cause an elongation of the ligand (R) bond, whereas holes (h^+) cause a contraction. Consequently, charge transport in NCR ensembles occurs via small polaron hopping.

There is a reasonable assumption that this charge transport mechanism also applies to NCLs, which are the bridging element between organic semiconductor molecules and semiconducting NCRs. In semiconducting molecules, polarons are formed due to a charge induced deformation of the conjugated molecule.[187,192] Similar deformations have recently been observed for Au_{25} NCLs due to the influence of the addition or removal of an electron.[90,193] Furthermore, electron-phonon interactions in Au_{25} and Au_{38} NCLs are subject of current research.[194] Consequently, the small polaron hopping model might be applicable for Au NCLs.

2.4.2. Experimental implementations

After having introduced a theoretical description of charge transport in NCR assemblies, the following provides an overview of experimental approaches in order to understand and control electronic properties. First, the influence of the ligand sphere and the interparticle distance is elucidated, followed by a comprehensive discussion of previous studies on the influence of structural order.

2.4.2.1. Influence of interparticle distance & ligands

The collective electronic properties of NCR ensembles have been the focus of numerous studies conducted to explore charge carrier transport and a possible evolution from hopping to band-like transport.[69] The native ligand shell of colloidal NCRs restricts an effective interparticle coupling due to long chain lengths and wide band gaps, creating transport barriers of considerable width and height, which in turn results in insulating NCR ensembles.[5,58] A typical strategy for improving the electronic coupling between NCRs is to shorten interparticle distances by replacing these native ligands by various shorter ligands, such as organic[6,113,195–197] or inorganic molecules.[5,11,39,198–201]

Charge carrier transport is most commonly investigated by means of conductivity and field-effect transistor (FET) measurements (see Section 2.6 for technical details). In a seminal work by Talapin et al.[5] the conductivity of PbSe NCR solids was improved by ~ 10 orders of magnitude by the use of hydrazine as a small cross-linker, shortening the interparticle distance from $\sim$ 1.1 nm to ~ 0.3 nm. Thus, ligand exchange has become a popular means to control interparticular distances and enhance the charge carrier mobilities of NCR FETs.[6,31,197] With this, semiconductive NCR assemblies with charge carrier mobilities of $\mu \approx 10^{-4}$ cm^2 V^{-1} s^{-1} up to exceedingly high values of $\mu \approx$ 1–24 cm^2 V^{-1} s^{-1} were achieved.[5,6,39,42,197,200]

By cross-linking PbSe NCRs with bidentate alkanedithiol-ligands of various lengths, Liu et al. have proven – as theoretically expected[28,202] – that the carrier mobility and thus the interparticle coupling increases exponentially with decreasing ligand length.[25] This exponential relation between the interparticular coupling and ligand length was further verified for semiconductive NCRs by other techniques.[196,203] Such an exponential decay of the conductivity with increasing ligand lengths was also reported for small Au cluster with ~ 1 order of magnitude per Å.[38,204] Larger Au nanoparticles feature the same behavior together with a metal-insulator transition for interparticle spacings of $\lesssim$ 0.5–0.7 nm.[205,206] Besides the described usage of different ligands, the oriented attachment of adjacent NCRs (mainly lead chalcogenides) results in honeycomb or square lattice structures, where comparable improvements of the interparticular coupling can be obtained.[35,117,160,207,208] These low-dimensional SLs exhibit high charge carrier mobilities in the range of $\mu \approx$ 0.2–13 cm^2 V^{-1} s^{-1}.[53,207,209]

Although NCR assemblies can indeed exhibit very high carrier mobilities as discussed above, it is heavily debated in literature whether or not band-like transport has been achieved in semiconductive NCR SLs so far.[11,45,179,185,210–212]

However, these strategies for improving interparticular coupling by replacing or removing long native ligands have the decisive disadvantage of volume reduction, which creates cavities and cracks within the NCR assemblies.[6,69,213,214] This breaks the SL symmetry and inherently prevents distinct long-range order, which consequently inhibits an effective electronic coupling and band-like transport.[53,195,215,216]

An alternative approach is based on ligand exchange with larger π-conjugated semiconductive molecules, which results in long-range ordered and highly conductive SLs. The obtained hybrid material combines the particular benefits of NCRs with the chemical versatility of organic semiconductors.[217] The rigid and relatively long π-molecules with functional groups serve as linker between adjacent NCRs, where the interparticle spacing is determined by the head-to-head length of the linker.[31,59,126] Organic semiconductors are defined by a relatively narrow bandgap E_{gap} of approximately 1–2 eV.[192,218] Thus, the functionalization of NCRs with these molecules predicts a decrease of the barrier height ΔE, a change in E_{C} and a charge carrier delocalization over several particles through the bridging π-conjugated molecules.[121,202,219–222]

Indeed, it is not only the interparticular distance that plays a key role in electronic coupling, but also the nature of the ligands themselves.[219,223] In a remarkable study by Wessels et al. on Au nanoparticles, the use of π-conjugated ligands improved the conductivity and thus electronic coupling by one order of magnitude compared to ligands of the same length without π-conjugation.[219] Moreover, an exponential decay of the electronic coupling with increasing number of non-conjugated bonds within the ligand system was observed. Generally, the surface chemistry of NCRs is of significant importance.[18,70] It has been demonstrated by Brown et al. that the position of the $1S_{\mathrm{e}}$ and $1S_{\mathrm{h}}$ energy levels of PbS NCRs can be shifted by up to 0.9 eV by functionalization of the surface with different ligands.[75] Besides these energetic effects, it has been revealed that for larger ligands the SL domain sizes were more extended and the interdomain gaps were reduced, compared to shorter ligands.[122]

Accordingly, the energy barrier for charge transport is reduced without deteriorating the structural order and increasing the energetic disorder $\Delta\alpha$.[36,57–60,123,124] Indeed, previous studies on π-system functionalized PbS NCR SLs have demonstrated long-range order and enhanced electronic coupling. For instance, using different tetrathiafulvalene derivatives, PbS NCR SLs with interparticle spacings of $\sim$ 1 nm were obtained, featuring conductivities of $\sigma \approx 10^{-7}$–10^{-6} S m^{-1} and hole mobilities of up to $\mu \approx 10^{-5}$–10^{-3} cm^2 V^{-1} s^{-1}.[57,59] PbS NCRs with terthiophene linkers of $\sim$ 0.8 nm length exhibit an improved conductivity of $\sigma \approx 3 \cdot 10^{-5}$ S m^{-1} and a high electron

mobility of up to $\mu \approx 0.2$ cm^2 V^{-1} s^{-1},[224] whereas PbS NCR monolayers functionalized with Cu-4,4',4",4'''-tetraaminophthalocyanine (Cu4APc) show a hole mobility of up to $\mu \approx 1 \cdot 10^{-3}$ cm^2 V^{-1} s^{-1} for interparticle spacings of 1.3–1.5 nm.[123] Such metal phthalocyanine ligands were also used for other NCRs, resulting in significantly improved electronic coupling, which manifested itself by an increase in conductivity by 6–9 orders of magnitude.[124,125,225,226] These reported values are surprisingly high for the large interparticular distances of $\gtrsim 1$ nm, directly pointing out the advantageous function of the π-conjugated linkers.[202] Additionally, the presence of the organic semiconductor molecules includes further parameters to tune the optoelectronic properties of NCR assemblies.[225–231]

To conclude, the approach of π-functionalized NCRs is an ideal compromise between enabling long-range order and increasing electronic coupling within NCR SLs, which is a fundamental prerequisite to investigate potential structure-transport correlations.

2.4.2.2. Influence of structural order

The first evidence of collective electronic properties in NCR ensembles was found spectroscopically. A comparison of NCRs (semiconductive and metallic) in solution and in films has shown that additional optical transitions or a broadening and redshift occur in densely packed films. This was interpreted as an evolution from individual localized to collective electron states delocalized within at least a finite number of NCRs.[44,232–236]

Generally, the computationally predicted formation of minibands in highly ordered and strongly coupled NCR ensembles[43] is prevented in experimental SLs by the minimal amount of omnipresent disorder.[45,47,207] Accordingly, the NCR ensembles in the discussed experiments are all assigned to the weak coupling regime. The detrimental effect of macroscopic cracks and defects on charge transport has already been shown in a number of studies.[53,216,237] In this work, however, structure-transport relationships refer to intrinsic properties and not to the influence of such external effects.

A study on Au nanoparticle monolayers – where charge transport was limited by a Coulomb blockade – has shown that the voltage at which the Coulomb blockade can be overcome strongly depends on the amount of interparticle voids, which emphasizes the need for close-packed assemblies.[238]

In such close-packed assemblies, the size dispersity of NCRs results in both energetic disorder, due to variations in size, as well as spatial disorder, due to variations of the interparticle distances.[47] In a computational study it was observed that both spatial

and energetic disorder contribute to a transition from delocalized to localized states. Further, the critical disorder at which a transition occurs strongly depends on the SL type.[47] Experimentally, it was shown via spectroscopy that a size distribution-based disorder adversely affects the exciton diffusion rate in NCR assemblies.[239,240] An investigation on temperature-dependent transport measurements of large Ag nanoparticle monolayers revealed that the temperature at which the mechanism transits from a variable-range hopping to simple activated hopping depends on the size dispersity of the nanoparticles.[241] However, attempts to prove the detrimental effect of size dispersity disorder in semiconducting NCRs were unsuccessful, as Liu et al. have shown that the carrier mobility is essentially independent of the size distribution[25], although an effect was computationally predicted[242]. However, it could be argued that interparticle coupling in the investigated ensembles was too low to observe the effect.[61] The detrimental effect of NCR size distribution highlights the importance of size uniformity.

A possible indication of the influence of the degree of crystallinity on the electronic properties of assemblies of large Au nanoparticles was given by Nair et al., who reported substantially higher conductivities for polycrystalline ensembles compared to amorphous films.[49] A similar effect was observed for hydrazine-treated PbS NCRs, where the conductivity and mobility of polycrystalline films with grain sizes of ≤ 100 nm exceeded that of glassy films.[51] Nevertheless, those PbS NCR ensembles exhibit mobilities in the range of $\mu \approx 10^{-11}$–10^{-8} cm^2 V^{-1} s^{-1}, indicating insufficient electronic coupling. Further, both of those studies mentioned have the major shortcoming that the investigated assemblies do not feature long-range order. Recently, it was shown by applying time-resolved spectroscopy and X-ray scattering that the charge carrier hopping rate in PbS NCR SLS was enhanced by improving the degree of structural order and NCR alignment induced by thermal treatment.[52]

Computational studies have shown similar effects of NCR alignment. It was found that the electronic coupling between NCRs strongly depends on their orientation to each other.[44] The same study has revealed a strong effect of the NCR shape on the electronic coupling, as the coupling energy of cubic NCRs exceeds that of spherical NCRs, attributed to an improved degree of facet alignment. Another computational study has observed that the electronic coupling between two adjacent PbSe NCRs differs for electrons and holes, and is further facet dependent: electron coupling is generally stronger on smaller facets, whereas hole coupling is stronger on larger facets.[46] Consequently, for cuboctahedral NCRs where the {100} facets are larger than the {111} facets, electron coupling preferentially extends along the [111] direction, whereas the

hole coupling is stronger along [100]. Based on these computational considerations, an experimentally realized orientational alignment of the individual NCRs within a SL seems beneficial.

The different spatial orientations of preferred coupling directions further imply that charge transport in long-range ordered NCR SLs might be anisotropic. This hypothesis is further strengthened by an experimental study on individual $\sim$ 200 nm sized PbS (nano)crystals, having found facet-dependent electrical conductivity.[50] Contacting individual PbS crystals across different facets have shown high conductances on {100} and {110} facets, whereas the {111} facet remained insulating. Moreover, a remarkable computational study by Yazdani et al.[48] on small-polaron hopping in PbS NCR SLs concludes a similar facet-dependent charge transport anisotropy, as detailed above (see Section 2.4.1.4).

In the hopping regime the flow of electrons is diffusive and likely to favor easy paths.[45] Accordingly, one could expect that in an ideal SL without energetic disorder, charge carriers follow the nearest-neighbor direction, as the hopping probability is largest for the shortest distance.[28] Indeed, Kaushik et al. have computationally observed that both the electron and hole mobilities along the nearest-neighbor direction are 4–6 orders of magnitude larger compared to the direction of second-nearest neighbors for bcc and fcc lattices of PbSe NCRs.[46] The existence of anisotropic charge transport is already known for organic semiconductors[243] or metal-organic frameworks[244], where charge transport differs for different crystallographic directions. Additionally, in semiconductors of conjugated polymers a strong correlation between structural order and charge transport efficiency has been found.[245]

To conclude, this Section has shown how charge transport in self-assembled NCR SLs depends not only on the interparticle distance and their surroundings, but also on the degree of structural order. The complex interplay between energetic parameters defines the electronic coupling regime and thus, the mechanism of charge transport, ranging from activated hopping to band-like transport. Interestingly, the recently investigated small polaron hopping mechanism for NCR SLs theoretically predicts an anisotropic charge transport in highly ordered SLs. Such NCR SLs can be realized using PbS NCRs functionalized with π-conjugated ligands, resulting in long-range order along with sufficient electronic coupling. Although theoretical models exist to investigate the effects of structural order on the charge transport properties of NCR SLs, experimentally unravelling structure-transport relationships has proven to be challenging.[47,49,51,53]

2.5. Investigation of structural properties

The structural investigation of NCR assemblies and nanoscale systems in general is crucial for understanding their properties. Simple optical microscopy cannot be used, since the size of the NCRs is smaller than the wavelength of the visible light. More specialized characterization techniques are required to investigate the structure of a NCR assembly, meaning the SL structure and symmetry, the SL grain size as well as the position and rotational arrangement of the NCRs within. In principle two characterization approaches can be used: Real space (imaging) and reciprocal space (scattering) techniques represent a complementary set of approaches to determine structural information,[71,246] which are introduced in this Section.

2.5.1. Electron microscopy

To get a first impression of the structural order, an investigation of the NCR assemblies by imaging in real space is suitable. The following briefly introduces the basics of scanning and transmission electron microscopy, whereas details can be found elsewhere.[247–249]

2.5.1.1. Scanning electron microscopy

In scanning electron microscopy (SEM), a focused beam of electrons is gradually scanned over the sample to be analyzed. The incoming electrons can interact with the sample atoms in different ways and the imaging is indirectly realized by combining the resulting electron signal and the beam position. Elastic scattering of the beam electrons results in high energy backscattered electrons (BSE), originating from deeper sample regions. In contrast, inelastic scattering results in secondary electrons (SE), being emitted from the sample atoms. These low energy electrons originate from (near-)surface regions. Consequently, a detection of the SE signal enables the investigation of the surface topography of the sample. Along with a high resolution of up to ~ 1 nm,[195] it is a convenient tool to elucidate the surface morphology of NCR assemblies and yields first impressions of the degree of structural order.[71] Additionally, by tilting the sample with respect to the incoming beam, side view investigation can yield information on the thickness of NCR SL domains. A major advantage of SEM imaging is that the sample thickness is not a limiting factor. However, samples require an electrically conductive and grounded substrate in order to prevent the accumulation of electrostatic charge, rendering high resolution imaging impossible.

Throughout this thesis, SEM imaging was used as a standard technique to investigate a variety of devices and samples, mainly on silicon (Si) wafers with a silicon oxide (SiO_x) layer: the PbS NCR size, the morphology, structure and thickness of PbS NCR SLs, the dimensions of SL microchannels, Au_{32} NCL micro-crystals and thin films as well as microfabricated devices. Measurements were performed with a Hitachi SU 8030 SEM at the Institute of Physical and Theoretical Chemistry, University of Tübingen.

2.5.1.2. Transmission electron microscopy

A more sophisticated structural analysis of NCR SLs can be achieved by transmission electron microscopy (TEM). The sample is illuminated by a collimated electron beam and only the transmitted electrons are detected to directly create an image. Accordingly, a three-dimensional structure is displayed as a two-dimensional projection. A combination of SEM and TEM is the scanning transmission electron microscopy (STEM). Here, the electron beam is focussed and scanned over a thin sample to detect the transmitted electrons at each point. The main advantage of TEM is the capability to achieve atomic resolution.[56,78,117] Drawbacks, however, are the requirement of special electron transparent substrates and the limitation of the sample thickness to only ~ 100 nm.[127,152,160,250]

For the correlative study of structural and electronic properties of NCR SLs in this thesis, TEM/STEM imaging has turned out to be rather unsuitable. Besides the limited sample thickness, the requirement of mechanically stable substrates for the lithographic patterning of microelectrodes for contacting the SLs renders TEM substrates highly impractical.

2.5.2. X-ray scattering

To analyze complex structures and to obtain structural information averaged over a large sample volume, it is useful to investigate the structure in reciprocal space via X-ray scattering.

2.5.2.1. Basics of X-ray scattering

As in electron microscopy, X-ray scattering exploits the variation of the electron density of the sample to obtain structural information. Here, physical fundamentals of X-ray scattering are briefly introduced. A detailed description can be found elsewhere.[73,247,251]

In X-ray scattering experiments, an X-ray beam is directed at the material to be analyzed and a diffraction pattern is registered by a detector. The X-ray photons are

elastically scattered by interaction with the electron density of an atom. In a crystal the atoms form a regular arrangement composed of lattice planes separated by the distance d. The scattered X-ray photons interfere with each other, resulting in a characteristic diffraction pattern by constructive and destructive interference depending on the crystal lattice. This can be described by Bragg's law in Equation (2.5.1):

$$n\lambda = 2d\sin\theta \qquad , n \in \mathbb{N} \qquad . \tag{2.5.1}$$

Here, λ is the X-ray wavelength, n a positive integer (diffraction order) and θ the angle between the lattice plane and the X-ray beam (Bragg angle). Strong intensities in the diffraction pattern are obtained by constructive interference at the points where the scattering angles fulfill the Bragg condition, as schematically illustrated in Figure 2.10. Each group of parallel lattice planes has a characteristic lattice plane spacing d and hence a characteristic Bragg angle θ at which the constructive interference occurs.

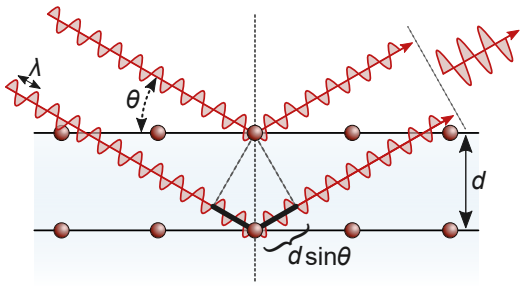

Figure 2.10: Geometric drawing of Bragg diffraction at a crystal. Two parallel beams with wavelength λ approach a solid at the Bragg angle θ and are scattered at lattice planes with distance d. Constructive interference occurs if the difference in path lengths $d\sin\theta$ is equal to an integer of λ.

Usually, a consideration in the reciprocal space, which is the Fourier transform of the real space, is more suitable. Therefore, the scattering vector q is introduced with $d = 2\pi/q$. Accordingly, Equation (2.5.1) can be rewritten to Equation (2.5.2):

$$q = \frac{2\pi}{d} = \frac{4\pi\sin\theta}{\lambda} \qquad . \tag{2.5.2}$$

Hence, the corresponding lattice planes distances d can be derived by determining q of the observed diffraction peaks. All lattice plane families within a cubic crystal structure can be described by the the Miller indices $\{h,k,l\}$. The spacing d of a lattice plane family within a cubic crystal system with lattice constant a can be described as follows:

$$d_{hkl} = \frac{a}{\sqrt{h^2 + k^2 + l^2}} \qquad . \tag{2.5.3}$$

In a hexagonal lattice, the Bravais-Miller notation with four indices $\{h,k,i,l\}$ is used, whereas i is always given as $i = -(h + k)$. For the different crystal structures, different lattice planes lead to constructive interferences and thus to signals. These allowed reflections are given by the selection rules: For simple cubic lattices any h, k, l are allowed, for bcc lattices only reflections where $h + k + l$ is even, for fcc lattices h, k, l must be all even or all odd and for hcp lattices l must be even and $h + 2k \neq 3n$, respectively.

2.5.2.2. Small- & wide-angle X-ray scattering

From Equation (2.5.2) it is obvious that larger spacings d scatter X-rays to lower angles (small q) while smaller spacings d scatter X-rays to wider angles (large q). Accordingly, small-angle X-ray scattering (SAXS) is used to investigate mesoscale systems, such as NCR SLs with NCR sizes and interparticle distances of several nanometers. In contrast, wide-angle X-ray scattering (WAXS) obtains information on atomic systems with smaller distances. The combination of the two techniques provides an incredibly powerful tool for a complete characterization of the SL structure (via SAXS) and the orientation of the atomic planes of the NCRs within (via WAXS).[252] This is schematically illustrated in Figure 2.11. Further information on SAXS and WAXS in nanoparticle research is given elsewhere.[246]

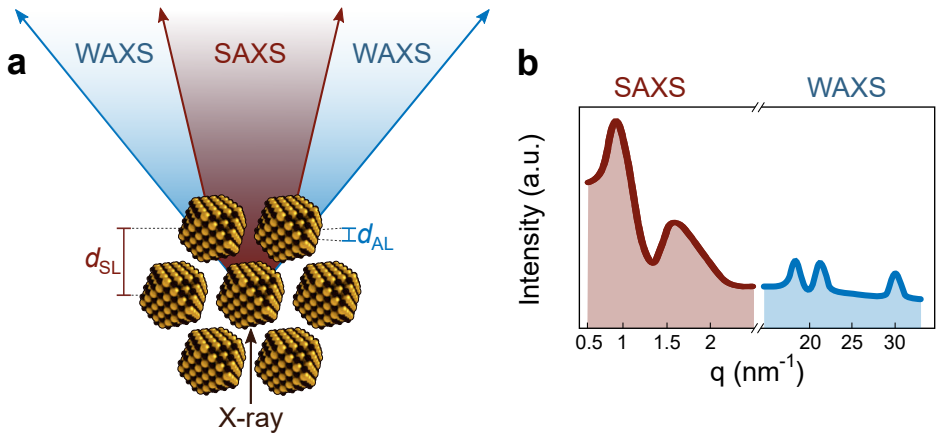

Figure 2.11: Schematic illustration of small-angle and wide-angle X-ray scattering (SAXS and WAXS) of a NCR SL. (**a**) The incoming X-ray beam penetrates the NCRs, causing scattering from the atomic lattice with spacings d_{AL} at wide angles (WAXS) and scattering from the SL with spacings d_{SL} at smaller angles (SAXS). (**b**) Azimuthally averaged intensity profiles of the SAXS ($q < 2.5$ nm^{-1}) and WAXS ($q > 15$ nm^{-1}) signals of PbS NCRs forming a hcp SL.

2.5.2.3. Grazing-incident small-angle X-ray scattering

SAXS and WAXS can be applied in both transmission and grazing incidence mode. In the former case, the X-ray beam penetrates through the sample, while in the latter the beam strikes the sample at a very flat angle.

Grazing-incident small-angle X-ray scattering (GISAXS) is a technique to study nanostructured surfaces and thin films. A schematic of the GISAXS setup geometry is given in Figure 2.12 and details can be found elsewhere.[253–255] This widely used technique is highly surface sensitive, as the incoming X-ray beam strikes the sample at an incidence angle α_i close to the critical angle of total external reflection.[254] The scattered photons are detected by a two-dimensional detector as a function of q_y and q_z, describing the in-plane and out-of plane components. The primary beam is blocked by a beamstop. As the X-ray beam has a large footprint along the sample, the resulting diffraction pattern contains averaged structural information of the probed area.[256] Accordingly, GISAXS is a powerful tool to characterize the structural order of thin film samples containing NCRs.[32,35,52,60,119,141,157,256,257]

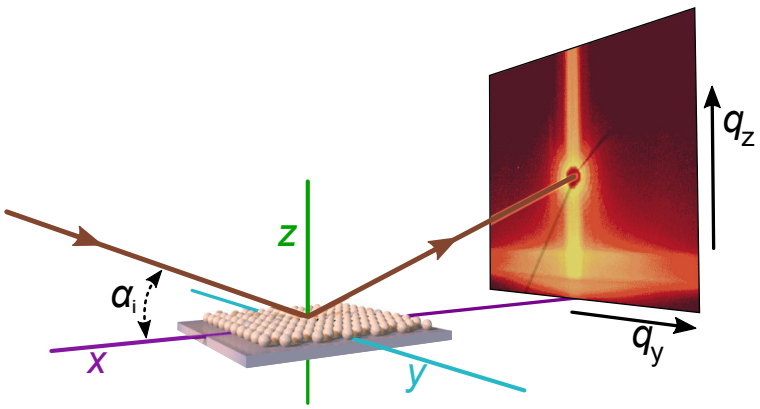

Figure 2.12: Schematic drawing of gracing-incident small-angle X-ray scattering (GISAXS). The incoming X-ray beam strikes the sample at an incidence angle α_i and the scattered photons are detected on a 2D detector as a function of q_y and q_z. [Adapted from Meyer[254] and modified.]

In this thesis, GISAXS was used to investigate the structural properties of Au_{32} NCL thin films and micro-crystals, presented in Chapter 5. Measurements were performed by Martin Hodas with a Xeuss 2.0 (Xenocs) in-house setup of the group of Prof. Frank Schreiber (Institute of Applied Physics, University of Tübingen).

2.5.2.4. Synchrotron radiation

The scattering acquisition time strongly depends on the intensity of the X-ray beam. A source of very intense X-ray beams are electron synchrotrons. Electron synchrotrons are facilities where X-ray beams are generated in an electron storage ring.[258] Bunches of electrons are accelerated to relativistic velocities close to the speed of light and inserted into the storage ring. This storage ring is divided into curved and straight sections and the electrons are deflected from their paths by bending magnets, causing the electrons to emit X-ray photons tangentially to the bending. According to Maxwell, a charged particle emits electromagnetic radiation when its speed or direction of motion is changed.[259] Additionally, insertion devices (undulators) are used in the straight sections to generate X-rays. These devices consist of rows of magnets with alternating polarity, forcing the passing electrons onto a sinusoidal path (wiggling), which in turn produces a large flux of monochromatic X-ray photons.[260] The X-rays generated in this way are directed to designated beamlines where a variety of desired experiments can be performed.

The synchrotron X-ray beams with high flux and brilliance and tunable energy have the advantage of high intensity, which allows the acquisition of diffraction patterns with high signal-to-noise ratio within short exposure times. Figure 2.13a,b displays the storage ring PETRA III (Positron-Elektron-Tandem-Ring-Anlage) at DESY (Deutsches Elektronen-Synchrotron) in Hamburg, Germany.

2.5.2.5. X-ray nano-diffraction

Besides the high intensity of the X-ray beam, synchrotron facilities offer unprecedented experimental setups, such as the X-ray nano-diffraction setup of the coherence beamline P10 of the PETRA III synchrotron source at DESY. Here, the GINIX (Göttingen instrument for nano-imaging with X-rays) endstation is used to focus the synchrotron X-ray beam down to a diameter of $\sim 400 \times 400$ nm^2 (FWHM).[263,264] Such small beam diameters cannot be realized with conventional laboratory X-ray sources, whose typical beam diameter are at least 1000× larger. The GINIX endstation is depicted in Figure 2.13c.

In contrast to GISAXS with a large footprint, here the X-ray scattering is performed in transmission mode, allowing the targeted structural investigation of defined small areas of the sample. In this thesis, X-ray nano-diffraction with a simultaneous detection of SAXS and WAXS is used to characterize highly ordered PbS NCR SLs in microchannels with typical sizes of ~ 4 µm^2 on X-ray transparent Kapton devices. Kap-

ton membranes are flexible films of polyimide, which are commonly used for windows on X-ray setups and detectors due to the high transmittance to X-rays,[265] and for flexible electronics due to their electrical insulation. Commercially available Kapton membranes are mechanically durable as well as solvent- and temperature-resistant.[266] Accordingly, this makes them unarguably the material of choice for our devices to perform X-ray nano-diffraction and conductivity measurements (see Section 2.6.1) of the same PbS NCR SL domains.

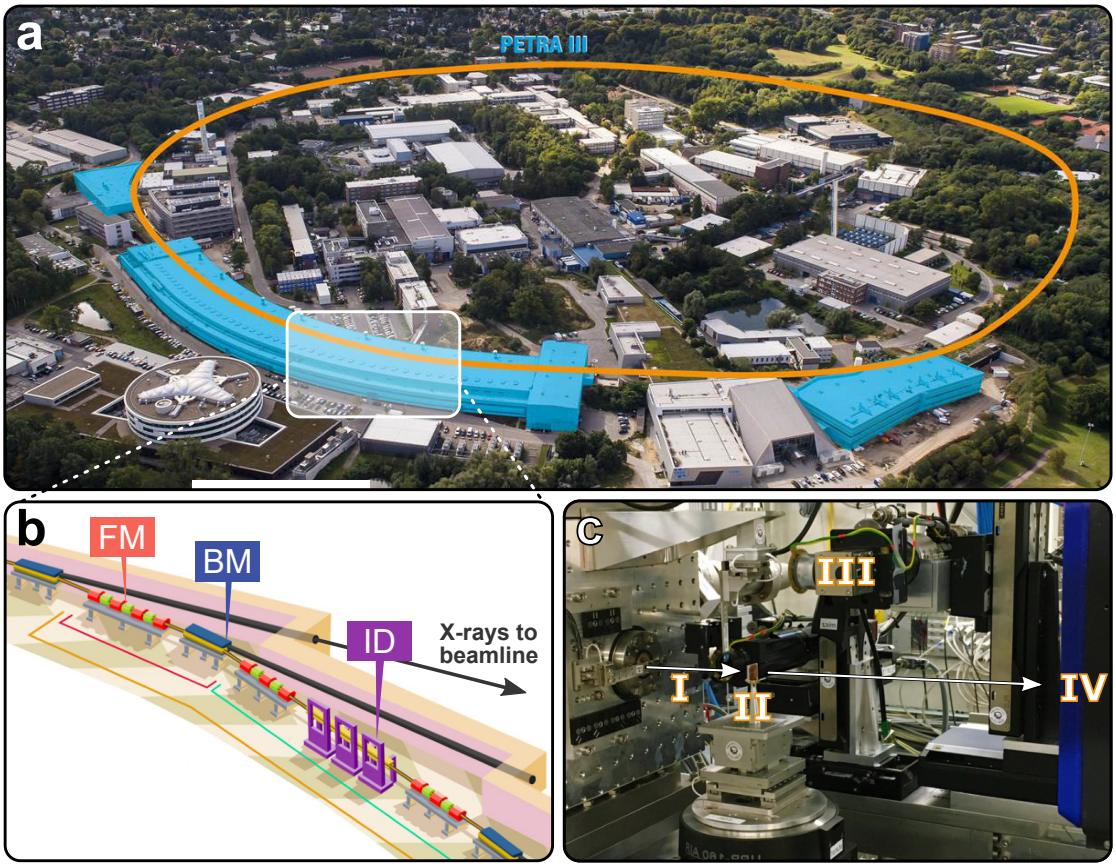

Figure 2.13: Illustration of an electron synchrotron facility to generate X-rays. (**a**) Photograph of the storage ring PETRA III at DESY. The expansion of the underground ring is indicated by the orange marking. The buildings highlighted in blue are the experimental halls. (**b**) Schematic drawing of a storage ring with its focusing magnets (FM), bending magnets (BM) and insertion devices (ID). The generated X-rays are directed to the beamline endstation. (**c**) Photograph of the coherence beamline P10 (DESY) endstation and the GINIX setup. The incomming X-ray beam is focused down to a spot size of $\sim 400 \times 400$ nm^2 (I) and focused onto the sample (II) mounted on a movable stage. A movable microscope with integrated camera facilitates a rough sample alignment (III). A two-dimensional detector positioned downstream allows simultaneous SAXS and WAXS detection (IV). [Figures (a,b) adapted from[261,262], respectively.]

The nano-focused X-ray beam with its high intensity allows to acquire diffraction patterns within sub-seconds that would have required several hours of integration time at a laboratory X-ray source. Hence, a mapping of targeted regions of only a few $\sim\mu m^2$ is feasible by collecting hundreds of diffraction patterns in a raster grid. Such a diffraction map is exemplarily shown in Figure 2.14a,b, including diffraction peaks from the SL and the atomic lattice (AL). With this, the degree of crystallinity of a SL domain can be identified (e.g. polycrystalline vs. monocrystalline) on both a local level (single patterns) and a more global level (averaging of several patterns).

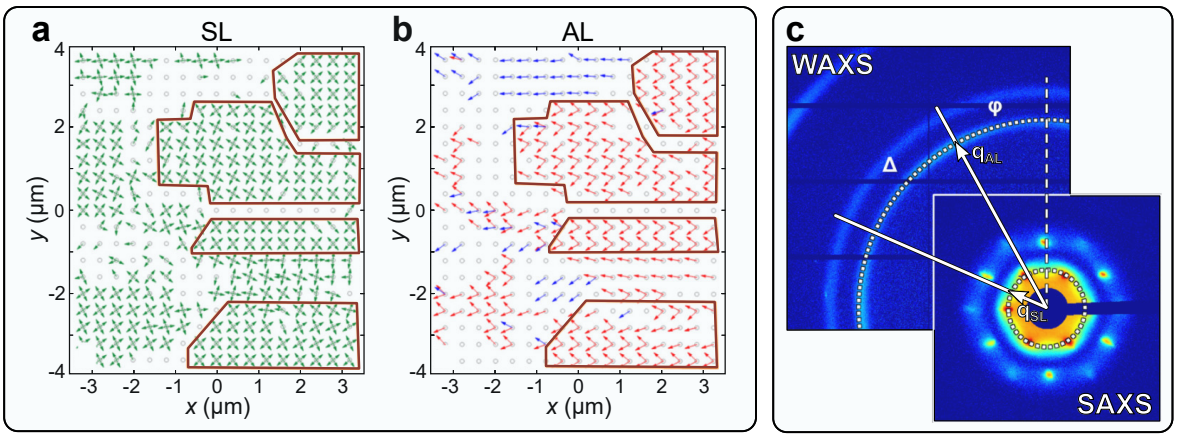

Figure 2.14: X-ray nano-diffraction & angular X-ray cross-correlation analysis (AXCCA). (**a**,**b**) Spatially resolved X-ray nano-diffraction maps of a PbS NCR SL with indicated angular positions of the SL (**a**) and AL (**b**), consisting of 323 individual diffraction patterns. The brown boxes indicate monocrystalline SL domains. (**c**) Schematic of AXCCA and graphical definition of the values required for the cross-correlation function (CFF). White arrows indicate the positions of Bragg peaks from the PbS AL in WAXS and SL in SAXS with the scattering vector q and angular position φ. The angle between the peaks is given by Δ. The SAXS area is enlarged for better visibility. [(a,b) Adapted with permission from Zaluzhnyy et al.[36] (Copyright 2017, American Chemical Society).]

2.5.2.6. Angular X-ray cross-correlation technique

Having collected diffraction patterns with SAXS and WAXS signals from NCR SLs, a powerful tool is required to properly decode the structural order. For this, angular X-ray cross-correlation analysis (AXCCA) is applied. This technique is a versatile method for characterizing the structure and angular order of disordered or partly ordered systems as colloids, liquid crystals and organic thin films[267–269] and recently NCR SLs.[36,37,270] While details and the mathematical background can be found in literature[271–273] and

Chapter 4 of this thesis, the main ideas of this method are introduced in the following. AXCCA is based on the evaluation of the angular cross-correlation function (CCF) of scattering intensity of a 2D detector.[271] By means of X-ray nano-diffraction, SAXS and WAXS signals are acquired and attributed to scattering from the NCR SL and AL of the individual NCRs within. A respective diffraction pattern is given in Figure 2.14c and the corresponding simplified CCF is defined in Equation (2.5.4):

$$C_{\mathrm{CCF}}(q_{\mathrm{AL}},q_{\mathrm{SL}},\Delta) = \int_{-\pi}^{\pi} I(q_{\mathrm{AL}},\varphi)I(q_{\mathrm{SL}},\varphi+\Delta)d\varphi \qquad . \tag{2.5.4}$$

Here, q_{AL} and q_{SL} are the scattering vectors of the AL (WAXS) and the SL (SAXS), respectively. $I(q,\varphi)$ is the corresponding intensity of the diffraction pattern at the scattering vector q and the angular position φ. The angular variable Δ is given by the distance between the two peaks, being in the range of $-\pi \leq \Delta \leq \pi$. Thus, the angular correlations between reflections in the WAXS and SAXS areas, resulting from the ALs and SLs, can be quantified by analyzing the number and positions Δ of the determined correlation peaks. With this, the orientation of individual NCRs within the SL can distinctly be determined.

In this thesis, X-ray nano-diffraction measurements were conducted at DESY in collaboration with the group of Prof. Ivan A. Vartanyants. Combined with AXCCA, which was mainly performed by Dmitry Lapkin, the structural order of PbS NCR SLs in microchannels has been characterized. This is presented in Chapter 4.

To conclude, SEM imaging along with GISAXS and the combination of X-ray nano-diffraction with AXCCA are ideally suited to precisely determine the structural order of assemblies and SLs consisting of Au_{32} NCLs and PbS NCRs.

2.6. Investigation of electronic properties

Having introduced the methods for identifying the structural properties of NCR SLs, the techniques applied to unravel the electronic properties are described in the following. Common techniques to investigate the charge transport properties of NCR SLs are conductivity and field-effect transistor (FET) measurements, briefly explained below. Further details can be found elsewhere.[67,218,248,274,275]

2.6.1. Conductivity measurements

Generally, the NCR SLs have to be integrated into a measurement device to establish electrical contact with an external circuit. Typical two-terminal devices for conductivity measurements consist of two electrodes on an insulating substrate forming a channel with length L and width W, as illustrated in Figure 2.15a. Using the NCR assembling techniques described in Section 2.2.3, assemblies of NCRs can be deposited and integrated into the channel.

In classical two-point conductivity measurements, a voltage difference V is applied between two electrodes, resulting in an electric field $\vec{E}$ inside the material under examination, which in turn produces a current flow I. A source-meter unit records the current flow for the applied voltage. For Ohmic contacts the work function of the metal electrode is close to the NCR energy level relevant for charge transport – i.e. $1S_h$/HOMO for p-type or $1S_e$/LUMO for n-type materials – resulting in a voltage independent resistance R.[67,276] Here, the current I through the material is proportional to the applied voltage V, commonly known as Ohm's law. As given in Equation (2.6.1), linearly fitting the slope of I as a function of V yields the conductance G, which is the reciprocal of R:

$$G = \frac{I}{V} = \frac{1}{R} \quad . \tag{2.6.1}$$

From this, the electrical conductivity σ can be determined by measuring the conductance G as well as the geometric parameters length L, width W and height h of a NCR SL channel, as given in Equation (2.6.2):

$$\sigma = \frac{G \cdot L}{W \cdot h} \quad . \tag{2.6.2}$$

Thus, σ is a measure of the ability of a material to conduct an electric current.[4,67]

To finally elucidate the charge transport mechanism of a given NCR SL device (see Section 2.4), temperature-dependent measurements need to be performed.

In this thesis, home-built X-ray transparent Kapton devices were used as insulating substrates to perform conductivity measurements as well as X-ray nano-diffraction (see Section 2.5.2.5) of the same PbS NCR SL domains. Additionally, Si/SiO_x wafers with an oxide thickness of 200 nm and 230 nm and prepatterned electrodes were also utilized throughout this thesis.

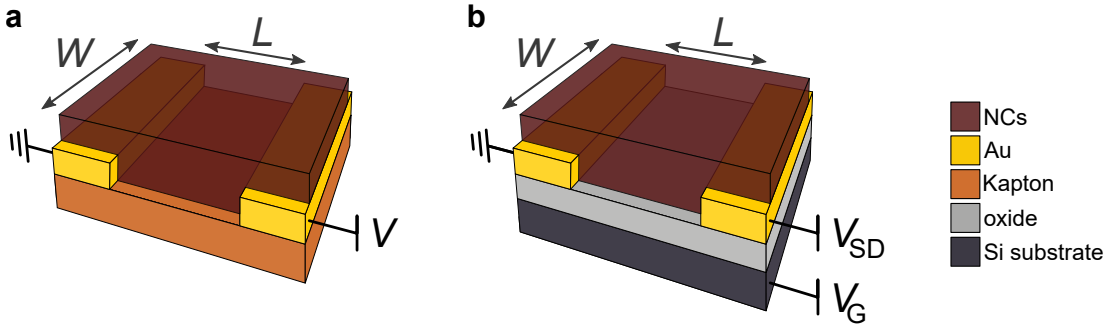

Figure 2.15: Schematic drawings of (**a**) an X-ray transparent Kapton device for conductivity measurements and X-ray nano-diffraction and (**b**) a field-effect transistor (FET) device in bottom-contact bottom-gate configuration. The NCR SLs are deposited on top of the Au electrodes, forming a channel of length L and width W. In both devices, the source electrode is grounded.

2.6.2. Field-effect transistor measurements

In semiconductor materials, σ depends on the mobility μ and concentration n of the present charge carriers, as given in Equation (2.6.3):

$$\sigma = en\mu \quad , \tag{2.6.3}$$

where e is the elementary charge. Thus, μ and n are additional parameters quantifying the electronic properties and electronic coupling of NCR SLs. The fabrication of FET devices of NCR ensembles allows to determine their semiconducting behavior and the field-effect mobility μ of the corresponding majority charge carriers. These are electrons e^- for n-type and holes h^+ for p-type semiconductors, respectively.[25,54,67]

FETs are three-terminal devices, where the current I_{SD} between the source and drain electrodes can be modulated by applying a gate voltage V_G at the gate electrode, which is separated from the semiconducting NCR channel by a thin dielectric layer

(Figure 2.15b). Commonly, the substrate consists of a heavily doped Si wafer with an insulating oxide (e.g. SiO_x) layer as the dielectric medium.

The working principle of NCR FETs can be understood by considering the corresponding band diagrams, which are schematically depicted in Figure 2.16a–d for an ideal p-type semiconductor thin film transistor. In p-type semiconductors, the Fermi level E_F is intrinsically closer to the VB. Without applied gate bias $V_G = 0$ V, equilibrium is established and the Fermi levels E_F of the metal gate and semiconductor are aligned (flatband condition, Figure 2.16a). If a negative gate bias $V_G < 0$ V is applied, E_F of the metal rises with respect to the semiconductor and the VB bends, coming closer to the semiconductor Fermi level E_F. Thus, holes are accumulated at the semiconductor-oxide interface (Figure 2.16b). For a positive gate bias $V_G > 0$ V, E_F is lowered, resulting in a downwards bending of the VB, which decreases the hole density at the interface (depletion, Figure 2.16c). Further increasing the positive gate bias $V_G >> 0$ V results in an inversion, as E_F of the semiconductor is closer to the CB than to the VB. This reverses the mobile charges from holes to electrons, causing a n-type behavior of the conductive channel due to accumulated electrons at the oxide interface (Figure 2.16d). Hence, for p-type semiconductors, the conductivity is increased by applying negative gate voltages due to the accumulation of holes at the semiconductor-oxide-interface and decreased for positive gate voltages. This behavior is vice versa for n-type semiconductors.

Investigating the behavior of a FET commonly includes two measurement types. In the output characteristic, I_{SD} is recorded as a function of V_{SD} for different V_G, as schematically illustrated in Figure 2.16e. For small V_{SD} ($V_{SD} << V_G$), the current of the conductive channel I_{SD} increases linearly with V_{SD}, which is referred to as the linear regime. If V_{SD} is sufficiently large to interfere with the effect of the applied V_G, the conductive channel is pinched-off. Then a depletion layer around the drain electrode is formed, resulting in a sublinear curve. Further increasing V_{SD} causes an expansion of the depletion layer towards the source electrode, which finally results a saturation of I_{SD}, since the increasing resistance compensates the increase of V_{SD}.

When measuring the transfer characteristic, I_{SD} is recorded as a function of V_G for a constant V_{SD}. A schematic transfer curve in the linear regime is depicted in Figure 2.16f. Here, the type of majority charge carriers can directly be identified by considering the derivation of the transfer curve $\frac{\partial I_{SD}}{\partial V_G}$, also referred to as transconductance g. Whereas a negative slope corresponds to p-type behavior, n-type semiconductors can be identified by a positive slope. From the derivation $\frac{\partial I_{SD}}{\partial V_G}$, the hole or electron

field-effect mobility μ can be calculated, using the gradual channel equation in the linear regime given in Equation (2.6.4):[25,67,218]

$$\mu = \frac{\partial I_{SD}}{\partial V_G} \cdot \frac{L}{W} \cdot \frac{t_{ox}}{\varepsilon_0 \varepsilon_r V_{SD}} \quad , \tag{2.6.4}$$

with the channel length L and width W, the thickness and the permittivity of the dielectric oxide layer t_{ox} and $\varepsilon_0\varepsilon_r$, respectively, and the applied source-drain voltage V_{SD}. Further, the ON/OFF ratio, which corresponds to the ratio of maximum and minimum values of I_{SD}, as well as the threshold voltage V_{th}, being the gate voltage at

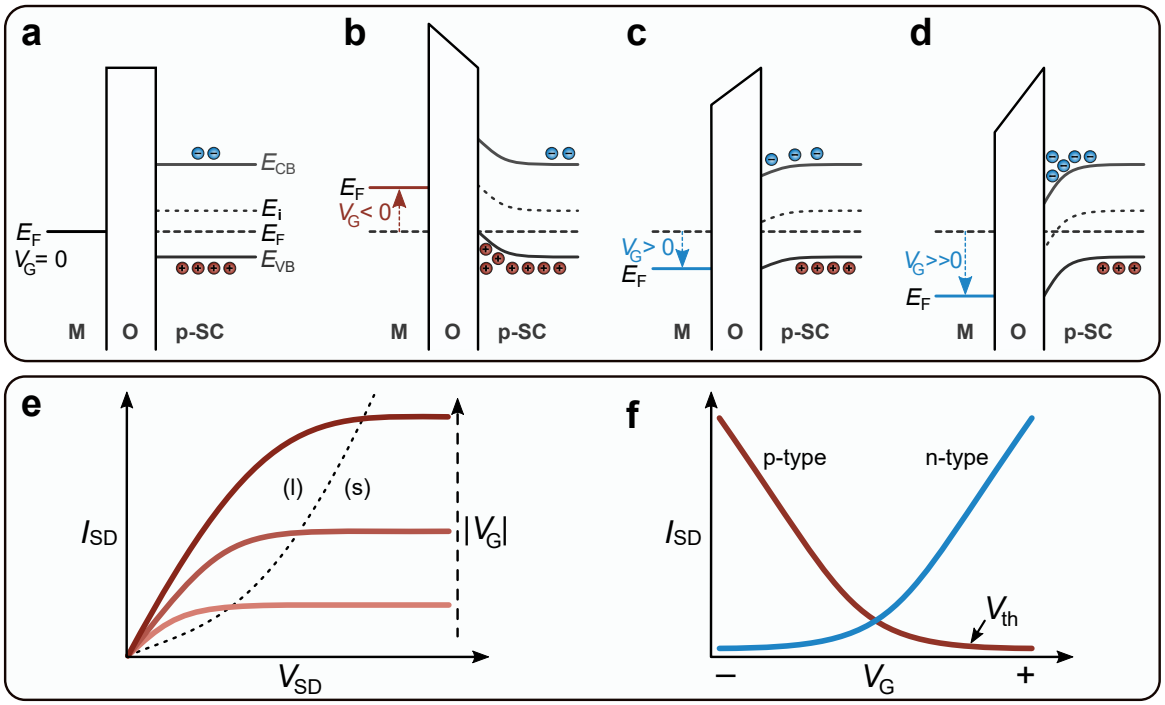

Figure 2.16: Operation principle of a FET. (**a**–**c**) Energy band diagrams of an ideal FET, where a p-type semiconductor (p-SC) is separated from a metallic gate (M) by an oxide layer (O). (**a**) Flatband condition: for $V_G = 0$, E_F of M and p-SC are aligned. E_{CB}, E_{VB} and E_i correspond to the energy of the CB edge, the VB edge and the intrinsic Fermi level, respectively. (**b**) Accumulation: for $V_G < 0$, E_F of M rises, causing band bending and the accumulation of h^+. (**c**) Depletion: for $V_G > 0$, E_F is lowered, resulting in a decreased h^+ concentration. (**d**) Inversion: for $V_G >> 0$, E_{CB} approaches E_F of the p-SC and the concentration of e^- exceeds that of h^+, causing n-type behavior. (**e**–**f**) Characteristic measurements of an ideal FET. (**e**) Output curve: I_{SD} as a function of V_{SD} for different V_G. The dotted line separates the linear (l) and the saturation (s) regime. (**f**) Transfer curve: I_{SD} as a function of V_G at a constant V_{SD} for a p-type (red) and a n-type (blue) semiconductor. V_{th} is indicated for the p-type channel. Figure modified from Hehenberger[277].

which a conductive channel is formed, can be determined. Both are common parameters describing the performance of NCR FETs.

In this thesis, commercially available as well as home-built Si/SiO_x devices with various channel dimensions L and W were used to investigate the semiconducting behavior of PbS NCR and Au_{32} NCL assemblies. In a typical FET measurement, the device under consideration was placed in a probe station (Lake Shore, CRX-6.5K) under nitrogen atmosphere or vacuum. The source and drain electrodes were contacted by W-tips connected to a source-meter-unit (Keithley, 2636B) and a metallic base plate served as the third electrode contacting the gate of the device. Both drain and gate electrodes were referenced to the grounded source electrode. The I_{SD} as well as the leakage current through the dielectric layer I_G was recorded. The detected current was corrected as $I_{SD} = I_{SD}(V_{SD}) - I_{SD}(V_{SD} = 0\,V)$ and $I_G = I_G(V_{SD}) - I_G(V_{SD} = 0\,V)$.

To conclude, conductivity as well as FET measurements are appropriate means to quantify the electronic properties of NCR assemblies and thus the electronic coupling between the NCRs. Together with the described techniques for structural investigation, a correlative study of structure-transport relationships can be pursued.

2.7. Microfabrication techniques

In physical and chemical sciences one can distinguish between top-down and bottom-up processes. The self-assembly of NCR building blocks to larger ensembles can be assigned to a bottom-up process, while typical standard microfabrication techniques belong to the top-down processes.

2.7.1. Conventional lithography & microfabrication

The following briefly introduces conventional (photo-)lithographic processes and microfabrication techniques relevant for this thesis for readers unfamiliar with these methods. Further details can be found elsewhere.[278–281]

2.7.1.1. Photolithography

The conventional technique of patterning structures in microfabrication is photolithography, commonly applied in modern semiconductor industry and research. The first step in this multi step process is the coating of the desired substrate with an UV-sensitive resist. This is typically applied by spin-coating, whereby the film thickness can be controlled by the rotation speed and by the properties of the resist, such as viscosity. The resist film is then thermally cured (soft-bake). Next, the resist is locally exposed to UV radiation, which is realized by blocking some parts of the radiation by applying a structured photomask having opaque and transparent parts on top of the substrate. The partially exposed resist, usually consisting of polymers, changes its chemical structure and thus solubility. This is finally utilized by selectively removing the soluble parts of the resist in a development step. When using positive photoresists, the UV radiation renders the resist soluble, while the resist covered by the opaque parts is protected and remains nearly insoluble. Thus, unexposed parts remain on the substrate after development in a suitable solution. In contrast, for negative photoresists, the unexposed parts remain soluble and can be removed, while the exposed parts become polymerized and thus insoluble. Finally, the patterned resist is then used as a mask in subsequent deposition or etching steps. In this high-throughput technique of contact photolithography, the resolution of defined patterns is limited by the wavelength λ of the radiation and the photomask used, allowing minimum feature sizes of ~ 1 µm.[279,282] In electron beam lithography, where the resist is exposed by electrons with much shorter λ, smaller structures can be realized. However, as the electron beam is gradually scanned over the sample, this process requires significantly more time.

2.7.1.2. Metallization

For subsequent material deposition, thermal evaporation is a standard technique to deposit thin layers of metals or oxides onto the lithographically patterned sample. The sample is placed in a vacuum chamber, where the coating material is heated typically to a temperature above its melting point by resistively heating a boat or by electron beam. The material evaporates and condenses in turn as a solid layer on the substrate. The thickness of the film can be controlled by a quarz crystal microbalance. Finally, the resist is dissolved, which also removes the remaining material on top (lift-off). Consequently, the material in direct contact with the substrate remains and features structures according to the pattern defined by the resist. Typical applications of material deposition and lift-off are the thermal evaporation of metals (e.g. Au or Ti) to realize electrode structures on substrates.

2.7.1.3. Wet etching

For pattern transfer by subsequent material removal, etching can be used. Here, the partially (resist-) protected substrate is exposed to an etching medium, which can either be a solution (wet) or plasma/ions (dry). In a wet etching process, the partially patterned sample is immersed in a solution, which chemically reacts with the sample surface to transfer the solid material into soluble compounds. The basic prerequisite is that the etch mask, e.g. the patterned resist or an (silicon) oxide layer, is not or significantly less attacked than the layer to be etched. Etching processes can be described by the figures of merit selectivity and isotropy. Selectivity is defined as the ratio of etching rates for two different materials and is of relevance for samples containing multiple materials. Isotropy describes the direction dependency of the etching. While in isotropic etching the material is equally removed in all directions, in an anisotropic etching process, certain directions are favored, resulting in different etching rates.

As an example, the anisotropic etching of silicon by potassium hydroxide (KOH) is based on the different etch rates along distinct crystallographic axes, caused by different activation energies. The etch rate of the {100} crystal plane is about two orders of magnitude higher as that of the {111} plane.[283,284] A typical example of isotropic wet etching is the etching of silicon dioxide (SiO_2) by hydrofluoric acid (HF).[285]

2.7.1.4. Reactive ion etching

Another way for subsequent etching of lithographically patterned samples are dry etching processes. A common type of dry etching is reactive ion etching (RIE).[286] In a parallel plate RIE system, the sample is placed inside an evacuated chamber on a sample stage. Depending on the desired process, certain gases are then introduced into the chamber. By applying a radio frequency electric field between the sample stage and the chamber wall, a plasma is ignited, consisting of ionized molecules, free electrons and neutral molecules. Due to their small mass, the electrons can follow the oscillating field and move alternatingly towards the sample stage and the chamber wall. While they can flow off at the grounded chamber wall, a negative charge (of a few hundred volts) builds up at the insulated sample stage. Due to the higher mass, the positively charged ions are hardly affected by the oscillating field. However, they are then accelerated within the positively charged plasma towards the negatively charged sample stage by the built up static electric field. Here, the impinging ions can interact with the sample in two ways, by sputtering/milling atoms from the sample due to the high kinetic energy (physical etching) and by chemically reacting with the surface atoms to transfer them into the gas phase. The desired requirements of selectivity, etch rate and the degree of isotropy can be precisely adjusted by the selected process parameters, such as used gases, gas flow, pressure and power.

A typical example of RIE is the anisotropic etching of resist-patterned SiO_2 structures on silicon, where fluoroform CHF_3 gas is used due to its high selectivity of SiO_2 against Si.[286] Common applications of etching are the fabrication of MOSFETs, cavities and micromolds.

2.7.1.5. Profilometry

Profilometry can be used to measure the surface topography of a sample. In mechanical profilometers, a diamond stylus is brought into contact with the sample and scanned linearly across the surface.[287] The stylus tip follows the contours and the corresponding height is recorded at each position. This allows line scans of up to cm lengths over the surface topography of the sample, enabling the determination of the surface roughness or height profile of e.g. resist patterns with nm resolution.

2.7.2. Soft-lithography & microcontact printing

Whereas the fundamentals of conventional lithography are given above in Section 2.7.1, here the basics of soft-lithography and microcontact printing (µCP) are introduced. A more detailed description can be found in literature.[20,288–292]

Soft-lithography methods are widely used to fabricate nano- and micro-structured surfaces and thin films. Whereas conventional (photo-)lithography is limited to the usage of photoresists, soft-lithography techniques can be used to pattern a variety of materials, ranging from small molecules to proteins and nanoparticles.[288] In the following, the material of interest, which might e.g. be dissolved or present as a continuous layer on a surface, is referred to as ink.[289] These techniques are all based on the usage of a structured elastomer for pattern transfer, where these elastomers can be utilized as molds, stamps or masks.[288,291] However, the following focusses on microcontact printing (µCP), where stamps with a patterned relief structure are used as the transfer medium, as illustrated in Figure 2.17. Generally, the versatile and low-cost procedure of µCP includes three major steps: the fabrication of the stamp, the inking of the stamp with the material to be transferred and the printing step, where the material is printed onto a desired substrate.[20]

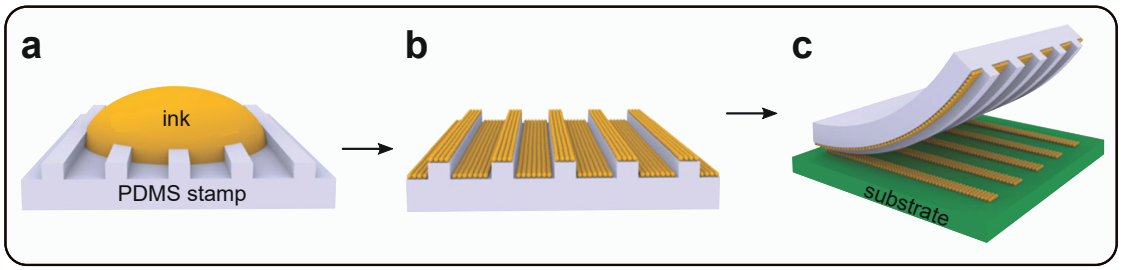

Figure 2.17: Illustration of the microcontact (µCP) process. (**a**) An elastomeric stamp made of PDMS with a patterned relief structure is inked with the material to be transferred, e.g. small molecules, polymers or nanoparticles. (**b**) After drying, a thin film is formed on the stamp. (**c**) The patterned thin film is transferred from the protruding regions to the target substrate by µCP. [Figure adapted with permission and modified from Yang et al.[20] (Copyright 2016, Wiley).]

The elastomer stamps typically consist of polydimethylsiloxane (PDMS), which is a cross-linked polymer containing a $-Si(CH_3)_2-O-$ backbone.[289] It is prepared by casting a mixture of a prepolymer and cross-linking agent onto a master template featuring the inverse of the desired pattern, followed by curing at elevated temperatures. Finally, the patterned PDMS stamp can be peeled from the master template. These reusable masters are prepared by conventional lithography methods described in Section 2.7.1. PDMS

is an ideal material for soft-lithography processes, featuring a unique combination of properties, such as elasticity, low interfacial surface energy, chemical inertness, thermal stability, gas permeability and optical transparency.[288,291]

Having prepared the stamps, the inking takes place (Figure 2.17a). Inking can be achieved by covering the patterned face of the stamp with the ink solution, by dipping it into the solution or by pressing it onto a surface containing an ink layer.[289] After drying, the ink is selectively transferred from the raised regions of the PDMS stamp by stamping onto the desired substrate (Figure 2.17b,c). Conformal contact of the protruding regions of the elastic stamp with the substrate is key for a successful transfer of the ink.[290] The substantially lower surface energy of the PDMS stamp ($\sim$ 20 mJ m^{-2}) compared to typical target substrates (e.g. Si or SiO_x with $>$ 200 mJ m^{-2}), together with the high adhesive affinity of the ink components, allows the patterned films to be readily transferred from the stamp to the target.[20,155] This technique has been successfully applied to produce patterned monolayer films and three-dimensional nanoparticle SLs.[155,222,293,294]

In this thesis, the microfabrication techniques introduced above were used to fabricate Kapton and Si/SiO_x devices with patterned Au electrodes. In combination with µCP, this allows the fabrication of PbS NCR SL microchannels with channel dimensions approaching the size of typical single-crystalline domains. Further, these large-scale microelectrode devices were used to individually contact self-assembled micro-crystals of Au_{32} NCLs.

3. Fabrication of nanocrystal superlattice microchannels by soft-lithography for electronic measurements of single crystalline domains

Andre Maier[1,2*], *Ronny Löffler*[2] *and Marcus Scheele*[1,2]

[1] Institute of Physical and Theoretical Chemistry, University of Tübingen, Auf der Morgenstelle 18, D-72076 Tübingen, Germany

[2] Center for Light-Matter Interaction, Sensors & Analytics LISA$^+$, University of Tübingen, Auf der Morgenstelle 15, D-72076 Tübingen, Germany

[*] Corresponding author

This Chapter is based on the publication in Nanotechnology.

3.1. Abstract

We report a high-throughput and easy-to-implement approach to fabricate microchannels of nanocrystal superlattices with dimensions of ~ 4 µm^2, thus approaching the size of typical single-crystalline domains. By means of microcontact printing, highly ordered superlattices with microscale dimensions are transferred onto photolithographically prepatterned microelectrodes, obtaining well-defined superlattice microchannels. We present step-by-step guidelines for microfabrication, nanocrystal self-assembly and patterning to archive large quantities of up to 330 microchannels per device for statistically meaningful investigations of charge transport in single-crystalline superlattice domains. As proof-of-concept, we perform conductivity and field-effect transistor measurements on microchannels of PbS nanocrystal superlattices. We find that the electric transport within microchannel superlattices is orders of magnitude more efficient than within conventional large-scale channels, highlighting the advantage of the near single-crystalline microchannels presented in this paper.

3.2. Introduction

Colloidal nanocrystals (NCRs) are of high interest in academic research and technological applications, due to their size-tunable optoelectronic properties.[2,18,67] The self-assembly of NCRs into highly ordered superlattices (SLs) provides a powerful platform for the development of numerous solution-processed optoelectronic devices.[4,5,24,26,54] These periodic arrays mimic classical crystals in which atoms have been replaced by NCRs. In analogy to atomic crystals, electronic coupling between neighboring NCRs can occur, resulting in novel collective properties by design. SLs of NCRs are commonly fabricated by the self-assembly of NCRs from solution, comprising the solvent-evaporation based methods of drop-casting, spin-coating, dip-coating and the assembly at the liquid/air interface[71]. This allows NCR arrays to be realized with structures ranging from 2D monolayers[123,156,157] to 3D arrays with standard SL structures (e.g. bcc, fcc, hcp lattices)[81,130,133] and more sophisticated binary lattices.[127,153,155] Further, SLs with oriented attachment of atomically connected NCRs with honeycomb or square lattice structures can be achieved.[117,160,207] Despite their vast structural versatility, all NCR assemblies suffer from one mayor drawback that restricts the exploration of the fundamental electronic properties of these novel artificial solids: the assemblies are rather heterogeneous and typical SL grain sizes are yet only a few to tens µm

wide[36,37,136,295] such that the coupling between NCRs is limited to small domains, caused by grain boundaries, cracks, voids and disorder.[28,67,215] However, typical devices to investigate the electronic properties of NCR SLs involve active areas with much larger dimensions of $\sim 10^4$–10^5 µm^2.[5,6,39,119,123,207] Thus, measuring the electronic properties of these SL devices averages over the intrinsic properties of all present domains, concealing the expected collective effects of single-domain NCR SLs. Accordingly, to really pinpoint the intrinsic properties of NCR SLs, the active channel area between two contacts has to be decreased to allow single-grain measurements.[71,207,296] In this respect, we explicitly do not refer to contactless measurement techniques (e.g. terahertz spectroscopy),[53,123,215,297] since an actual implementation of SLs into real devices requires contacting by electrodes. First indications of the effect of reducing the measuring dimensions have been provided by Mentzel et al.,[216] where nanopatterned NCR films prepared by electron beam lithography have revealed 180× higher conductivities compared to macroscopic films. Evers et al.[53] have used scanning tunneling microscope tips with distances of 500 nm to probe field-effect mobilities of single-grain SLs, reporting that the absence of long-range order is limiting the mobility.

Here, we demonstrate our high-throughput, low-cost and easy-to-implement approach of fabricating microchannels of lead sulfide (PbS) NCR SLs to define active areas with dimensions close to single domains. By means of microcontact printing (µCP), we transfer periodic stripes of highly ordered NCR SLs with microscale dimensions onto photolithographically prepatterned electrode devices. This leaves most of the substrate area uncoated and is key to obtain well-defined microchannels. In the soft-lithography technique of µCP, a patterned elastomeric stamp is used to transfer a NCR SLs to a substrate while the stamp pattern is maintained.[289,298] Channels with dimensions of $\sim 1 \times 4$ µm^2 fabricated in this way allow performing electronic measurements of single crystalline SL domains. We provide a step-by-step protocol to fabricate devices with several hundreds of microchannels for a statistically meaningful investigation of the electronic properties of single-crystalline SLs. This protocol is not limited to PbS NCRs and applicable for a broad range of NCR materials and SL types.

3.3. Methods

3.3.1. Materials

All required materials and equipment for the fabrication of microchannels are listed below. Positive tone resist (ma-P 1205), negative tone resist (ma-N 405), developer (ma-D 331/S) and remover (mr-Rem 660) were purchased from micro resist technology GmbH, Polydimethylsiloxane (PDMS) Sylgard 184 prepolymer and cross-linker from Dow Corning GmbH and hexamethyldisilazane (HMDS) as well as Tridecafluoro-(1,1,2,2)-tetrahydrooctyl-trichlorosilane (F_{13}TCS) from Sigma Aldrich. For the electrode devices, we used (100)-Si wafers with 200 nm SiO_2 (Siegert Wafer GmbH). However, other substrates or wafers can also be used. (100)-Si wafers were used for the stamp master fabrication, ideally with a SiO_2 layer of 100–200 nm. Standard chemicals as acetone, isopropanol, ultrapure water, potassium hydroxide (KOH) pellets and buffered oxide etch solution (BOE 7:1, (87.5% NH_4F : 12.5% HF)) were used.

Oleic acid stabilized PbS NCRs were synthesized according to Weidman et al.[55] Cu-4,4',4",4"'-tetraaminophthalocyanine (Cu4APc) was synthesized according to Jung et al.[299] Hexane, octane, acetonitrile and dimethyl sulfoxide, were purchased from Acros Organics.

3.3.2. Fabrication process of Au electrode devices with µm-gaps

(100)-Si wafers with a 200 nm SiO_2 layer were cut into 15 × 15 mm^2 pieces. HMDS as an adhesion layer was applied: The samples were heated to 150 °C in a closed glass Petri dish under nitrogen flow. After 15 min, the temperature was set to 120 °C and one drop of HMDS was placed with a syringe next to the wafer pieces while the petri dish was kept closed. After 5 min, the samples were slowly cooled down to room temperature. A thin layer of the negative tone photoresist ma-N 405 was applied (100 µl, maximum spin speed of 10,000 rpm, 30 s), followed by a soft bake at 95 °C for 60 s. The thickness of the resist was 310 nm, measured by profilometry (Bruker, Dektak XT). For exposure, an optical mask with the electrode structures as opaque parts was used. The substrates were exposed for 45 s (365 nm, 325 W, Karl Süss MA6 mask aligner) followed by development for 5–7.5 min in ma-D 331/S to remove the unexposed parts, stopped by placing the sample into ultrapure water. The samples were placed in a thermal evaporation system (Pfeiffer Vacuum PLS 570) under high

vacuum conditions (10^{-7} mbar). As an adhesion layer, $\sim$ 2.5 nm of Ti was evaporated, followed by $\sim$ 8 nm of Au. The thickness and evaporation rate were controlled by a quartz crystal microbalance. Finally, lift-off was performed in mr-Rem 660 assisted by ultrasonication.

3.3.3. Fabrication of silicon stamp masters

First, the (100)-Si wafers were thermally oxidized for 75 min at 1,050 °C to yield a SiO_2 layer of around 100 nm. Alternatively, (100)-Si wafers with an initial SiO_2 layer can be used. The Si/SiO_2 wafer were cut in 15×15 mm^2 pieces, with the cutting line precisely aligned to the $\langle 110 \rangle$ Si direction (indicated by the wafer flat). HMDS was applied as an adhesion layer, as described above. A 500 nm thick layer of the positive tone photoresist ma-P 1205 was applied (100 µl, 3,000 rpm, 30s), followed by a soft bake at 90 °C for 60 s. An optical mask with 15 µm wide stripes as transparent parts was used. The stripes were aligned parallel to the $\langle 110 \rangle$ direction. Exposure for 1 s and development for 60 s in ma-D 331/S removes the exposed parts (stripe profile). Next, SiO_2 etching was performed in a reactive ion etching (RIE) system (Oxford Instruments, Plasmalab 80 Plus) with the following process parameters: a mixture of CHF_3 and O_2 (45 sccm and 5 sccm, respectively), a chamber pressure of 40 mTorr and a power of 150 W were used. The ideal etch time was 180 s (see Figure 3.3). Before and after the CHF_3-RIE, the substrates were cleaned with an oxygen plasma (50 sccm O_2, 10 s, 100 mTorr, 40 W). Residual resist was removed by acetone. Before KOH etching, the substrates were immersed in 1.2% HF solution for 60 s (1 ml of BOE 7:1 in 10 ml ultrapure water) and then directly mounted in a home-built Teflon holder placed in an 8.8 M (36 wt%) KOH solution (27 g KOH in 48 ml ultrapure water) heated to 60 °C via a water bath under stirring. The substrates were etched for 20–40 min and rinsed with ultrapure water to stop the etching process. The substrates were immersed into an 1.2% HF bath for 20 min and rinsed with ultrapure water to remove the SiO_2 etch mask. For the surface functionalization, the substrates were heated to 150 °C in a closed Petri dish under nitrogen flow. After 15 min, one drop of F_{13}TCS was placed with a syringe in the Petri dish, which was then kept closed for 30 min. The functionalized silicon masters were slowly cooled down to room temperature and rinsed with acetone and isopropanol to remove excess F_{13}TCS.

3.3.4. Fabrication of elastomeric stamps

The functionalized silicon masters were placed into a home-built Teflon chamber (3×3 masters). PDMS base and curing agent (Sylgard 184) were mixed in a 10:1 ratio (33 ml in total to obtain 9 stamps of roughly 10 mm thickness) and stirred thoroughly for ~ 3 min. The mixture was placed in a vacuum desiccator to remove trapped bubbles by multiple evacuation and re-pressurization steps and final evacuation for ~ 20 min. The degassed PDMS mixture was poured onto the silicon masters in the Teflon well. The well was placed in the desiccator and evacuated for another ~ 5 min to remove air bubbles trapped at the master-PDMS interface. The PDMS was then cured overnight (~ 16 h) in an oven at 150 °C. Shorter curing times increase the softness of the PDMS stamps. The cured PDMS block was cooled down to room temperature and carefully released from the Teflon well. Since a small amount of PDMS normally also wetted the backside of the silicon master, this thin layer was removed with a razor blade and the masters were then carefully peeled off (parallel to the trenches) from the PDMS block. The stamps were cut into $10 \times 10 \times 10$ mm^3 pieces with a razor blade, cleaned by sonication in isopropanol and dried under pressurised nitrogen flow. The cubic shape allows easy handling of the stamps by hand.

3.3.5. Self-assembly of NCR superlattice films at the liquid/air interface

PbS NCRs with a diameter of 5.8 ± 0.5 nm, stabilized with oleic acid, were dispersed in hexane:octane with ratios from 1:0–0:1 at concentrations of 4–10 µM. A home-built Teflon chamber with an area of 10×10 mm^2 was filled with 1 ml acetonitrile and equipped with a lid to seal the Teflon chamber. A needle containing a PbS NCR dispersion was mounted just above the acetonitrile subphase and connected to a syringe pump. Another needle containing the ligand solution (Cu4APc in dimethyl sulfoxide), connected to another syringe pump, was mounted within the subphase. The PbS NCR dispersion (70–100 µl) was injected on top of the acetonitrile subphase, whereas the injection speed was controlled by the syringe pump. The ligand solution (150 µl, ~ 0.1 mg ml^{-1}) was injected at the bottom of the liquid subphase and ligand exchange was performed over a duration of 4 h.

3.3.6. Microcontact printing of NCR superlattice microchannels

A micropatterned PDMS stamp was parallelly brought into contact with the floating NCR SL film for ~ 5 s and excess liquid was removed from the stamp with a tissue. The coated stamp was placed onto the Si/SiO_2 substrate with prepatterned electrodes for ~ 30 s and then removed in a tilted manner (parallel to the stripe profile). The stamped substrates were vacuum-dried for a few minutes to remove excess liquid. The substrates were then placed on a spin coater and covered with acetone to remove unbound ligands. After 30 s, the acetone meniscus was removed by spinning at 1,200 rpm for 30 s. The washing step was repeated once. This assembly and µCP process was performed in a glovebox in nitrogen atmosphere (level of $O_2 < 0.5$ ppm and $H_2O = 0$ ppm).

3.3.7. Characterization of superlattice stripes and microchannels

Scanning electron microscopy (SEM) imaging was performed with a HITACHI model SU8030 at 30 kV. For sideview investigation of SL stripes, devices were analysed under a tilt angle of 85°. The thickness of the transferred SL stripes were investigated by atomic force microscopy (AFM), conducted with a Bruker MultiMode 8 HR. Electrical measurements were performed at room temperature in a nitrogen-flushed probe station (Lake Shore, CRX-6.5K). Individual electrode pairs with a connected SL stripe were contacted with W-tips, connected to a source-meter-unit (Keithley, 2636B). A base plate served as third electrode contacting the gate of Si/SiO_2 devices. Two-point conductivity measurements of individual microchannels were performed by applying several voltage sweeps of ± 1 V and ± 200 mV and detecting the current between the electrodes as well as the leak current. Field-effect transistor (FET) measurements were conducted by applying a constant source-drain voltage of $V_{SD} = 5$ V, while the current flow was modulated by applying voltage sweeps in the range of $40\,\text{V} \leq V_G \leq 40\,\text{V}$ on the gate electrode. The detected current was corrected as $I_{SD} = I_{SD}(\text{V}_{SD} = 5\text{V}) - I_{SD}(\text{V}_{SD} = 0\text{V})$ and $I_G = I_G(\text{V}_{SD} = 5\,\text{V}) - I_G(\text{V}_{SD} = 0\,\text{V})$. The gradual channel approximation was used to calculate the field-effect mobility μ of individual microchannels (see Supplementary information in Section 3.6 for details).

3.4. Results

We emphasize that the described process can easily be implemented in any laboratory as long as the following standard microfabrication equipment is generally available: Photolithography equipment like a spin coater, a mask aligner and an optical microscope, a thermal evaporation system, a RIE system with O_2 and CHF_3 as process gases, and other standard laboratory equipment such as Teflon petri dishes and a magnetic hotplate stirrer.

3.4.1. Microchannel device layout

First, for a µCP process with a high success rate, an elastomeric stamp with an optimal aspect ratio of its relief features has to be designed. Here, the width W of the stripes is set to $\sim$ 4 µm which is a typical grain size of SLs. The stamp feature height H and feature distance D are chosen to have an ideal aspect ratio (H/W) according to $0.5 < H/W > 5$ and $H/D > 0.05$ to prevent lateral collapse and pairing of the elastomeric stamp features.[290,292,300] Accordingly, a feature height of $H = 8$ µm and a feature periodicity of 80 µm ($D = 76$ µm) is selected.

Next, the layout of the finger electrodes is adjusted: The electrodes from opposite directions overlap at their ends. The length of the overlap corresponds to the periodicity of the stamp features of 80 µm. Thus, only one orthogonally transferred stripe connects adjacent electrodes. With this device geometry, well-defined microchannels can be realized where an entirely homogeneous electric field is established within the channel and the direction of the electric field vector is well-known. One set of 12 electrodes form 11 individually addressable microchannels. On one substrate, 30 of these electrode sets are present, yielding a total number of 330 microchannels per device (see Figure S3.1 in the Supplementary information).

3.4.2. Fabrication process of Au electrode devices with µm-gaps

To warrant high throughput, Au electrodes with $\sim$ 1 µm gaps are fabricated by UV photolithography (Figure 3.1). The lift-off technique with a negative tone resist is chosen for high-resolution patterning. As photolithography is diffraction limited, the resolutions scales with $\sim \sqrt{\lambda h}$, where λ is the wavelength of exposure and h the thickness of the photoresist.[282] Next to a short exposure wavelength, a resist thickness as thin

as possible while retaining its functionality is required. This was empirically identified as a thickness in the range of 250–350 nm, achieved by spin-coating the substrate with a low viscosity resist at maximum spin speed. Furthermore, the photomask exhibits opaque electrode structures which are separated by gaps of only 0.6 µm. The layout of the photomask is given in Figure S3.1. Due to diffraction, the sub-µm gaps result in $\sim$ 1 µm photolithography pattern transfer. Negative tone resist tends to form undercut structures after development (Figure 3.1b), which are well-suited for lift-off processes. After metallization with $\sim$ 2.5 nm Ti and $\sim$ 8 nm Au, the lift-off of the residual resist and metal layer on top results in Au electrodes with $\sim$ 1 µm gaps, referred to as channel length L, and smooth edges (Figure 3.1c). Thin electrodes with smooth edges are desirable as they prevent breaking of the transferred SL stripes at the edges.

The presented guideline for the fabricated Au electrodes with $\sim$ 1 µm gaps on Si wafers with an SiO_2 layer of 200 nm allows to perform e.g. two- and four-point measurements as well as field-effect transistor measurements. Generally, this approach can easily be adjusted for other substrates, such as glass slides or polyimide membranes.

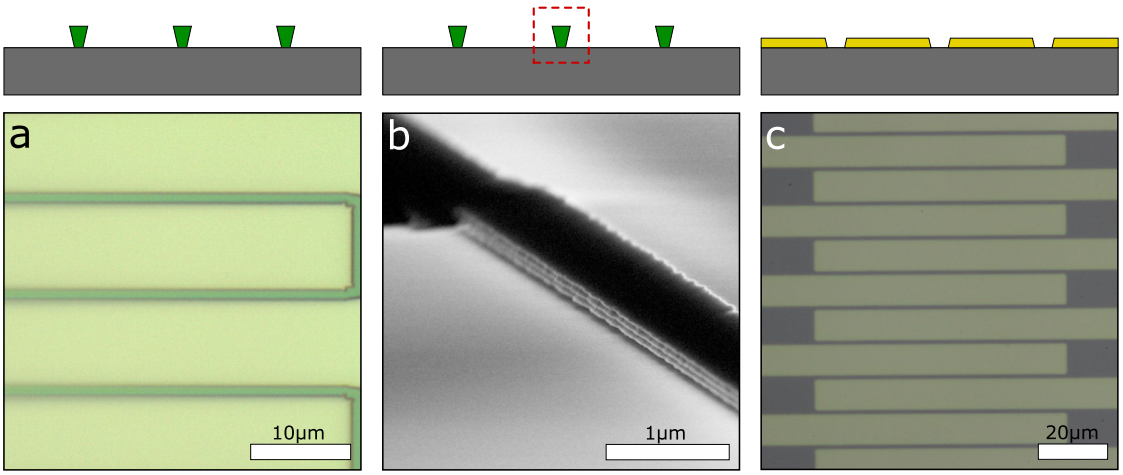

Figure 3.1: Fabrication of prepatterned electrode devices. (**a**) Optical micrograph of a Si/SiO_2 substrate with developed negative tone resist pattern (dark green) of $\leq$ 1 µm width and a thickness of 310 nm. (**b**) SEM micrograph of an $\sim$ 800 nm wide resist patterns under a tilted view of 85°. (**c**) Optical micrograph of the substrate after metallization and lift-off. Well-defined electrodes with gaps of $\leq$ 1 µm are formed. The respective schematic drawings are provided at the top of each subfigure.

3.4.3. Fabrication process of silicon masters and elastomeric stamps

To meet the above-mentioned requirements for the elastomeric stamps, especially the relatively large relief height of 8 µm, a silicon master fabrication by means of anisotropic etching in aqueous KOH solution was chosen. We used (100)-Si wafers for the etching process, as this can produce trenches with inclined {111} walls.[284] The etch rate of silicon differs for the crystal planes, caused by different activation energies. The selectivity of the etch rate of the crystal planes {100}:{111} is about 100:1.[283] Thus, the {111} plane effectively serves as an etch stop. This technique provides the advantages of atomically flat defined sidewalls and the possibility to adjust the width of the stamp features by controlling the etching depth/time, while the inclined (non-vertical) sidewalls of the final elastomeric stamps improve their stability. In comparison, photoresist-based masters suffer from only poorly defined side-walls and lower thermal stability. This may alter the shape of the resist profiles during the fabrication and molding (PDMS baking) process. Further, changing the relief width requires a new lithography mask.

The fabrication process of stamp masters of atomically precise silicon relief with dimensions introduced above is schematically illustrated in Figure 3.2 and detailed in the methods. The relief pattern can be changed considering the standard µCP concepts[290] and the process can easily be adjusted.

First, the desired stripe profile pattern is transferred by standard photolithography, using positive tone resist with high stability against dry etching processes (Figure 3.2a–d). Alternatively, negative tone resist together with an inverted photomask could be used. The photomask contains a stripe pattern with a periodicity of 80 µm, matching the electrode overlaps. Considering the angle of 54.7° between the {100} and {111} silicon planes, the width of the stripes is set to 15 µm (Supplementary information in Section 3.6 and Figure S3.2 for details). This finally results in 4 µm wide trenches after etching to a depth of 8 µm. Since the desired anisotropic etching of Si strongly depends on the orientation of the crystallographic planes, it is crucial that the patterns are parallel to the ⟨110⟩ direction (Figure 3.2d).

To transfer the pattern into the SiO_2, which serves as a mask during KOH etching, the substrates are etched in a RIE system using CHF_3 (Figure 3.2e) due to its high selectivity between silicon and SiO_2.[286] The residual resist is removed and the depths of the etched trenches are measured by profilometry (Figure 3.2f). As apparent in Figure 3.3, after etching for 150 s the etch rate declines from ~ 42 nm min^{-1} for SiO_2 to ~ 2 nm min^{-1} for Si, as the 100 nm thick SiO_2 layer is fully removed and the silicon

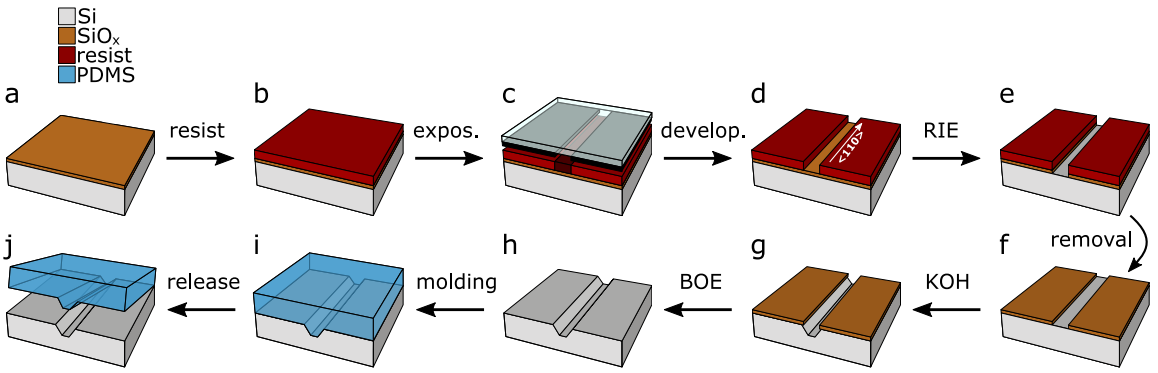

Figure 3.2: Fabrication process of silicon master. (**a**) (100) Si wafer with a 100 nm thick SiO_2 layer. (**b**) Positive tone resist ($\sim$ 500 nm) is applied, (**c**) UV exposure with an optical mask with transparent stripes of 15 µm width and a periodicity of 80 µm. The stripes are aligned parallel to the $\langle 110 \rangle$ Si direction. (**d**) After development, SiO_2 is exposed and (**e**) removed via reactive ion etching. (**f**) Residual resist is removed, exposing the patterned SiO_2, which serves as an etch mask in the anisotropic KOH etching (**g**). The $\{111\}$ plane serves as etch stop, resulting in inclined trenches with an angle of 54.7°, a base width of $\sim$ 4 µm and a depth of $\sim$ 8 µm. (**h**) Removal of the SiO_2 layer with buffered oxide etch yields Si masters. After functionalization with F_{13}TCS as an anti-sticking layer, they can be used as molds for soft-lithography stamps made of PDMS with the negative relief (**i**,**j**).

surface is exposed. Thus, an etch time of $t > 150$ s is chosen to ensure a full removal of the exposed SiO_2 areas ($t = 180$ s). The SiO_2 pattern prepared in this way serves as an etch mask during the KOH etching, which allows to transfer the pattern into silicon. Before KOH etching, the native $\sim$ 2 nm thick SiO_2 layer formed at ambient conditions[301] needs to be removed by a HF dip.

During anisotropic KOH etching, the substrates are mounted in a home-built Teflon holder that enables to suspend the substrates vertically into the KOH bath, with the line pattern parallel to the flow direction of the stirred KOH solution (Figure 3.2g). This facilitates the removal of H_2 bubbles formed during etching. After 40 min, trenches with base widths of $\sim$ 4 µm are observed, corresponding to an etch depth of $\sim$ 8 µm, as shown in Figure 3.4a,b. The line patterns are oriented parallel to the $\langle 110 \rangle$ silicon direction, resulting in well-defined trenches with an inclination angle of 54.7°, caused by the $\{111\}$ facets serving as an etch stop. The undercut at the edges of the SiO_2 etch mask can clearly be identified, as well as residual SiO_2 agglomerations accumulated at the base of the trench. The undercut of several hundreds of nm is formed as etching of the $\{111\}$ facet is marginally present. The experimental etch rate of the $\{100\}$ facet is calculated to be $\sim$ 200–250 nm min^{-1}. This is in good agreement with the expected etch rate of $\sim$ 300 nm min^{-1} by Seidel et al for an 8.8 M KOH solution at 60 °C, which

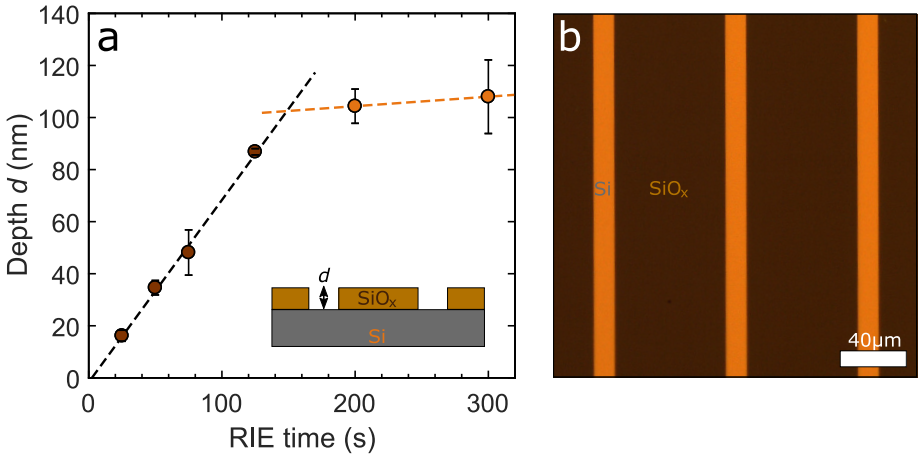

Figure 3.3: Etch rate of SiO_2 by CHF_3-RIE. (**a**) Measured depth of the etched part as a function of etch time (CHF_3-RIE). After etching for 150 s, the etch rate declines as the SiO_2 is fully removed and the Si surface is exposed. The etch rate at $t < 150$ s is ~ 42 nm min^{-1} and corresponds to SiO_2, whereas at $t > 150$ s the rate is ~ 2 nm min^{-1} and corresponds to Si. The thickness of SiO_2 can be determined to be ~ 100 nm. Error bars represent the standard deviation of several measurements. The colour code indicates the transition from SiO_2 to Si. This step corresponds to Figure 3.1d–f. (**b**) Optical micrograph of a sample after RIE and resist removal. The trenches in the SiO_2 layer exposing bare Si can easily be identified. This corresponds to the schematic drawing in Figure 3.2f.

further shows a SiO_2 etch rate of ~ 0.1 nm min^{-1}.[283] To remove the residual SiO_2 etch mask and agglomerations at the base of the trenches, the substrates are treated with BOE (Figure 3.2h), resulting in atomically defined side walls (Figure 3.4c–f).

Finally, the surfaces of the patterned Si substrates are functionalized with F_{13}TCS as an anti-sticking layer, adapted from Beck et al.,[302] which prevents the sticking of the cured elastomeric stamps to the silicon surface.[290,302] When showing a highly hydrophobic surface, the modification of the samples was successful. The final silicon masters can be reused dozens of times to serve as molds for PDMS curing (Figure 3.2i,j). Figure 3.4g,h shows a cured PDMS stamp, which is exactly the negative of the stamp master: a stripe relief with a periodicity of 80 µm, where the individual protrusions have an inclination angle of 54.7° and a base width of ~ 4 µm.

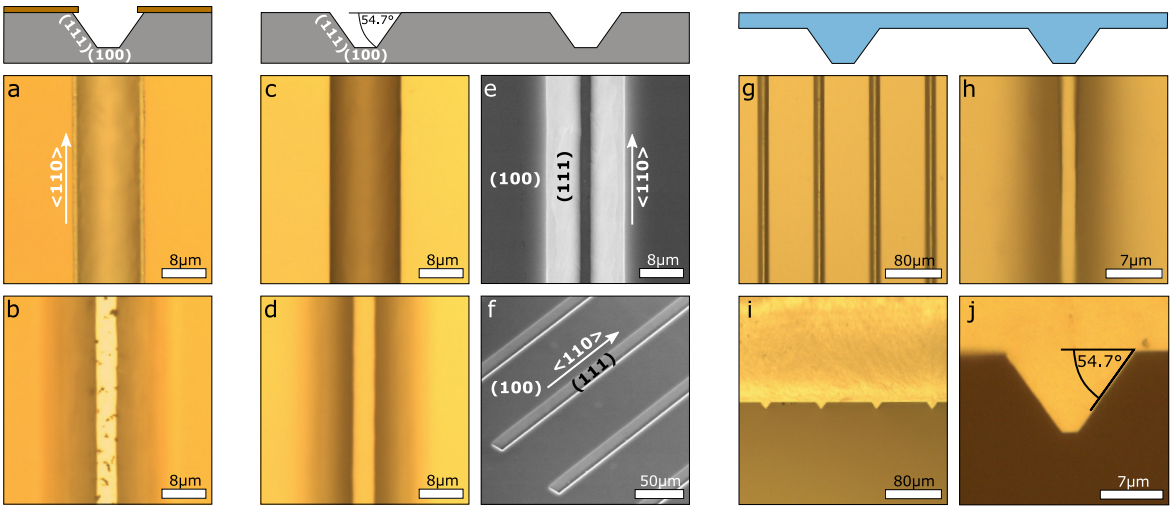

Figure 3.4: Stamp master fabrication and molding of PDMS stamps. (**a**,**b**) Optical micrographs of the stamp master after anisotropic KOH etching for 40 min, focused at the upper edge (**a**) and the base (**b**), respectively. (**c**,**d**) Optical micrographs of the same stamp master after removal of the SiO_2 etching mask by BOE treatment. The SiO_2 undercut (**c**) and the residual SiO_2 parts accumulated at the base (**d**) are clearly removed, resulting in atomically defined side walls. (**e**,**f**) Corresponding SEM micrographs of a stamp master in top view (**e**) and under a tilt view of 40° (**f**). (**g**,**h**) Optical micrographs of the cured PDMS stamp, which is exactly the negative of the stamp master, given by the inclination angle of 54.7°. The corresponding side-views of the PDMS stamp are shown in (**i**,**j**), respectively. The respective schematic drawings are drawn at the top of each subfigure.

3.4.4. Microcontact printing of microchannels

We emphasize that the fabrication of SL microchannels is neither limited to the nanocrystals/nanoparticles we have used, nor to self-assembly of the NCRs at the liquid/air interface.

Here, we use PbS NCRs functionalized with the organic π-system Cu4APc as a model system. Cu4APc replaces the native oleic acid ligands, resulting in highly conductive SLs together with long-range ordering.[123] The organic semiconductor Cu4APc with its functional groups serves as a linker between adjacent NCRs and couples them chemically through binding to the NCR surface (long-range order) and electronically via potentially near-resonant alignment of suitable energy levels and reducing the energy barrier between adjacent NCRs (enhanced conductivity).[58,60] As the native oleic acid stabilized PbS NCRs are soluble in alkanes, the liquid/air interface method developed by Dong et al. can be applied.[119] This is schematically illustrated in Figure 3.5a–c. The NCR dispersion is spread onto the surface of a polar liquid and after evaporation

of the solvent, the NCRs self-assemble into a floating SL film. The thickness and homogeneity of the film can be controlled to a certain degree (e.g. monolayer vs. thick film) by changing the NCR dispersion volume, concentration, injection speed, and the evaporation controlled by the adjustable sealing. After injecting a ligand solution into the polar subphase, the Cu4APc ligands diffuse through the liquid subphase to the NCR SL film and replace the insulating native oleic acid ligands, which renders the highly ordered SL conductive.[123] The floating SL film can now be transferred onto a patterned PDMS stamp by approaching the stamp onto the liquid/air interface (Figure 3.5d,e). Well-defined stripes of the NCR SL film are finally printed to a solid substrate with prepatterned electrodes by µCP, as displayed in Figure 3.5f,g. Adjacent electrodes are connected by an orthogonal SL stripe, forming an individual microchannel with length $L \approx 1$ µm and width $W \approx 4$ µm, respectively (Figure 3.5h).

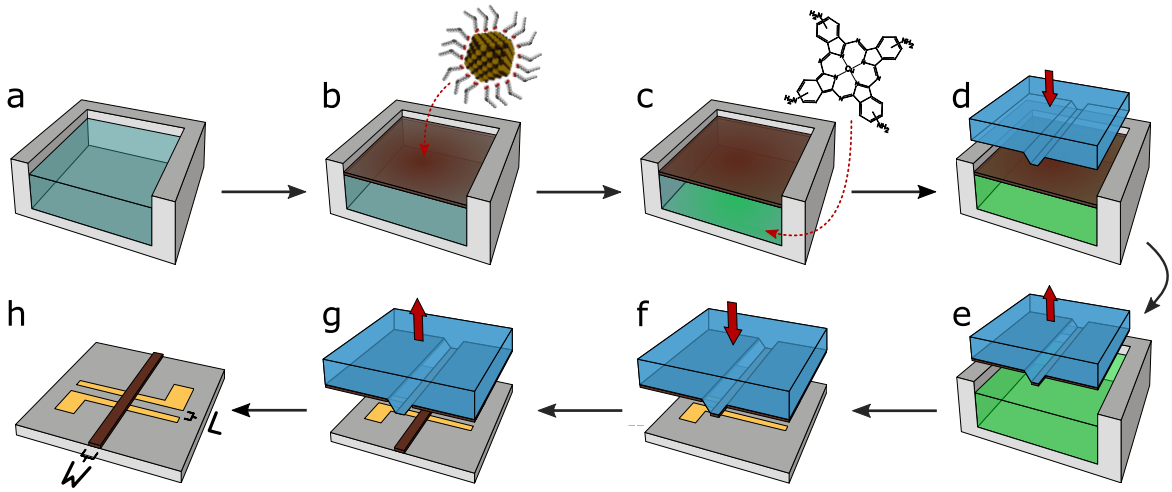

Figure 3.5: Schematic of the self-assembly and ligand exchange of PbS NCR SLs and µCP to form microchannels. (**a**) A home-built Teflon chamber is filled with acetonitrile as the liquid subphase. (**b**) A dispersion of oleic acid stabilized PbS NCRs is injected on top of the subphase and as the dispersion solvent evaporates, the NCRs form a freely floating SL film. (**c**) The ligand solution (Cu4APc in dimethyl sulfoxide) is injected into the bottom of the liquid subphase, the Cu4APc ligands diffuse through the subphase and replace the native oleic acid ligands of the PbS NCRs. (**d**,**e**) A micropatterned PDMS stamp is inked with the SL film by parallelly approaching the floating film. (**f**,**g**) The inked stamp is brought in contact with the electrode device, transferring stripes of the self-assembled SL film. (**h**) Adjacent electrodes are connected by an orthogonal SL stripe, forming an individual microchannel with length $L \approx 1$ µm and width $W \approx 4$ µm, respectively. Up to 330 microchannels can be realised per device.

Figure 3.6a–d shows a PDMS stamp coated with a SL film before and after µCP. After stamping onto a substrate, the film is successfully transferred from the base of the stripes, whereas the spaces between the bases are still coated. Accordingly, µm-patterned areas of SL films can be transferred (Figure 3.6e). The own weight of the ~ 1 cm^3 sized PDMS stamp is sufficient for a highly successful transfer rate of the SL films. The application of additional pressure deforms the elastomeric PDMS stamp (sagging) and, consequently, parts of the interspace between the protruding stripes are transferred, which is undesired (Figure 3.6f,g).

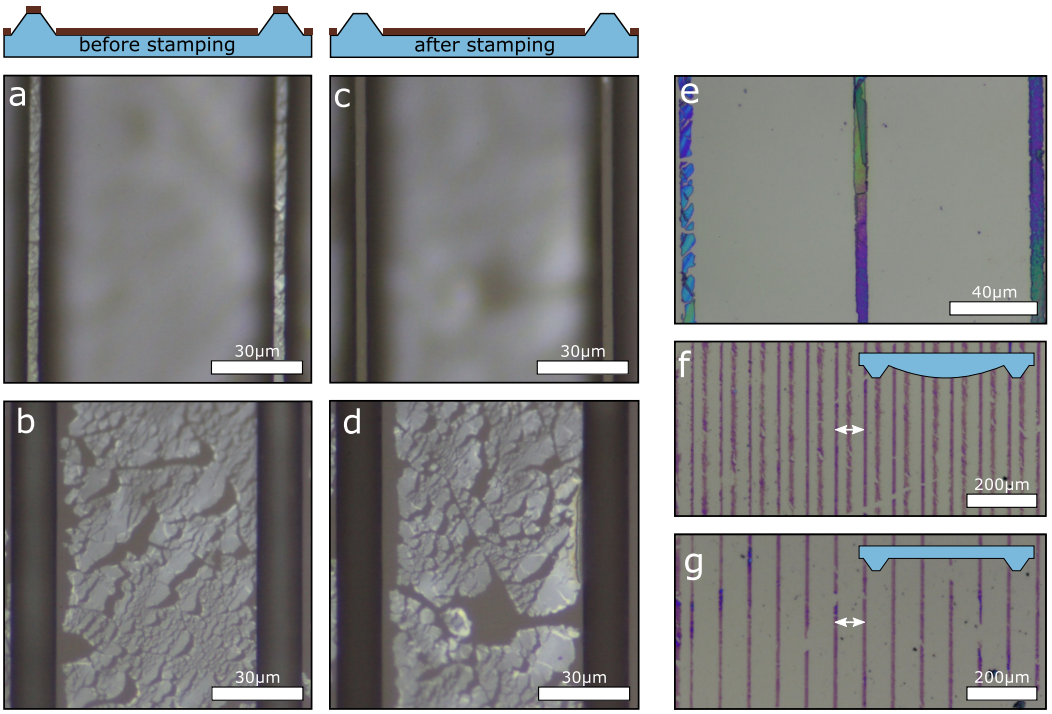

Figure 3.6: Soft-lithography stamps coated with NCR thin films. (**a**,**b**) Optical micrographs of a PDMS stamp after coating with a NCR SL film. Both the base of the stripe (**a**) as well as the space between the stripes (**b**) are coated. (**c**,**d**) After stamping the PDMS stamp onto a substrate, the SL film is transferred from the stripe base (**c**), whereas the space between the bases is still covered (**d**). The respective schematic drawings are drawn at the top of each subfigure. (**e**) Optical micrograph of three microcontact printed SL stripes on a Si/SiO_2 substrate. The different colorations indicate the need for microchannels to characterize single-crystalline domains. (**f**,**g**) Optical micrograph of a Si/SiO_2 substrate after µCP with a coated PDMS stamp. (**f**) Pressure which is to high causes deformation of the elastomeric stamp and parts of the space between the protruding stripes are transferred. (**g**) The own weight of the PDMS stamp is sufficient for a transfer of the thin film with $\sim 100\%$ success rate. The white arrows indicate the periodicity of 80 µm.

Figure 3.7a,b displays microchannels of self-assembled NCR SLs, where one of the transferred well-defined SL stripe connects adjacent electrodes. The formed microchannel is defined by the length between two adjacent electrodes ($L \approx 1$ µm), the width of the transferred stripe ($W \approx 4$ µm) and the thickness h of the NCR SL (Figure 3.7c,d). Remarkably, SLs of different thicknesses (ranging from continuous monolayer to 3D films with thicknesses of up to 2 µm) can be transferred (Figure 3.7e), as the film morphology (meaning areas of different thicknesses) is preserved during the stripe stamping process.

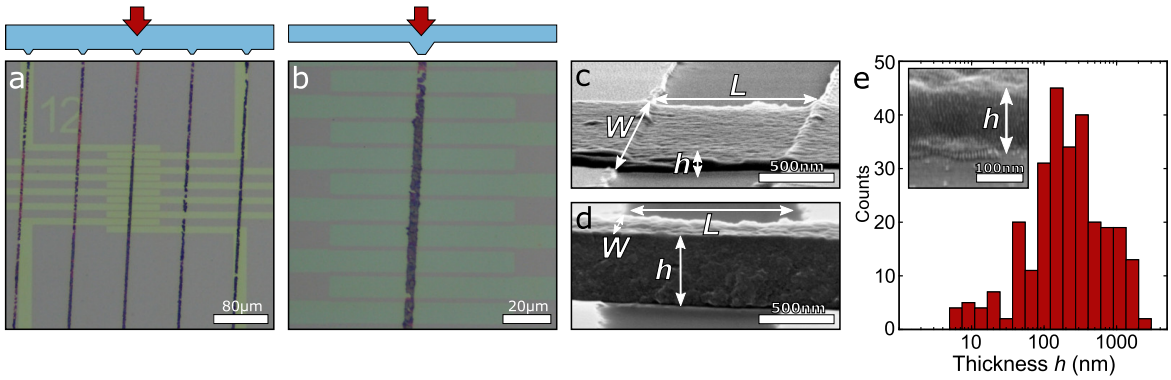

Figure 3.7: PbS NCR SL microchannels formed by µCP. (**a**,**b**) Optical micrographs of a set of electrode pairs (yellow) on a Si/SiO_2 device, where an orthogonally stamped PbS NCR stripe (brown) connects adjacent electrodes to form microchannels which can be contacted individually. The schematics indicate the µCP process with the patterned stamp. (**c**,**d**) Scanning electron micrographs in sideview (85° from normal) of typical microchannels of PbS NCR SL stripes microcontact-printed across two Au electrodes. (**e**) Distribution of the thickness h of transferred SL stripes shows that SLs in a wide range of thicknesses can be transferred ($n = 276$ from several samples). Inset: High-resolution scanning electron micrograph of the well-defined edge of a transferred NCR SL stripe (sample tilted by 85° from normal).

3.4.5. Electronic measurements of superlattice microchannels

Figure 3.8a shows a microchannel, where the NCRs within the SL are highly ordered over the entire channel dimension (Figure S3.3). In these microchannels, the dimensions of the channel itself and the grain-size of typical SLs match. Remarkably, the structural order of the micrometer-sized crystalline SL domains is preserved, which was not achieved in previous attempts.[303] After successful fabrication of SL microchannels, a proof of concept of electronic measurements is given in the following.

Figure 3.8b displays a characteristic two-point conductance measurement of one individual microchannel, showing Ohmic behavior in the range of ±1 V. This allows determining the conductance value G, which is the slope of the I-V curve,

and the conductivity $\sigma = (G \cdot L)/(W \cdot h)$. Measuring approximately two hundred individual microchannels yields a distribution of electric conductivities in the range of $\sigma = 10^{-6}$–10^{-3} S m^{-1}.

In addition to conductivity measurements, field-effect transistor (FET) measurements can be performed on individual microchannels, as shown in the exemplary transconductance curve in Figure 3.8c. The microchannels consisting of PbS NCRs functionalized with the organic π-system Cu4APc show p-type behavior, which agrees with our previous study on the same material.[123] Using the gradual channel approximation (see Supplementary information in Section 3.6 for details), the field-effect hole mobilities $\mu(h^+)$ can be estimated to be in the range of $\mu(h^+) = 10^{-6}$–10^{-4} cm^2 V^{-1} s^{-1}, reaching values of up to 2×10^{-4} cm^2 V^{-1} s^{-1} (Figure 3.8d). The transconductance curve exhibits a hysteresis, which is commonly observed in NCR transistors and attributed to charge carrier trapping at the dielectric/NCR interface or NCR trap states.[304]

Finally, we compare the tailored microchannels with conventional channels, where interdigitated electrodes probe large areas of ~ 1–20×10^4 µm^2 (with 2.5 µm $\leq L \leq$ 50 µm and W up to 1 cm), as displayed in Figure 3.8e. Accordingly, using such conventional channel averages over different SL domains and their properties present in the channel. Figure 3.8f shows the geometry-normalized conductance values $G_{\text{geom}} = G \cdot (L/W)$ of conventional channels and microchannels. For large conventional electrode devices with inhomogeneous SL coatings, the conductivity cannot be calculated due to nonuniform thicknesses. However, the distributions of G_{geom} can clearly be separated, and it is apparent that the normalized conductance of microchannels exceed that of conventional interdigitated electrode devices. Thus, electric transport within microchannel SLs is orders of magnitude more efficient than within the larger state-of-the-art electrode system. This highlights the advantage of the near single-crystalline microchannels presented in this paper.

However, some limitations should be noted. Here, the SL film morphology can only be controlled to a certain degree. As the morphology is preserved during the stripe stamping process, microchannels with different SL thicknesses are obtained. Further optimizing the liquid/air interface method could yield more homogeneous thickness distributions.

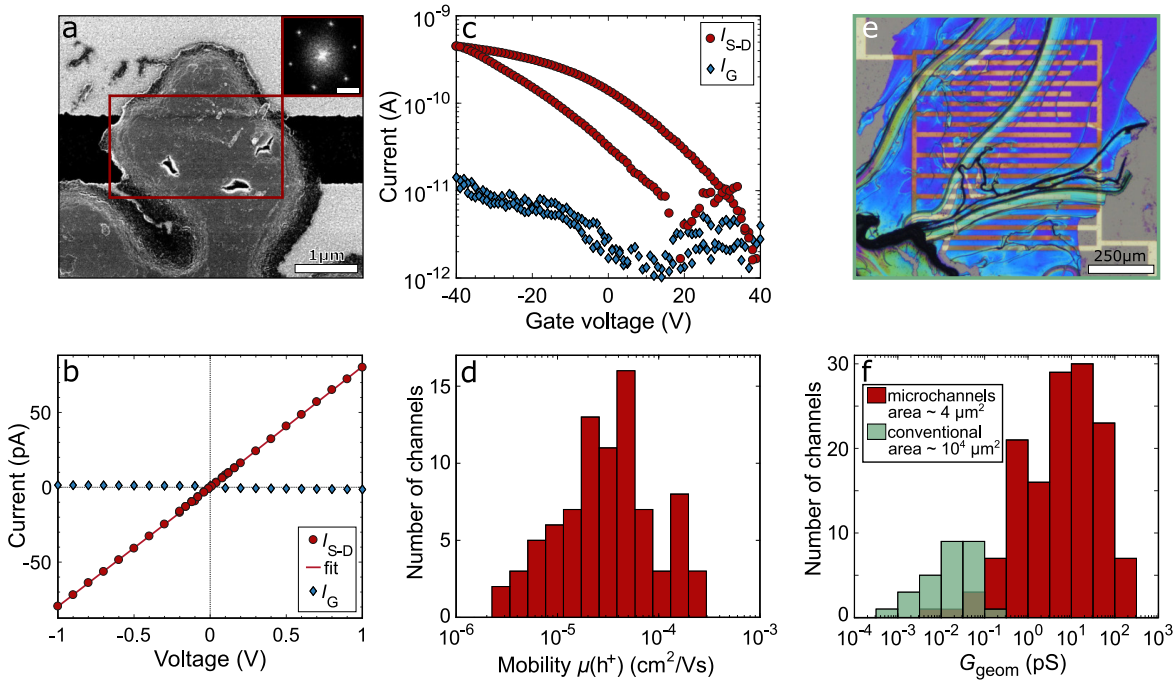

Figure 3.8: Electronic measurements of SL microchannels. (**a**) Scanning electron micrograph of a typical SL microchannel with $L = 1$ µm and $W = 3.0 \pm 0.4$ µm. The inset shows the fast Fourier transform, taken at the highlighted area (red box), indicating highly-ordered NCRs over the entire microchannel. The scale bar of the inset corresponds to 0.6 nm^{-1}. A high-resolution micrograph of this SL is given in Figure S3.3. (**b**) Typical I-V-curve of a microchannel of a PbS NCR SL, showing Ohmic behavior. The linear fit of the current I_{SD} yields the conductance. The leak current I_G is negligible ($V_G = 0$ V). (**c**) Transconductance curve of a microchannel where the source-drain current I_{SD} is modulated by the applied gate voltage V_G (constant source-drain voltage of $V_{SD} = 5$ V). The leak current I_G is orders of magnitude lower. (**d**) Distribution of field-effect hole mobilities $\mu(h^+)$ of $n = 84$ individual microchannels. (**e**) Optical micrograph of a typical conventional channel coated with a PbS NCR SL film. Interdigitated electrodes probe areas of $\sim 10^4$ µm^2 ($L = 20$ µm, $W = 1$ cm). (**f**) Distribution of geometry-normalized conductance of conventional channels (green, $n = 28$) and microchannels (red, $n = 211$), $V_G = 0$ V. Here, $G_{geom} = G \cdot (L/W)$.

In addition to the effect of single-crystallinity, the effect of an increased probability for the formation of percolative networks might play a role. In a previous report, we have already verified that contact resistance of these materials on the conventional substrates is insignificant compared to the bulk resistance.[123] While we cannot rule out that contact resistance may play a role with the microchannels presented here, its effect would most probably be an increase of the overall resistance. Thus, it cannot explain the improved transport properties shown here in Figure 3.8.

3.5. Conclusion

To conclude, we have fabricated microchannels of NCR SLs, where the channel dimensions approach the typical grain size of self-assembled SLs of a few μm^2 by using the soft-lithography technique of µCP. This was achieved by combining the top-down processes of anisotropic etching of silicon and photolithography together with the bottom-up process of NCR self-assembly and ligand exchange at the liquid/air interface. Step-by-step protocols are provided which are easily adjustable for different NCR and SL types. We demonstrate proof-of-principle by fabricating microchannels of near single-crystalline domains of highly ordered coupled PbS NCRs and measuring the electric conductivities as well as field-effect mobilities. A comparison of the SL microchannels with conventional state-of-the-art electrode devices reveals the advantageous effect of the near single-crystalline microchannels, presented in this paper. These microchannel NCR SLs enable novel opportunities for studying fundamental physical properties of NCR ensembles, such as anisotropic electric transport.[305]

3.6. Supplementary information

Layout of photomasks

Figure S3.1 displays the design layout and the photomask for the fabrication process of electrodes with µm-sized gaps. As negative tone resist is used for high-resolution patterning, the electrode structures are opaque.

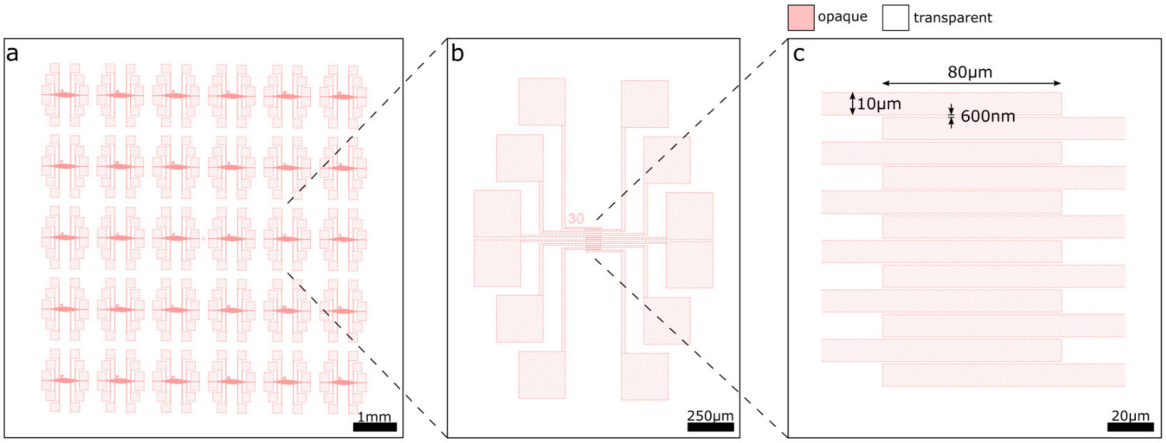

Figure S3.1: Layout of the photomask to create electrode gaps for the microchannels. (**a**) Schematic of the photomask of an entire substrate with 15×15 mm^2. 30 electrode sets are arranged in a 5×6 matrix. (**b**) Schematic of an individual electrode set consisting of 12 electrodes converging from opposed directions in an alternating manner. Each electrode can be contacted by a 250×250 µm^2 contact pad. Labels provide orientation. (**c**) The alternating electrodes form 11 electrode gaps with an overlap of 80 µm. The distance between two electrodes is set to 600 nm. In total, 330 electrode gaps are present.

Figure S3.2 displays the design layout and the photomask for the fabrication process of the stamp masters. The stripes are transparent, since positive tone resist was used. As the final stamp dimensions width and height are set to $W = 4$ µm and $H = 8$ µm, respectively, the width of the photomask stripes is $W^* = 15$ µm, considering the angle of 54.7° between the (100) and (111) Si plane: $x = \frac{H}{\tan(54.7°)} = 5.6$ µm and $W^* = 2x + W = 15.2$ µm.

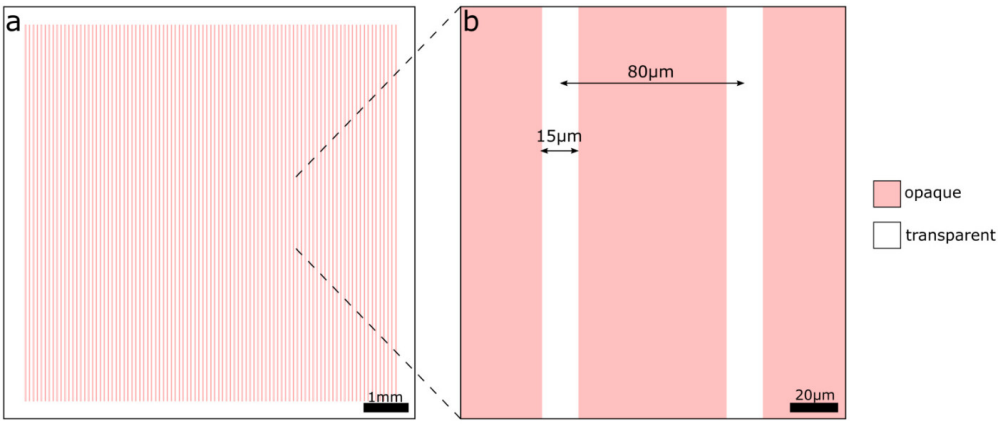

Figure S3.2: Layout of the photomask to fabricate Si-based stamp masters. (**a**) Schematic of the photomask of an entire 15 × 15 mm^2 substrate. (**b**) Transparent stripes with periodicity of 80 µm and a width of 15 µm are present.

Field-effect transistor measurements on microchannels

To calculate the field-effect mobility μ of individual microchannels, the gradual channel equation is used, given in equation S3.1.[25]

$$\mu = \frac{\partial I_{SD}}{\partial V_G} \cdot \frac{L}{W} \cdot \frac{t_{ox}}{\varepsilon_0 \varepsilon_r V_{SD}} \tag{S3.1}$$

$\frac{\partial I_{SD}}{\partial V_G}$ corresponds to the derivation of the transconductance curve (I_{SD} as the detected source-drain current and V_G as the applied gate voltage). L and W are the microchannels length and width. t_{ox} and $\varepsilon_0 \varepsilon_r$ are the thickness and the permittivity of the dielectric SiO_x layer, respectively. V_{SD} corresponds to the applied source-drain voltage. While the geometry of our microchannels is not ideal for FET measurements, this approach is sufficient for a qualitative comparison of different microchannels.

SEM and AFM investigation

Scanning electron micrographs of transferred PbS NCR SLs are given in Figure S3.3. An atomic force micrograph of a SL microchannel is given in Figure S3.4.

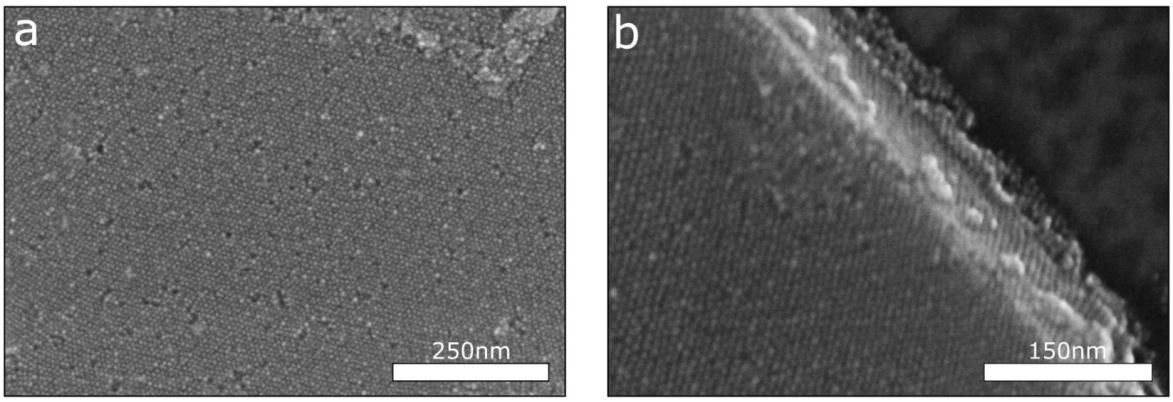

Figure S3.3: Scanning electron micrograph of typical PbS NCR SLs transferred via µCP. (**a**) Magnification of the SL of the microchannel shown in Figure 3.8a. (**b**). High-resolution micrograph of a SL edge. Well-defined edges are present and structural order is preserved.

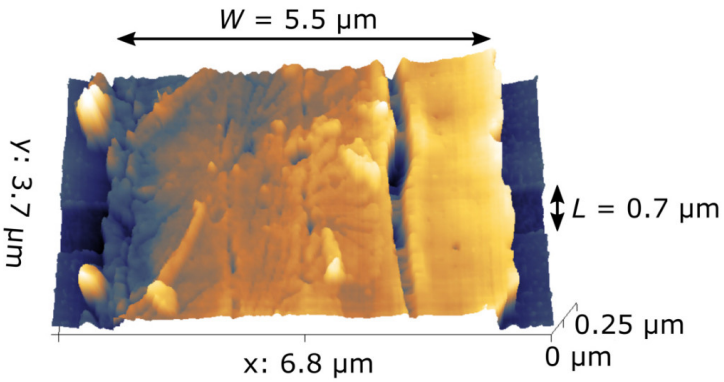

Figure S3.4: Atomic force micrograph of a typical SL microchannel. The dimensions of the microchannel are $L = 0.7$ µm, $W = 5.5$ µm and $h = 250$ nm. Additional to the 4 µm wide stamped SL (left side), an additional part from the inclined side-wall is transferred (right side).

4. Structure-transport correlation reveals anisotropic charge transport in coupled PbS nanocrystal superlattices

Andre Maier[1,4], *Dmitry Lapkin*[2], *Nastasia Mukharamova*[2], *Philipp Frech*[1], *Dameli Assalauova*[2], *Alexandr Ignatenko*[2], *Ruslan Khubbutdinov*[2,5], *Sergey Lazarev*[2,6], *Michael Sprung*[2], *Florian Laible*[3,4], *Ronny Löffler*[4], *Nicolas Previdi*[1], *Annika Bräuer*[3,4], *Thomas Günkel*[3], *Monika Fleischer*[3,4], *Frank Schreiber*[3,4], *Ivan A. Vartanyants*[2,5*], *Marcus Scheele*[1,4*]

[1] Institut für Physikalische und Theoretische Chemie, Universität Tübingen, Auf der Morgenstelle 18, D-72076 Tübingen, Germany

[2] Deutsches Elektronen-Synchrotron DESY, Notkestraße 85, D-22607 Hamburg, Germany

[3] Institut für Angewandte Physik, Universität Tübingen, Auf der Morgenstelle 10, D-72076 Tübingen, Germany

[4] Center for Light-Matter Interaction, Sensors & Analytics LISA$^+$, Universität Tübingen, Auf der Morgenstelle 15, D-72076 Tübingen, Germany

[5] National Research Nuclear University MEPhI (Moscow Engineering Physics Institute), Kashirskoe shosse 31, 115409 Moscow, Russia

[6] National Research Tomsk Polytechnic University (TPU), pr. Lenina 30, 634050 Tomsk, Russia

[*] Corresponding authors

This Chapter is based on the publication in Advanced Materials.

4.1. Abstract

The assembly of colloidal semiconductive nanocrystals into highly ordered superlattices predicts novel structure related properties by design. However, those structure-property relationships, such as charge transport depending on the structure or even directions of the superlattice, have remained unrevealed so far. Here, electric transport measurements and X-ray nano-diffraction are performed on self assembled lead sulfide nanocrystal superlattices to investigate direction-dependent charge carrier transport in microscopic domains of these materials. By angular X-ray cross-correlation analysis, the structure and orientation of individual superlattices is determined, which are directly correlated with the electronic properties of the same microdomains. By that, strong evidence for the effect of superlattice crystallinity on the electric conductivity is found. Further, anisotropic charge transport in highly ordered monocrystalline domains is revealed, which is attributed to the dominant effect of shortest interparticle distance. This implies that transport anisotropy should be a general feature of weakly coupled nanocrystal superlattices.

4.2. Introduction

Semiconductive nanocrystals (NCRs) can be self-assembled into ordered superlattices (SLs) to create artificial solids with emerging collective properties.[2,24,69] Computational studies have predicted that properties such as electronic coupling or charge transport are determined not only by the individual NCRs but also by the degree of their organization and structure.[28,44,46,48] However, experimental proof for a correlation between structure and charge transport in NCR SLs is still pending. Previous experimental research on NCR SLs has either focused solely on the process of self-organization and structural order[32,34–36,141,195] or, in separate studies, on charge transport and electronic properties.[5,25,40,42,53,207] In order to reveal potential transport anisotropy, a correlated investigation of charge transport and structural order on the same NCR SL is required. This allows addressing a variety of fundamental questions. Are the electronic properties of NCR SLs influenced by the SL type and orientation? Do polycrystalline and monocrystalline SLs differ in conductivity? What is the degree of transport anisotropy in NCR SLs?

Here, we address these questions by a direct correlation of the structural and electronic properties of SLs composed of electronically coupled PbS NCRs. We

perform X-ray nano-diffraction and apply angular X-ray cross-correlation analysis (AXCCA)[36,37,271] to characterize the structure of the SL, which are correlated with electric transport measurements of the same microdomains. By that, we reveal anisotropic charge transport in highly ordered monocrystalline hexagonal close-packed (hcp) lead sulfide (PbS) NCR SLs and find strong evidence for the effect of SL crystallinity on charge transport.

4.3. Results & discussion

4.3.1. Microchannels of self-assembled PbS NCRs

As a model system we use oleic acid (OA) capped PbS NCRs with a diameter of 5.8 ± 0.5 nm, which are self-assembled and functionalized with the organic π-system Cu4APc (Cu-4,4',4",4"'-tetraaminophthalocyanine) at the liquid-air interface (details in Figure S4.1–S4.2).[119] This results in long-range ordered and highly conductive SLs, since the rigid and relatively long ligands reduce the energy barrier for charge transport without deteriorating structural order, as it was shown previously.[60,123] Hence, the hybrid system of PbS NCRs and Cu4APc is an ideal compromise between increased electronic coupling and long-range ordered SLs, which was a fundamental prerequisite for this study. By means of soft-lithographic microcontact printing (µCP),[290] we transfer stripes of PbS NCR-Cu4APc SLs with a width (W) of roughly 4 µm onto trenches of $\sim$ 1 µm length (L) between two gold contacts on X-ray transparent Kapton and Si/SiO_x substrates. This defines individually addressable microchannels with $L \approx 1$ µm, $W \approx 4$ µm, and thickness h (Figure 4.1a–e). Since this area is comparable to the typical grain size of PbS NCR SLs,[37] these microchannels enable transport measurements in single-crystalline PbS SLs.

4.3.2. Electric transport measurements

In Figure 4.2, we display the charge transport characteristics of the microchannels as well as its dependence on the thickness of the SL and the probed area. The conductivity σ is calculated as $\sigma = (G \cdot L)/(W \cdot h)$ for all individual microchannels from two-point probe conductance (G) measurements (Figure 4.1e, Figure 4.2a). Within the approximately two hundred individual microchannels measured, we observe electric conductivities in a wide range of values (10^{-6}–10^{-3} S m^{-1}) (Figure 4.2b). This distribution correlates with the thickness of the SL (Figure 4.2c), which also varies by two orders of magnitude

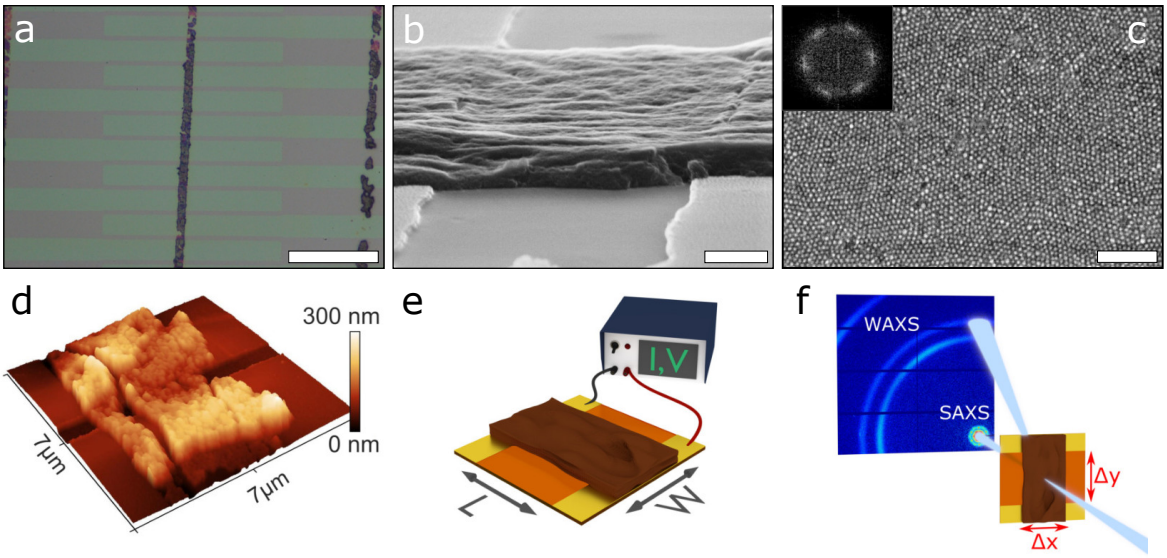

Figure 4.1: Microchannels of PbS NCR SL for conductivity and X-ray nano diffraction measurements. (**a**) Optical micrograph of an orthogonal PbS NCR stripe connecting adjacent electrodes to form individually addressable microchannels. Scale bar: 40 µm. (**b**) Scanning electron micrograph in sideview (85° from normal) of a typical microchannel consisting of a $\sim$ 200 nm thick PbS NCR SL stripe across two Au electrodes. Scale bar: 300 nm. (**c**) High-resolution SEM micrograph showing self-assembled PbS NCRs within a microchannel with near-range order, as indicated by the fast Fourier transform (inset). Scale bar: 100 nm. (**d**) AFM micrograph of a microchannel on a Kapton substrate. (**e**–**f**) Schematics of a SL domain on a Kapton device forming a microchannel with length $L \approx 1$ µm and width $W \approx 4$ µm to characterize the electronic properties (**e**) as well as the structural properties with X-ray nano-diffraction by means of SAXS and WAXS (**f**). Spatial mapping is performed along x and y directions.

over the large number of microchannels analysed here. The correlation is non-linear with a maximum in σ for thicknesses from 70 to 200 nm. Using Si/SiO_x as substrate, we performed field-effect transistor (FET) measurements of the PbS NCR-Cu4APc SLs, revealing p-type behavior, which agrees with our previous study (Figure S4.3).[123] The microchannels show hole-mobilities up to $\mu \sim 10^{-4}$ cm^2 V^{-1} s^{-1}. Based on these transport properties and previous reports on the importance of mid-gap states in PbS NCR materials, we believe that transport in the present material occurs predominantly via hopping through trap states close to the valence eigenstate (the $1S_h$ state).[48,306,307]

We tested the effect of domain boundaries within the SL on electric transport on the same substrates measuring the geometry-normalized conductance of PbS NCR SLs over large active channel areas of $\sim 10^4$ µm^2 (Figure S4.4). As shown in Figure 4.2d, electric transport in this case is approximately two orders of magnitude less efficient

than within the microchannels of ~ 4 µm^2, indicating the advantageous effect of the near single-crystalline channels present in the latter case (see below).

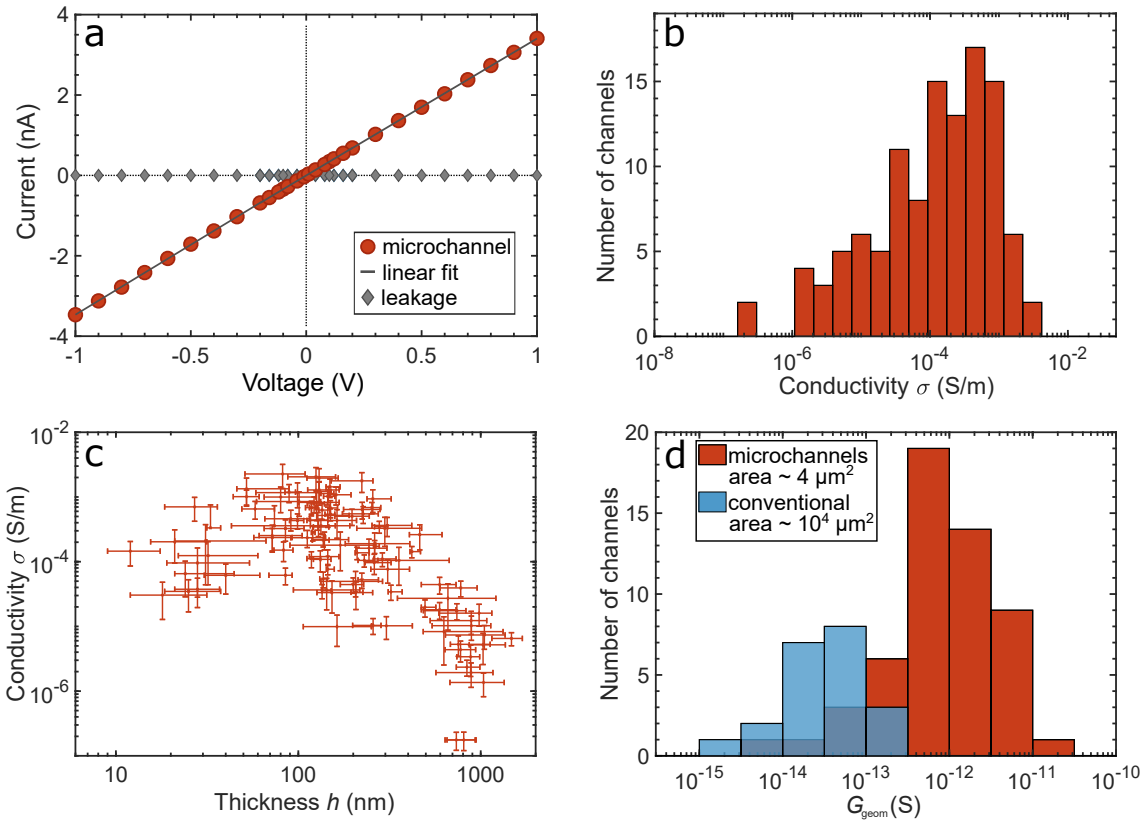

Figure 4.2: Electrical transport measurements of SL microchannels. (**a**) Typical I-V-curve of a PbS NCR SL within a microchannel showing Ohmic behavior (red). The leak current through the dielectric substrate is negligible (grey). (**b**) Distribution of the electric conductivities of 200 individual microchannels. (**c**) Conductivity of the microchannels as a function of PbS NCR SL thickness. Error bars represent the standard deviation of conductivity and the range of thickness determined by AFM, respectively. (**d**) Distribution of geometry normalized conductance of conventional large area and microchannels, probing effective areas of $\sim 10^4$ µm^2 (blue) and ~ 4 µm^2 (red), respectively. Measured conductance values are normalized to the channel geometry (L/W). Dark blue color corresponds to the overlap of the distributions.

4.3.3. X-ray nano-diffraction

Further investigations of structural properties of the same microchannels on Kapton substrates using X-ray nano-diffraction in correlation with conductivity measurements are the focus of this study (Figure 4.1e–f, Figure S4.5). We determined the structural details of all microchannels by X-ray nano-diffraction (Experimental Section 4.4 and

Figure S4.6–S4.9). Using a nano-focused X-ray beam, we collected diffraction patterns at different positions in each channel (Figure 4.1f). Two typical small- and wide-angle (SAXS and WAXS, respectively) diffraction patterns from representative microchannels, averaged over all positions within these channels, are shown in Figures 4.3a,g(b,h). For some of the microchannels we observe several orders of Bragg peaks in SAXS attributed to monocrystalline SLs (Figure 4.3a), whereas the rest of the channels demonstrate continuous Debye-Scherrer rings with low intensity modulations corresponding to polycrystalline SLs (Figure 4.3g). From the angular-averaged profiles, shown in Figures 4.3c,i, we revealed two dominant SL structures: a monocrystalline, random hexagonal close-packed (rhcp) lattice mainly oriented along the $[0001]_{\mathrm{SL}}$, and a polycrystalline, body-centered cubic (bcc) lattice primarily oriented along the $[110]_{\mathrm{SL}}$ (SEM micrographs given in Figure S4.13). From the peak positions in SAXS, we estimated the unit cell parameters (a_{rhcp} and a_{bcc}) for each channel and corresponding nearest-neighbor distances (NND), that are $d_{\mathrm{NN}} = a_{\mathrm{rhcp}}$ for rhcp and $d_{\mathrm{NN}} = (\sqrt{3}/2) \cdot a_{\mathrm{bcc}}$ for bcc. The averaged NNDs for all rhcp and bcc channels are 7.8 ± 0.4 nm and 6.9 ± 0.2 nm, respectively. In WAXS (Figures 4.3b,h), we observe parts of three Debye-Scherrer rings corresponding to $\{111\}_{\mathrm{AL}}$, $\{200\}_{\mathrm{AL}}$, $\{220\}_{\mathrm{AL}}$ reflections of the PbS atomic lattice (AL). From the single WAXS pattern analysis we found different degrees of angular disorder of NCRs: roughly 24° for rhcp and 16° for bcc channels (Figure S4.9).

To study the relative orientation of the NCRs inside the SL, we applied AX-CCA,[271] which is based on the analysis of the cross-correlation functions (CCFs), to the measured scattering data (Figure S4.10–S4.12). We evaluated the CCFs for the SL and AL peaks for both rhcp and bcc structures. We found that in the rhcp monocrystalline channels (Figure 4.3d) the $[111]_{\mathrm{AL}}$ and $[110]_{\mathrm{AL}}$ directions of the NCRs are collinear to the $[0001]_{\mathrm{SL}}$ and $[2\bar{1}\bar{1}0]_{\mathrm{SL}}$ directions, respectively (Figure 4.3f). In bcc polycrystalline channels (Figure 4.3j), all corresponding SL and AL directions are aligned (e.g. $\langle 100 \rangle_{\mathrm{SL}}$ and $\langle 100 \rangle_{\mathrm{AL}}$), as shown in Figure 4.3l. The similarity between the experimental CCFs and simulated CCFs for these structures confirms the obtained angular orientation of the NCRs in the SL (Figure 4.3d,e and 4.3j,k, respectively).

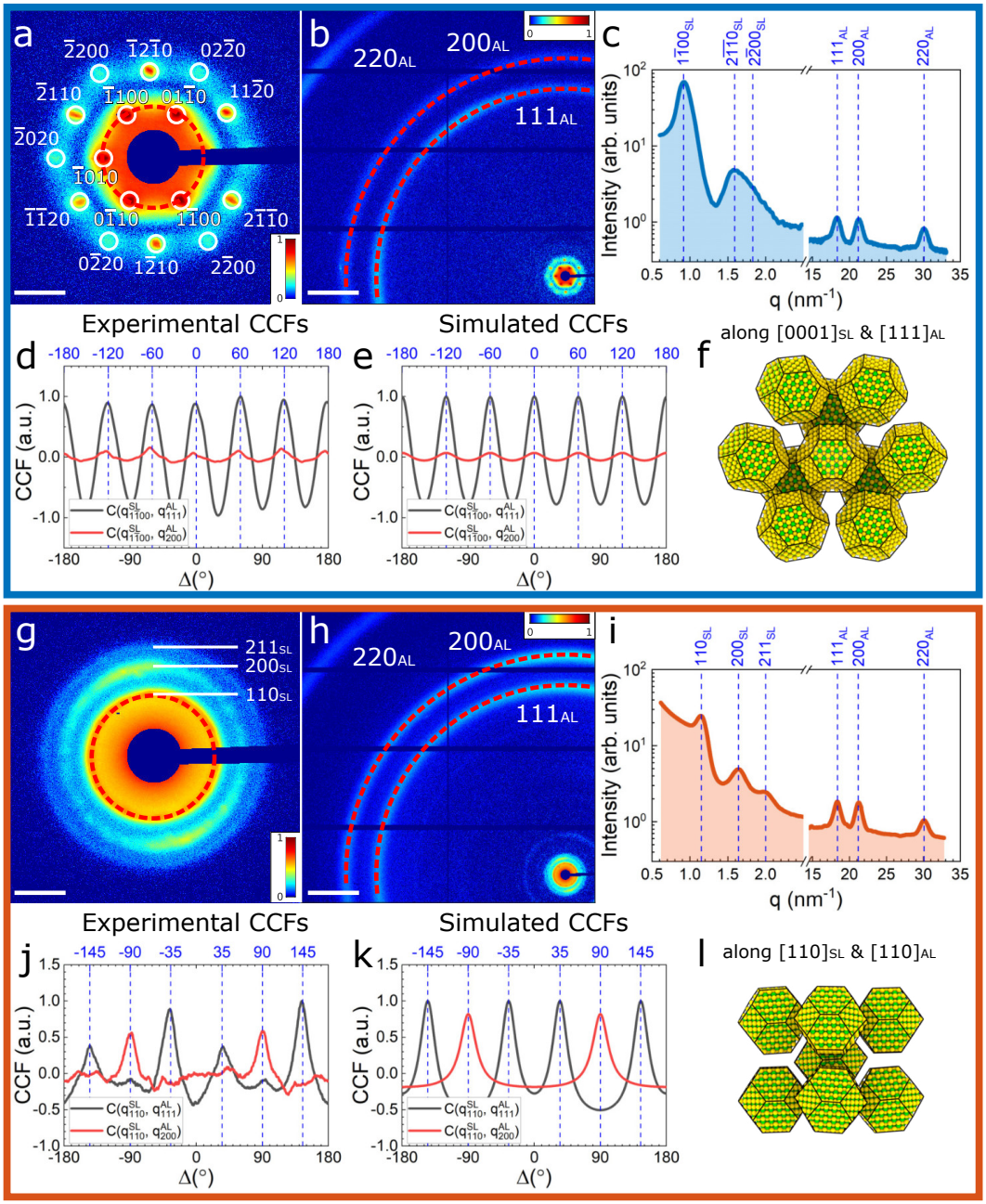

Figure 4.3: Structural investigation of the SL structures. Exemplary SAXS (**a**,**g**) and WAXS (**b**,**f**) patterns averaged over one microchannel for two typical cases: a monocrystalline rhcp SL oriented along $[0001]_{\mathrm{SL}}$ (**a**,**b**) and a polycrystalline bcc SL oriented along $[110]_{\mathrm{SL}}$ (**g**,**h**). (**c**,**i**) Azimuthally averaged intensity profiles of SAXS ($q < 2.5$ nm^{-1}) and WAXS ($q > 15$ nm^{-1}) signals of the two SL types. (**d**,**j**) Averaged CCFs for the two SLs, calculated for the first SAXS peaks ($\langle 1\bar{1}00\rangle_{\mathrm{SL}}$ in the rhcp case (**d**) and $\langle 110\rangle_{\mathrm{SL}}$ in the bcc case (**j**)) and the $\langle 111\rangle_{\mathrm{AL}}$ or $\langle 200\rangle_{\mathrm{AL}}$ WAXS peaks. (**e**,**k**) Simulated CCFs for the two models shown in (f,l). (**f**,**l**) Schematic drawing of the proposed SL structures: (**f**) $[0001]_{\mathrm{SL}}$-oriented rhcp SL of PbS NCRs, where the NCRs are aligned as indicated and (**l**) $[110]_{\mathrm{SL}}$-oriented bcc SL of PbS NCRs, where all the corresponding SL and AL directions are aligned. For clarity, ligand spheres are omitted. Scale bars in (a,g) and (b,h) correspond to 1 nm^{-1} and 5 nm^{-1}, respectively.

4.3.4. Evaluation of structure-transport correlations

Upon correlating the X-ray with the electric transport measurements, we found that microchannels containing the polycrystalline bcc SLs exhibit higher conductivity than monocrystalline rhcp SLs over the entire range of thicknesses (Figure 4.4a). This can in part be understood in terms of the shorter NND which exponentially increases the hopping probability (Figure 4.4b).[25,28] The microchannels exhibit strong characteristic Raman signals for Cu4APc (750 cm^{-1} and 1,050–1,650 cm^{-1}, Figure 4.4c) which vanish for probing areas outside the microchannels, verifying the specific functionalization of the NCRs with the organic π-system (Figure S4.14). We used the intensity of the two characteristic Raman bands to compare the relative density of Cu4APc molecules within different SLs. We found that polycrystalline bcc SLs with the smaller NND exhibit generally stronger Raman signals from Cu4APc than monocrystalline rhcp SLs with larger NND (Figure 4.4c, Figure S4.14). This means that in monocrystalline rhcp SLs fewer native OA molecules have been exchanged by Cu4APc, resulting in larger interparticle distances, which adversely affects conductivity. From Figure 4.4b one can identify several cases of monocrystalline rhcp SLs having conductivities as high as those of polycrystalline bcc SLs ($\sigma \sim 10^{-4}$–10^{-3} S m^{-1}), although the NND is much larger. We consider this as supporting evidence that the degree of SL crystallinity (poly vs. mono) has a significant effect on the conductivity, which, in the present example, compensates the effect of the much larger interparticle distance. The SLs with smaller interparticle distance exhibit stronger Raman signals from Cu4APc compared to larger SLs (Figure S4.14), corroborating a correlation between interparticle distance and ligand exchange. In fact, the smallest lattice parameter of $\sim$ 6.8 nm in Figure 4.4b corresponds to an interparticle distance of $\sim$ 1 nm, which is approximately the length of one Cu4APc molecule or the minimal width of a fully exchanged ligand sphere. In contrast, residual OA leads to greater interparticle distances due to steric interactions of adjacent OA shells,[81] explaining the spread of the NNDs (Figure 4.4b, Figure S4.8). The occurrence of the two SL types (rhcp and bcc) found here may be related to the previously observed hcp-bcc transition for OA-capped PbS NCR SLs upon tailored solvent evaporation.[134] Similarly, our polycrystalline bcc SLs are assembled from PbS NCRs dispersed in hexane, whereas hexane-octane mixtures resulted in monocrystalline rhcp SLs. This invokes different solvent evaporation rates, which may lead to distinct SL unit cells.[81,195]

From the single WAXS pattern analysis (Figure S4.9) we found that NCRs are aligned in the SL with different degrees of angular disorder: roughly 16° for bcc channels

and 24° for rhcp channels. We believe that the NCRs are oriented in the SL due to facet specific ligand-ligand interactions. The functionalization of NCRs with shorter Cu4APc ligands leads to the formation of a SL with higher symmetry, such as bcc, in which the NCRs are highly aligned.[136] In contrast, a large spherical ligand shell leads to a close-packed structure with a lower degree of NCRs orientation, such as rhcp.

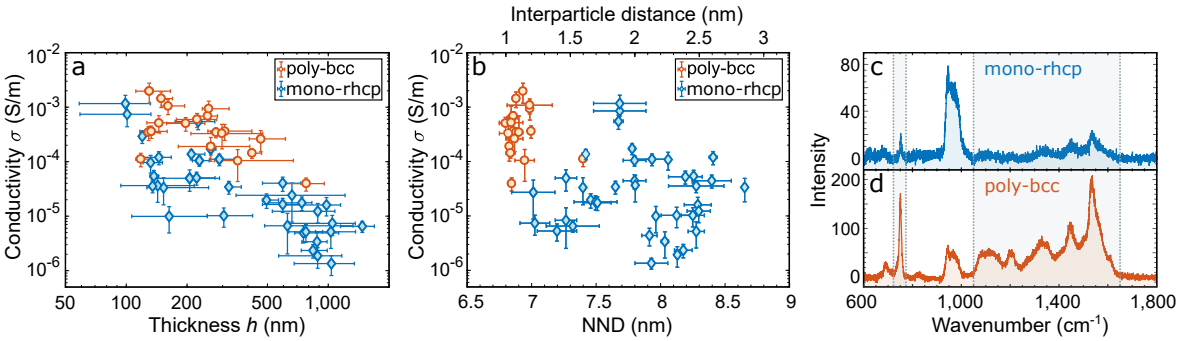

Figure 4.4: Parameters for structure-transport correlations. (**a**,**b**) Conductivity of individual microchannels as a function of SL thickness (**a**) and nearest-neighbor distance NND (**b**). The SL type is indicated by the color code. (**c**,**d**) Typical Raman spectra of a monocrystalline rhcp (**c**) and a polycrystalline bcc (**d**) SL, featuring characteristic Cu4APc signals at 750 cm^{-1} and 1,050–1,650 cm^{-1} (highlighted regions). The signal at $\sim$ 950 cm^{-1} originates from the Si/SiO_x substrate.

In view of the non-monotonic correlation between conductivity and SL thickness, we note that very thin NCR films exhibit holes/microcracks, which are reduced with increasing thickness.[213] In contrast, the conductivity in thick films may be affected by a fringing electric field. The electric field is not homogeneous along the sample normal, and current flows mainly in the bottom layers close to the contacts. However, the conductivity is calculated over the entire channel where the full height is used.

4.3.5. Anisotropic charge transport

We now turn to the key novelty of this work, the transport anisotropy, that is, the influence of the SL orientation with respect to the electric field on the electric conductivity. For this, it is mandatory to account for the effect of SL thickness, incomplete ligand exchange and crystallinity and only compare SLs which are very similar in this regard. In doing so, we found strong evidence for a favored angular direction of charge carrier hopping, indicating anisotropic charge transport within the SL. Figure 4.5a,d displays exemplary SAXS patterns averaged over each microchannel of two monocrystalline rhcp SLs with identical structure, i.e. lattice parameter and thickness (Figure S4.15a). They

differ only in terms of the azimuthal orientation with respect to the applied electric field. We define the azimuthal angle α between the electric field vector E (which is oriented vertically due to horizontal electrode edges) and the nearest-neighbor direction d_{NN} (one of the $\langle 2\overline{1}\overline{1}0\rangle_{\mathrm{SL}}$ directions pointing to the nearest-neighbors). The angle α can vary from 0° to 30° for the sixfold in-plane symmetry. For $\alpha = 0°$, the d_{NN} direction is oriented parallel to the vector of electric field E, whereas for $\alpha = 30°$, the angular (in-plane) offset between the vectors E and d_{NN} is maximized. Our key result is that for any two otherwise comparable channels, we observe higher conductivity for the respective channels with lower angle α. The two extremes ($\alpha = 0°$ and $\alpha = 30°$) are shown in the corresponding real space SEM micrographs of the $(0001)_{\mathrm{SL}}$ plane of two rhcp SLs in Figure 4.5b,e. The difference in conductivity between two otherwise identical SLs is 40–50%. A statistical investigation of other microchannels with monocrystalline rhcp SLs reveals similar α-dependent conductivity differences (Figure S4.15). This correlation between σ and α indicates anisotropic charge transport, for which the direction of nearest neighbors is assumed to be the most efficient for transport.

In contrast to atomic crystals with transport anisotropy, which exhibit strong electronic coupling and ballistic transport (e.g. black phosphorus), the NCR SLs studied here are in the weak coupling regime. This implies temperature-activated hopping as the predominant charge transport mechanism and invokes a strong dependence on the hopping distance.[25,28] Our results suggest that charge transport is most efficient if the applied electric field is iso-oriented with the nearest-neighbor direction d_{NN} in the SL plane, since this leads to the shortest hopping distance (Figure 4.5c). Any other orientation (Figure 4.5f) results either in a larger hopping distance (straight arrow) or a deviation from the direction of the electric field together with an increased number of required jumps for electrons to travel the same distance (zig-zag path), which is detrimental to charge transport. This implies that transport anisotropy should be a general feature of weakly coupled, monocrystalline NCR SLs, originating from the dominant effect of the shortest interparticle distance. Accordingly, one could predict the favored direction of charge transport within different SL types, such as simple cubic, fcc or bcc, being the $\langle 100\rangle$, $\langle 110\rangle$ or $\langle 111\rangle$ SL directions, respectively. A similar charge transport anisotropy was computationally predicted for bcc and fcc SLs.[46] Further, we note that the orientational order of the NCRs observed here might be an additional source for anisotropic charge transport as different coupling strengths have been predicted along particular AL directions.[46,48] In the present case, the most efficient transport occurs if the $[110]_{\mathrm{AL}}$ direction of all NCRs is iso-oriented with the electric field.

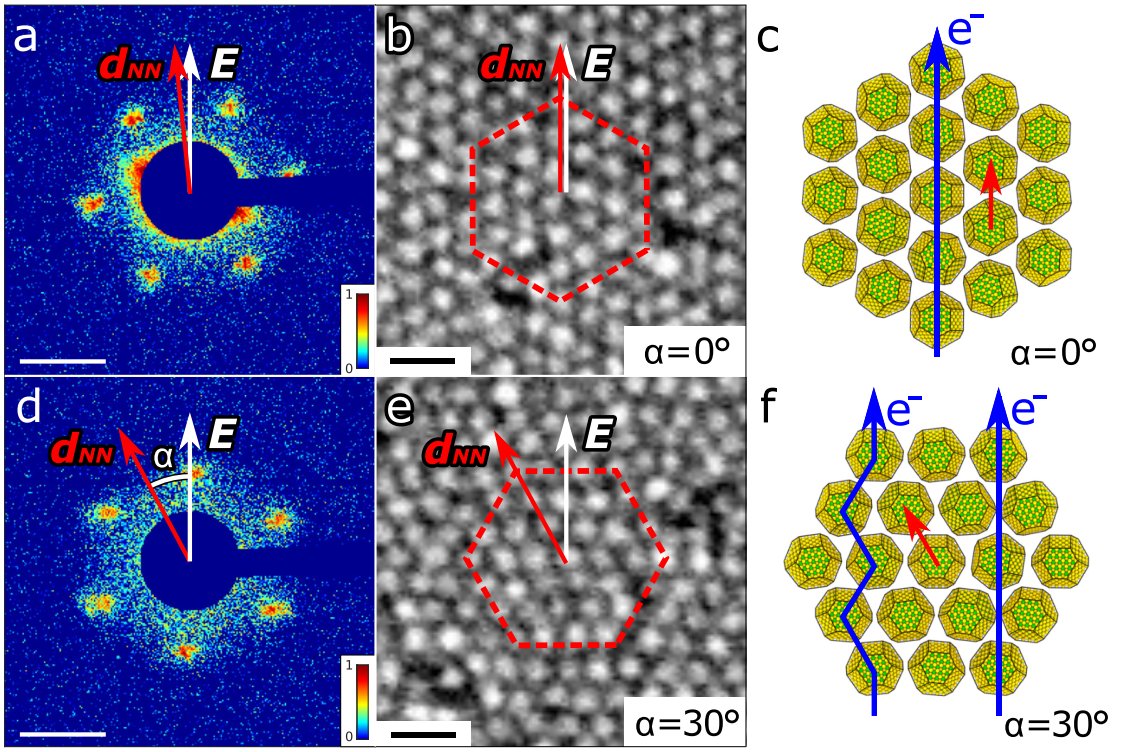

Figure 4.5: Anisotropic charge transport in monocrystalline NCR SLs. (**a**,**d**) Exemplary averaged SAXS diffraction patterns of comparable monocrystalline rhcp microchannels, oriented along $[0001]_{SL}$. The azimuthal orientation is defined by the relative angle α between the electric field vector E and the nearest-neighbor direction d_{NN}. SLs with low values of α feature 40–50% higher conductivities than their counterparts with large α. Scale bar: 1 nm^{-1} . (**b**,**e**) Corresponding real-space SEM micrographs of the SL oriented along $(0001)_{SL}$ with $\alpha = 0°$ and 30°. The hexagon indicates the orientation of the SL. d_{NN} points along the alignment of the NCRs (nearest neighbors). For $\alpha = 0°$, the vector d_{NN} is parallel to E, resulting in enhanced conductivity. Scale bar: 15 nm. (**c**,**f**) Schematic of the rhcp SL and the favored hopping path for $\alpha = 0°$ (blue arrow) along the d_{NN} direction (red arrow) (**c**). For an in-plane offset ($\alpha = 30°$), the larger hopping distance or the zig-zag path are detrimental to charge transport (**f**). Ligand spheres of NCRs are omitted for clarity.

A high degree of control provided over the SL type and orientation would enable the exploitation of such transport anisotropy also with more complex NCR assemblies (e.g. binary NCR SLs[127] or honeycomb structures[160]) for application in functional electronic devices with tailored transport anisotropy. Furthermore, these results constitute an important step towards the understanding of the intrinsic properties and fundamental limits of these fascinating new NCR-based systems.

4.4. Experimental section

4.4.1. Superlattice microchannel fabrication

Oleic acid-stabilized PbS NCRs were synthesized according to Weidman et al.[55] and dispersed in hexane/octane (ratio of 4:1 and 1:0, $c = 4$ µmol l^{-1}). Sizing-curves to UV-Vis absorption spectra and SEM investigation yield a particle size of 5.8 ± 0.5 nm (Figure S4.1).[76] The NCRs were self-assembled at the liquid-air interface according to Dong et al.[119] and ligand exchanged with the organic π-system Cu-4,4',4",4"'-tetraaminophthalocyanine. For µCP, a micropatterned PDMS stamp was inked with the SL film and stamped onto devices with prepatterned Au electrodes (Kapton membranes of 125 µm thickness or Si/SiO_x wafers with 200 nm SiO_x). Individual microchannels consisting of an electrode pair and a connecting SL stripe were obtained with $L \approx 1$ µm and $W \approx 4$ µm. The preparation was performed in a nitrogen glovebox.

4.4.2. Transport measurements

All devices were measured at room temperature in a nitrogen flushed probe station (Lake Shore, CRX-6.5K). Individual electrode pairs were contacted and analysed by a source-meter-unit (Keithley, 2636B).

4.4.3. X-ray nano-diffraction

Nano-diffraction measurements were performed at Coherence beamline P10 of the PETRA III synchrotron source at DESY. An X-ray beam with $\lambda = 0.898$ Å ($E = 13.8$ keV) was focused down to a spot size of $\sim 400 \times 400$ nm^2 (FWHM) at the GINIX nano-diffraction endstation.[263] The two-dimensional detector EIGER X4M (Dectris) with 2070×2167 pixels and a pixel size of 75×75 µm^2 was positioned 370 mm downstream from the sample and ~ 9 cm off-centre to allow simultaneous detection of SAXS and WAXS signals. Diffraction mapping of individual microchannels was performed, collecting 100–200 diffraction patterns on a raster grid in x and y direction with 250 nm step size and an acquisition of 0.5 s. From averaged diffraction patterns for every channel, the SL structure was deduced and from azimuthally-averaged radial profiles the SAXS peak positions were extracted. AXCCA was applied and two-point cross-correlation functions (CCFs) for all channels were calculated,

according to Equation (4.1):

$$C_{\mathrm{CCF}}(q_{\mathrm{AL}},q_{\mathrm{SL}},\Delta) = \langle \tilde{I}(q_{\mathrm{AL}},\varphi), \tilde{I}(q_{\mathrm{SL}},\varphi+\Delta)\rangle_{\varphi} \quad , \tag{4.1}$$

where $\tilde{I}(q,\varphi) = I(q,\varphi) - \langle I(q,\varphi)\rangle_{\varphi}$ and $I(q,\varphi)$ is an intensity value taken at the point (q,φ) which are polar coordinates in the detector plane.[36,37,271] $\langle ... \rangle_{\varphi}$ denotes averaging over all azimuthal φ angles. q_{SL} correspond to SAXS peaks and q_{AL} to WAXS peaks.

4.4.4. Microchannel characterization

SEM imaging was conducted with a HITACHI model SU8030 at 30 kV and AFM investigations with a Bruker MultiMode 8 HR in contact mode and Raman spectroscopy with a confocal Raman spectrometer LabRAM HR800 (Horiba Jobin-Yvon) at $\lambda = 632.8$ nm (He-Ne-laser).

Details on materials, the self-assembly and fabrication processes, X-ray nano-diffraction and AXCCA are given in the Supporting information Section 4.5.

4.5. Supplementary information

4.5.1. Experimental details

Materials

The following chemicals and materials were used as received. Negative tone resist (ma-N 405), developer (ma-D 331/S) and remover (mr-Rem 660) were purchased from micro resist technology GmbH, polydimethylsiloxane (PDMS) Sylgard 184 prepolymer and cross-linker from Dow Corning GmbH and tridecafluoro-(1,1,2,2)-tetrahydrooctyl-trichlorosilane (F_{13}TCS) from Sigma Aldrich. Kapton® polyimide membranes (125 µm thickness) were purchased from DuPont. Si/SiO_x wafers (200 nm SiO_x thickness) were purchased from Siegert Wafer GmbH. Oleic acid stabilized PbS NCRs were synthesized according to Weidman et al.[55] and Cu-4,4',4",4"'-tetraaminophthalocyanine (Cu4APc) according to Jung et al.[299] Acetone (99.8%, extra dry), acetonitrile (99.9+%, extra dry), dimethyl sulfoxide (99.7+%, extra dry), n-hexane (96+%, extra dry) and n-octane (99%, extra dry) were purchased from Acros Organics.

Characterization of PbS NCRs

Figure S4.1 displays the size investigation of oleic acid-stabilized PbS NCRs, synthesized according to Weidman et al.[55] Applying sizing curves to UV-Vis absorption spectra (in tetrachlorethylene) and SEM investigation yield a particle diameter of 5.8 ± 0.5 nm (size distribution of 8%).[76]

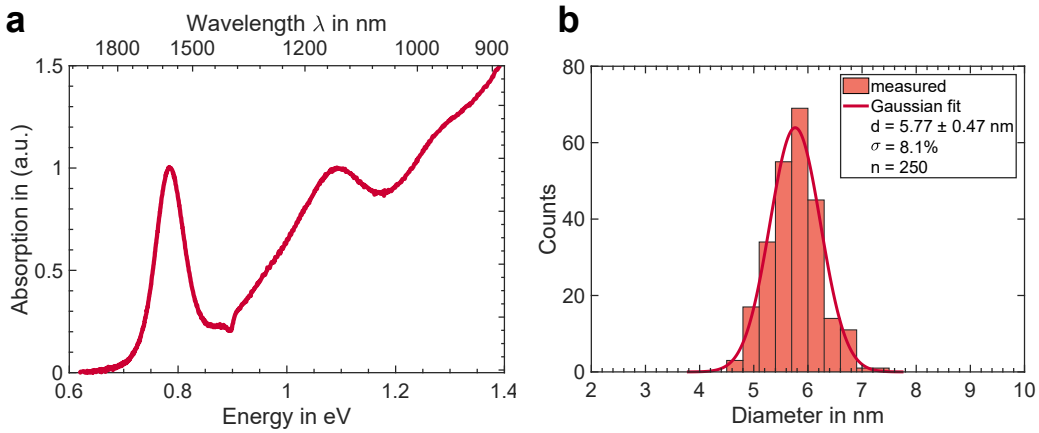

Figure S4.1: PbS NCR size analysis. (**a**) Absorption spectrum of native oleic acid-stabilized PbS NCRs in tetrachlorethylene. The first excitonic transition is observed at 787 meV (1580 nm). (**a**) Distribution of the diameter of 250 PbS NCRs, measured by SEM. Gaussian fit reveals a diameter of 5.80 ± 0.5 nm (size distribution of 8%).

Layout of microchannel devices

We developed microchannel devices, where individual electrode pairs with an overlap of 80 µm form channels, which can be addressed individually. Up to 330 channels per device could be realised. By means of µCP,[237,290] we transfer periodic stripes of self-assembled SLs with widths of 4 µm and a periodicity of 80 µm using prepatterned PDMS stamps. Thus, most of the substrate area remains uncoated. The microchannels are formed by pairs of overlapping electrodes, which are connected by one perpendicularly printed stripe of PbS NCR SL. The electrode thickness was chosen to be $\sim$ 10 nm in order to avoid breaking of PbS NCR stripes at the edges. Due to the channel geometry, an entirely homogeneous electric field is established within the channel and the direction of the electric field vector is well-known.

Device fabrication

For the microchannel device fabrication, we used photolithography techniques to pattern Au microelectrodes on Kapton membranes (125 µm thickness) or Si/SiO_x wafers (200 nm SiO_x). After exposure and development of the negative tone resist, 2.5 nm Ti as an adhesion layer and 8 nm Au were thermally evaporated under high vacuum conditions. Ultrasonic-assisted lift-off was performed to remove the resist and the metal layer on top, revealing electrodes with gaps of 0.7 to 1.7 µm (referred to as channel length L). Stamp masters based on silicon were fabricated by means of photolithography and pattern transfer via reactive ion etching. Defined trenches of 4 µm width and a periodicity of 80 µm were fabricated via anisotropic KOH etching of silicon.[284] Stamp masters were functionalized with F_{13}TCS as an anti-sticking layer. Degassed PDMS (10:1 ratio prepolymer and cross-linker) was poured onto the masters and cured at 150 °C overnight. Stamps were released from the master, cleaned by sonication in isopropanol and dried under pressurized nitrogen flow.

Self-assembly and ligand exchange of PbS NCR films

PbS NCRs were self-assembled via the liquid-air interface method developed by Dong et al.[115,119] and modified as previously reported.[59,60,123,124] Figure S4.2a–c displays a schematic of the fabrication process. A certain volume (70–100 µl) of a PbS NCR dispersion was injected on top of an acetonitrile subphase in a home-built Teflon chamber with an area of 1×1 cm^2. The injection speed was controlled by a syringe pump. The evaporation rate of the dispersion solvent can be controlled by an adjustable lid/sealing. As the dispersion solvent evaporated, the NCRs formed a freely floating membrane. The Cu4APc ligand solution (dissolved in dimethyl sulfoxide) was injected

at the bottom of the liquid subphase. Cu4APc ligands diffuse through the liquid subphase to the NCR membrane and replace the insulating native oleic acid ligands over a duration of 4 h. The thickness of the floating film can be controlled to a certain degree (e.g. monolayer vs. thick film) by changing the NCR dispersion volume, concentration and injection speed.

Microcontact printing of PbS NCR stripes

Figure S4.2d–g schematically illustrates the process. A micropatterned PDMS stamp was parallelly brought into contact with the free floating PbS NCR membrane for 5 s. Excess liquid was removed from the stamp with a tissue. The coated stamp was slightly pressed onto the substrate with prepatterned Au-electrodes for 30 s. One half of the coated stamp was pressed onto a Kapton device, the other half onto a Si/SiO_x device. Afterwards, the stamp was removed in a tilted manner.

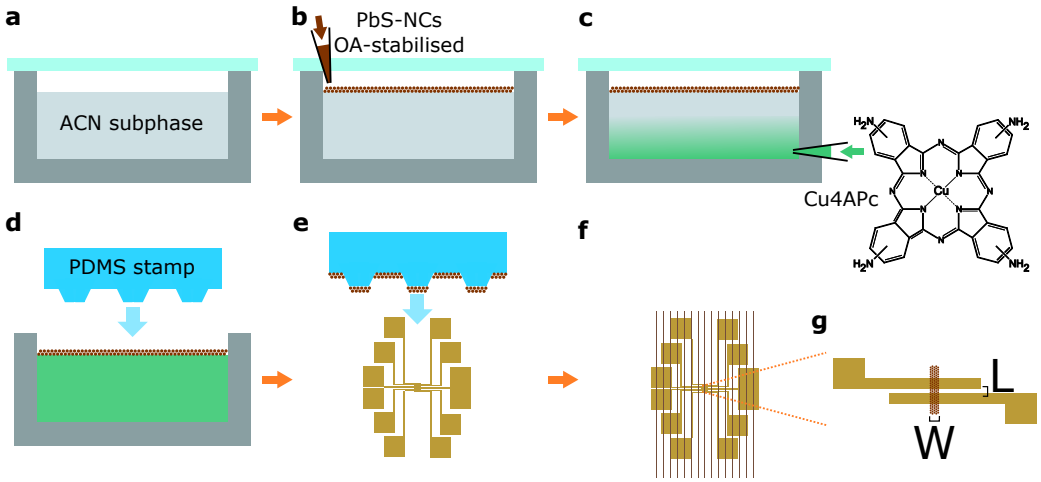

Figure S4.2: Schematic drawing of the fabrication process of PbS NCR SLs and µCP to form microchannels. (**a**) A home-built Teflon chamber is filled with acetonitrile (ACN) as a subphase and covered with a lid. (**b**) A PbS NCR dispersion is injected on top of the subphase. As the dispersion solvent evaporates, the NCRs form a freely floating membrane. (**c**) The ligand solution (Cu4APc in dimethyl sulfoxide) is injected into the bottom of the liquid subphase. Cu4APc ligands diffuse through the liquid subphase and replace the insulating native oleic acid ligands over a duration of 4 h. (**d**) A micropatterned PDMS stamp is parallelly brought into contact with the free floating PbS NCR membrane. (**e**) The coated stamp is slightly pressed onto a Kapton or Si/SiO_x devices with prepatterned Au-electrodes (µCP). This results in stripes of self-assembled PbS NCR SLs on electrode structures, as shown in (**f**). (**g**) This electrode-structure contains 11 individual channels with length L and width W of about 1 µm and 4 µm, respectively. Up to 30 electrode-structures are present on one device (330 individual microchannels).

Vacuum-dried stamped substrates were placed on a spin coater and covered with acetone to remove unbound ligands. After 30 s, the solvent meniscus was removed by spinning at 1,200 rpm for 30 s. This process was repeated twice. All preparation steps were performed in a nitrogen glovebox (level of $O_2 < 0.5$ ppm and $H_2O = 0$ ppm). Finally, the coated substrates were brought to ambient atmosphere for a defined time of 60 min to be transferred into the nitrogen flushed probe station.

Electrical measurements

All measurements of Si/SiO_x and Kapton devices were performed at room temperature in a nitrogen flushed probe station (Lake Shore, CRX-6.5K). Individual Au-electrode pairs with a connected PbS NCR stripe were contacted with W-tips, connected to a source-meter-unit (Keithley, 2636B). A third electrode contacts the gate electrode (Si/SiO_x device) or the rear of the dielectric (Kapton device). For two-point conductivity measurements of individual microchannels, several voltage sweeps of ±1 V and ±200 mV were applied and the current detected (between two electrodes as well as leakage). For field-effect transistor (FET) measurements on Si/SiO_x, a source-drain voltage of $|V_{SD}| = 5$ V was applied and the current flow along the channel was modulated by applying a voltage sweep on the gate electrode ($40\ V \leq V_G \leq 40\ V$). Using the gradual channel approximation given in Equation (S4.1), the field-effect mobility μ of individual microchannels was calculated.

X-ray nano-diffraction details

X-ray nano-diffraction was performed at Coherence beamline P10 of the PETRA III synchrotron source at DESY with the GINIX nano-diffraction endstation ($\lambda = 0.898$ Å, $E = 13.8$ keV, spot size (FWHM) $\sim 400 \times 400$ nm^2, focus depth ~0.5 mm).[263] The two-dimensional EIGER X4M (Dectris) detector (2070 × 2167 pixels, pixel size of 75×75 µm^2) was positioned 370 mm downstream from the sample and aligned off-centre (~ 9 cm) to allow simultaneous detection of small-angle (SAXS) and wide-angle (WAXS) X-ray scattering.

With an optical microscope, the most promising channels (based on electric transport measurements) were roughly localized. Precise localization of the individual channels was done using the WAXS scattering intensity of the Au {111} ($q_{111}^{Au} = 26.8$ nm^{-1}), as well as the PbS {111} and {200} reflections ($q_{111}^{PbS} = 18.3$ nm^{-1}, $q_{200}^{PbS} = 21.8$ nm^{-1}). We then performed diffraction mapping of the entire coated area in each channel. Within this scanning region, diffraction patterns were collected on a raster grid with about 250 nm step size in both directions perpendicular to the incident beam. A sketch of

the experimental scheme is shown in Figure 4.1f. The acquisition time was chosen to be 0.5 s in order to sustain a non-destructive regime of measurements. The chosen geometry allowed detecting the scattering signal from the NCR SL as well as from the PbS AL simultaneously, but only a part of reciprocal space in WAXS was accessible.

Using the nano-focused beam, it was possible to collect 100 to 200 diffraction patterns for each channel at different points within the channel. Integrating the WAXS intensity, we built diffraction maps of the microchannels (Figure S4.6b). A gap between two gold electrodes and the PbS NCR SL across the microchannel are well observed. Noteworthily, the intensity modulation coincides with the AFM map of the same microchannel, shown in Figure 4.1d.

Averaging all individual diffraction patterns collected for a channel, we were able to study the average structure of the channel. From the azimuthally-averaged radial profiles we extracted the peak positions in SAXS and used them to calculate the SL unit cell parameter a. This analysis was performed for all measured channels.

Angular X-ray Cross-Correlation Analysis details

To study the relative orientation of the NCRs inside the SL, we applied an angular X-ray cross-correlation analysis (AXCCA) approach.[36,37,271] Details are given below. We calculated two-point cross-correlation functions (CCFs) for the first SAXS peaks ($\langle 1\bar{1}00\rangle_{\mathrm{SL}}$ in the rhcp case (Figure 4.3d) and $\langle 110\rangle_{\mathrm{SL}}$ in the bcc case (Figure 4.3j)) and the $\langle 111\rangle_{\mathrm{AL}}$ or $\langle 200\rangle_{\mathrm{AL}}$ WAXS peaks. From the peak positions at the CCFs we derived preferred angles between the corresponding SL and AL crystallographic directions. We proposed structural models satisfying the obtained angles. Based on the models, we simulated CCFs for each case (Figure 4.3e,k). Good agreement between the experimental and simulated CCFs verifies the proposed models. The basic principle is further explained below.

Additional characterization methods

Helium ion microscopy (HIM) imaging of Kapton devices was performed with a Zeiss ORION Nanofab at 30 kV. Using a flood gun, charge neutralisation on the sample can be achieved, to investigate insulating Kapton devices. For HIM as well as SEM sideview investigation of PbS NCR stripes, devices were analysed under a tilt angle of 85°.

4.5.2. Supplementary results

Field-effect transistor measurements on microchannels

We conducted field-effect transistor (FET) measurements on microchannels. Figure S4.3a shows a typical transconductance curve, indicating p-type behavior. Using the gradual channel approximation given in Equation (S4.1),[25] FET hole mobilities can be calculated, as indicated in Figure S4.3b. The p-type behavior and hole-mobilities are in line with previous studies.[123]

$$\mu = \frac{\partial I_{\mathrm{SD}}}{\partial V_{\mathrm{G}}} \cdot \frac{L}{W} \cdot \frac{t_{\mathrm{ox}}}{\varepsilon_0 \varepsilon_{\mathrm{r}} V_{\mathrm{SD}}} \tag{S4.1}$$

Here, $\frac{\partial I_{\mathrm{SD}}}{\partial V_{\mathrm{G}}}$ is the derivation of I_{SD} in the transconductance curve, V_{SD} the applied source-drain voltage, $\varepsilon_0\varepsilon_{\mathrm{r}}$ and t_{ox} the permittivity and the thickness of the dielectric SiO_x layer, respectively. While the geometry of our microchannels is not ideal for typical FET measurements, this approach is sufficient for a qualitative comparison of different microchannels.

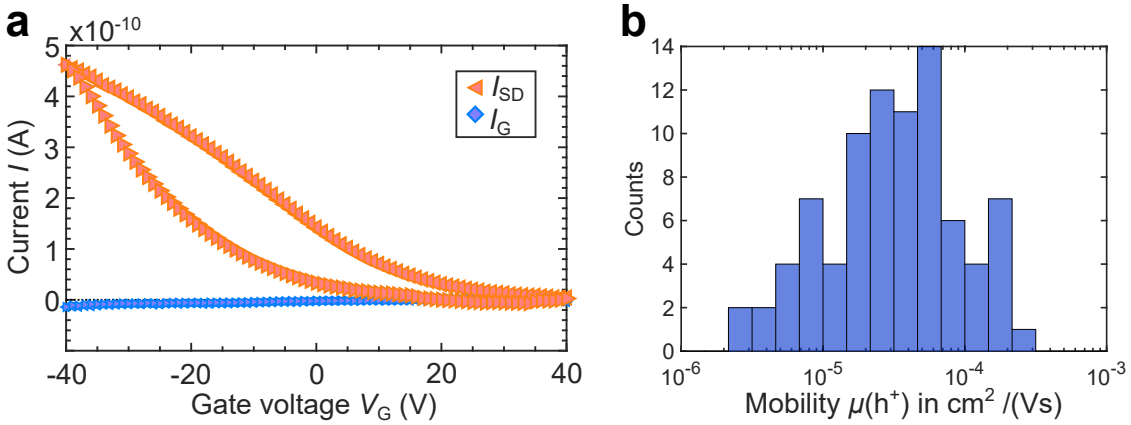

Figure S4.3: FET measurements on microchannels. (**a**) Transconductance curve of a PbS NCR stripe on a Si/SiO_x device. The source-drain current I_{SD} can be modulated by the applied gate voltage V_{G}. The source drain voltage is set to $V_{\mathrm{SD}} = 5$ V. The leak current I_{G} through the dielectric substrate is negligible. The channels show p-type behavior and the hole mobility can be calculated. (**b**) Distribution of field-effect hole mobilities $\mu(\mathrm{h}^+)$ of individual microchannels. A log-normal distribution and a spread over 2 orders of magnitude is observed.

Comparison of microchannels and state-of-the-art channels

In conventional state-of-the-art electrode devices, interdigitated electrodes probe areas of approximately 1–20 $\times$ 10^4 µm^2 (L ranging from 2.5 µm to 20 µm and $W \leq 1$ cm). Typically, different domains are connected by the electrodes after coating (ranging from monolayer to several hundred nm), as exemplarily shown in Figure S4.4a. We normalized the conductance of 21 conventional channels and 54 microchannels (Figure S4.4b) of different thicknesses to the geometry ($G_{\text{geom}} = G \cdot [L/W]$). For huge conventional electrode devices, the conductivity cannot be calculated due to nonuniform thicknesses. The distributions (Figure S4.4c) can clearly be separated and the normalized conductance values of microchannels exceed those of conventional electrode devices.

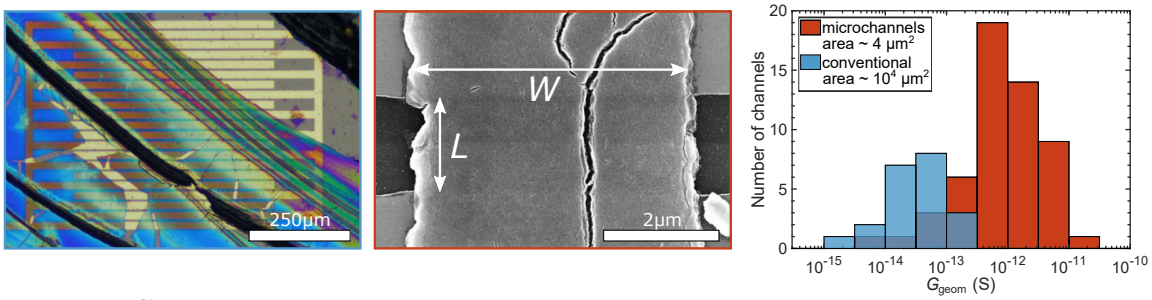

Figure S4.4: Comparison of conventional and microchannels. (**a**) Optical micrograph of a typical conventional state-of-the-art device of interdigitated electrodes with $L = 2.5 - 20$ µm and $W \leq 1$cm. Active areas of $1 - 20 \times 10^4$ µm^2 are probed. (**b**) SEM micrograph of a typical microchannel with $L \approx 1 - 1.5$ µm and $W \approx 4$ µm. Active areas of only few µm^2 are probed. (**c**) Distribution of geometry-normalized conductance of conventional and microchannels (blue and red, respectively). Here, measured conductance values are normalized to the geometry of the channels (L/W).

Microchannels on X-ray transparent Kapton device

A typical Kapton device with 330 microchannels is shown in Figure S4.5. Kapton foil (polyimide, DuPont$^{\text{TM}}$) with a thickness of 125 µm was used as an X-ray transparent substrate. At this thickness, the Kapton foil is durable enough to warrant robust electric contacting and sufficiently X-ray transparent to enable scattering experiments. Further, it is robust enough for the photolithographic electrode fabrication process and allows fabrication of large-scaled devices (15 $\times$ 15 mm^2). This allows performing X-ray diffraction on the entire substrate. The conductance of microchannels on Kapton devices can be determined and different channels exhibit different conductance with a large spread, as indicated in Figure S4.5f. We verified that the electronic transport measurements are not significantly influenced by the substrate (Si/SiO_x or Kapton) itself.

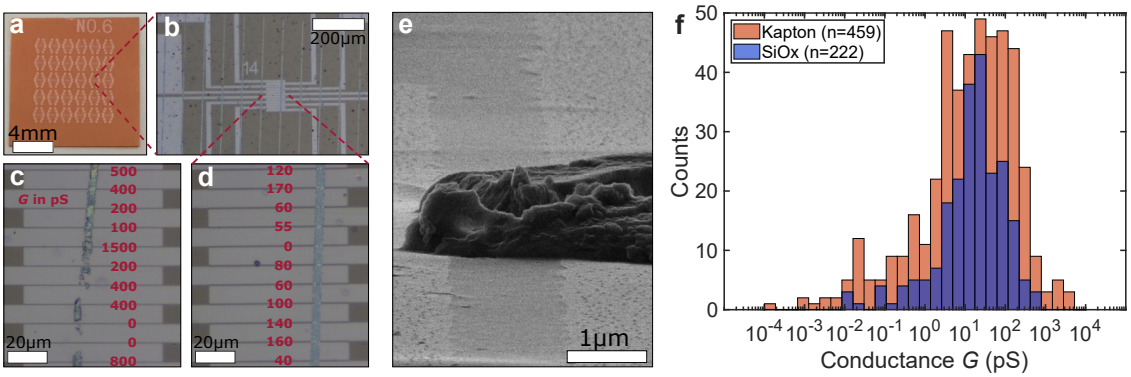

Figure S4.5: Microchannels on X-ray transparent devices. (**a**) Photograph of a Kapton device with 30 electrode structures. (**b**) Optical micrograph of a typical electrode set with PbS NCR stripes across. (**c**,**d**) Optical micrographs of eleven individual microchannels each, which can be individually addressed and show different conductance values (indicated by values in red, G in pS). (**e**) Helium-ion microscopy micrograph showing side view of a typical microchannel (tilt angle of 85°). (**f**) Distribution of conductance values of n microchannels on Kapton and Si/SiO_x devices.

X-ray nano-diffraction signal detection and sample requirements

We note that acceptable signal-to-noise ratios during X-ray scattering were obtained only for thicker samples (> 100 nm). Figure S4.6a displays the SL thickness required to obtain the XRD-signals. Structural properties can only be investigated of SLs with a minimum thickness of 100–200 nm. For microchannels with stripes of the required thickness, diffraction peaks in the SAXS region can clearly be identified. Hence, the PbS NCRs within the stripes are highly ordered.

Mapping areas of interest using the WAXS scattering intensity (the {111} Au ($q_{111}^{\mathrm{Au}} = 26.8\ \mathrm{nm}^{-1}$), {111} and {200} PbS reflections ($q_{111}^{\mathrm{PbS}} = 18.3\ \mathrm{nm}^{-1}$, $q_{200}^{\mathrm{PbS}} = 21.8\ \mathrm{nm}^{-1}$)) allows to precisely localize the individual channels and the PbS NCR SL within the latter. Figure S4.6b shows a typical diffraction map of a PbS NCR SL in a microchannel. Every pixel corresponds to a single diffraction pattern. The horizontal electrode gap and the PbS NCR SLs across can clearly be identified. The intensity modulation coincides with the AFM map of the same microchannel, shown in Figure 4.1d.

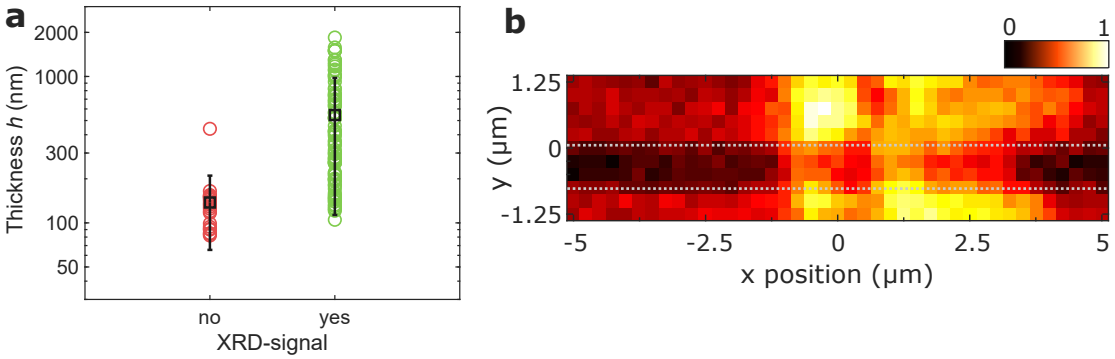

Figure S4.6: X-ray nano-diffraction signal detection. (**a**) Thickness of microchannel SL and corresponding XRD-signal. The mean thickness (± standard deviation) of SLs with and without XRD-signal is 140 ± 82 nm and 545 ± 432 nm, respectively. (**b**) Typical intensity map of a PbS NCR SL in a microchannel with pixel sizes of 250×250 nm^2. Every pixel corresponds to a single diffraction pattern. Averaging all diffraction patterns of a single microchannel allows to fully characterize the SL within. The color code indicates the XRD signal intensity. The diffraction map coincides with the AFM map of the same microchannel (Figure 4.1d).

SAXS analysis for superlattice structure determination

Analyzing averaged diffraction patterns for all measured channels, we found two groups among them. The first group of channels showed monocrystalline SAXS diffraction patterns (an example is shown in Figure S4.7a) and the second one showed Debye-Scherrer rings with relatively low angular intensity modulation in SAXS (Figure S4.7d). The monocrystalline patterns are of 6-fold symmetry and contain the Bragg peaks at q_1, $q_2 = \sqrt{3} \cdot q_1$ and $q_3 = 2 \cdot q_1$ (see Figure S4.7c for the radial profile), which can be attributed to a $[0001]_{\mathrm{SL}}$-oriented random hexagonal close-packed structure (rhcp) SL (see details below). The presence of the Bragg peaks at q_1, $q_2 = \sqrt{2} \cdot q_1$ and $q_3 = \sqrt{3} \cdot q_1$ for the polycrystalline channels (see Figure S4.7f for the radial profile) is a clear evidence of a bcc SL structure. A single diffraction pattern for the polycrystalline channels contains the Bragg peaks from several grains with different orientations (see Figure S4.7e), thus the grain size is smaller than the beam size ($< 400 \times 400$ nm^2).

The obtained q-values were utilized to calculate the nearest-neighbor (center-to-center) distance between adjacent NCRs in channels with both types of lattices. The distances are 6.9 ± 0.2 nm and 7.8 ± 0.4 nm for the poly- and monocrystalline channels, respectively (by fitting with normal distribution, see Figure S4.8). We use nearest-neighbor distances instead of unit-cell sizes in order to allow for a direct comparison between different SL types. The interparticle distances are calculated by subtracting the mean NCR diameter from the nearest-neighbor distance (NND).

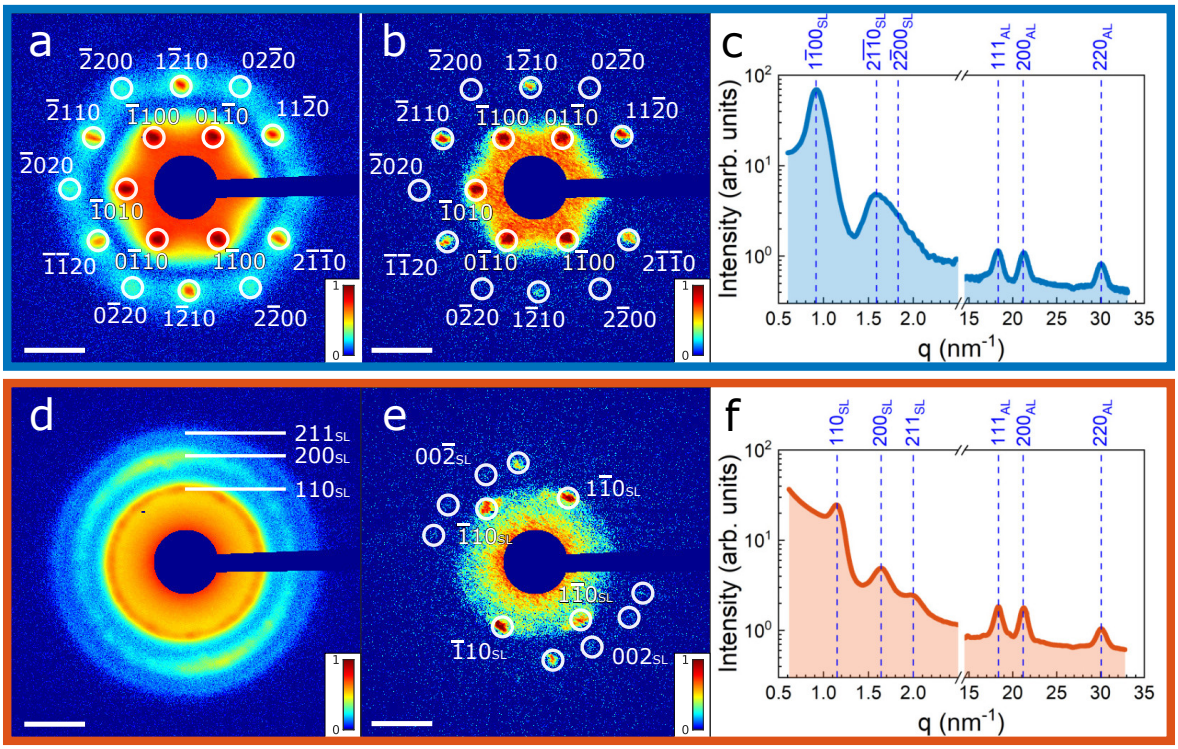

Figure S4.7: Superlattice structure determination for (**a**–**c**) mono- and (**d**–**f**) polycrystalline channels. (**a**,**d**) Averaged SAXS patterns; (**b**,**e**) examples of single SAXS patterns; (**c**,**f**) average radial profiles. Scale bars correspond to 1 nm^{-1}.

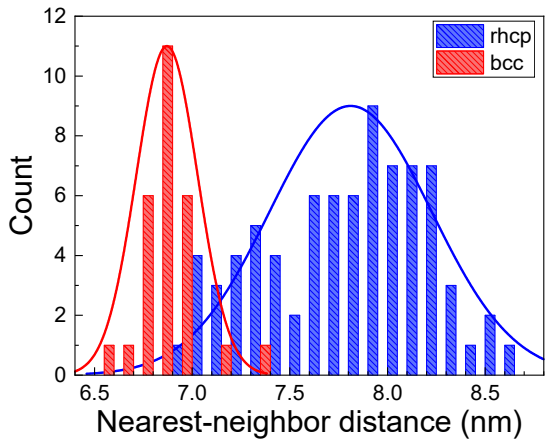

Figure S4.8: Distribution of NND values for two types of channels. Solid lines are fits by normal distribution.

Superlattice structure of the monocrystalline channels

The outline of our experiment (transmission geometry in one direction normal to the substrate) makes analysis of the monocrystalline samples quite complicated. The 6-fold patterns observed for the monocrystalline channels (Figure S4.9a) can be attributed to the hexagonal hcp lattice as well as to cubic bcc and fcc lattices. Indeed, the peak positions with respect to the first peak at q_1, $q_2 = \sqrt{3} \cdot q_1$ and $q_3 = 2 \cdot q_1$ correspond to all of them. NNDs are $d_{\text{c-c}} = 2\pi/q_1 \cdot (2/\sqrt{3})$, $2\pi/q_1 \cdot 2$ and $2\pi/q_1 \cdot (\sqrt{6}/2)$ for the hcp, fcc and bcc lattices, respectively. Using the mean q_1 value, one can obtain the NNDs of 7.8 nm, 13.5 nm and 8.3 nm. In comparison to the size of the used NCRs ($\sim$ 6.0 nm), the value obtained for the fcc seems to be unreasonable and we excluded this structure from our consideration.

The decision between hcp and bcc cannot be made based only on the diffraction patterns. First of all, we assumed the SL to have the same structure as the polycrystalline channels – a bcc SL with the NCRs aligned with all SL directions. But in this case, the results of the cross-correlation analysis (see below, Figure S4.11c) are not consistent with the experimentally observed data. The NCRs can be rotated inside the SL around the beam direction by 30°, but it would break the symmetry of the lattice. A possible arrangement of NCRs in a hcp lattice is shown in Figure S4.11d and gives a cross-correlation function consistent with the experimental one (Figure S4.11c). This lattice has a higher symmetry than the proposed bcc lattice with rotated NCRs. Also, the comparably big NND supposes a more sphere-like shape of the NCRs covered with organic shell. A thicker shell makes interactions between adjacent NCRs more isotropic. It is confirmed by the study of WAXS reflections from the NCR ALs, that the angular disorder of NCRs is higher for the monocrystalline channels than for the polycrystalline ones (see details below). On an average WAXS pattern of a monocrystalline channel typically only Debye-Scherrer rings are visible (Figure S4.9a). In this case, sphere-like particles with anisotropic interactions are likely to form close-packed structures like hcp. Thus, we assume the monocrystalline channels having a hcp structure. However, the close-packed structures are prone to form stacking faults leading to alternation of hcp and fcc structures. In our geometry (scattering along $[0001]_{\text{SL}}$ direction), we are not able to reveal fractions of both motifs. Thus, the correct description for the structure would be “random hcp (rhcp) lattice”. We used this description throughout the manuscript, using the hcp-like indexing of the Bragg peaks (Figure S4.7a,b).

WAXS analysis for NCR alignment determination

Analyzing the WAXS patterns from different types of channels, we noticed a drastic difference. The single patterns of the monocrystalline rhcp channels contain continuous Debye-Scherrer rings with low intensity modulations (Figure S4.9a), whereas for polycrystalline bcc channels, we found relatively sharp Bragg peaks of PbS atomic lattice (AL) reflections (Figure S4.9d). The difference in the intensities between the 111_{AL} and 200_{AL} reflections is caused by different out-of-plane NCRs orientations with respect to the incident beam (the substrate).

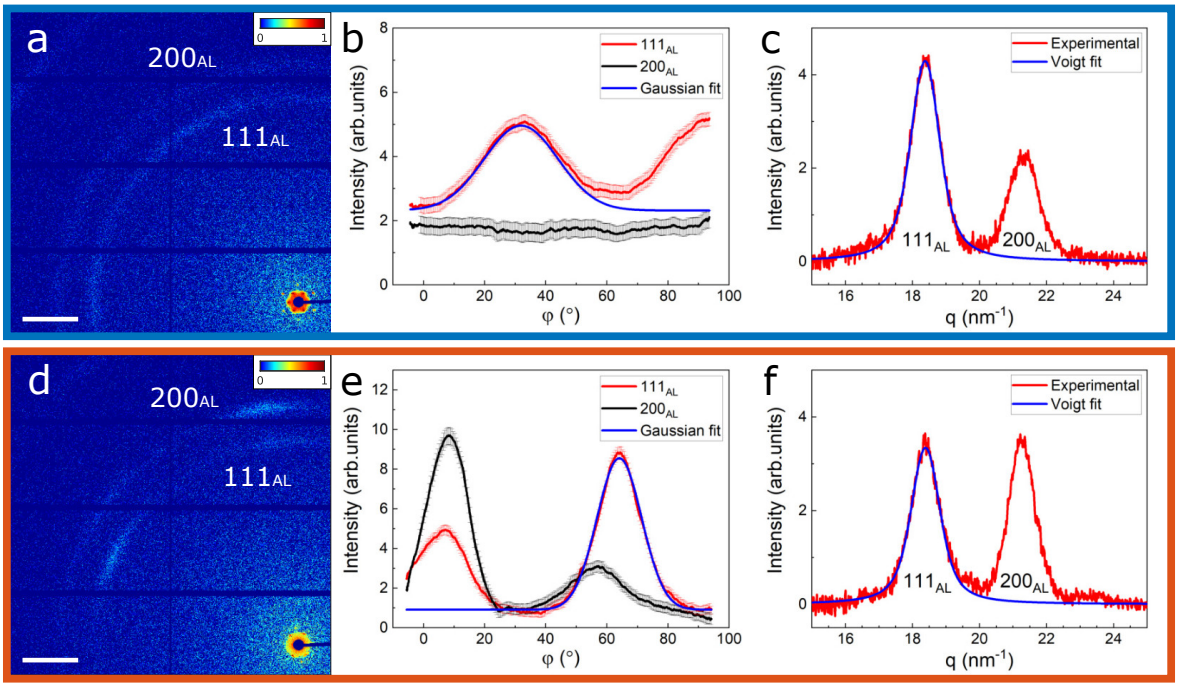

Figure S4.9: WAXS study of mono- (**a**–**c**) and polycrystalline (**d**–**f**) channels: (**a**,**d**) examples of a single WAXS diffraction pattern; (**b**,**e**) azimuthal and (**c**,**f**) radial profiles of the 111_{AL} and 200_{AL} reflections. A Voigt fit of the 111_{AL} Bragg peaks is shown in blue. The 0° angle for the azimuthal profiles corresponds to the top of the diffraction patterns. The positive angular direction is counterclockwise. Scale bars in (a,d) correspond to 5 nm^{-1}.

To quantitatively characterize angular disorder, we assumed that WAXS peak broadening is caused by two factors: Scherrer broadening due to the small size of the NCRs and orientational disorder of the NCRs in sites of the SL. The first factor affects both the radial and the azimuthal width of the peaks while the second one influences only the azimuthal width of the peaks. Assuming that these two factors are independent, we can estimate the value of the orientational disorder $\Delta\Phi$ from the relationship between

the radial and azimuthal widths of the peak:

$$\delta_{az}^2 = \delta_{rad}^2 + \Delta\Phi^2 \quad , \tag{S4.2}$$

where δ_{az} and δ_{rad} are the FWHM values of the peak angular size in the azimuthal and radial directions obtained from a Gaussian and Voigt fitting, respectively.

We analyzed the radial and azimuthal profiles for 111_{AL} and 200_{AL} reflections on a single pattern. Azimuthal profiles are shown in Figure S4.9b,e for mono- and polycrystalline channels, respectively. Azimuthal profiles for a monocrystalline channel contain relatively wide Bragg peaks of 111_{AL} reflections, and no peaks of 200_{AL} reflections are observed. Both profiles have anisotropic offsets corresponding to many disordered NCRs besides the ordered ones. The 111_{AL} Bragg peak was fitted by a Gaussian profile giving the FWHM value of $24.5 \pm 1.0°$. Azimuthal profiles for a polycrystalline channel contain sharp Bragg peaks for both, 111_{AL} and 200_{AL} reflections. Fitting the 111_{AL} Bragg peak gives the FWHM value of $16.7 \pm 0.5°$.

Radial profiles of the 111_{AL} and 200_{AL} reflections are shown in Figure S4.9c,f for mono- and polycrystalline channels, respectively. Fitting of the 111_{AL} reflection by a Voigt profile gives the FWHM value of 1 nm^{-1} (3.1°) for both types of channels. According to the Scherrer equation, this value corresponds to the 6.9 nm-sized coherently scattering domains. Taken the precision of the method, it is in good agreement with the NCR size ($\sim$ 5.8 nm) and SL unit cell parameters studied in this work.

Considering the obtained values, the orientational disorder ($\Delta\Phi$) of the atomic lattices of NCRs is roughly 24° for monocrystalline and 16° for polycrystalline channels. The value for polycrystalline channels is similar to the recently reported $\Delta\Phi$ for SLs of oleic acid- and tetrathiafulvalene-linked PbS NCRs.[36,271]

Basics of angular X-ray cross-correlation analysis

The angular X-ray cross-correlation analysis (AXCCA) method is widely used for the analysis of disordered or partially ordered systems such as colloids, liquid crystals, polymers, etc. It is capable of providing insights into hidden symmetries, such as bond-orientational order or partial alignment of particles in the system. This method was also shown to be highly useful to study the angular correlations in mesocrystals.[36,37] While details and mathematical background on this method can be found elsewhere,[272] here we briefly summarize the main concepts.

AXCCA is based on the analysis of a two-point angular cross-correlation function (CCF) that can be calculated for each diffraction pattern, as given in Equation (S4.3)

(and Equation (4.1) in the main text):

$$C_{\mathrm{CCF}}(q_{\mathrm{AL}},q_{\mathrm{SL}},\Delta) = \int_{-\pi}^{\pi} \tilde{I}(q_{\mathrm{AL}},\varphi)\tilde{I}(q_{\mathrm{SL}},\varphi+\Delta)d\varphi \tag{S4.3}$$

where $\tilde{I}(q,\varphi) = I(q,\varphi) - \langle I(q,\varphi)\rangle_{\varphi}$ and $I(q,\varphi)$ is an intensity value taken in the point with (q,φ) polar coordinates in the detector plane and $\langle ...\rangle_{\varphi}$ denotes averaging over all azimuthal φ angles. All values used in this definition are shown in Figure S4.10.

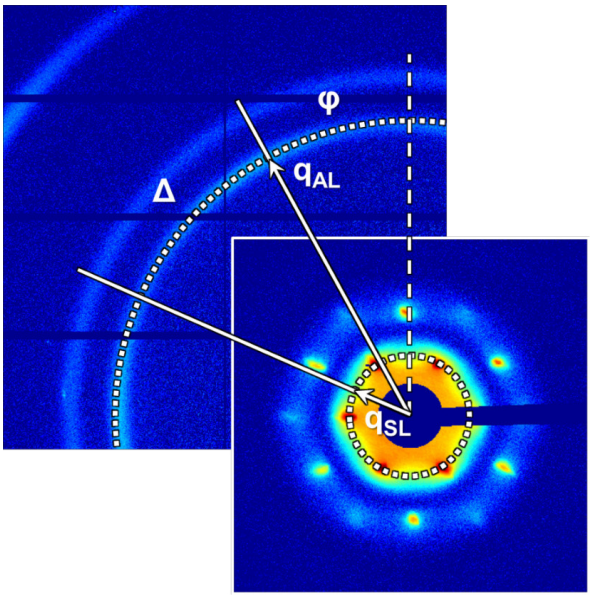

Figure S4.10: Angular X-ray cross-correlation analysis. White arrows point to the Bragg reflections from the PbS AL and SL with momentum transfer values from the center of the pattern q_{AL} and q_{SL}, respectively. The angle Δ between these Bragg peaks is shown. SAXS area is enlarged for better visibility.

Experimentally obtained diffraction patterns contain features that block the scattering signal, such as detector gaps, beamstop, beamstop holder, etc. In order to take their presence into account, we introduce into Equation (S4.3) the mask function

$$W(q,\varphi) = \begin{cases} 0, & \text{gaps, beamstop etc.} \\ 1, & \text{otherwise} \end{cases} . \tag{S4.4}$$

This yields the final form of the CCF as follows:

$$C_{\mathrm{CCF}}(q_{\mathrm{AL}},q_{\mathrm{SL}},\Delta) = \int_{-\pi}^{\pi} \tilde{I}(q_{\mathrm{AL}},\varphi)W(q_{\mathrm{AL}},\varphi)\tilde{I}(q_{\mathrm{SL}},\varphi+\Delta)W(q_{\mathrm{SL}},\varphi+\Delta)d\varphi \quad . \tag{S4.5}$$

Taking the values of q_{SL} and q_{AL} indicated in the main text, we studied the correlations between reflections in the WAXS and SAXS areas. To obtain statistically meaningful data, CCFs were averaged over all diffraction patterns for each channel.

The CCF functions were simulated on the basis of the determined real-space structures. The Bragg peaks in both WAXS and SAXS areas were assumed to have Gaussian shapes in the angular direction, and the intensity on the corresponding ring was calculated as follows:

$$I(\varphi) = \sum_i \exp\left[-\frac{(\varphi-\varphi_i)^2}{\delta^2}\right] \exp\left[-\frac{(\theta-2\theta_B)^2}{\delta^2}\right] \quad , \tag{S4.6}$$

where φ_i is the azimuthal angular position of the i-th Bragg peaks in the SAXS/WAXS area, θ and θ_B are the angle between the detector plane and Ewald sphere and the Bragg angle for the considered reflection (used only for WAXS reflections). The angular sizes of the SAXS/WAXS peak δ were chosen to fit the experimental data.

The simulated CCFs were evaluated as

$$C_{CCF,sim}(q_{AL},q_{SL},\Delta) = \int_{-\pi}^{\pi} \tilde{I}_{SAXS}(q_{AL},\varphi)\tilde{I}_{WAXS}(q_{SL},\varphi+\Delta)d\varphi \tag{S4.7}$$

and then normalized by the maximum value of all CCFs for each channel.

Results of angular X-ray cross-correlation analysis

We calculated the CCFs for the first SAXS peaks ($\langle 1\bar{1}00\rangle_{AL}$ in the rhcp case) and the 111_{AL} or 200_{AL} WAXS peaks to reveal preferred angles between corresponding directions of the NCRs and SL. Examples of the obtained CCFs for a monocrystalline rhcp channel are shown in Figure S4.11c.

For the monocrystalline channels, there are 6 peaks at 0°, ±60°, ±120° and 180° for both $C_{CCF}(q^{SL}_{1\bar{1}00},q^{AL}_{111},\Delta)$ and $C_{CCF}(q^{SL}_{1\bar{1}00},q^{AL}_{200},\Delta)$. The intensity ratio between them is ~ 8. These features correspond to the [0001] orientation of a rhcp SL, where the NCRs are aligned as follows: $[111]_{AL}||[0001]_{SL}$ and $[110]_{AL}||[2\bar{1}\bar{1}0]_{SL}$. This configuration is shown in Figure 4.3h and confirmed by simulations (Figure S4.11f). It should be noted, that, as it follows from the WAXS analysis (see Figure S4.9), only a part of the NCRs is aligned as shown.

However, a bcc SL oriented along $[111]_{SL}$ would give the same SAXS pattern. To verify the proposed rhcp structure, we simulated a CCFs for the bcc structure observed

in polycrystalline channels. In such a bcc SL, all NCRs directions are aligned with the corresponding directions of the SL. Thus, the orientation along $[111]_{SL}$ gives the same NCRs orientation – $[111]_{AL}$. A real-space model of the considered SL is shown in Figure S4.11g. But the CCFs simulated for this structure do not correspond to the experimentally obtained ones (Figure S4.11i). To achieve the observed angular correlation between the SL and the NCRs, the latter should be rotated by 30° around the $[111]_{AL}$ directions. The resulting structure is shown in Figure S4.11j. Indeed, such a structure gives the correct CCFs (shown in Figure S4.11l), but the assumed rotation breaks the symmetry of the entire structure and implies different NCR orientations in the equivalent $\{111\}_{SL}$ planes.

Thus, we suppose that the monocrystalline channels form a symmetrical rhcp structure, where, for some fraction of the NCRs, the $[111]_{AL}||[0001]_{SL}$ and $[110]_{AL}||[2\overline{1}\overline{1}0]_{SL}$ directions are collinear.

The CCFs for polycrystalline channels were calculated for the first SAXS peaks ($\langle 110\rangle_{SL}$ in the bcc case) and the 111_{AL} or 200_{AL} WAXS peaks. Examples of the obtained CCFs for a polycrystalline bcc channel are shown in Figure S4.12c. There are 4 peaks at ±35°, ±145° for $C_{CCF}(q_{110}^{SL},q_{111}^{AL},\Delta)$ and two peaks at ±90° for $C_{CCF}(q_{110}^{SL},q_{200}^{AL},\Delta)$. These features correspond to the $[110]_{SL}$ orientation of a bcc SL, where all crystallographic directions of the NCRs are aligned with corresponding directions of the SL. This configuration is shown in Figure S4.12d and confirmed by simulations (see Figure S4.12f).

In the polycrystalline channels many different orientations are possible, but, according to our analysis, the $[110]_{SL}$ orientation is the primary one. To verify the latter, we simulated CCFs for other typical orientations. Examples for the same structures oriented along $[111]_{SL}$ (Figure S4.12g) and $[100]_{SL}$ (Figure S4.12j) are shown in Figures S4.12i,l, respectively. However, the features characteristic for these orientations are not observed in the experimental CCFs. Only a small fraction of the $[111]_{SL}$-oriented structures can contribute to the additional small peaks observed at ±90° for the experimental $C_{CCF}(q_{110}^{SL},q_{111}^{AL},\Delta)$ (see Figure S4.12c). Other features can originate from the polycrystallinity (correlations between reflections from different grains are not compensated due to the lack of statics).

Thus, we assume the polycrystalline channels to have bcc SL structure, where all NCRs are aligned with the corresponding SL directions (e.g. $[100]_{AL}||[100]_{SL}$ and $[010]_{AL}||[010]_{SL}$).

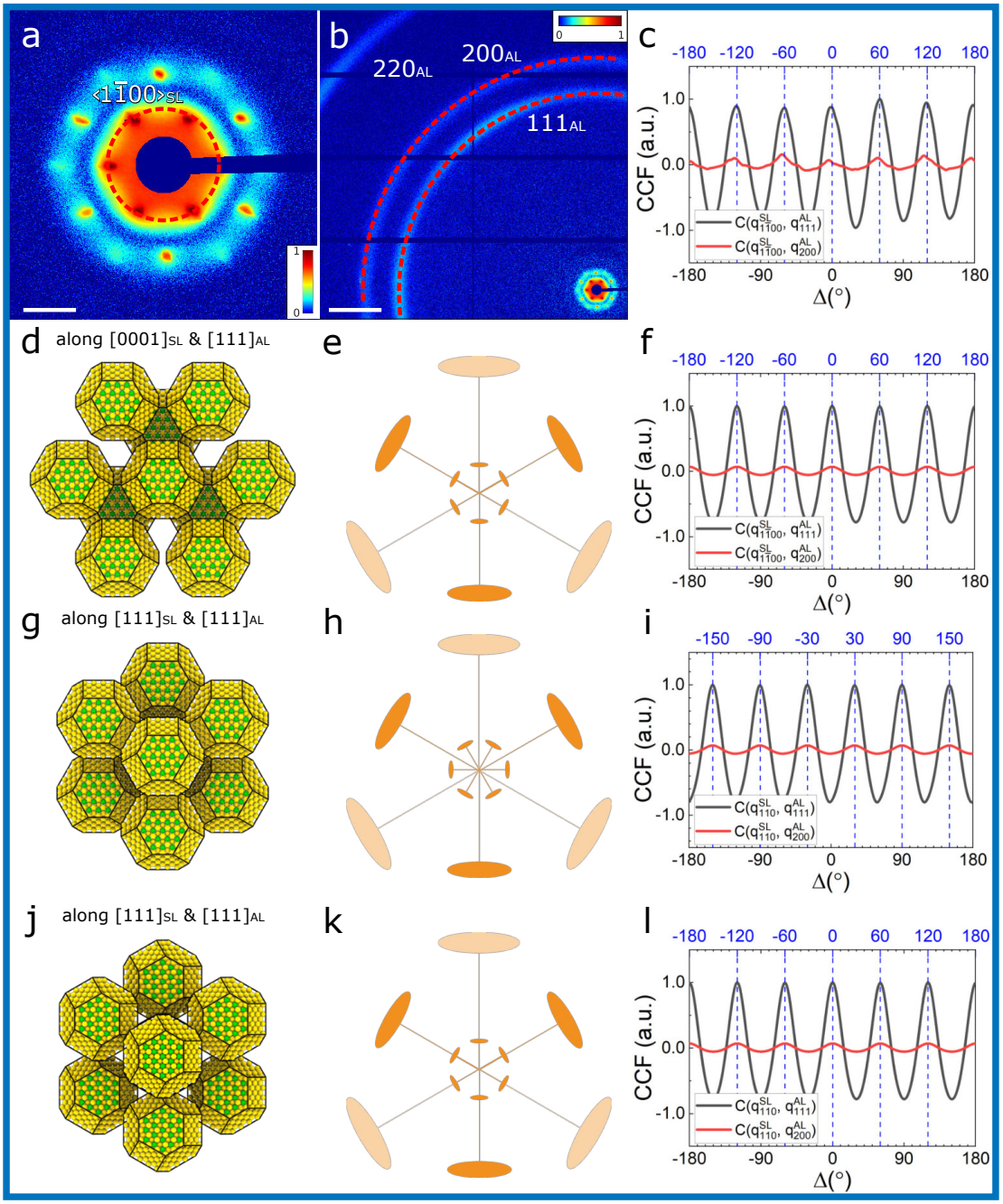

Figure S4.11: AXCCA of the monocrystalline rhcp SL. (**a**) An average SAXS pattern for the monocrystalline channel. The $1\bar{1}00_{SL}$ reflections used for AXCCA are shown with a red dashed line. The scale bar corresponds to 1 nm^{-1}. (**b**) An average WAXS pattern for a monocrystalline channel. The 111_{AL} and 200_{AL} reflections used for AXCCA are shown with red dashed lines. The scale bar corresponds to 5 nm^{-1}. (**c**) Calculated CCFs for the monocrystalline channel. (**d**) Proposed real-space rhcp SL model with $[111]_{AL}||[0001]_{SL}$ and $[110]_{AL}||[2\bar{1}\bar{1}0]_{SL}$; (**g**) considered bcc SL model with $[100]_{AL}||[100]_{SL}$ and $[010]_{AL}||[010]_{SL}$; (**j**) considered bcc SL model with $[111]_{AL}||[111]_{SL}$ and $[1\bar{1}0]_{AL}||[2\bar{1}\bar{1}]_{SL}$; (**e**,**h**,**k**) corresponding diffraction patterns (schematically, not to scale); (**f**,**i**,**l**) corresponding simulated CCFs for the first SAXS peaks ($\langle 1100\rangle_{SL}$ in the rhcp case (**f**) and $\langle 110\rangle_{SL}$ in the bcc case (**i**,**l**)) and the 111_{AL} or 200_{AL} WAXS peaks.

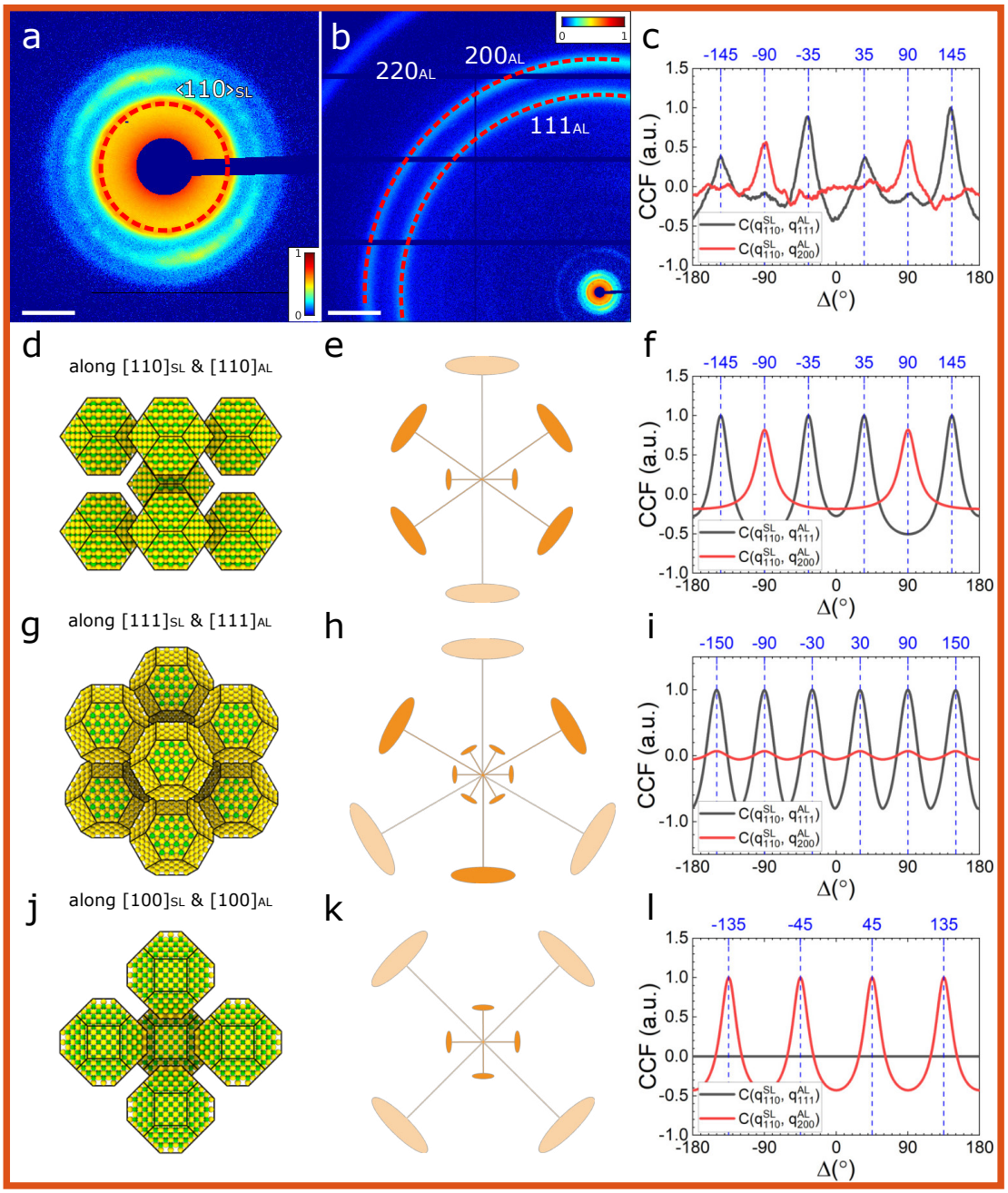

Figure S4.12: AXCCA of the polycrystalline bcc SL. (**a**) An average SAXS pattern for the polycrystalline channel. The 110_{SL} reflections used for AXCCA are shown with a red dashed line. The scale bar corresponds to 1 nm^{-1}. (**b**) An average WAXS pattern for a polycrystalline channel. The 111_{AL} and 200_{AL} reflections used for AXCCA are shown with red dashed lines. The scale bar corresponds to 5 nm^{-1}. (**c**) Calculated CCFs for the polycrystalline channel. (**d**,**g**,**j**) Proposed real-space bcc SL models with $[100]_{\mathrm{AL}}||[100]\mathrm{SL}$ and $[001]_{\mathrm{AL}}||[010]_{\mathrm{SL}}$ oriented along (**d**) $[110]_{\mathrm{SL}}$; (**g**) $[111]_{\mathrm{SL}}$; (**j**) $[100]_{\mathrm{AL}}$; (**e**,**h**,**k**) corresponding diffraction patterns (schematically, not to scale); (**f**,**i**,**l**) corresponding simulated CCFs for the first $\langle 110\rangle_{\mathrm{SL}}$ SAXS peaks and the 111_{AL} or 200_{AL} WAXS peaks.

SEM investigation of the PbS NCR superlattice types

Figure S4.13 shows scanning electron microscopy (SEM) micrographs of the different SL types, as described in the main text. SEM imaging corroborates the structural properties, revealed by the X-ray nano-diffraction.

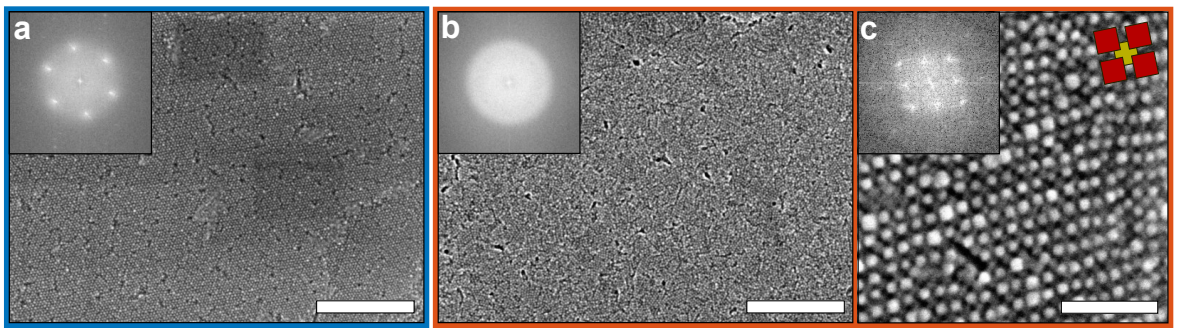

Figure S4.13: SEM investigation of the two types of PbS NCR SLs. (**a**) Monocrystalline SL with rhcp structure. Scale bar: 300 nm. (**b**) Polycrystalline SL with bcc structure. Scale bar: 300 nm. (**c**) High-resolution image of a bcc SL. Schematic drawing indicates alignment of individual NCRs. Scale bar: 50 nm. The fast Fourier transformations (insets) support the polycrystalline and monocrystalline nature as well as the structure of the SLs, as deduced from the X-ray nano-diffraction data.

Semi-quantitative Raman-spectroscopy analysis

The SLs within microchannels exhibit strong characteristic Raman signals for Cu4APc (750 cm^{-1} and 1,050–1,650 cm^{-1}),[308] as displayed in Figure S4.14a. Probing areas outside the SL stripes, these characteristic signals vanish, verifying the specific functionalization of the NCRs with the organic π-system (see line scan in Figure S4.14b). Raman-spectroscopy was performed on the corresponding Si/SiO_x substrates, as the characteristic polyimide signals of the Kapton devices overlay with those of Cu4APc.

Figure S4.14c shows the Raman-spectroscopy analysis to semi-quantify the degree of ligand exchange and its correlation to SL type. Stronger Cu4APc signals are observed for polycrystalline bcc SLs with a smaller lattice parameter (NND), compared to monocrystalline rhcp lattices. This supports the hypothesis of incomplete oleic acid (OA) ligand exchange in rhcp monocrystals. Raman signal from OA cannot be detected (Figure S4.14e).

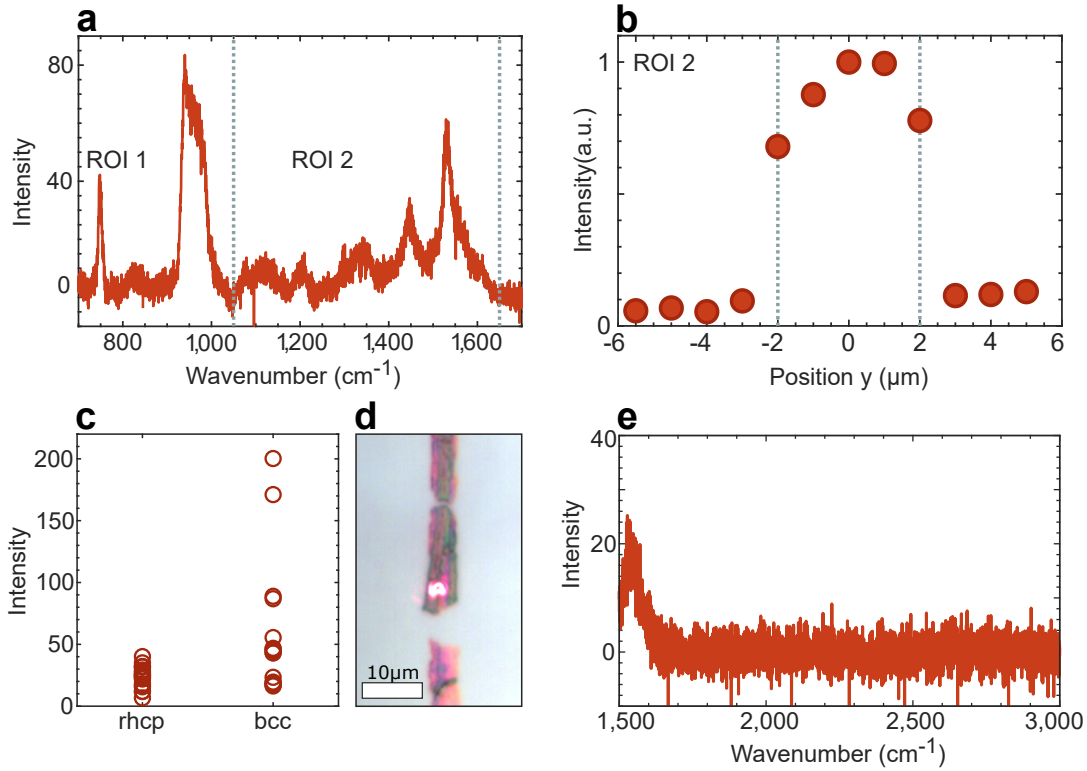

Figure S4.14: Semi-quantitative Raman-spectroscopy analysis. (**a**) Raman spectrum of a microcontact-printed SL stripe of PbS NCRs functionalized with Cu4APc, showing characteristic signals of the ligand molecule at 750 cm^{-1} and 1,050–1,650 cm^{-1}, indicated as ROI 1 and ROI 2, respectively. The signal at $\sim$ 950 cm^{-1} corresponds to the silicon background. (**b**) In a line scan across a stripe, signal from the characteristic fingerprint region of Cu4APc (ROI 2) is only detected on the PbS NCR stripe. (**c**) Comparison between the two SL types. The polycrystalline bcc SLs with smaller lattice parameters (NND) exhibit stronger Raman signal from Cu4APc, supporting our hypothesis in the main text. (**d**) Typical PbS NCR stripe on a Si/SiO_x device with the 632 nm laser focus of the Raman-setup. (**e**) Raman-spectrum of a PbS NCR stripe with monocrystalline hcp SL. The spectrum clearly lacks signal from OA, which is supposed to appear at $\sim$ 2,800 cm^{-1}.

Qualitative investigation of anisotropic charge transport

Figure S4.15a displays the graphical approach of identifying monocrystalline channels for which the parameters nearest-neighbor distance NND and thickness h are identical. Exactly four monocrystalline channels (2 pairs of 2) fulfil those requirements and can directly be compared. We observe higher conductivity σ for the channels with lower angle α.

For monocrystalline SLs with similar crystalline order and lattice parameter (NND) but varying thickness, we normalize the measured electric conductivities by applying

an empirical correction of the thickness dependence, for better comparability. This correction is obtained from fitting the thickness-dependent conductivity data of twenty individual microchannels (Figure S4.15b–c). Figure S4.15b shows the conductivity of microchannels as a function of SL thickness.

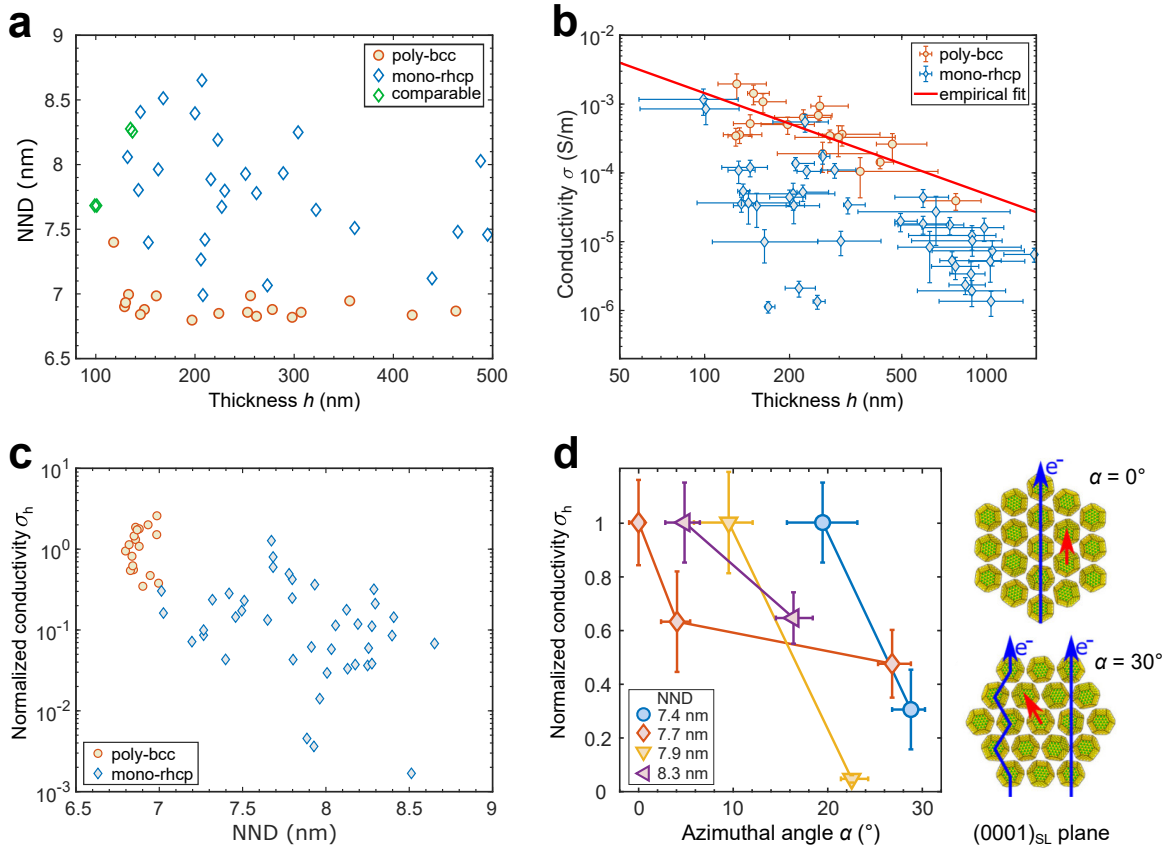

Figure S4.15: Anisotropy of charge transport in monocrystalline NCR SLs. (**a**) Graphical illustration of nearest-neighbor distance (NND) and thickness of investigated SLs. Comparable monocrystalline channels with identical NND and h are highlighted in green. (**b**) Conductivity of microchannels as a function of SL thickness. Polycrystalline and monocrystalline microchannels are displayed. The red line corresponds to an empirical fit, which is applied for the thickness-normalization. (**c**) Conductivity normalized to the thickness as a function of NND. Now, channels with the same lattice parameter (NND) can be compared. (**d**) Comparison of rhcp monocrystals. Thickness-normalized conductivity of monocrystalline channels as a function of azimuthal angle α. The color code indicates comparable SLs with identical NND and the connecting lines are guides for the eye. For clarity, the conductivity of the respective more conductive SL is set to one. Inset: Schematic of the rhcp SL and the favored hopping path for $\alpha = 0°$ (blue arrow) along the d_{NN} direction (red arrow). For an in-plane offset ($\alpha = 30°$), the larger hopping distance or the zig-zag path are detrimental to charge transport. Ligand spheres of NCRs are omitted for clarity.

All polycrystalline bcc SLs exhibit almost identical lattice parameters and structural order. Thus, the difference in conductivity can only be attributed to different SL thicknesses. As described in the main text, the influence of h on σ is attributed to a fringing electric field along the height (sample normal), resulting in an inhomogeneous current flow. This effect should be identical for all SL types. The red line corresponds to the empirical fit of this conductivity-thickness dependence of polycrystalline channels. Applying this dependency to other microchannels allows us to normalize the conductivity of all channels to their corresponding thickness. This thickness-normalized conductivity is shown in Figure S4.15c as a function of nearest-neighbor distance. Here, monocrystalline rhcp SLs with the same NND can be directly compared.

Figure S4.15d shows the thickness-normalized conductivity of monocrystalline rhcp microchannels as a function of azimuthal angle α. For the sake of clarity, the conductivity of the respective more conductive SL is set to one. As a general result, the SLs with lower value of α show higher conductivity. This finding strongly supports the hypothesis of anisotropic charge transport, as discussed in the main text.

On the origin of error bars

Error of the nearest-neighbor distance: Mean values are calculated from the multiple (1–3) Bragg peaks registered for one microchannel. Errors correspond to the standard deviation of those values.

Error of thickness h: The thickness h is determined by SEM imaging under a tilted view of 85° with respect to the incoming beam (Si/SiO_x devices) and AFM (Kapton devices). Mean values and ranges are determined by multiple measurements (SEM) or averaged height profiles (AFM).

Error of conductivity σ: Mean values of conductivity are calculated as described in the main text. Errors are calculated by Gaussian error propagation, given in Equation (S4.8).

$$\frac{\Delta\sigma}{\sigma} = \sqrt{\left(\frac{\Delta G}{G}\right)^2 + \left(\frac{\Delta L}{L}\right)^2 + \left(\frac{\Delta W}{W}\right)^2 + \left(\frac{\Delta h}{h}\right)^2} \tag{S4.8}$$

Here, ΔG corresponds to the error of G, determined by multiple I-V curves of one microchannel. ΔL and ΔW correspond to the uncertainty of L and W determined by AFM. Δh corresponds to the thickness variation measured by AFM.

Error of azimuthal orientation: The mean values correspond to the central peak position ($q^{SL}_{1\bar{1}00}$), and the error indicates the FWHM of the peak.

5. Structural order enhances charge carrier transport in self-assembled Au nanoclusters

Florian Fetzer[1#], *Andre Maier*[2,3#], *Martin Hodas*[4], *Olympia Geladari*[2,3], *Kai Braun*[2,3], *Alfred J. Meixner*[2,3], *Frank Schreiber*[3,4], *Andreas Schnepf*[1*], *Marcus Scheele*[2,3*]

[1] Institut für Anorganische Chemie Universität Tübingen, Auf der Morgenstelle 18, D-72076 Tübingen, Germany

[2] Institut für Physikalische und Theoretische Chemie, Universität Tübingen, Auf der Morgenstelle 18, D-72076 Tübingen, Germany

[3] Center for Light-Matter Interaction, Sensors & Analytics LISA$^+$, Universität Tübingen, Auf der Morgenstelle 15, D-72076 Tübingen, Germany

[4] Institut für Angewandte Physik, Universität Tübingen, Auf der Morgenstelle 10, D-72076 Tübingen, Germany

[#] These authors contributed equally.

[*] Corresponding authors.

This Chapter is based on the publication in Nature Communications.

5.1. Abstract

The collective properties of self-assembled nanoparticles with long-range order bear immense potential for customized electronic materials by design. However, to mitigate the short-coming of the finite size distribution of nanoparticles and thus, the inherent energetic disorder within assemblies, atomically precise nanoclusters are the most promising building blocks.

We report an easy and broadly applicable method for the controlled self-assembly of atomically precise $Au_{32}(^{n}Bu_3P)_{12}Cl_8$ nanoclusters into micro-crystals. This enables the determination of emergent optoelectronic properties which resulted from long-range order in such assemblies. Compared to the same nanoclusters in glassy, polycrystalline ensembles, we find a 100-fold increase in the electric conductivity and charge carrier mobility as well as additional optical transitions. We show that these effects are due to a vanishing energetic disorder and a drastically reduced activation energy to charge transport in the highly ordered assemblies. This first correlation of structure and electronic properties by comparing glassy and crystalline self-assembled superstructures of atomically precise gold nanoclusters paves the way towards functional materials with novel collective optoelectronic properties.

5.2. Introduction

Using the collective properties of self-assembled molecules and particles as building blocks bears immense opportunities for microelectronic applications.[29,30,129] Already implemented applications of self-assembled thin films range from light emitting diodes (LED) over field-effect transistors (FET) to optical sensors.[4] Inorganic nanoparticles, organic π-systems and conjugated polymers are the most widely used components for such self-assembly.[69,245,309,310] For instance, previous studies have shown the possibility to form three-dimensional assemblies with long-range order using gold nanoparticles as building blocks.[311] However, these nanoparticles consist of a few hundred to thousands of atoms, are not atomically precise, exhibit finite size distributions and, thus, an inherent energetic disorder in ensembles. To mitigate this short-coming, atomically precise, inorganic molecular clusters have been suggested as promising building blocks for customized electronic materials by design of their structure.[96,165,312,313] These materials exhibit larger dielectric constants than organic semiconductors with profound consequences for their excited-state properties, such as the ability to exploit quantum

confinement effects. A variety of such molecular clusters, often referred to as superatoms, has already been used for the formation of solid-state materials.[314–318] A special interest is thereby focused on the influence of the structure of the assembled materials onto their properties, possibly enabling the creation of materials with desired properties by design.[66,319] Atomically precise metalloid nanoclusters (NCLs) form a subgroup of this material class.[19,99] The exact knowledge of their structure and composition along with usually smaller sizes, enhanced quantum confinement and the prospect of single-electron switching at room temperature promotes NCLs as building blocks for self-assembly.[62,63]

Previous studies on Au NCL ensembles have yet either reported conductivity measurements of polycrystalline assemblies,[320] along with the first observation of semiconducting properties,[65] or the formation of highly ordered micro-crystals.[63,64,66,321] However, attempts to quantify the influence of perfect order on the electronic properties of such micro-crystals have remained unsuccessful.[322] Overcoming this challenge would allow exploiting the distinct properties of perfectly ordered NCL micro-crystals, such as superconductance in metalloid $Ga_{84}R_{20}^{4-/3-}$ clusters.[173,318,323]

In this paper, we show that assemblies of $Au_{32}(^{n}Bu_3P)_{12}Cl_8$ NCLs form idiomorphic micro-crystals with high crystallographic phase purity and a strongly preferred growth direction. The crystals are semiconducting and exhibit p-type hopping transport which is limited by Coulomb charging. Energetic disorder is negligible in these micro-crystals. In contrast, disordered assemblies of the same clusters show a decrease in the electric conductivity by two orders of magnitude and an over 50% larger activation energy for hopping transport due to the disorder.

5.3. Results

5.3.1. Self-assembly of Au_{32} NCL micro-crystals

The atomically precise building blocks of metalloid $Au_{32}(^{n}Bu_3P)_{12}Cl_8$ nanoclusters (abbreviated as Au_{32} NCLs) with a Au-core size of $\sim$ 0.9 nm are synthesized as previously described.[100] Including the full ligand shell of twelve phosphine ligands and eight chloride atoms, the building block size is about 1.3 nm, displayed in Figure 5.1a. Single crystal X-ray diffraction of macroscopic crystals of Au_{32} NCLs yields a triclinic unit cell containing two crystallographically independent NCLs (a_{uc} = 1.91 nm, b_{uc} = 1.93 nm, c_{uc} = 3.32 nm; α_{uc} = 73.2°, β_{uc} = 86.7°, γ_{uc} = 63.4°, space group $P\bar{1}$).[100]

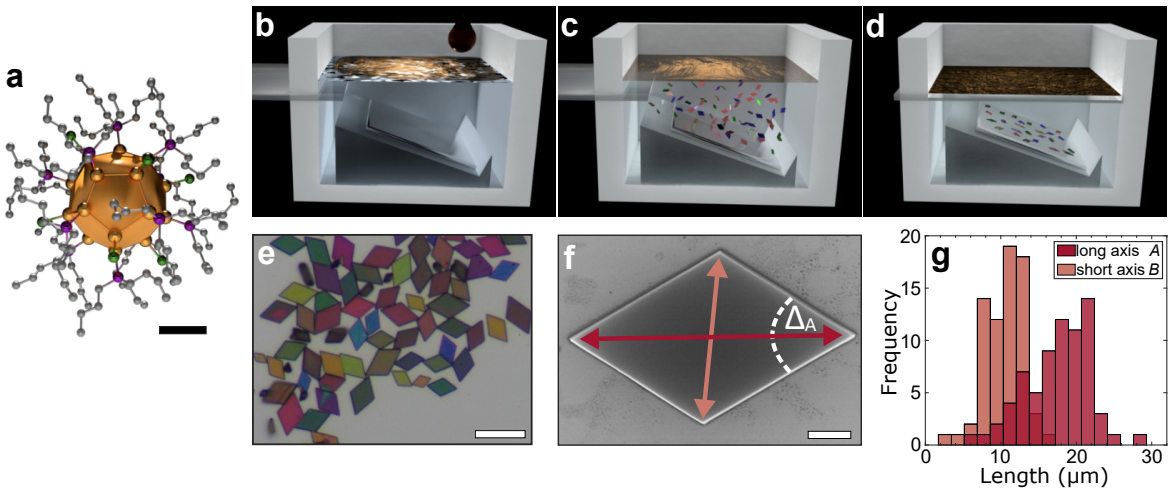

Figure 5.1: Au_{32} NCL self-assembly into micro-crystals. (**a**) Structural drawing of a $Au_{32}(^nBu_3P)_{12}Cl_8$ NCL. The different colors represent the Au- (gold), Cl- (green), P- (purple) and C- (grey) atoms, while hydrogens are omitted for clarity. The Au-core has a diameter of $\sim$ 0.9 nm, while the size of the entire NCL is about 1.3 nm. Scale bar: 0.4 nm. (**b-d**) Schematic illustration of the assembly process. A Au_{32} NCL solution is injected onto the liquid subphase within a Teflon chamber. The Au_{32} NCLs self-assemble into micro-crystals and sink down through the subphase onto the immersed substrate. Details are given in the Methods Section 5.5. (**e**) Optical micrograph of self-assembled Au_{32} NCL micro-crystals on a Si/SiO_x substrate. The crystals are µm-sized and exhibit a parallelogram shape. Different sizes and thicknesses (color) can be observed. Scale bar: 15 µm. (**f**) SEM micrograph of a self-assembled micro-crystal with indicated long axis A, short axis B and angle Δ_A. Scale bar: 2 µm. (**g**) Distribution of long and short axis revealing typical crystal sizes of $A = 17.4 \pm 4.2$ µm, $B = 10.6 \pm 2.5$ µm (dispersity of $Đ = 1.07$, see Supplementary information in Section 5.6 for details).

The preparation process, where dispersed Au_{32} NCLs self-assemble into micro-crystals at the liquid-air interface and sink into the liquid subphase, is schematically illustrated in Figure 5.1b–d. This method allows the preparation of micro-crystals onto any substrate of interest. (Further details on the preparation can be found in the Methods Section 5.5 and Supplementary information in Section 5.6.) By "micro-crystals" we understand micrometer-sized idiomorphic single crystals of Au_{32} NCLs with high crystallographic phase purity and a strongly preferred growth direction, as detailed below. Figure 5.1e shows a typical ensemble of self-assembled Au_{32} NCL micro-crystals with parallelogram shape on a silicon wafer. The crystal shape can be quantified by its geometrical properties of long axis A, short axis B, angle at the sharp edge Δ_A and thickness h, as illustrated in the SEM micrograph in Figure 5.1f. The lateral expansion (5–30 µm) is 2–3 orders of magnitude larger than the thickness (50–600 nm, see Supplementary Figure S5.1), indicating a strongly preferred growth direction. An analysis of SEM

micrographs of individual micro-crystals yields a distribution of long and short axis, revealing a typical lateral size of $A = 17.4 \pm 4.2$ µm and $B = 10.6 \pm 2.5$ µm, as indicated in Figure 5.1g. The lateral size dispersion is calculated to 24%. Further, we observe an aspect ratio of long and short axis of $A/B = 1.64$ and a sharp edge angle of $\Delta_A = 63°$ for all micro-crystals. This aspect ratio corresponds to the associated ratio found in the unit cell of macroscopic Au_{32} NCL crystals, and the angle Δ_A suits the γ_{uc}-angle of the unit cell of $\gamma_{uc} = 63.4°$.[100] Hence, the shape of the micro-crystals strongly resembles the aforementioned unit cell which renders the crystals idiomorphic. High resolution SEM images (see Supplementary Figure S5.1) reveal perfectly defined edges and extremely flat surfaces, indicating a high crystalline phase purity. Different color impressions in Figure 5.1e originate from interference phenomena indicating different thicknesses.

5.3.2. Structural investigation of self-assembled Au_{32} NCL micro-crystals

To verify the crystallinity of self-assembled micro-crystals, grazing-incidence small-angle X-ray scattering (GISAXS) measurements are performed, which is a common technique to investigate the structural properties of nanoparticle assemblies in thin films or at interfaces.[32,60,141] The GISAXS pattern of an ensemble of hundreds of individual micro-crystals with different azimuthal orientation (Figure 5.1e) is shown in Figure 5.2a. Sharp peaks are obtained (Figure 5.2c), indicating the high crystallinity of the sample. Doubled peaks in z direction can be observed, caused by a peak splitting phenomenon as previously described.[324] The fit of the obtained peaks yields a triclinic unit cell ($a_{uc} = 1.9$ nm, $b_{uc} = 1.94$ nm, $c_{uc} = 3.48$ nm and $\alpha_{uc} = 72°$, $\beta_{uc} = 86°$, $\gamma_{uc} = 59°$), which is simulated onto the diffraction pattern. The fit is in excellent agreement with the previously determined unit cell of a macroscopic Au_{32} NCL single crystal ($a_{uc} = 1.91$ nm, $b_{uc} = 1.93$ nm, $c_{uc} = 3.32$ nm and $\alpha_{uc} = 73.2°$, $\beta_{uc} = 86.7°$, $\gamma_{uc} = 63.4°$).[100] Considering the GISAXS data together with the morphological appearance of self-assembled Au_{32} NCL micro-crystals, the unit cell of the micro-crystals can be described by a triclinic structure with axis ratios and angles corresponding to a macroscopic single crystal of Au_{32} (Figure 5.2d). Thus, micro-crystals are µm-sized single crystals, built from individual building blocks of Au_{32} NCLs. A typical micro-crystal consist of $\sim$ 5,000 unit-cells laterally along the long axis A and ~15–200 unit-cells out-of-plane ($\sim 10^9$ Au_{32} NCLs per micro-crystal). Furthermore, the dominant first peak in z direction at $q_z \approx 0.37$ Å^{-1} corresponds to a distance of about $d = 1.7$ nm. Assuming this to be the {002}-peak (based on the bulk structure), an unit cell edge of 3.4 nm

can be calculated which is in good agreement with the unit cell length $c_{uc} = 3.32$ nm of the macroscopic NCL crystal, indicating that the c_{uc} axis of the unit cell is aligned along the surface normal. In combination with the missing peaks at {200} and {020}, we conclude that most micro-crystals lay flat on the substrate surface, with axis a_{uc} and b_{uc} oriented parallel to the substrate, as it is observed by microscopy techniques (Supplementary Figure S5.2). Some peaks along the ring-like features at $q \approx 0.37$ Å^{-1} are observed and attributed to single-crystals which are not oriented flat on the surface and residual agglomerations which are not Au_{32} NCL micro-crystals (see Supplementary Figure S5.2).

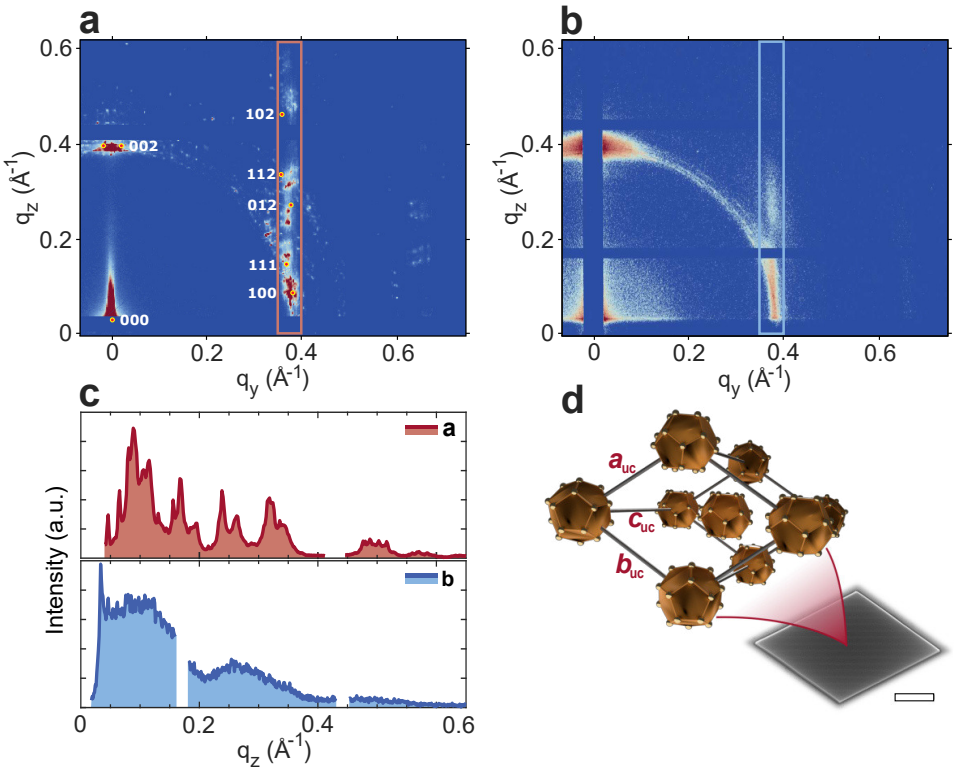

Figure 5.2: Structure of Au_{32} NCL micro-crystals. (**a**) Grazing-incidence small-angle X-ray scattering (GISAXS) pattern of an ensemble of hundreds of micro-crystals with different azimuthal orientation. Diffraction spots are simulated according to a triclinic unit cell ($a_{uc} = 1.90$ nm, $b_{uc} = 1.94$ nm, $c_{uc} = 3.48$ nm and $\alpha_{uc} = 72°$, $\beta_{uc} = 86°$, $\gamma_{uc} = 59°$). (**b**) GISAXS pattern of a spin-coated thin film of Au_{32} NCLs. (**c**) Line scans along q_z at $q_y = 0.37$ Å^{-1} of the pattern in red (a) and blue (b), respectively, highlighted by the rectangular boxes. The ensemble of micro-crystals (a) show distinct sharp peaks, indicating the high crystallinity. The polycrystalline sample (b) shows broad signals while lacking clear peaks, indicating the polycrystalline and defect-rich structure. Gaps correspond to detector edges. (**d**) Schematic drawing of the triclinic unit cell with axis a_{uc}, b_{uc} and c_{uc} indicating the idiomorphic growth of the displayed micro-crystal. The unit cell contains two crystallographically independent NCLs. Ligand spheres are omitted for clarity. The scale bar of the SEM micrograph of a micro-crystal corresponds to 3 µm.

In comparison to micro-crystals, the GISAXS pattern of a spin-coated 30 ± 2 nm thin film is given in Figure 5.2b. Instead of sharp peaks, more ring-like and smeared peaks are observed, clearly indicating the polycrystalline and defect-rich structure of the sample. Throughout this work we refer to these samples as "polycrystalline", to indicate their low degree of crystallinity and high angular disorder.

5.3.3. Optical properties of Au_{32} NCL micro-crystals

The comprehensive characterization of the micro-crystals is concluded by optical and electronic investigations. Figure 5.3a displays the energy-corrected absorbance spectra of a Au_{32} NCLs dispersion, a thin film and a micro-crystal. Dispersed Au_{32} NCLs in solution exhibit several distinct peaks and shoulders, attributed to molecular-like transitions (full spectrum in Supplementary Figure S5.3). While the most prominent absorption peak is observed at 2.58 eV (481 nm), the first absorption peak at 1.55 eV (800 nm) corresponds to the HOMO-LUMO transition.[89,325] Most strikingly, only in micro-crystals of Au_{32} NCLs this peak is strongly enhanced as shown in Figure 5.3a (additional spectra of individual micro-crystals are given in Supplementary Figure S5.4).

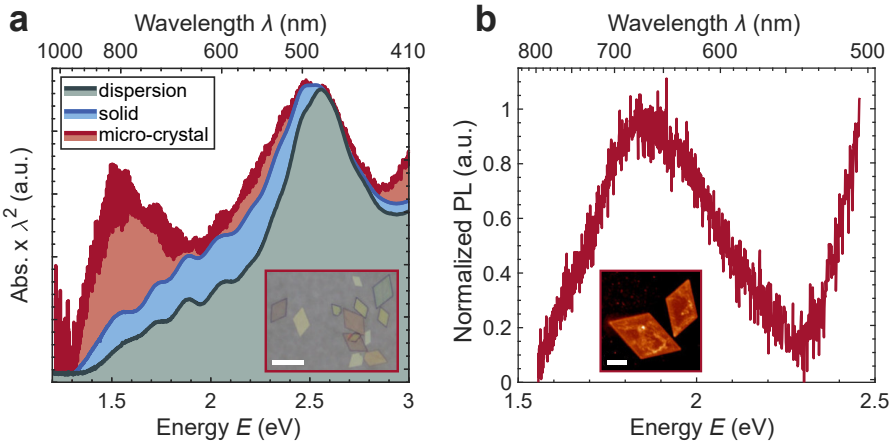

Figure 5.3: Optical properties of Au_{32} NCLs and micro-crystals. (**a**) Absorbance spectra of Au_{32} NCLs dispersed in hexane (green), in a thin film (blue) and in micro-crystals (red) on glass. Individual micro-crystals show enhanced absorption at 800 nm (1.55 eV), corresponding to the HOMO-LUMO transition. The prominent absorption peak at 481 nm (2.58 eV) for dispersed NCLs, is slightly redshifted to 483 nm (2.51 eV) and broadened for Au_{32} NCLs in thin films and micro-crystals. All spectra are normalized to the prominent peak at 481 nm. The inset shows an optical micrograph of individual micro-crystals on a glass substrate. Scale bar: 15 µm. (**b**) Photoluminescence (PL) spectrum of an individual micro-crystal shows a broad emission peak at around 670 nm. The inset displays the luminescence of two micro-crystals upon excitation with 488 nm. Scale bar: 5 µm.

Further, the absorption onset as well as the most prominent peak at 2.57 eV are red-shifted by approximately 100 meV and 10 meV, respectively. A generally enhanced absorption at lower energies and a broadening/shoulder formation at 2.48 eV (500 nm) are observed in micro-crystals and thin films of Au_{32} NCLs. We attribute these findings to a gradual progression from virtually no electronic coupling between the Au_{32} NCLs in solution to weak coupling in thin films and enhanced electronic interactions in the highly ordered micro-crystals.[5,30,322,326]

While no emission of the Au_{32} NCLs is observed in solution, Au_{32} NCL micro-crystals exhibit photoluminescence resulting in a broad emission peak at 670 nm (1.85 eV) after excitation at $\lambda_{ex} = 488$ nm, as shown in Figure 5.3b.

5.3.4. Electronic properties of Au_{32} NCL micro-crystals

To study the possible electronic coupling between individual Au_{32} NCLs observed via optical spectroscopy, we perform (temperature-dependent) conductivity and field-effect transistor (FET) measurements on single Au_{32} NCL micro-crystals. Most remarkably, we find that the conductivity of highly ordered Au_{32} NCLs within micro-crystals exceeds that of polycrystalline assemblies by two orders of magnitude, corroborating our hypothesis of enhanced electronic coupling.

We designed electrode devices, in which deposited micro-crystals bridge adjacent electrodes to be addressed and probed individually. Details on the device layout are given in the Supplementary information in Section 5.6 (Supplementary Figure S5.5 and S5.6). Figure 5.4a shows a SEM micrograph of a 120 nm thick micro-crystal deposited on two Au-electrodes with a gap of $L = 2.8$ µm on a Si/SiO_x device. Figure 5.4b displays a typical I-V curve of an individual micro-crystal in the range of ±200 mV. Ohmic behavior (at room-temperature) in the low-field regime (up to ±1 V) is observed. Electrical conductivity values with typical uncertainties of $< 10\%$ are calculated from these measurements for 54 individual micro-crystal channels on different devices. Figure 5.4c displays the narrow distribution of conductivity values, showing a mean conductivity of $\sigma = 1.56 \times 10^{-4}$ S m^{-1} with a standard deviation of $\pm 0.90 \times 10^{-4}$ S m^{-1}. In contrast, the mean conductivity of polycrystalline thin films of Au_{32} NCLs is only $\sigma \approx 1 \times 10^{-6}$ S m^{-1} (Supplementary Figure S5.7). These devices are obtained by spin-coating on substrates with interdigitated electrodes of channel length $L = 2.5$ µm and width $W = 1$ cm. The film thicknesses are in the range of 30 ± 2 nm to 47 ± 4 nm (Supplementary Figure S5.8 and S5.9).

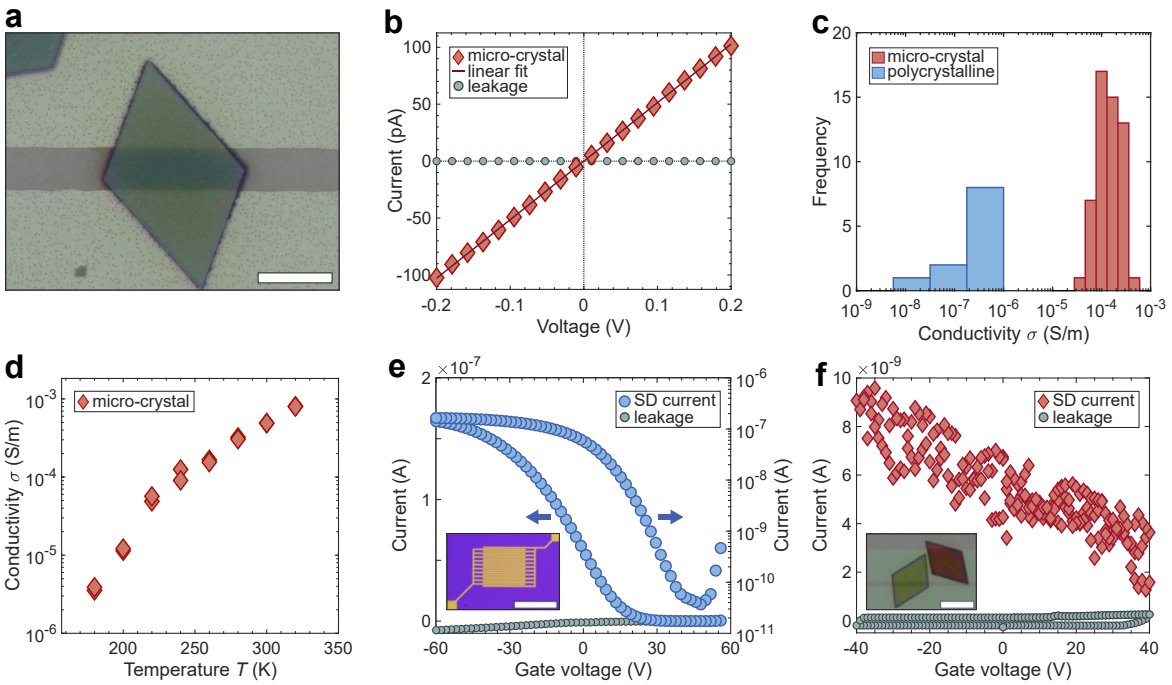

Figure 5.4: Electronic properties of Au_{32} NCL micro-crystals. (**a**) SEM micrograph of an individual micro-crystal deposited on two horizontal Au-electrodes on a Si/SiO_x device. The electrodes form a channel with length $L = 2.8$ µm. The width and height of the contacted micro-crystal are $W = 7.9 \pm 0.4$ µm and $h = 120$ nm. SEM and optical micrographs are merged. Scale bar: 5 µm. (**b**) Typical I-V curve of an individually probed micro-crystal. Ohmic behavior is observed in the low voltage regime. (**c**) Distribution of conductivity σ of 54 individual micro-crystals and 19 polycrystalline thin films. The conductivity of micro-crystals exceeds that of polycrystalline films by ~ 2 oders of magnitude. (**d**) Temperature-dependent conductivity of Au_{32} NCL micro-crystals with two individual measurements per temperature step. (**e**) FET transfer curve (blue) of a polycrystalline film of Au_{32} NCLs on an interdigitated electrode device with $L = 2.5$ µm, $W = 1$ cm, measured at $V_{SD} = 10$ V on a linear and logarithmic scale together with the negligible leak current (grey). Arrows indicate the corresponding y-axis. (**f**) FET transfer curve (red) of an individual micro-crystal device with $L = 1.5$ µm, $W = 10.4 \pm 0.2$ µm, measured at $V_{SD} = 5$ V, together with the negligible leak current (grey). The insets in (e) and (f) display optical micrographs of the two devices. Scale bars correspond to 500 µm and 10 µm, respectively.

To shed light on the charge-transfer mechanism of electronic transport within micro-crystals and polycrystalline films of Au_{32} NCLs, we perform temperature-dependent conductivity measurements at $T = 340$–170 K (Figure 5.4d). Below this range, the measured current approaches the noise level. The measured temperature dependence can be described by an Arrhenius-type temperature-activated hopping (Supplementary Figure S5.10).[181] Fitting the conductivity data accordingly, we obtain activation

energies of $E_A = 227 \pm 17$ meV for individual micro-crystals and $E_A = 366 \pm 62$ meV for the spin-coated polycrystalline Au_{32} NCLs thin films.

To further characterize the electronic properties of self-assembled Au_{32} NCL micro-crystals and polycrystalline films, FET measurements are performed. Strikingly, a field-effect can be observed, indicating semiconducting behavior of the metal NCL assemblies. The tri-butyl-phosphine ligands covering the cluster cores limit the electronic coupling enough to prevent metallic behavior.[65] Figure 5.4e shows the FET transfer curve of a polycrystalline thin film of Au_{32} NCLs on interdigitated electrodes with channel dimensions of $L = 2.5$ µm, $W = 1$ cm and $h = 30 \pm 2$ nm. p-type behavior is observed, indicating holes (h^+) as majority charge carriers. The current flow can be modulated by more than three orders of magnitude (ON/OFF ratio of $\sim$ 4,000). Ambipolar behavior is also observed for very high threshold voltages of $V_G > 40$ V. The calculated hole mobility of spin-coated Au_{32} NCL films is in the range of $\mu(h^+) \sim 10^{-6}$–10^{-5} cm^2 V^{-1} s^{-1}.

Figure 5.4f displays the FET transfer curve of an individual Au_{32} NCL micro-crystal, which also indicates p-type behavior. Note that the current flows through a much smaller channel width W of 5–10 µm in this case. Here, the mean value and standard deviation of the hole mobility of individual micro-crystals can be calculated to be $\mu(h^+) = 0.8 \times 10^{-4} \pm 0.58 \times 10^{-4}$ cm^2 V^{-1} s^{-1}. Values up to 2×10^{-4} cm^2 V^{-1} s^{-1} are observed (Supplementary Figure S5.11). The noise in current flow and the low modulation can be attributed to the non-ideal channel geometry. Further, the quality of contact between the dielectric SiO_x layer and the micro-crystal is not known. The non-ideal contact might influence the appearance of transfer curves (details are given in Supplementary Figure S5.12). We have verified that the contact resistance of Au_{32} NCL micro-crystal and thin film devices is negligible (Supplementary Figure S5.13).

Knowing the charge carrier mobility $\mu(h^+)$ and the conductivity of individual Au_{32} NCL crystals, we calculate the charge carrier concentration to be $n(h^+) = 2 \times 10^{17}$ cm^{-3}. This correspond to one free charge carrier per 1,000 Au_{32} NCLs, as the concentration of individual Au_{32} NCLs within a crystal is 1.9×10^{20} cm^{-3}.

5.4. Discussion

The Au_{32} NCL HOMO-LUMO gap of 1.55 eV (Figure 5.3a) is consistent with earlier reports on other Au NCLs and the expected degree of quantum confinement. Specifically, for NCLs with 11 and 25 Au atoms and, thus, stronger quantum confinement, HOMO-LUMO transitions of 2.97 eV and 1.84 eV have been reported.[65,327] In line with this, $(AuAg)_{34}$ NCLs exhibit a HOMO-LUMO transition of around 1.4 eV.[66] A related size-dependent study of NCLs with 10 to 39 Au core atoms revealed HOMO-LUMO transitions from 3.7 eV to 1.7 eV.[328] The solid state luminescence of the Au_{32} NCLs (Figure 5.3b) at 1.85 eV is fully consistent with the emission of other Au NCLs,[19,328–331] such as Au_{25},[89,332–334] and may be attributed to aggregation-induced emission.[333,335,336] In contrast to the HOMO-LUMO transition, which is believed to involve a (mostly dark) sp-intraband transition, the luminescence in Au_{25} and Au_{28} NCLs results from a sp→d interband transition, which may also be the case in Au_{32}.[331,332] We note, however, that Au_{25} NCLs consist of an icosahedral Au_{13} core, while the core of the Au_{32} NCL is a hollow Au_{12} icosahedron with potentially different optical properties.[19,100,337]

The conductivity (Figure 5.4c) and mobility (Figure 5.4e) of the thin polycrystalline Au_{32} NCL films are in good agreement with previously reported values for Au_{25} and Au_{38} NCLs.[65,338] In contrast to the study by Galchenko et al. on Au_{25} NCLs with n-type transport,[65] we observe here p-type behavior or ambipolar transport with extremely high threshold voltages of approximately $V_G = +50$ V. In a recent study by Yuan et al.[66], single crystals of $(AuAg)_{34}$ NCLs also exhibit p-type behavior with mobilities of $\sim 2 \times 10^{-2}$ cm^2 V^{-1} s^{-1} and an ON/OFF ratio of $\sim$ 4,000. The conductivity of Au_{32} NCL micro-crystals exceed that of monomeric and polymerized $(AuAg)_{34}$ NCL crystals (6×10^{-8} S m^{-1} and 1.5×10^{-5} S m^{-1}, respectively).[66]

The key finding of this work is that the above-mentioned properties change dramatically as long-range order is introduced to the NCL ensembles (Figure 5.2a). While the seminal work by Li et al.[64] reported electric transport measurements on similar single crystals for the first time, we provide a direct comparison of the transport properties in the ordered vs. the glassy state. This uniquely allows us to quantify the value of long-range order for electric transport in Au NCL ensembles.

To this end, we use the experimentally determined activation energies to charge transport in the Au_{32} NCLs, either as micro-crystals ($E_A = 227 \pm 17$ meV) or as polycrystalline thin films ($E_A = 366 \pm 62$ meV). Transport in weakly coupled nanostructures depends on the transfer integral β, the Coulomb charging energy E_C and the energetic disorder $\Delta\alpha$.[28] Strongly temperature-activated transport (Figure 5.4d) suggests that

even the Au_{32} NCL micro-crystals are in the Mott regime with $E_C >> \beta$. Thus, charge transport is dominated by E_C and possibly $\Delta\alpha$. E_C can be referred to as the self-capacitance of the NCL and it describes the required energy for addition or removal of an additional charge carrier to the NCL. We estimate E_C of the micro-crystals to 276 meV (for details, see Supplementary information in Section 5.6), which is consistent with the full activation energy. Thus, charge carrier transport in the micro-crystals depends solely on the charging energy and the energetic disorder is negligible. In contrast, E_A in the polycrystalline thin films largely exceeds E_C, suggesting a significant degree of energetic disorder, which is caused by structural, orientational or chemical disorder of the individual NCLs. Since the NCLs are atomically precise, we hold only structural defects, such as grain boundaries, cracks and a lack of orientational order to be responsible for the occurrence of a non-zero $\Delta\alpha$ in the polycrystalline films.[339] This effect is especially pronounced here, as systems with large E_C are generally very sensitive towards structural disorder.[321] In contrast, Au_{32} NCL micro-crystals not only consist of chemically identical building blocks but also exhibit structural perfection, which manifests in a vanishing value of $\Delta\alpha$. We suggest that this is the reason for the enhanced electronic coupling and altered optoelectronic properties. Future attempts to further increase coupling in Au NCL micro-crystals should focus on increasing the transfer integral, for instance by reducing the distance between adjacent clusters or by covalent coupling with conjugated linkers. If $\beta \approx E_C$, a Mott insulator-metal transition occurs and band-like transport becomes possible. The basis for this will be atomically defined building blocks in combination with a suitable coupling as pioneered here.

In conclusion, atomically precise $Au_{32}(^nBu_3P)_{12}Cl_8$ NCLs are self-assembled into micro-crystals with high crystallographic phase purity and a strongly preferred growth direction. Individual micro-crystals exhibit semiconducting p-type behavior and temperature activated hopping transport, limited by Coulomb charging. Most strikingly, additional optical transitions emerge, and charge carrier transport is enhanced by two orders of magnitude in the micro-crystals compared to polycrystalline thin films, highlighting the advantageous effect of long-range structural order. This study implies that utilizing atomically precise building blocks for the self-assembly into SLs eliminates energetic disorder and provides a promising route towards self-assembled nanostructures with emergent optoelectronic properties.

5.5. Methods

5.5.1. Materials

All chemicals were used as received unless otherwise noted. Octane, ethanol, dichloromethane and acetonitrile were bought from Sigma-Aldrich and were degassed and distilled before usage. $NaBH_4$ was bought from Acros Organics. Silicon/silicon dioxide (Si/SiO_x) wafers with 200 nm SiO_x layer and n-doped Si were purchased from Siegert Wafer. Photoresist, developer and remover (ma-N 405, ma-D 331/S and mr-Rem 660, respectively) were purchased from micro resist technology GmbH, Berlin.

5.5.2. Synthesis of $Au_{32}(^nBu_3P)_{12}Cl_8$

1 mmol of $^nBu_3PAuCl$ was dissolved in 20 ml of ethanol before a suspension of 38 mg of $NaBH_4$ in ethanol was added. The reaction solution was stirred for one hour before the solvent was removed under reduced pressure. The residual black solid was extracted with CH_2Cl_2 and layered with three times the amount of diethyl ether. After one week a gold mirror formed while a dark supernatant remained. The dark brown supernatant was filtered off and reduced under vacuum. Crystals of $Au_{32}(^nBu_3P)_{12}Cl_8$ formed by storing the solution at $-30°C$ for a few days.

5.5.3. Self-assembly of Au_{32} NCL micro-crystals

The formation of crystals via liquid-air interface method is schematically illustrated in Figure 5.1b-d. A solution of Au_{32} NCLs in octane (200 µl, 0.5 mM) was added onto a subphase of acetonitrile inside a home-built Teflon chamber (Figure 5.1b). The self-assembly of Au_{32} NCLs into micro-crystals took place at the phase boundary between the acetonitrile subphase and the NCL solution upon evaporation of the solvent. The micro-crystals started to sink down through the subphase and stuck to the desired substrate which was previously placed inside the liquid subphase (Figure 5.1c). After 45 min a glass slide was horizontally inserted into the subphase to separate the residual Au_{32} NCL membrane (floating on the liquid-air interface) from the bottom substrate (Figure 5.1d). The liquid subphase was removed and the substrate dried at ambient conditions. Micro-crystal fabrication took place at ambient condition. Further details are given in the Supporting information and Figure S5.14.

5.5.4. Micro-crystal device fabrication

For the micro-crystal electrode devices, standard photolithography technique (negative tone resist) was used to pattern Au electrodes on Si/SiO_x substrates (200 nm SiO_x). Au (8–10 nm) and Ti ($\sim$ 2.5 nm) as an adhesion layer were thermally evaporated under high vacuum conditions. Ultrasonic-assisted lift-off in mr-Rem 660 removed the residual resist and metal layer. Electrodes with gaps of 1.5–2.5 µm (channel length L) were realized. Devices were coated with micro-crystals as described above and checked with a basic light microscope to identify channels, where a single micro-crystal bridges two adjacent electrodes.

5.5.5. Thin film fabrication

Thin film samples for absorbance, GISAXS and electronic measurements were prepared as follows. For thin film electronic devices with interdigitated electrodes, commercially available OFET substrates (Fraunhofer IPMS, Dresden) were purchased. For GISAXS and absorbance measurements, Si wafers with 200 nm SiO_x layer and glass slides were used, respectively. The substrates (15×15 mm^2) were coated with 100 µl of a 0.5 mM Au_{32} NCL solution (hexane or heptane) and spin-coated after 2 min with a speed of 760 rpm or 2,000 rpm for 30 s. All devices were prepared at ambient conditions in a fume-hood. The thickness of thin films was determined by profilometry (Dektak XT-A, Bruker), details are given in the Supporting information.

5.5.6. Grazing-incidence small-angle X-ray scattering

GISAXS measurements were conducted on a Xeuss 2.0 setup (Xenocs). A CuKα X-ray beam with wavelength $\lambda = 1.5418$ Å ($E = 8.04$ keV) and a beam size of $\sim 500 \times 500$ µm^2 (FWHM) was used. A two-dimensional detector Pilatus 300K (Dectris) with 487×619 pixels of 175×175 µm^2 was positioned 365 mm downstream the sample. The samples (micro-crystal ensemble or thin film on Si wafer with 200 nm SiO_x layer, both described as above) were probed at an incidence angle of 0.2°. Acquisition times of 60 min and 30 min were used to obtain the GISAXS maps in Figure 5.2a and Figure 5.2b, respectively. Simulated peaks correspond to a triclinic unit cell with $a_{uc} = 1.90$ nm, $b_{uc} = 1.94$ nm, $c_{uc} = 3.48$ nm and $\alpha_{uc} = 72°$, $\beta_{uc} = 86°$, $\gamma_{uc} = 59°$, which is in good agreement with the X-ray diffraction data from macroscopic Au_{32} NCL crystals ($a_{uc} = 1.91$ nm, $b_{uc} = 1.93$ nm, $c_{uc} = 3.32$ nm and $\alpha_{uc} = 73.2°$, $\beta_{uc} = 86.7°$, $\gamma_{uc} = 63.4°$). Simulations were performed using the MATLAB toolbox GIXSGUI.[340]

5.5.7. Optical measurements

Absorbance spectra of Au_{32} NCL in solutions (0.5 mM in hexane) were acquired with an UV-Vis-NIR spectrometer (Cary 5000, Agilent Technologies). For thin films spin-coated on glass slides (as described above), a Perkin Elmer Lambda 950 spectrometer was used. For individual micro-crystals on glass slides, an inverted microscope (Nikon Eclipse Ti-S) with a spectrometer was used. The sample was illuminated with unpolarized white light by a 100 W halogen lamp. The transmitted light was collected by a 60× objective (Nikon, CFI S Plan Fluor ELWD, NA = 0.7). The collected light was passed to a grating spectrograph (Andor Technology, Shamrock SR-303i) and detected with a camera (Andor Technology, iDusCCD). All absorbance spectra were energy corrected using the expression $I_{abs}(E) = I_{abs}(\lambda) \cdot \lambda^2$.[89,341] Photoluminescence images and emission spectra of individual Au_{32} NCL micro-crystals were acquired with a home-built confocal laser scanning microscope. The diode laser (iBeam smart, Toptica Photonics) was operated in continuous wave Gaussian mode at an excitation wavelength of $\lambda_{ex} = 488$ nm. Luminescence images were obtained with a photon counting module (SPCM-AQR-14, PerkinElmer) and spectra were acquired with an UV-Vis spectrometer (Acton SpectraPro 2300, Princeton Instruments). The background was subsequently subtracted from the emission spectra.

5.5.8. Scanning electron microscopy

SEM imaging of micro-crystals on Si/SiO_x devices was performed with a HITACHI model SU8030 at 30 kV. To estimate the thickness of micro-crystals, samples were titled by 85° with respect to the incoming electron beam.

5.5.9. Electrical measurements

All electrical measurements were conducted under vacuum in a probe station (Lake Shore, CRX-6.5K). All samples were placed under vacuum over night before measurement (pressure of $< 10^{-5}$ mbar). Au-electrode pairs were contacted with W-tips, connected to a source-meter-unit (Keithley, 2636 B). A back electrode worked as gate electrode. For two-point conductivity measurements, voltage sweeps in a certain range of ±1 V were applied and the current (as well as leak current) detected. Fitting the linear I-V curve yielded the conductance value G. Conductivity σ was calculated as $\sigma = (G \cdot L)/(W \cdot h)$. The dimensions length, width, thickness (L, W, h) were determined by SEM imaging for micro-crystals or profilometry for spin-coated thin films (Dektak XT-A, Bruker).

For FET measurements (bottom-gate, bottom-contact configuration), a source-drain voltage of V_{SD} was applied and I_{SD} was measured, modulated by applied gate voltages V_G. Using the gradual channel approximation, field-effect mobilities μ were calculated (Supplementary Equation (S5.2)).

For temperature-dependent measurements, the devices were cooled down to 8 K and gradually heated with a Lake Shore temperature controller (model 336). Current was detected in the temperature range 170–340 K. At least two measurements were taken for every temperature. After reaching 340 K, measurements were repeated at lower temperature, to verify the reversibility. The temperature-activated hopping behavior can be described as an Arrhenius-type, which is expressed in Equation (5.1).[181]

$$\sigma = \sigma_0 \exp\left(\frac{-E_A}{k_B T}\right) \tag{5.1}$$

Here, E_A is the activation energy, k_B the Boltzmann constant, T the temperature and σ_0 a constant. E_A was obtained from the slope of $\ln(\sigma)$ as a function of T^{-1}.

5.6. Supplementary information

SEM imaging of micro-crystals

Figure S5.1a displays a SEM micrograph of a micro-crystal. Well-defined edges as well as an extremely flat surface are observed. Figures S5.1b–d show side-views of micro-crystals with different thicknesses. In side-view the sample is tilted by 85° with respect to the incoming electron beam. From this, the thickness of individual micro-crystals can be investigated.

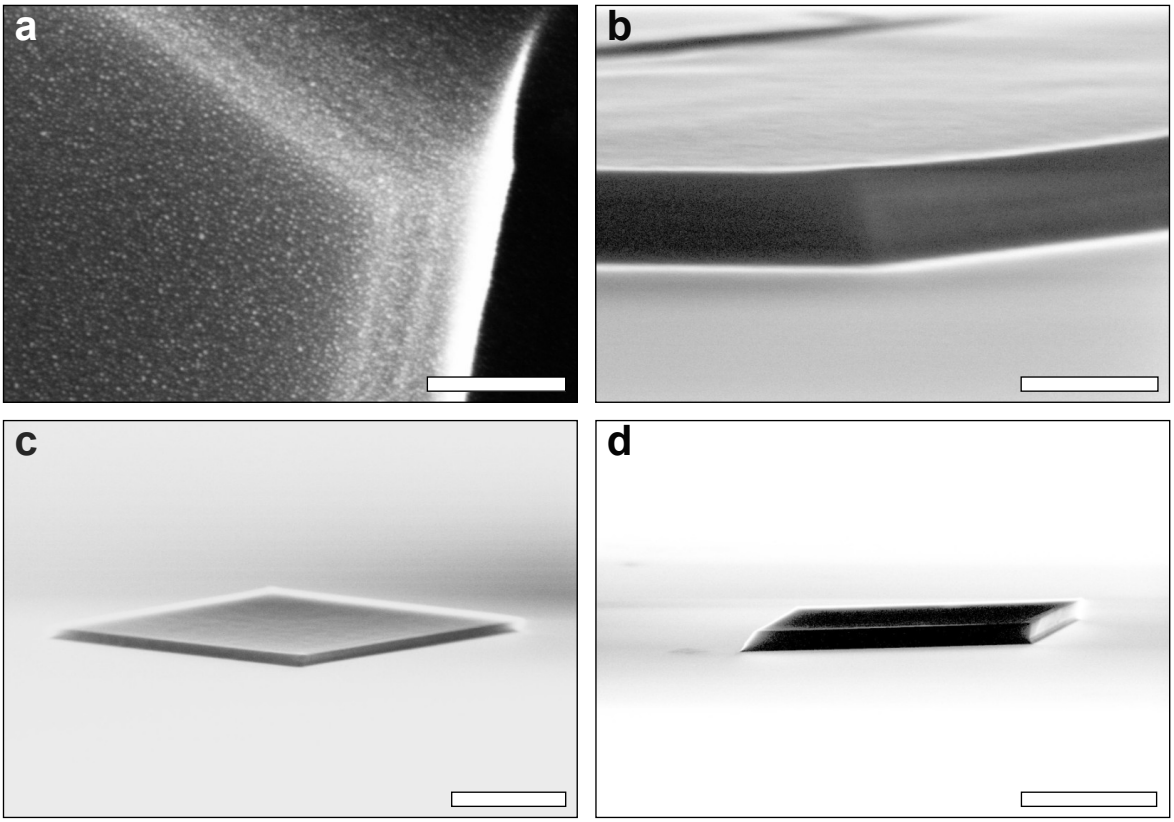

Figure S5.1: SEM investigation of Au_{32} NCL micro-crystals. (**a**) High-resolution SEM micrograph of an edge of a micro-crystal. Individual NCLs can be identified on the top-most layer as well as on the slightly tilted sidewall. However, structural arrangement of NCLs cannot be resolved. Scale bar: 100 nm. (**b**–**d**) Side-view of different micro-crystals with thicknesses of $\sim$ 200 nm (**b**), $\sim$ 100 nm (**c**) and $\sim$ 450 nm (**d**) under incident angle of 85°. Scale bars correspond to 300 nm (b), 1 µm (c) and 3 µm (d).

Micro-crystal sample for GISAXS measurements

Figure S5.2 shows an optical micrograph of the micro-crystal sample used for GISAXS. The majority of micro-crystals is oriented flat on the surface. Minor agglomerates cause distortions of the resulting GISAXS pattern, as described in the main text.

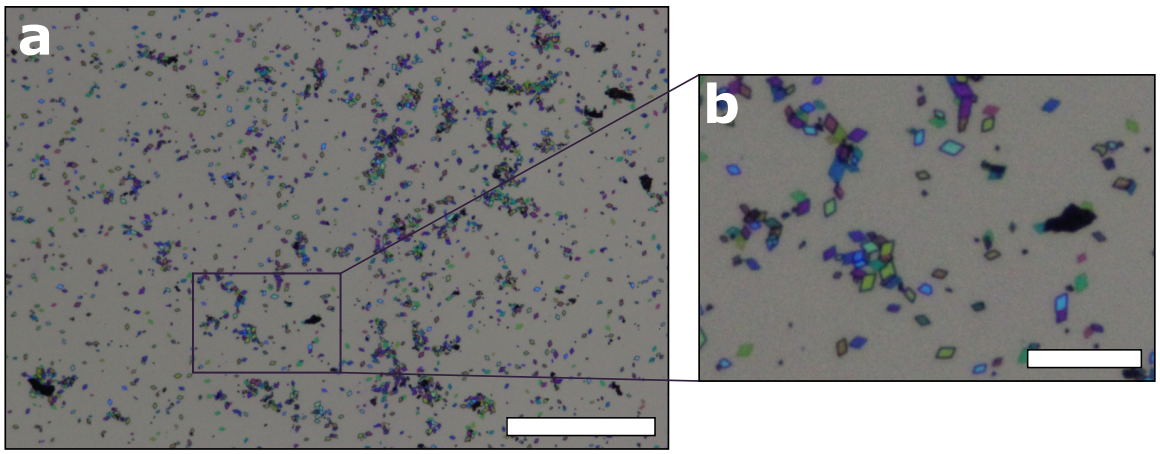

Figure S5.2: Optical micrograph of a Si/SiO_x sample with an ensemble of hundreds of individual micro-crystals used for GISAXS measurements. Scale bars in (a) and (b) correspond to 200 µm and 50 µm, respectively.

Dispersity of the micro-crystals

To determine the dispersity of the micro-crystals, scanning electron micrographs were used to measure the axis lengths of the micro-crystals (ImageJ software). The dispersity $Đ$ is calculated according the IUPAC definition using the following Equation (S5.1)

$$Đ = \frac{M_w}{M_n} \quad , \tag{S5.1}$$

where $M_w = \frac{\Sigma_i N_i M_i^2}{\Sigma_i N_i M_I}$ and $M_n = \frac{\Sigma_i N_i M_i}{\Sigma_i N_i}$. N is given as the number of crystals with axis length M. Using this equation with measured axis lengths of ~ 100 micro-crystals yielded a dispersity of $Đ = 1.07$.

Optical spectrum of $Au_{32}(^{n}Bu_3P)_{12}Cl_8$ nanoclusters

Figure S5.3 shows an optical absorbance spectrum of Au_{32} NCLs dissolved in hexane. Several distinct molecular-like transitions are observed, together with a HOMO-LUMO transition at 1.55 eV.

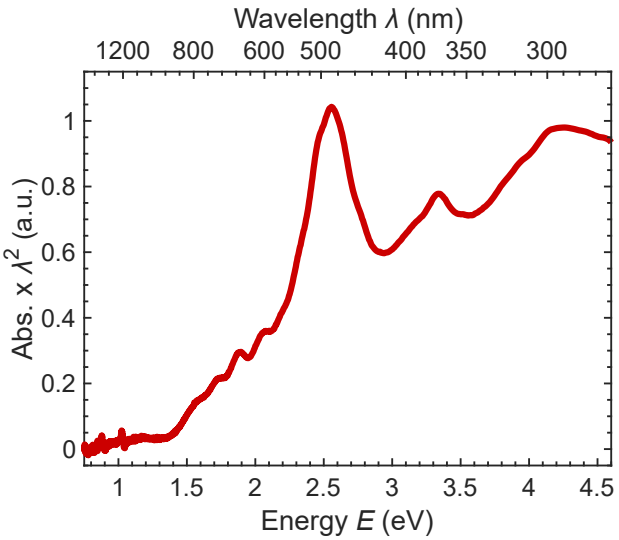

Figure S5.3: Optical spectrum of Au_{32} NCLs. Absorbance spectra of Au_{32} NCLs dispersed in hexane. Absorbance is energy corrected using the expression $I_{abs}(E) = I_{abs}(\lambda) \cdot \lambda^2$. The peak at 1.55 eV (800 nm) is attributed to the HOMO-LUMO transition. This spectrum corresponds to the spectrum shown in Figure 5.3a with larger energy range.

Optical spectra of individual Au_{32} NCL micro-crystals

Figure S5.4 shows the absorbance spectra of several individual Au_{32} NCL micro-crystals, all exhibiting the enhanced peak at around 1.55 eV (800 nm).

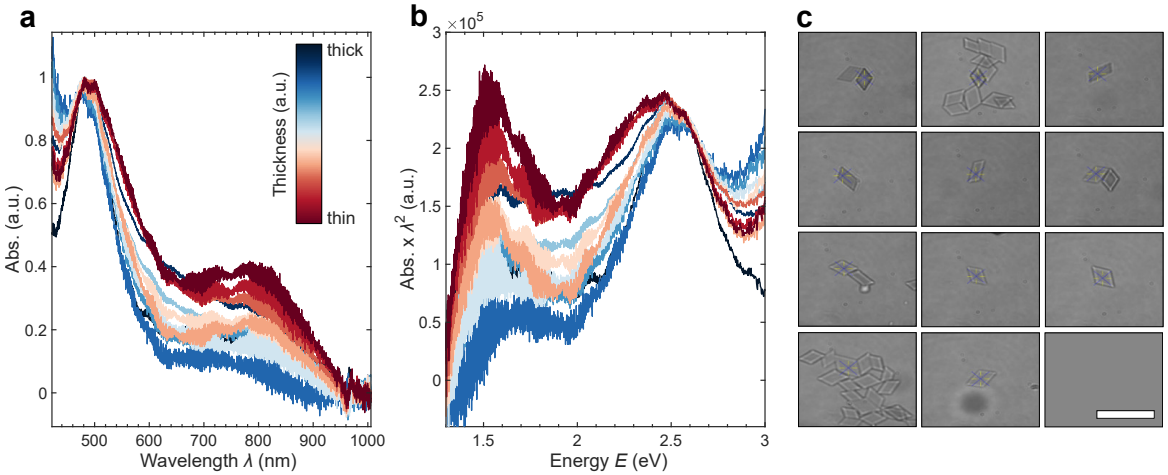

Figure S5.4: Absorbance spectra of individual Au_{32} NCL micro-crystals. (**a**) Absorbance as a function of wavelength λ of eleven micro-crystals on glass. The legend indicates the qualitative thickness of the corresponding micro-crystals, determined via the grayscale values from the optical micrographs in (c). (**b**) The spectra from (a) with energy corrected absorbance (using the expression $I_{\mathrm{abs}}(E) = I_{\mathrm{abs}}(\lambda) \cdot \lambda^2$ as a function of energy. All micro-crystals exhibit the enhanced absorbance peak at around 1.55 eV (800 nm). All curves are normalized to the local maximum at 2.58 eV (480 nm). (**c**) Optical micrographs (camera images) of the eleven micro-crystals where absorbance was measured (labeled). From top left to bottom right, the grayscale value of the micro-crystals decreases, assuming the thickness to decrease as well. The scale bar corresponds to 40 µm and applies to all subfigures.

Electrode layout for electronic measurements of individual micro-crystals
Optical micrographs of typical electrode devices (Si/SiO_x substrate) are given in Figure S5.5. Adjacent electrodes form channels due to overlapping ends. The width of the overlap is 80 µm and the distance between electrodes defines the channel length L. On a single device, up to 330 individual channels are realized. By contacting the contact-pads of adjacent electrodes, every channel can be addressed individually. The devices are coated with micro-crystals as described in the Methods Section 5.5. Micro-crystals which are bridging two adjacent electrodes can be contacted and probed individually. On a typical device, 10–40 individual micro-crystals can be investigated. Due to the relatively thin electrode thickness of $\sim$ 10 nm, contacted micro-crystals are not free-standing but establish contact to the SiO_x layer, manifested by the observed field-effect.

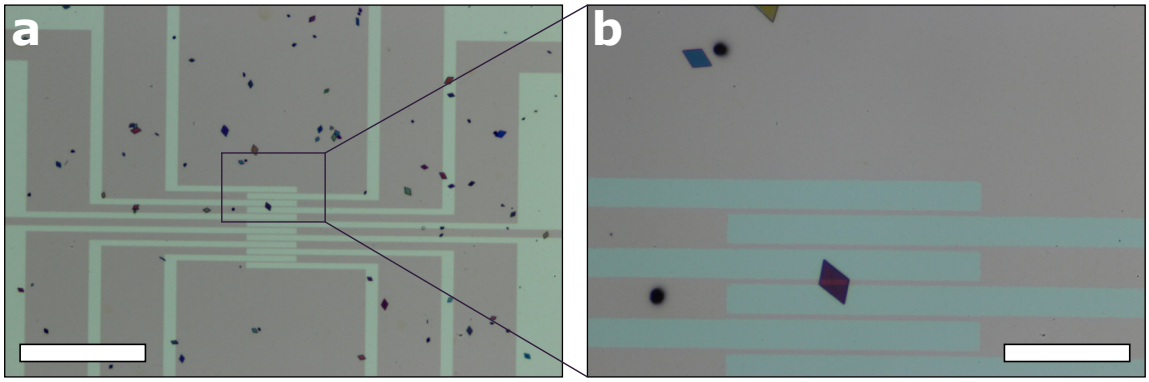

Figure S5.5: Optical micrographs of a typical electrode device with micro-crystals. Micro-crystals which are bridging two adjacent electrodes can be contacted and probed individually. (10 nm Au-electrodes on Si/SiO_x wafer with 200 nm oxide thickness). Scale bars of (a) and (b) correspond to 200 µm and 40 µm, respectively.

Evaluating the effective width of a micro-crystal within a channel

The effective width of a micro-crystal on a channel is described best by the mean of W along the channel. Figure S5.6 shows a SEM micrograph of a micro-crystal covering two channels. The measured conductance G of the channels is different, due to differences in effective width. For every channel, different widths are present (caused by the parallelogram shape). The calculated conductivities σ of the two channels should be the same, since the same micro-crystal is probed. Normalizing the measured conductance G with the channel geometry L/W gives essentially the same value (as thickness h is the same). This geometry normalized conductance values, using the mean width, are identical with 39.5 pS and 39.9 pS for the micro-crystals in the two different channels, respectively. Thus, using the mean width along the electric field is the most appropriate dimension.

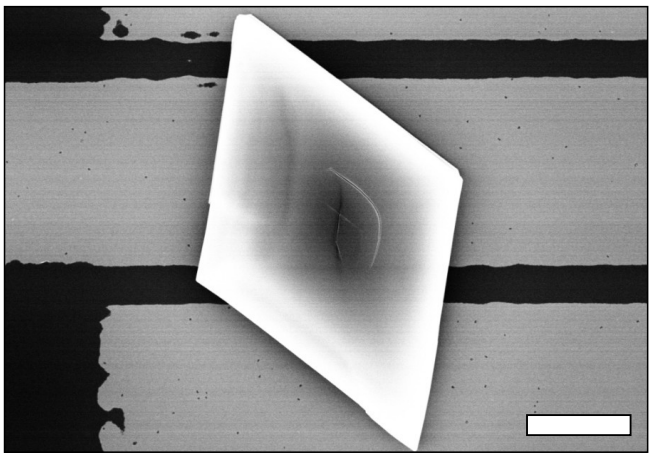

Figure S5.6: SEM micrograph of an individual micro-crystal, covering two different channels. Using the mean value of W to calculate the conductivity σ yields the same value for geometry normalized conductance for both channels bridged by the same micro-crystal. Scale bar: 5 µm.

I-V curves of Au_{32} NCL devices

Figure S5.7 shows representative I-V curves of a self-assembled Au_{32} NCL micro-crystal with conductivity $\sigma_{\text{crystal}} = 2.4 \times 10^{-4}$ S m^{-1} and a spin-coated Au_{32} NCL thin film with $\sigma_{\text{film}} = 4.4 \times 10^{-6}$ S m^{-1}.

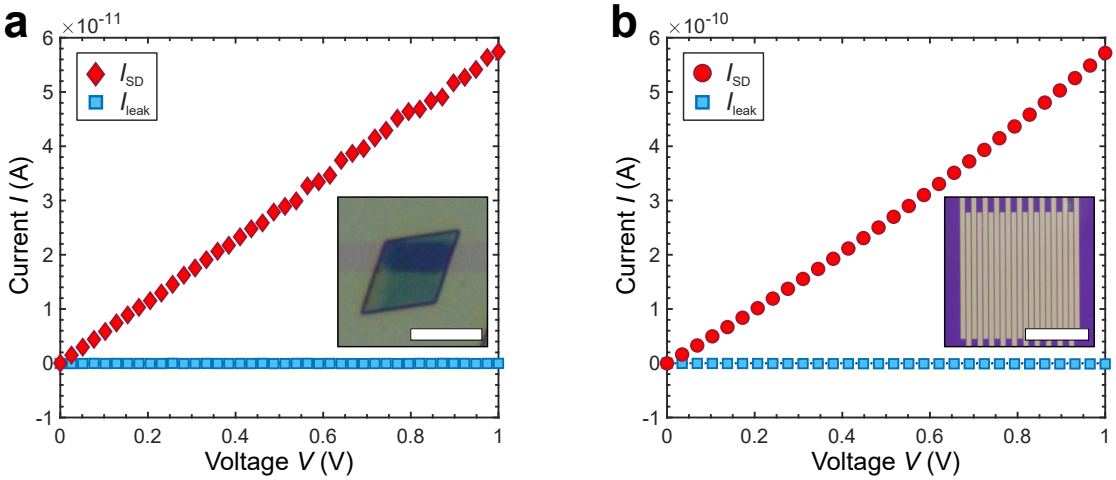

Figure S5.7: I-V curves of Au_{32} NCL devices. (**a**) Typical I-V curve of an individually probed micro-crystal. Fitting I_{SD} (red) yields the conductance $G_{\text{crystal}} = 57$ pS. The leakage (blue) is negligible. The inset displays the corresponding micro-crystal with $L = 2.8$ µm, $W = 6.8$ µm and $h = 98$ nm. The conductivity can be calculated to $\sigma_{\text{crystal}} = 2.4 \times 10^{-4}$ S m^{-1}. Scale bar: 7 µm. (**b**) Typical I-V curve of Au_{32} NCL thin film. Fitting I_{SD} (red) yields the conductance $G_{\text{film}} = 533$ pS. The leakage (blue) is negligible. The inset displays the corresponding device with $L = 2.5$ µm, $W = 1$ cm and $h = 30 \pm 2$ nm. The conductivity can be calculated to $\sigma_{\text{film}} = 4.4 \times 10^{-6}$ S m^{-1}. Scale bar: 250 µm.

Details on spin-coated thin film samples

All thin film samples were prepared by spin-coating and no post-coating techniques were applied. The samples were stored overnight to ensure full evaporation of residual solvents. Thin film samples for electronic measurements were placed under vacuum overnight in the probe station and measured under vacuum conditions (pressure of $\leq 10^{-5}$ mbar). Figure S5.8 displays optical and scanning electron micrographs of typical spin-coated Au_{32} NCL thin films.

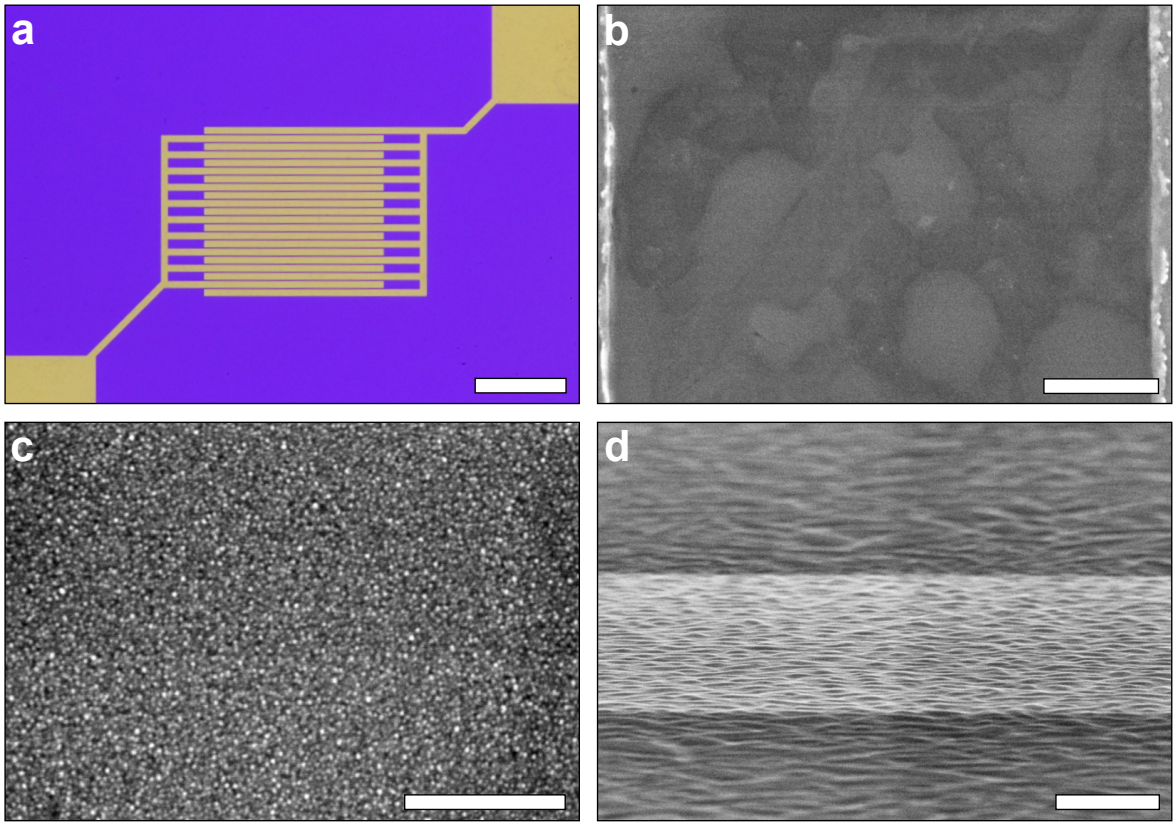

Figure S5.8: Micrographs of spin-coated Au_{32} NCL thin films. (**a**) Optical micrograph of a 30 ± 2 nm thin film on interdigitated Au electrodes of a Si/SiO_x substrate. Optically, the thin film appears homogeneous over the entire displayed area of ~ 1.5 mm^2. Scale bar: 250 µm. (**b**) Scanning electron micrograph of the same film within a channel of $L = 2.5$ µm (Au electrodes at left and right side). A continuous film with individual grains of 440 ± 130 nm length can be observed. Scale bar: 500 nm. (**c**) High-resolution SEM micrograph of the Au_{32} NCL thin film. Scale bar: 100 nm. (**d**) SEM micrograph under incident angle of 85° of a thin film within a channel of $L = 2.5$ µm (Au electrodes in dark, channel gap in bright). A smooth and uniform surface can be observed. Scale bar: 1.5 µm.

Thickness characterization of Au_{32} NCL thin films

Figure S5.9 displays the thickness characterization of spin-coated Au_{32} NCL thin films by profilometry (Bruker, Dektak XT). The samples were prepared with a scratch (Figure S5.9a) to identify the absolute film thickness by scanning across (Figure S5.9b). Several height profiles were taken per sample to calculate the mean value and standard deviation of the film thickness. Measuring the thickness on several positions of the samples and calculating the mean value ± standard deviation yields values of 30 ± 2 nm and 47 ± 4 nm (relative deviations of 6.7–8.5%).

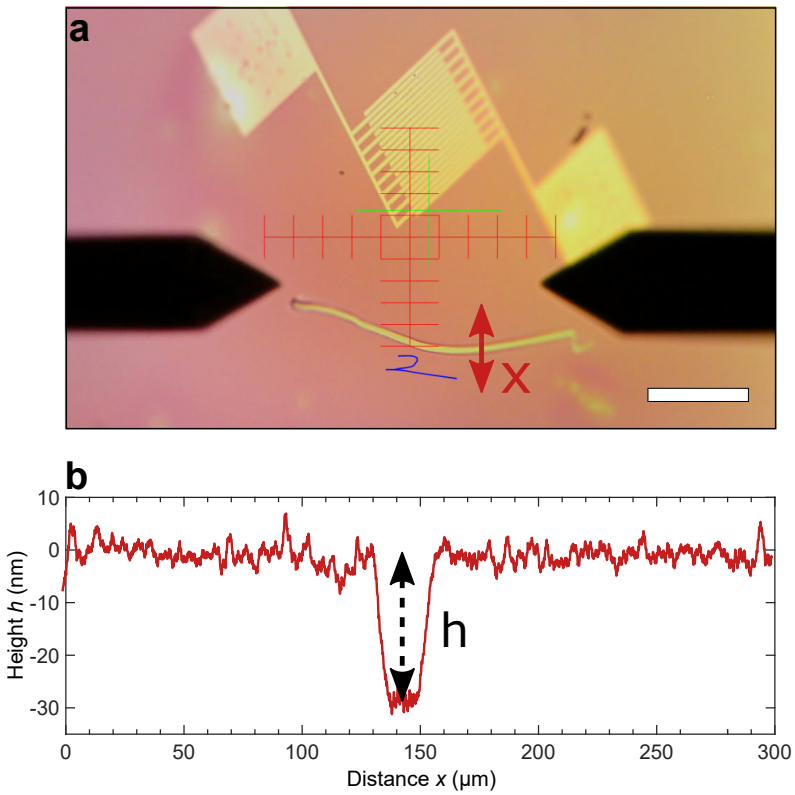

Figure S5.9: Thickness characterization of Au_{32} NCL thin films by profilometry. (**a**) Camera image of the profilometer showing an electrode device with a spin-coated Au_{32} NCL thin film and the stylus (as well as its reflection). The red arrow indicates the scanning direction x across a scratch within the thin film. Scale bar: 500 µm. (**b**) Corresponding height profile of the thin film revealing a thickness of $h = 30$ nm and a root-mean-square roughness of 2.2 nm.

Temperature-dependent conductivity measurements

Figure S5.10a and S5.10c display typical plots of temperature-dependent conductivity of a Au_{32} NCL micro-crystal and a spin-coated thin film, respectively. Figure S5.10b and S5.10d show the corresponding Arrhenius plot, where $\ln(\sigma)$ is plotted as a function of T^{-1}. Fitting the linear curve yields the activation energy E_A.

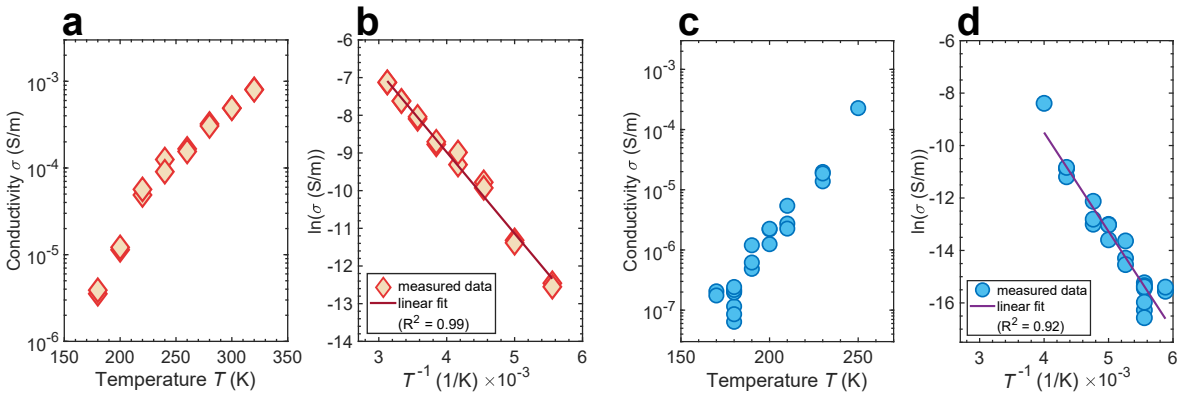

Figure S5.10: Temperature-dependent conductivity measurements of a Au_{32} NCL micro-crystal (a,b) and a spin-coated thin film (c,d). (**a**) Conductivity as a function of temperature of an individual micro-crystal with $L = 2.8$ µm, $W = 7.9 \pm 0.4$ µm and $h = 120$ nm. At every temperature step, several measurements were performed. This Figure corresponds to Figure 5.4d. (**b**) Arrhenius-plot of the data points shown in (a). The linear fit yields the activation energy $E_A \approx 0.2$ eV. The R^2 value of 0.99 indicates the goodness of the linear fitting. (**c**) Conductivity as a function of temperature of a thin film channel with $L = 2.5$ µm, $W = 1$ cm and $h = 30 \pm 2$ nm. At every temperature step, several measurements were performed. (**d**) Corresponding Arrhenius-plot of (c). The linear fit yields the activation energy $E_A \approx 0.33$ eV. The R^2 value of 0.92 indicates the goodness of the linear fitting. In the manuscript, we report the mean value of E_A for micro-crystals and thin films, including the standard deviation, based on the evaluation of 25 and 7 of such plots, respectively. This yields $E_A = 227 \pm 17$ meV for micro-crystals and $E_A = 366 \pm 62$ meV for the thin films.

Equations used for the investigation of electronic properties

The field-effect mobilities μ of individual micro-crystals or polycrystalline thin films are calculated using the gradual channel approximation, given in Equation (S5.2). The charge carrier concentration n is calculated using Equation (S5.3).

$$\mu = \frac{\partial I_{SD}}{\partial V_G} \cdot \frac{L}{W} \cdot \frac{t_{ox}}{\varepsilon_0 \varepsilon_r V_{SD}} \tag{S5.2}$$

$$n = \frac{\sigma}{e\mu} \tag{S5.3}$$

Being $\frac{\partial I_{SD}}{\partial V_G}$ the derivation of I_{SD} in FET transfer curves, V_{SD} the source-drain voltage, $\varepsilon_0\varepsilon_r$ and t_{ox} the permittivity and the thickness (230 nm for interdigitated electrodes, 200 nm for micro-crystal devices) of the dielectric SiO_x layer, respectively, and e the elementary charge.

Field-effect mobility of individual Au_{32} NCL micro-crystals

Figure S5.11 shows the distribution of the field-effect hole mobility $\mu(h^+)$ of individual micro-crystals.

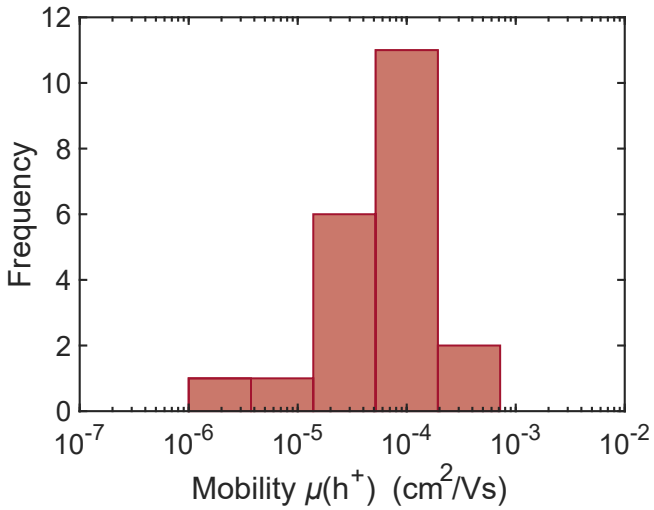

Figure S5.11: Distribution of the field-effect hole mobility $\mu(h^+)$ of 21 individual micro-crystals. All micro-crystals show p-type behavior. The mean value and standard deviation can be calculated to be $\mu(h^+) = 0.8 \times 10^{-4} \pm 0.58 \times 10^{-4}$ cm^2 V^{-1} s^{-1}. Values up to 2×10^{-4} cm^2 V^{-1} s^{-1} are observed.

A schematic drawing of the devices is given in Figure S5.12. The micro-crystals are deposited onto the electrodes with a thickness of ~ 10 nm. Accordingly, there is a gap between the micro-crystals and the dielectric of 0–10 nm. This is what we refer to as non-ideal channel geometry. In contrast, the spin-coated films form a relatively conformal layer within the channel, which leads to much better contact. Nonetheless, there is still an appreciable transconductance in the micro-crystals, which – after renormalization for the different channel geometry – is ~ 30 higher for the micro-crystals compared to the spincoated films. This further indicates the more efficient charge transport in highly ordered micro-crystals.

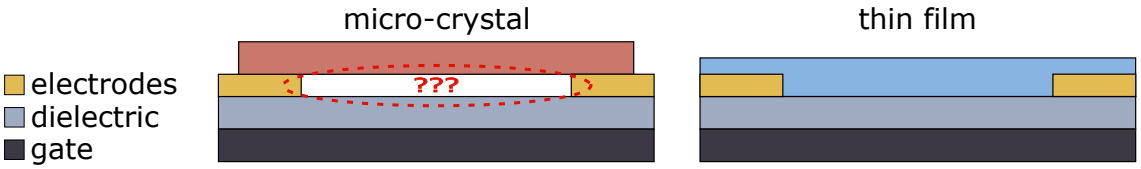

Figure S5.12: Schematic drawing of FET devices of a micro-crystal (left) and a thin film (right).

Details about the current normalization considering the different channel geometries:

$$\text{thin film:} \qquad I_{\text{film}}(-40\ V_{\text{G}}, 5\ V_{\text{SD}}) = 5.5 \times 10^{-8}\ \text{A} \tag{S5.4}$$

$$\text{micro-crystal:} \qquad I_{\text{crystal}}(-40\ V_{\text{G}}, 5\ V_{\text{SD}}) = 9.0 \times 10^{-9}\ \text{A} \tag{S5.5}$$

Normalized to geometry:

$$\text{thin film:} \qquad \frac{I_{\text{film}} \cdot L}{W \cdot h} = \frac{5.5 \times 10^{-8}\ \text{A} \cdot 2.5 \times 10^{-6}\ \text{m}}{0.01\ \text{m} \cdot 30 \times 10^{-9}\ \text{m}} \tag{S5.6}$$

$$= 4.58 \times 10^{-4}\ \text{A/m} \tag{S5.7}$$

$$\text{micro-crystal:} \qquad \frac{I_{\text{crystal}} \cdot L}{W \cdot h} = \frac{9.0 \times 10^{-9}\ \text{A} \cdot 1.5 \times 10^{-6}\ \text{m}}{10 \times 10^{-6}\ \text{m} \cdot 100 \times 10^{-9}\ \text{m}} \tag{S5.8}$$

$$= 1.35 \times 10^{-2}\ \text{A/m} \tag{S5.9}$$

Ratio:

$$\frac{1.35 \times 10^{-2}\ \text{A/m}}{4.58 \times 10^{-4}\ \text{A/m}} = 29.5 \tag{S5.10}$$

Evaluation of the contact resistance of Au_{32} NCL devices

To measure the contact resistance R_C of the Au_{32} NCL devices, we apply the Y-function method (YFM), which is a common technique for the evaluation of MOSFETs and OFETs.[342–344] Figure S5.13 illustrates the YFM technique to estimate the R_C of a FET device (exemplarily shown for a Au_{32} NCL thin film channel).

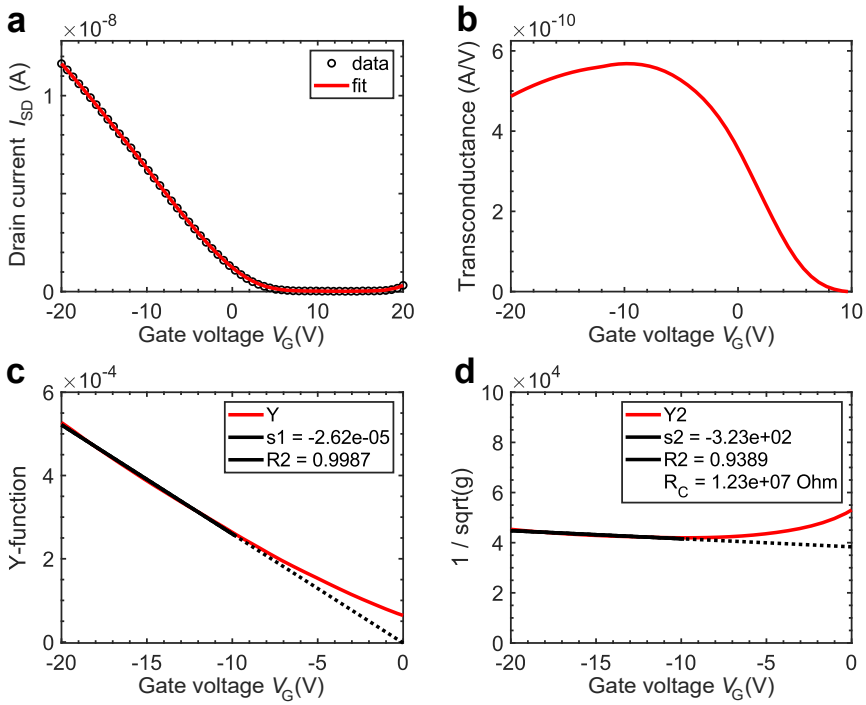

Figure S5.13: Y-function method (YFM) to estimate the contact resistance R_C of an individual FET device. (**a**) Transfer characteristic of a Au_{32} NCL thin film p-type FET at $V_{SD} = 1$ V ($L = 2.5$ µm, $W = 1$ cm). (**b**) Transconductance versus gate voltage V_G. (**c**) Y-function versus V_G. Fitting the linear regime yields the slope $s1$. (**d**) $\frac{1}{\sqrt{g}}$ versus V_G. Fitting the linear regime yields the slope $s2$. The R^2 values in (c) and (d) verify the goodness of the linear fit. R_C is calculated to 1.2×10^7 Ω. The total resistance of this device is 1.9×10^9 Ω.

From the transfer characteristic I_{SD} vs. V_G (Figure S5.13a) the transconductance g is determined as $g = \partial I_{SD}/\partial V_G$ (Figure S5.13b). The Y-function is defined in Equation (S5.11) as

$$Y = \frac{I_{SD}}{\sqrt{g}} \tag{S5.11}$$

and fitting Y as a function of V_G in the linear regime yields the slope $s1$ (Figure S5.13c). Next, the function $\frac{1}{\sqrt{g}}$ versus V_G is determined and linearly fitted to calculate the slope

s2 (Figure S5.13d). The contact resistance R_C is calculated using Equation (S5.12) as

$$R_C = V_{SD} \times \frac{s2}{s1} \quad . \tag{S5.12}$$

Using this method, we determine the contact resistance of thin films and micro-crystal channels as $R_{C,films} \approx 1\text{–}3 \times 10^7\ \Omega$ and $R_{C,crystals} \approx 2 \times 10^8\ \Omega$, respectively. In contrast, the total resistances are $R_{film} \approx 0.5\text{–}2 \times 10^9\ \Omega$ and $R_{crystals} \approx 2\text{–}20 \times 10^9\ \Omega$. Thus, the contact resistances are only $\sim 2\%$ and $\sim 1\text{–}10\%$ for thin film and micro-crystal devices, respectively. Hence, the Y-function method verifies the applicability of simple 2-point-probe measurements, as the effect of R_C is negligible.[342–344]

Calculation of the Coulomb charging energy E_C

The estimation of the Coulomb charging energy is performed as described below. The Coulomb charging energy E_C is given in Equation (S5.13).

$$E_C = \frac{e^2}{2C_\Sigma} \tag{S5.13}$$

Here, e is the elementary charge and C_Σ the total capacitance of the particle to its surrounding. The interparticle capacitance can be estimated using Equation (S5.14).[339,345]

$$C \approx 2\pi\varepsilon_0\varepsilon_r r \ln\left(\frac{r+d}{d}\right) \tag{S5.14}$$

Here, ε_0 is the vacuum permittivity, ε_r the dielectric constant of the surrounding medium ($\sim$ 2.0–2.5 for alkanes and phosphine), r is the NCL radius ($\sim$ 0.45 nm) and $2d$ the interparticle distance. Knowing that individual micro-crystals are oriented face-on to the surface, the in-plane Au core-core distance corresponds to the axis a_{uc} and b_{uc} with $\sim$ 1.9 nm. As the core size is 0.9 nm the interparticle distance is $2d \approx 1.0$ nm. As each NCL in the array has eight nearest neighbors, the total capacitance can be calculated to $C_\Sigma = 8C$. Accordingly, an estimation of charging energy yields $E_C \approx 276$ meV.

Details on the self-assembly process of Au_{32} NCL micro-crystals

Different parameters have been investigated to tune the morphology and amount of the micro-crystals. Using a larger quantity of particle solution leads to a higher amount of micro-crystals on the substrate (Figure S5.14). The same effect can be achieved by increasing the preparation time which allows more crystals to trickle through the subphase. Empirically, 45 min and a volume of 200 µl have shown best results in terms of crystal density along with reasonable preparation times. The influence of the chosen solvent is the following: Au_{32} NCL dispersions with hexane yield thicker micro-crystals (up to several hundreds of nanometers), whereas octane lead to the formation of thinner micro-crystals (thicknesses of 50–100 nm). For heptane, intermediate thicknesses can be achieved.

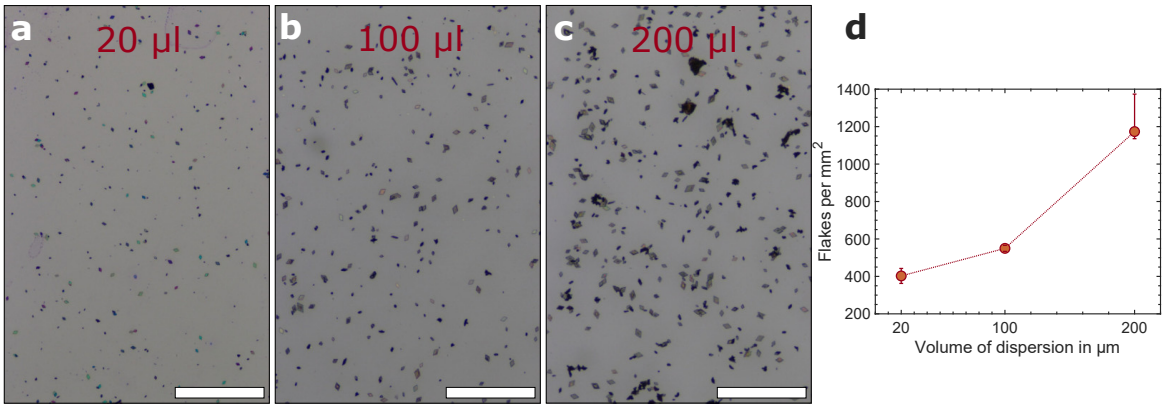

Figure S5.14: Effect of dispersion volume on self-assembly process. At a fixed dispersion solvent (heptane) and concentration (0.5 mM), the number of micro-crystals can be varied. Dispersion volumes of (**a**) 20 µl, (**b**) 100 µl and (**c**) 200 µl were used. (**d**) Number of micro-crystals per mm^2 as a function of dispersion volume. Scale bars correspond to 200 µm.

Mechanism of micro-crystal self-assembly

To investigate the place and process of the formation of the micro-crystals, a self-built interference reflection microscope was used. A Framos Lt 225 camera with 16 nm/px resolution was used along with a Nikon TIRF objective with oil immersion and a numerical aperture of NA = 1.52. The sample was illuminated by a Rebel High Power LED with a wavelength of 460 nm. A Teflon tube was sealed onto a glass cover slide, filled with acetone and placed onto the microscope. The microscope was focused just above the glass slide into the subphase. A Au_{32} NCL solution (0.5 mM, octane) was added onto the subphase to start the process of self-assembly. After the duration of

15 min, the sudden appearance of micro-crystals was observed. From this, we deduce that the process of crystallization does not take place at the substrate but at the liquid-air interface. From there, the micro-crystals start to sink down through the subphase as soon as they reach a critical mass. After reaching the glass slide/substrate, the micro-crystals are able to move laterally within the subphase along the bottom. Upon removal of the subphase, the micro-crystals are deposited onto the substrate.

6. Conclusion & outlook

This section provides a summary of the main findings of this thesis and concludes with an outlook for further research.

Experimentally addressing the question *"Does structural order have a significant effect on the (opto-)electronic properties of nanocrystal assemblies?"* posed in the introduction of this thesis requires suitable model systems and primarily devices where electronic transport and structural properties of the same NCR SL domains can be investigated.

Thus, at first, a high-throughput and easy-to-implement soft-lithography technique was developed to realize micrometer-sized channels of Cu4APc-functionalized PbS NCR SLs. This was achieved by combining the top-down processes of photolithography and anisotropic etching of silicon with the bottom-up processes of NCR self-assembly and ligand exchange at the liquid/air interface. By means of µCP, patterns of well-defined stripes of highly ordered PbS SLs with widths of ~ 4 µm were transferred onto orthogonally oriented electrodes with gaps of ~ 1 µm. Hence, most of the substrate area remains uncoated, which is key to obtain well-defined NCR SL microchannels. The created channels with lengths of ~ 1 µm and widths of ~ 4 µm approach the size of typical single-crystalline domains and thus enable conductivity and FET measurements of single grains. As a proof-of-concept, a comparison of these microchannels with conventional and commonly used large-scale channels revealed that charge transport is orders of magnitude more efficient within the microchannels developed in this thesis. This strongly points to a beneficial effect of the single-crystallinity on charge transport. This approach of microchannel fabrication via µCP is ideally suited, as it is not limited to PbS NCRs and could easily be implemented for other systems of interest by following the detailed step-by-step protocols provided. These results have been published in *Nanotechnology*, 31, 405302 (2020). Details are given in Chapter 3.

Secondly, after being able to determine the electronic properties of single-crystalline domains, a full structural investigation of those domains was required. This was realised by X-ray nano-diffraction measurements at DESY in collaboration with the group of Prof. Ivan A. Vartanyants. Therefore, by means of the developed

µCP approach, X-ray transparent Kapton devices containing SL microchannels of Cu4APc-functionalized PbS NCRs were established. Within pre-selected microchannels, for which the conductivity was determined, the SLs were scanned by a nanofocused X-ray beam of $\sim 400 \times 400$ nm^2 in transmission mode to simultaneously detect SAXS and WAXS signals. This enabled us to generate spatially resolved maps containing structural information of the SL and the atomic lattice of the NCRs within. By applying AXCCA, the structure of hundreds of PbS NCR SLs were resolved and correlated to their determined conductivities. This was the first time a full characterization of SL structures was done in parallel with conductivity measurements of the same domains. Thus, the influence of SL type, crystallinity, unit cell size and orientation was determined and the computational prediction of anisotropic charge transport was tested experimentally.

We identified two types of microchannels of either polycrystalline bcc SLs or monocrystalline rhcp SLs. Although the nearest-neighbor distance of the monocrystalline rhcp SLs is much larger, their conductivities can be as high as those of polycrystalline bcc SLs. This is considered to be an indication that the degree of crystallinity (poly vs. mono) compensates the effect of the much larger interparticle distance and thus has a significant effect on the conductivity.

Further, strong evidence of anisotropic charge transport within long-range ordered SLs was found. For monocrystalline rhcp SLs oriented with the $[0001]_{SL}$ direction normal to the substrate, the influence of the in-plane SL orientation with respect to the electric field direction on the conductivity was investigated. We observed a 40–50% higher conductivity for SLs where the nearest-neighbor direction is oriented parallel to the electric field, compared to otherwise identical SLs with an in-plane rotation. This parallel orientation results in the shortest hopping distance, while an in-plane offset leads to an increase of the effective hopping distance or a deviation from the direction of the electric field. This intrinsic property of anisotropic charge transport is attributed to the dominant effect of most efficient charge carrier hopping along the shortest interparticle distance and, thus, is assumed to be a general feature of weakly coupled NCR SLs. As a consequence, one could predict favored directions for charge transport within other SL types, such as simple cubic, fcc or bcc, being the $\langle 100 \rangle$, $\langle 110 \rangle$ or $\langle 111 \rangle$ SL directions, respectively. This is schematically illustrated for a bcc SL in Figure 6.1.

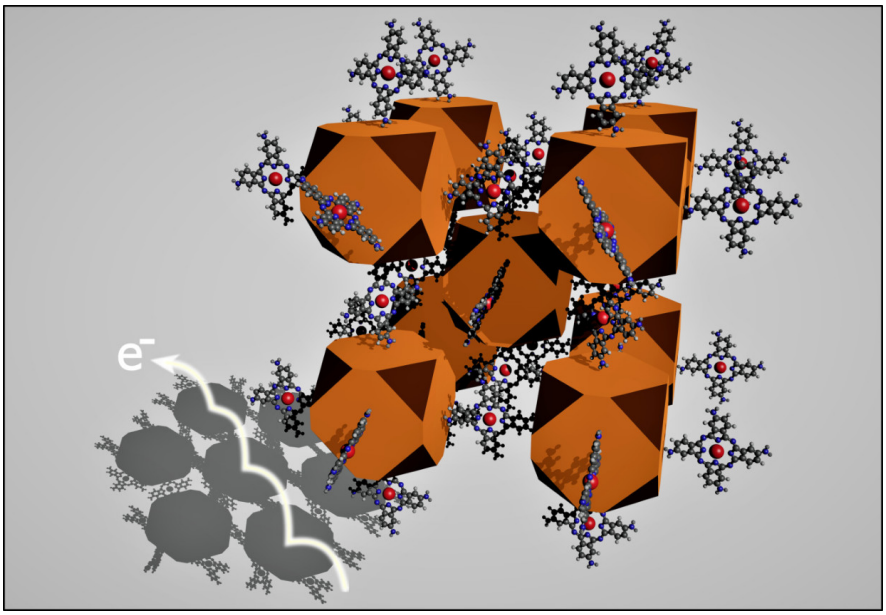

Figure 6.1: Schematic of the predicted anisotropic charge transport in a coupled bcc SL of Cu4APc-functionalized PbS NCRs. The precise arrangement of the NCRs in a highly ordered SL facilitates charge carrier transport (e^-) along a certain direction. For a bcc SL, the predicted direction is $\langle 111 \rangle$, caused by the shortest interparticle distance.

Moreover, caused by the mesocrystallinity of the rhcp SLs, the $[110]_{AL}$ directions of all NCRs are iso-oriented with the nearest-neighbor distance. Thus, the orientational order of the NCRs might be an additional source for the occurrence of a favored charge transport direction. The results of this chapter have been published in *Advanced Materials*, 32, 2002254 (2020). Details are given in Chapter 4.

Finally, $Au_{32}(^nBu_3P)_{12}Cl_8$ NCLs were utilized as another model system, differing from larger NCRs with an inherent size distribution by their atom-precise structural composition. A method was developed to self-assemble Au_{32} NCLs into SLs of the shape of idiomorphic micro-crystals with high crystallographic phase purity and a strongly preferred growth direction. Compared to glassy/polycrystalline ensembles, the identical but highly ordered Au_{32} NCLs in micro-crystals exhibit additional optical transitions, strongly pointing to an increased electronic coupling between adjacent NCLs. By depositing the micro-crystals onto electrode devices, the electronic properties of individual micro-crystals were investigated and semiconducting p-type behavior was found. Further, the predicted enhancement of electronic coupling was verified, as the conductivity and charge carrier mobility of micro-crystals exceed that of polycrystalline ensembles by

two orders of magnitude. This allowed quantifying the effect of solely structural disorder in NCL ensembles. Due to the eliminated energetic disorder of Au_{32} NCL ensembles, caused by the atomic and structural precision, the remaining disorder within the Au_{32} NCL ensembles is only of structural nature. In contrast, ensembles of larger NCRs with an inherent size distribution feature both structural disorder (due to structural defects) and energetic disorder (due to inhomogeneities of the NCLs), rendering it very difficult to distinguish those effects. Consequently, the highly enhanced charge transport within long-range ordered domains could be attributed to a vanishing degree of structural disorder, whereas the presence of only near-range order in glassy/polycrystalline domains is detrimental to the electronic coupling and charge transport. These results have been published in *Nature Communications*, 11, 6188 (2020). Details are given in Chapter 5.

To conclude, the findings for PbS NCRs and Au_{32} NCLs reported in this thesis strongly support the hypothesis of the advantageous effect of a high degree of crystallinity and long-range order on the electronic coupling and charge carrier transport within SLs. Hence, strong evidence is provided that structural order does indeed have a significant effect on the (opto-)electronic properties of NCR ensembles.

Accordingly, this thesis opens up further questions that should be investigated in future projects, for which the methodological approaches have been successfully demonstrated here. For example, other structure-transport-relationships in coupled NCR SLs should be explored, as this thesis strongly hints at additional effects determining the electronic properties. A comparison of different SL types, such as bcc and fcc, with similar nearest-neighbor distances could give further insight into the effect of electronic coupling along certain SL axes or the effect of packing density. Moreover, the degree of NCR alignment might also play a role for charge transport. In highly mesocrystalline SLs, the electronic coupling is expected to exceed that of a similar SL with randomly rotated NCRs. This assumption is based on a potential facet-specific electronic coupling for iso-oriented NCRs. A first hint was given in this thesis, since the direction of the preferential charge transport in PbS NCR SLs is co-linear to the $[110]_{AL}$ direction of the NCRs. Whether this NCR orientation influences the anisotropic charge transport or not requires further research.

Applying the concept of preferred carrier hopping along the nearest-neighbor direction in PbS NCR SLs to Au_{32} NCL micro-crystals, a significantly stronger anisotropic charge transport is to be expected. Charge transport might be highly favored along

the a_{uc} and b_{uc} axes ($\sim$ 1.9 nm) compared to the larger c_{uc} axis ($\sim$ 3.3 nm). The investigation of a possible charge transport anisotropy in Au_{32} NCL domains could be subject of future research to test the hypothesis that this effect is a general feature of weakly coupled NCL and NCR SLs.

Generally, the theoretically predicted formation of minibands in NCR SLs as a consequence of the long-range order has not yet been experimentally demonstrated, due to the weak degree of interparticle coupling of the materials reported in literature. Therefore, future studies must advance the realization of highly ordered NCR SLs with even stronger electronic coupling, in order to fully understand electronic coupling and charge transport of NCR ensembles and finally explore the potential plethora of structure-related NCR devices.

However, dedicated research towards a controlled assembly of NCRs is needed, which seems to be the bottleneck for further studies. In this context, atom-precise NCLs might arguably be more suitable than NCRs, as much more defined SLs can be realized. This has been demonstrated in this thesis, as the distribution of conductivity values of the well-defined Au_{32} NCLs micro-crystals is extremely narrow ($\sim$ 58% deviation), while conductivities in a wide range of three orders of magnitude were observed for PbS NCR SL domains. This is consistent with the higher degree of structural order present for the SLs of NCLs. Thus, another subject of future research should focus on the self-assembly of larger NCLs, accompanied with ligand exchange procedures to realize strongly coupled SLs.

As shown above, this thesis raises a number of exciting new questions, the foundation of which – namely the existence of structure-transport correlations in self-assembled NCR SLs – has been laid in this thesis. Thus, this work helps to understand the fundamental principles of structure-related charge transport properties of NCR ensembles and hopefully inspires others to strive for the understanding and application of those, which might one day lead to a promising future for advanced customizable and low-cost next-generation devices based on NCRs and NCLs.

List of abbreviations

ACN	Acetonitrile
AFM	Atomic force microscope
AL	Atomic lattice
Au_{32}	$Au_{32}(^nBu_3P)_{12}Cl_8$
AXCCA	Angular X-ray cross-correlation analysis
bcc	Body-centered cubic
BOE	Buffered oxide etch
BSE	Backscattered electrons
CB	Conduction band
CCF	Cross-correlation function
CHF_3	Fluoroform
Cu4APc	Cu-4,4',4",4"'-tetraaminophthalocyanine
DESY	Deutsches Elektronen-Synchrotron
F_{13}TCS	Tridecafluoro-(1,1,2,2)-tetrahydrooctyl-trichlorosilane
fcc	Face-centered cubic
FET	Field-effect transistor
FWHM	Full width half maximum
GINIX	Göttingen instrument for nano-imaging with X-rays
GISAXS	Grazing incidence small-angle X-ray scattering
hcp	Hexagonal closed-packed
HF	Hydrofluoric acid
HMDS	Hexamethyldisilazane
HOMO	Highest occupied molecular orbital
KOH	Potassium hydroxide
LED	Light emitting diode
LUMO	Lowest unoccupied molecular orbital
MOSFET	Metal-oxide-semiconductor field-effect transistor
NA	Numerical aperture
NCL	Nanocluster
NCR	Nanocrystal
NND	Nearest-neighbor distance

OA	Oleic acid
OFET	Organic field-effect transistor
PbS	Lead(II) sulfide
PDMS	Polydimethylsiloxane
PETRA III	Positron-Electron-Tandem-Ring-Accelerator III
PL	Photoluminescence
rhcp	Random hexagonal closed-packed
RIE	Reactive ion etching
SAXS	Small-angle X-ray scattering
SE	Secondary electrons
SEM	Scanning electron microscope
Si	Silicon
SiO_2, SiO_x	Silicon (di-)oxide
SL	Superlattice
UV	Ultraviolet
UV-Vis	Ultraviolet-visible
VB	Valence band
WAXS	Wide-angle X-ray scattering
XRD	X-ray diffraction
YFM	Y-function method
µCP	Microcontact printing

List of symbols

$1S_e$	Conductance band edge
$1S_h$	Valence band edge
a_{uc}, b_{uc}, c_{uc}	Unit cell vectors
A, B	Long and short micro-crystal axes
c	Concentration
C	Interparticle capacitance
C_Σ	Total capacitance of a particle
C_{CCF}	Cross-correlation function
d	Lattice plane spacing
$d_{c\text{-}c}$	Center-to-center distance
$Đ$	Dispersity
D, H, W	Distance, height and width of stamp features
e	Elementary charge
e^-	Electrons
E	Energy
E_A	Activation energy
E_C	Coulomb charging energy
E_{CB}	Energy of the conduction band edge
E_F	Energy of the Fermi level
E_{gap}	Band gap energy
E_i	Energy of the intrinsic Fermi level
E_{VB}	Energy of the valence band edge
g	Transconductance
G	Conductance
G_{geom}	Geometry-normalized conductance
h	height/thickness
$\hbar$	Reduced Planck constant
h^+	Holes
I	Current
I_{abs}	Intensity
I_G	Gate (leakage) current

I_{SD}	Source drain current
k_{B}	Boltzman constant
L	Length of channel
m^*	Charge carrier effective mass
n	Charge carrier concentration
q	Scattering vector
r	Radius
R_{C}	Contact resistance
$s1, s2$	Parameters of the Y-function method
t	Time
t_{ox}	Thickness of oxide
T	Temperature
V	Voltage
V_{G}	Gate Voltage
V_{SD}	Source drain voltage
W	Width of channel
x, y	Scanning directions
Y	Y-function
α	Azimuthal angle
$\alpha_{\mathrm{uc}}, \beta_{\mathrm{uc}}, \gamma_{\mathrm{uc}}$	Unit cell angles
β	Transfer integral
Γ	Tunneling rate
δ_{az}	Azimuthal peak width
δ_{rad}	Radial peak width
Δ	Angle between Bragg peaks
ΔE	Tunneling barrier heigth
ΔG	Change of Gibbs free energy
ΔH	Change of enthalpy
ΔS	Change of entropy
Δx	Tunneling barrier width
$\Delta\alpha$	Energetic disorder
$\Delta\Phi$	Orientational disorder
Δ_{A}	Sharp edge angle of micro-crystals
ε_0	Vacuum permittivity
ε_{r}	Dielectric constant
θ	Detector plane-Ewald sphere angle

θ_{B}	Bragg angle
λ	Wavelength
Λ	Reorganization energy
μ	Charge carrier mobility
ξ	Polaronic hopping rate
σ	Conductivity
φ	Azimuthal angle in AXCCA

List of figures

Bibliography

[1] Ro, C. (BBC). How the microchip powered pandemic life (2020, accessed 14th December 2020). URL https://www.bbc.com/future/bespoke/made-on-earth/how-the-microchip-powered-pandemic-life.html.

[2] Alivisatos, A. P. Semiconductor clusters, nanocrystals, and quantum dots. *Science* **271**, 933–937 (1996).

[3] Schmid, G. *et al.* Current and future applications of nanoclusters. *Chemical Society Reviews* **28**, 179–185 (1999).

[4] Kagan, C. R., Lifshitz, E., Sargent, E. H. & Talapin, D. V. Building devices from colloidal quantum dots. *Science* **353** (2016).

[5] Talapin, D. V. & Murray, C. B. PbSe nanocrystal solids for n- and p-channel thin film field-effect transistors. *Science* **310**, 86–89 (2005).

[6] Zarghami, M. H. *et al.* p-type PbSe and PbS quantum dot solids prepared with short-chain acids and diacids. *ACS Nano* **4**, 2475–2485 (2010).

[7] Nozik, A. J. *et al.* Semiconductor quantum dots and quantum dot arrays and applications of multiple exciton generation to third-generation photovoltaic solar cells. *Chemical Reviews* **110**, 6873–6890 (2010).

[8] Carey, G. H. *et al.* Colloidal quantum dot solar cells. *Chemical Reviews* **115**, 12732–12763 (2015).

[9] Caruge, J. M., Halpert, J. E., Wood, V., Bulović, V. & Bawendi, M. G. Colloidal quantum-dot light-emitting diodes with metal-oxide charge transport layers. *Nature Photonics* **2**, 247–250 (2008).

[10] Kim, T.-H. *et al.* Full-colour quantum dot displays fabricated by transfer printing. *Nature Photonics* **5**, 176–182 (2011).

[11] Lee, J.-S., Kovalenko, M. V., Huang, J., Chung, D. S. & Talapin, D. V. Band-like transport, high electron mobility and high photoconductivity in all-inorganic nanocrystal arrays. *Nature Nanotechnology* **6**, 348–352 (2011).

[12] Gao, J., Nguyen, S. C., Bronstein, N. D. & Alivisatos, A. P. Solution-processed, high-speed, and high-quantum-efficiency quantum dot infrared photodetectors. *ACS Photonics* **3**, 1217–1222 (2016).

[13] Harman, T. C., Taylor, P. J., Walsh, M. P. & LaForge, B. E. Quantum dot superlattice thermoelectric materials and devices. *Science* **297**, 2229–2232 (2002).

[14] Lu, W., Fang, J., Ding, Y. & Wang, Z. L. Formation of PbSe nanocrystals: A growth toward nanocubes. *The Journal of Physical Chemistry. B* **109**, 19219–19222 (2005).

[15] Moreels, I. *et al.* Composition and size-dependent extinction coefficient of colloidal PbSe quantum dots. *Chemistry of Materials* **19**, 6101–6106 (2007).

[16] Goesmann, H. & Feldmann, C. Nanoparticulate functional materials. *Angewandte Chemie (International ed. in English)* **49**, 1362–1395 (2010).

[17] Moreels, I. *et al.* Size-tunable, bright, and stable PbS quantum dots: A surface chemistry

study. *ACS Nano* **5**, 2004–2012 (2011).

[18] Kovalenko, M. V. *et al.* Prospects of nanoscience with nanocrystals. *ACS Nano* **9**, 1012–1057 (2015).

[19] Chakraborty, I. & Pradeep, T. Atomically precise clusters of noble metals: emerging link between atoms and nanoparticles. *Chemical Reviews* **117**, 8208–8271 (2017).

[20] Yang, J., Choi, M. K., Kim, D.-H. & Hyeon, T. Designed assembly and integration of colloidal nanocrystals for device applications. *Advanced Materials* **28**, 1176–1207 (2016).

[21] Ebina, A. *et al.* One-, two-, and three-dimensional self-assembly of atomically precise metal nanoclusters. *Nanomaterials* **10**, 1105 (2020).

[22] Pileni, M.-P. (ed.) *Nanocrystals Forming Mesoscopic Structures* (Wiley, 2005).

[23] Bishop, K. J. M., Wilmer, C. E., Soh, S. & Grzybowski, B. A. Nanoscale forces and their uses in self-assembly. *Small* **5**, 1600–1630 (2009).

[24] Murray, C. B., Kagan, C. R. & Bawendi, M. G. Self-organization of CdSe nanocrystallites into three-dimensional quantum dot superlattices. *Science* **270**, 1335–1338 (1995).

[25] Liu, Y. *et al.* Dependence of carrier mobility on nanocrystal size and ligand length in PbSe nanocrystal solids. *Nano Letters* **10**, 1960–1969 (2010).

[26] Collier, C. P., Vossmeyer, T. & Heath, J. R. Nanocrystal superlattices. *Annual Review of Physical Chemistry* **49**, 371–404 (1998).

[27] Hanrath, T. Colloidal nanocrystal quantum dot assemblies as artificial solids. *Journal of Vacuum Science & Technology A: Vacuum, Surfaces, and Films* **30**, 030802 (2012).

[28] Remacle, F. & Levine, R. D. Quantum dots as chemical building blocks: Elementary theoretical considerations. *ChemPhysChem* **2**, 20–36 (2001).

[29] Pileni, M.-P. Self-assembly of inorganic nanocrystals: Fabrication and collective intrinsic properties. *Accounts of Chemical Research* **40**, 685–693 (2007).

[30] Nie, Z., Petukhova, A. & Kumacheva, E. Properties and emerging applications of self-assembled structures made from inorganic nanoparticles. *Nat. Nanotechnol.* **5**, 15–25 (2010).

[31] Weidman, M. C., Yager, K. G. & Tisdale, W. A. Interparticle spacing and structural ordering in superlattice PbS nanocrystal solids undergoing ligand exchange. *Chemistry of Materials* **27**, 474–482 (2015).

[32] Geuchies, J. J. *et al.* In situ study of the formation mechanism of two-dimensional superlattices from PbSe nanocrystals. *Nature Materials* **15**, 1248–1254 (2016).

[33] Santra, P. K., Palmstrom, A. F., Tassone, C. J. & Bent, S. F. Molecular ligands control superlattice structure and crystallite orientation in colloidal quantum dot solids. *Chemistry of Materials* **28**, 7072–7081 (2016).

[34] Novák, J. *et al.* Site-specific ligand interactions favor the tetragonal distortion of PbS nanocrystal superlattices. *ACS Applied Materials & Interfaces* **8**, 22526–22533 (2016).

[35] Whitham, K., Smilgies, D.-M. & Hanrath, T. Entropic, enthalpic, and kinetic aspects of interfacial nanocrystal superlattice assembly and attachment. *Chemistry of Materials* **30**, 54–63 (2018).

[36] Zaluzhnyy, I. A. *et al.* Quantifying angular correlations between the atomic lattice and the superlattice of nanocrystals assembled with directional linking. *Nano Letters* **17**, 3511–3517 (2017).

[37] Mukharamova, N. *et al.* Revealing grain boundaries and defect formation in nanocrystal superlattices by nanodiffraction. *Small* **15**, e1904954 (2019).

[38] Wuelfing, W. P., Green, S. J., Pietron, J. J., Cliffel, D. E. & Murray, R. W. Electronic conductivity of solid-state, mixed-valent, monolayer-protected Au clusters. *Journal of the American Chemical Society* **122**, 11465–11472 (2000).

[39] Koh, W.-K., Saudari, S. R., Fafarman, A. T., Kagan, C. R. & Murray, C. B. Thiocyanate-capped PbS nanocubes: Ambipolar transport enables quantum dot based circuits on a flexible substrate. *Nano Letters* **11**, 4764–4767 (2011).

[40] Oh, S. J. *et al.* Stoichiometric control of lead chalcogenide nanocrystal solids to enhance their electronic and optoelectronic device performance. *ACS Nano* **7**, 2413–2421 (2013).

[41] Scheele, M. *et al.* Nonmonotonic size dependence in the hole mobility of methoxide-stabilized PbSe quantum dot solids. *ACS Nano* **7**, 6774–6781 (2013).

[42] Balazs, D. M. *et al.* Electron mobility of 24 cm^2 V^{-1} s^{-1} in PbSe colloidal-quantum-dot superlattices. *Advanced Materials* **30**, 1–9 (2018).

[43] Lazarenkova, O. L. & Balandin, A. A. Miniband formation in a quantum dot crystal. *Journal of Applied Physics* **89**, 5509–5515 (2001).

[44] Liljeroth, P. *et al.* Variable orbital coupling in a two-dimensional quantum-dot solid probed on a local scale. *Physical Review Letters* **97**, 1–4 (2006).

[45] Guyot-Sionnest, P. Electrical transport in colloidal quantum dot films. *The Journal of Physical Chemistry Letters* **3**, 1169–1175 (2012).

[46] Kaushik, A. P., Lukose, B. & Clancy, P. The role of shape on electronic structure and charge transport in faceted PbSe nanocrystals. *ACS Nano* **8**, 2302–2317 (2014).

[47] Yang, J. & Wise, F. W. Effects of disorder on electronic properties of nanocrystal assemblies. *The Journal of Physical Chemistry C* **119**, 3338–3347 (2015).

[48] Yazdani, N. *et al.* Charge transport in semiconductors assembled from nanocrystal quantum dots. *Nature Communications* **11**, 2852 (2020).

[49] Nair, A. S. & Kimura, K. Temperature dependence on the charge transport behaviour of 3-D superlattice crystals of mercaptosuccinic acid-protected gold nanoparticles. *Physical Chemistry Chemical Physics* **11**, 9346–9350 (2009).

[50] Tan, C.-S. *et al.* Facet-dependent electrical conductivity properties of PbS nanocrystals. *Chemistry of Materials* **28**, 1574–1580 (2016).

[51] Sainato, M. *et al.* Long-range order in nanocrystal assemblies determines charge transport of films. *ACS Omega* **2**, 3681–3690 (2017).

[52] Chen, W. *et al.* Structure and charge carrier dynamics in colloidal PbS quantum dot solids. *The Journal of Physical Chemistry Letters* **10**, 2058–2065 (2019).

[53] Evers, W. H. *et al.* High charge mobility in two-dimensional percolative networks of PbSe quantum dots connected by atomic bonds. *Nature Communications* **6**, 1–8 (2015).

[54] Tang, J. & Sargent, E. H. Infrared colloidal quantum dots for photovoltaics: Fundamentals and recent progress. *Advanced Materials* **23**, 12–29 (2011).

[55] Weidman, M. C., Beck, M. E., Hoffman, R. S., Prins, F. & Tisdale, W. A. Monodisperse, air-stable PbS nanocrystals via precursor stoichiometry control. *ACS Nano* **8**, 6363–6371 (2014).

[56] Zherebetskyy, D. *et al.* Hydroxylation of the surface of PbS nanocrystals passivated

with oleic acid. *Science* **344**, 1380–1384 (2014).

[57] Scheele, M. *et al.* PbS nanoparticles capped with tetrathiafulvalenetetracarboxylate: Utilizing energy level alignment for efficient carrier transport. *ACS Nano* **8**, 2532–2540 (2014).

[58] Scheele, M., Brütting, W. & Schreiber, F. Coupled organic-inorganic nanostructures (COIN). *Physical Chemistry Chemical Physics* **17**, 97–111 (2015).

[59] André, A. *et al.* Toward conductive mesocrystalline assemblies: PbS nanocrystals cross-linked with tetrathiafulvalene dicarboxylate. *Chemistry of Materials* **27**, 8105–8115 (2015).

[60] Maiti, S. *et al.* Understanding the formation of conductive mesocrystalline superlattices with cubic PbS nanocrystals at the liquid/air interface. *The Journal of Physical Chemistry C* **123**, 1519–1526 (2019).

[61] Scheele, M. For what it's worth: Long-range order and orientation in nanocrystal superlattices. *Bunsen-Magazin* **3**, 57–61 (2020).

[62] Schmid, G. Nanoclusters – building blocks for future nanoelectronic devices? *Advanced Engineering Materials* **3**, 737–743 (2001).

[63] Schmid, G. The relevance of shape and size of Au_{55} clusters. *Chemical Society Reviews* **37**, 1909–1930 (2008).

[64] Li, Q. *et al.* Modulating the hierarchical fibrous assembly of Au nanoparticles with atomic precision. *Nature Communications* **9**, 3871 (2018).

[65] Galchenko, M., Black, A., Heymann, L. & Klinke, C. Field effect and photoconduction in Au_{25} nanoclusters films. *Advanced Materials* **31**, e1900684 (2019).

[66] Yuan, P. *et al.* Solvent-mediated assembly of atom-precise gold-silver nanoclusters to semiconducting one-dimensional materials. *Nature Communications* **11**, 2229 (2020).

[67] Talapin, D. V., Lee, J.-S., Kovalenko, M. V. & Shevchenko, E. V. Prospects of colloidal nanocrystals for electronic and optoelectronic applications. *Chemical Reviews* **110**, 389–458 (2010).

[68] O'Brien, M. N., Jones, M. R. & Mirkin, C. A. The nature and implications of uniformity in the hierarchical organization of nanomaterials. *Proceedings of the National Academy of Sciences of the United States of America* **113**, 11717–11725 (2016).

[69] Kagan, C. R. & Murray, C. B. Charge transport in strongly coupled quantum dot solids. *Nature Nanotechnology* **10**, 1013–1026 (2015).

[70] Boles, M. A., Ling, D., Hyeon, T. & Talapin, D. V. The surface science of nanocrystals. *Nature Materials* **15**, 141–153 (2016).

[71] Boles, M. A., Engel, M. & Talapin, D. V. Self-assembly of colloidal nanocrystals: From intricate structures to functional materials. *Chemical Reviews* **116**, 11220–11289 (2016).

[72] Murray, C. B., Kagan, C. R. & Bawendi, M. G. Synthesis and characterization of monodisperse nanocrystals and close-packed nanocrystal assemblies. *Annual Review of Materials Science* **30**, 545–610 (2000).

[73] Kittel, C. *Einführung in die Festkörperphysik* (Oldenbourg, München, 2006), 14th edn.

[74] Wise, F. W. Lead salt quantum dots: The limit of strong quantum confinement. *Accounts of Chemical Research* **33**, 773–780 (2000).

[75] Brown, P. R. *et al.* Energy level modification in lead sulfide quantum dot thin films

through ligand exchange. *ACS Nano* **8**, 5863–5872 (2014).

[76] Moreels, I. *et al.* Size-dependent optical properties of colloidal PbS quantum dots. *ACS Nano* **3**, 3023–3030 (2009).

[77] Bealing, C. R., Baumgardner, W. J., Choi, J. J., Hanrath, T. & Hennig, R. G. Predicting nanocrystal shape through consideration of surface-ligand interactions. *ACS Nano* **6**, 2118–2127 (2012).

[78] Bertolotti, F. *et al.* Crystal symmetry breaking and vacancies in colloidal lead chalcogenide quantum dots. *Nature Materials* **15**, 987–994 (2016).

[79] Fang, C., van Huis, M. A., Vanmaekelbergh, D. & Zandbergen, H. W. Energetics of polar and nonpolar facets of PbSe nanocrystals from theory and experiment. *ACS Nano* **4**, 211–218 (2010).

[80] Chen, O. *et al.* Compact high-quality CdSe–CdS core–shell nanocrystals with narrow emission linewidths and suppressed blinking. *Nature Materials* **12**, 445–451 (2013).

[81] Weidman, M. C., Nguyen, Q., Smilgies, D.-M. & Tisdale, W. A. Impact of size dispersity, ligand coverage, and ligand length on the structure of PbS nanocrystal superlattices. *Chemistry of Materials* **30**, 807–816 (2018).

[82] Jin, R. Atomically precise metal nanoclusters: stable sizes and optical properties. *Nanoscale* **7**, 1549–1565 (2015).

[83] Jin, R. Quantum sized, thiolate-protected gold nanoclusters. *Nanoscale* **2**, 343–362 (2010).

[84] Zheng, J., Nicovich, P. R. & Dickson, R. M. Highly fluorescent noble-metal quantum dots. *Annual Review of Physical Chemistry* **58**, 409–431 (2007).

[85] Zhou, M. *et al.* Evolution from the plasmon to exciton state in ligand-protected atomically precise gold nanoparticles. *Nature Communications* **7**, 13240 (2016).

[86] Jin, R., Zeng, C., Zhou, M. & Chen, Y. Atomically precise colloidal metal nanoclusters and nanoparticles: Fundamentals and opportunities. *Chemical Reviews* **116**, 10346–10413 (2016).

[87] Schmid, G., Pfeil, R., Boese, R., Bandermann, F., Meyer, S., Calis, G. H., & van der Velden, J. W. $Au_{55}[P(C_6H_5)_3]_{12}Cl_6$ - ein Goldcluster ungewöhnlicher Größe. *Chemische Berichte* **114**, 3634–3642 (1981).

[88] Zhu, M., Aikens, C. M., Hollander, F. J., Schatz, G. C. & Jin, R. Correlating the crystal structure of a thiol-protected Au_{25} cluster and optical properties. *Journal of the American Chemical Society* **130**, 5883–5885 (2008).

[89] Shibu, E. S., Muhammed, M. A. H., Tsukuda, T. & Pradeep, T. Ligand exchange of $Au_{25}SG_{18}$ leading to functionalized gold clusters: spectroscopy, kinetics, and luminescence. *The Journal of Physical Chemistry C* **112**, 12168–12176 (2008).

[90] Tofanelli, M. A. *et al.* Jahn-teller effects in $Au_{25}(SR)_{18}$. *Chemical Science* **7**, 1882–1890 (2016).

[91] McKenzie, L. C., Zaikova, T. O. & Hutchison, J. E. Structurally similar triphenylphosphine-stabilized undecagolds, $Au_{11}(PPh_3)_7Cl_3$ and $Au_{11}(PPh_3)_8Cl_2Cl$, exhibit distinct ligand exchange pathways with glutathione. *Journal of the American Chemical Society* **136**, 13426–13435 (2014).

[92] Kenzler, S., Schrenk, C. & Schnepf, A. $Au_{108}S_{24}(PPh_3)_{16}$: A highly symmetric nanoscale

gold cluster confirms the general concept of metalloid clusters. *Angewandte Chemie International Edition* **56**, 393–396 (2017).

[93] Zhou, M. *et al.* On the non-metallicity of 2.2 nm $Au_{246}(SR)_{80}$ nanoclusters. *Angewandte Chemie* **129**, 16475–16479 (2017).

[94] Sakthivel, N. A., Theivendran, S., Ganeshraj, V., Oliver, A. G. & Dass, A. Crystal structure of Faradaurate-279: $Au_{279}(SPh{-}t Bu)_{84}$ plasmonic nanocrystal molecules. *Journal of the American Chemical Society* **139**, 15450–15459 (2017).

[95] Knight, W. *et al.* Electronic shell structure and abundances of sodium clusters. *Physical Review Letters* **52**, 2141–2143 (1984).

[96] Claridge, S. A. *et al.* Cluster-assembled materials. *ACS Nano* **3**, 244–255 (2009).

[97] Yan, J. *et al.* Co-crystallization of atomically precise metal nanoparticles driven by magic atomic and electronic shells. *Nature Communications* **9**, 3357 (2018).

[98] Purath, A., Köppe, R. & Schnöckel, H. $[Al_7\{N(SiMe_3)_2\}_6]^-$: A first step towards aluminum metal formation by disproportionation. *Angewandte Chemie International Edition* **38**, 2926–2928 (1999).

[99] Schnepf, A. & Schnöckel, H. Metalloid aluminum and gallium clusters: Element modifications on the molecular scale? *Angewandte Chemie International Edition* **41**, 3532–3554 (2002).

[100] Kenzler, S. *et al.* Synthesis and characterization of three multi-shell metalloid gold clusters $Au_{32}(R_3P)_{12}Cl_8$. *Angewandte Chemie International Edition* **58**, 5902–5905 (2019).

[101] LaMer, V. K. & Dinegar, R. H. Theory, production and mechanism of formation of monodispersed hydrosols. *Journal of the American Chemical Society* **72**, 4847–4854 (1950).

[102] Brust, M., Walker, M., Bethell, D., Schiffrin, D. J. & Whyman, R. Synthesis of thiol-derivatised gold nanoparticles in a two-phase liquid–liquid system. *Journal of the Chemical Society, Chemical Communications* **0**, 801–802 (1994).

[103] Vanmaekelbergh, D. Self-assembly of colloidal nanocrystals as route to novel classes of nanostructured materials. *Nano Today* **6**, 419–437 (2011).

[104] Vogel, N., Retsch, M., Fustin, C.-A., del Campo, A. & Jonas, U. Advances in colloidal assembly: The design of structure and hierarchy in two and three dimensions. *Chemical Reviews* **115**, 6265–6311 (2015).

[105] Whitesides, G. M. & Grzybowski, B. Self-assembly at all scales. *Science* **295**, 2418–2421 (2002).

[106] Min, Y., Akbulut, M., Kristiansen, K., Golan, Y. & Israelachvili, J. The role of interparticle and external forces in nanoparticle assembly. *Nature Materials* **7**, 527–538 (2008).

[107] Bresme, F. & Oettel, M. Nanoparticles at fluid interfaces. *Journal of Physics: Condensed Matter* **19**, 413101 (2007).

[108] Zhang, R. *et al.* Direct imaging of short-range order and its impact on deformation in Ti-6Al (2019).

[109] Cowley, J. M. Short-range order and long-range order parameters. *Physical Review* **138**, A1384–A1389 (1965).

[110] Cölfen, H. & Antonietti, M. Mesocrystals: Inorganic superstructures made by highly parallel crystallization and controlled alignment. *Angewandte Chemie International Edition* **44**, 5576–5591 (2005).

[111] McCray, A. R. C., Savitzky, B. H., Whitham, K., Hanrath, T. & Kourkoutis, L. F. Orientational disorder in epitaxially connected quantum dot solids. *ACS Nano* (2019).

[112] Kinge, S., Crego-Calama, M. & Reinhoudt, D. N. Self-assembling nanoparticles at surfaces and interfaces. *ChemPhysChem* **9**, 20–42 (2008).

[113] Luther, J. M. *et al.* Structural, optical, and electrical properties of self-assembled films of PbSe nanocrystals treated with 1,2-ethanedithiol. *ACS Nano* **2**, 271–280 (2008).

[114] Dong, A., Chen, J., Vora, P. M., Kikkawa, J. M. & Murray, C. B. Binary nanocrystal superlattice membranes self-assembled at the liquid-air interface. *Nature* **466**, 474–477 (2010).

[115] Dong, A. *et al.* Multiscale periodic assembly of striped nanocrystal superlattice films on a liquid surface. *Nano Letters* **11**, 841–846 (2011).

[116] Choi, J. J., Bian, K., Baumgardner, W. J., Smilgies, D.-M. & Hanrath, T. Interface-induced nucleation, orientational alignment and symmetry transformations in nanocube superlattices. *Nano Letters* **12**, 4791–4798 (2012).

[117] Evers, W. H. *et al.* Low-dimensional semiconductor superlattices formed by geometric control over nanocrystal attachment. *Nano Letters* **13**, 2317–2323 (2013).

[118] Balazs, D. M., Dunbar, T. A., Smilgies, D.-M. & Hanrath, T. Coupled dynamics of colloidal nanoparticle spreading and self-assembly at a fluid-fluid interface. *Langmuir* **36**, 6106–6115 (2020).

[119] Dong, A., Jiao, Y. & Milliron, D. J. Electronically coupled nanocrystal superlattice films by in situ ligand exchange at the liquid-air interface. *ACS Nano* **7**, 10978–10984 (2013).

[120] Aleksandrovic, V. *et al.* Preparation and electrical properties of cobalt-platinum nanoparticle monolayers deposited by the langmuir-blodgett technique. *ACS Nano* **2**, 1123–1130 (2008).

[121] Liao, J. *et al.* Ordered nanoparticle arrays interconnected by molecular linkers: Electronic and optoelectronic properties. *Chemical Society Reviews* **44**, 999–1014 (2015).

[122] McPhail, M. R., Campbell, G. P., Bedzyk, M. J. & Weiss, E. A. Structural features of PbS nanocube monolayers upon treatment with mono- and dicarboxylic acids and thiols at a liquid-air interface. *Langmuir* **32**, 6666–6673 (2016).

[123] André, A. *et al.* Structure, transport and photoconductance of PbS quantum dot monolayers functionalized with a copper phthalocyanine derivative. *Chemical Communications* **53**, 1700–1703 (2017).

[124] Samadi Khoshkhoo, M., Maiti, S., Schreiber, F., Chassé, T. & Scheele, M. Surface functionalization with copper tetraaminophthalocyanine enables efficient charge transport in indium tin oxide nanocrystal thin films. *ACS Applied Materials & Interfaces* **9**, 14197–14206 (2017).

[125] Maiti, S. *et al.* Electronically coupled, two-dimensional assembly of $Cu_{1.1}S$ nanodiscs for selective vapor sensing applications. *The Journal of Physical Chemistry C* **122**, 23720–23727 (2018).

[126] Maiti, S. *et al.* Monitoring self-assembly and ligand exchange of PbS nanocrystal superlattices at the liquid/air interface in real time. *The Journal of Physical Chemistry Letters* **9**, 739–744 (2018).

[127] Shevchenko, E. V., Talapin, D. V., Kotov, N. A., O'Brien, S. & Murray, C. B. Structural diversity in binary nanoparticle superlattices. *Nature* **439**, 55–59 (2006).

[128] Rainò, G. *et al.* Superfluorescence from lead halide perovskite quantum dot superlattices. *Nature* **563**, 671–675 (2018).

[129] Wu, Z., Yao, Q., Zang, S. & Xie, J. Directed self-assembly of ultrasmall metal nanoclusters. *ACS Materials Letters* **1**, 237–248 (2019).

[130] Bian, K. *et al.* Shape-anisotropy driven symmetry transformations in nanocrystal superlattice polymorphs. *ACS Nano* **5**, 2815–2823 (2011).

[131] Mayence, A., Wang, D., Salazar-Alvarez, G., Oleynikov, P. & Bergström, L. Probing planar defects in nanoparticle superlattices by 3D small-angle electron diffraction tomography and real space imaging. *Nanoscale* **6**, 13803–13808 (2014).

[132] Yu, Y. *et al.* Orientationally ordered silicon nanocrystal cuboctahedra in superlattices. *Nano Letters* **16**, 7814–7821 (2016).

[133] Huang, X. *et al.* Understanding Fe_3O_4 nanocube assembly with reconstruction of a consistent superlattice phase diagram. *Journal of the American Chemical Society* (2019).

[134] Lokteva, I., Koof, M., Walther, M., Grübel, G. & Lehmkühler, F. Monitoring nanocrystal self-assembly in real time using in situ small-angle X-ray scattering. *Small* **15**, 1–8 (2019).

[135] Lokteva, I., Koof, M., Walther, M., Grübel, G. & Lehmkühler, F. Coexistence of hcp and bct phases during in situ superlattice assembly from faceted colloidal nanocrystals. *The Journal of Physical Chemistry Letters* **10**, 6331–6338 (2019).

[136] Choi, J. J. *et al.* Controlling nanocrystal superlattice symmetry and shape-anisotropic interactions through variable ligand surface coverage. *Journal of the American Chemical Society* **133**, 3131–3138 (2011).

[137] Quan, Z. *et al.* Tilted face-centered-cubic supercrystals of PbS nanocubes. *Nano Letters* **12**, 4409–4413 (2012).

[138] Wang, Z. *et al.* Correlating superlattice polymorphs to internanoparticle distance, packing density, and surface lattice in assemblies of PbS nanoparticles. *Nano Letters* **13**, 1303–1311 (2013).

[139] Kaushik, A. P. & Clancy, P. Solvent-driven symmetry of self-assembled nanocrystal superlattices–a computational study. *Journal of Computational Chemistry* **34**, 523–532 (2013).

[140] Goodfellow, B. W., Yu, Y., Bosoy, C. A., Smilgies, D.-M. & Korgel, B. A. The role of ligand packing frustration in body-centered cubic (bcc) superlattices of colloidal nanocrystals. *The Journal of Physical Chemistry Letters* **6**, 2406–2412 (2015).

[141] Weidman, M. C., Smilgies, D.-M. & Tisdale, W. A. Kinetics of the self-assembly of nanocrystal superlattices measured by real-time in situ X-ray scattering. *Nature Materials* **15**, 775–781 (2016).

[142] Fan, Z. & Grünwald, M. Orientational order in self-assembled nanocrystal superlattices. *Journal of the American Chemical Society* **141**, 1980–1988 (2019).

[143] Winslow, S. W., Swan, J. W. & Tisdale, W. A. The importance of unbound ligand in nanocrystal superlattice formation. *Journal of the American Chemical Society* **142**, 9675–9685 (2020).

[144] Winslow, S. W., Smilgies, D.-M., Swan, J. W. & Tisdale, W. A. Reversible temperature-induced structural transformations in PbS nanocrystal superlattices. *The Journal of Physical Chemistry C* **124**, 13456–13466 (2020).

[145] Bian, K., Wang, Z. & Hanrath, T. Comparing the structural stability of PbS nanocrystals assembled in fcc and bcc superlattice allotropes. *Journal of the American Chemical Society* **134**, 10787–10790 (2012).

[146] Nagaoka, Y., Chen, O., Wang, Z. & Cao, Y. C. Structural control of nanocrystal superlattices using organic guest molecules. *Journal of the American Chemical Society* **134**, 2868–2871 (2012).

[147] Wang, Z., Bian, K., Nagaoka, Y., Fan, H. & Cao, Y. C. Regulating multiple variables to understand the nucleation and growth and transformation of PbS nanocrystal superlattices. *Journal of the American Chemical Society* **139**, 14476–14482 (2017).

[148] Ziherl, P. & Kamien, R. D. Maximizing entropy by minimizing area: Towards a new principle of self-organization. *The Journal of Physical Chemistry B* **105**, 10147–10158 (2001).

[149] Zhang, Y. & Gang, O. Nanocrystal superlattices: The pathway to atomic alignment. *Nature Materials* **15**, 1225–1226 (2016).

[150] Boles, M. A. & Talapin, D. V. Binary assembly of PbS and Au nanocrystals: Patchy PbS surface ligand coverage stabilizes the CuAu superlattice. *ACS Nano* **13**, 5375–5384 (2019).

[151] Bahrig, L., Hickey, S. G. & Eychmüller, A. Mesocrystalline materials and the involvement of oriented attachment – a review. *CrystEngComm* **16**, 9408–9424 (2014).

[152] Simon, P. *et al.* Interconnection of nanoparticles within 2D superlattices of PbS/oleic acid thin films. *Advanced Materials* **26**, 3042–3049 (2014).

[153] Redl, F. X., Cho, K.-S., Murray, C. B. & O'Brien, S. Three-dimensional binary superlattices of magnetic nanocrystals and semiconductor quantum dots. *Nature* **423**, 968–971 (2003).

[154] Talapin, D. V. *et al.* Quasicrystalline order in self-assembled binary nanoparticle superlattices. *Nature* **461**, 964–967 (2009).

[155] Paik, T. *et al.* Hierarchical materials design by pattern transfer printing of self-assembled binary nanocrystal superlattices. *Nano Letters* **17**, 1387–1394 (2017).

[156] Bigioni, T. P. *et al.* Kinetically driven self assembly of highly ordered nanoparticle monolayers. *Nature Materials* **5**, 265–270 (2006).

[157] van der Stam, W. *et al.* Oleic acid-induced atomic alignment of ZnS polyhedral nanocrystals. *Nano Letters* **16**, 2608–2614 (2016).

[158] Momper, R. *et al.* Kinetic control over self-assembly of semiconductor nanoplatelets. *Nano Letters* (2020).

[159] Baumgardner, W. J., Whitham, K. & Hanrath, T. Confined-but-connected quantum solids via controlled ligand displacement. *Nano Letters* **13**, 3225–3231 (2013).

[160] Boneschanscher, M. P. *et al.* Long-range orientation and atomic attachment of nanocrys-

tals in 2D honeycomb superlattices. *Science* **344**, 1377–1380 (2014).

[161] Savitzky, B. H. *et al.* Propagation of structural disorder in epitaxially connected quantum dot solids from atomic to micron scale. *Nano Letters* **16**, 5714–5718 (2016).

[162] van Overbeek, C. *et al.* Interfacial self-assembly and oriented attachment in the family of PbX (X = S, Se, Te) nanocrystals. *The Journal of Physical Chemistry C* **122**, 12464–12473 (2018).

[163] Cui, J. *et al.* Colloidal quantum dot molecules manifesting quantum coupling at room temperature. *Nature Communications* **10**, 5401 (2019).

[164] Pinkard, A., Champsaur, A. M. & Roy, X. Molecular clusters: Nanoscale building blocks for solid-state materials. *Accounts of Chemical Research* **51**, 919–929 (2018).

[165] Castleman, A. W. & Khanna, S. N. Clusters, superatoms, and building blocks of new materials. *The Journal of Physical Chemistry C* **113**, 2664–2675 (2009).

[166] Talapin, D. V. *et al.* A new approach to crystallization of CdSe nanoparticles into ordered three-dimensional superlattices. *Advanced Materials* **13**, 1868 (2001).

[167] Zeng, C., Chen, Y., Kirschbaum, K., Lambright, K. J. & Jin, R. Emergence of hierarchical structural complexities in nanoparticles and their assembly. *Science* **354**, 1580–1584 (2016).

[168] Schmid, G., Pugin, R., Sawitowski, T., Simon, U. & Marler, B. Transmission electron microscopic and small angle X-ray diffraction investigations of $Au_{55}(PPh_3)_{12}Cl_6$ microcrystals. *Chemical Communications* 1303–1304 (1999).

[169] Schmid, G., Bäumle, M. & Beyer, N. Ordered two-dimensional monolayers of Au_{55} clusters. *Angewandte Chemie International Edition* **39**, 181–183 (2000).

[170] Schmid, G. *et al.* Naked Au_{55} clusters: Dramatic effect of a thiol-terminated dendrimer. *Chemistry – A European Journal* **6**, 1693–1697 (2000).

[171] Li, Y. & Jin, R. Seeing ligands on nanoclusters and in their assemblies by X-ray crystallography: Atomically precise nanochemistry and beyond. *Journal of the American Chemical Society* **142**, 13627–13644 (2020).

[172] Lee, G. S. H. *et al.* $[S_4Cd_{17}(SPh)_{28}]^{2-}$, the first member of a third series of tetrahedral $[S_wM_x(SR)y]^{z-}$ clusters. *Journal of the American Chemical Society* **110**, 4863–4864 (1988).

[173] Hagel, J. *et al.* Superconductivity of a crystalline Ga_{84}-cluster compound. *Journal of Low Temperature Physics* **129**, 133–142 (2002).

[174] Beverly, K. C. *et al.* Quantum dot artificial solids: understanding the static and dynamic role of size and packing disorder. *Proceedings of the National Academy of Sciences of the United States of America* **99**, 6456–6459 (2002).

[175] Vanmaekelbergh, D. & Liljeroth, P. Electron-conducting quantum dot solids: novel materials based on colloidal semiconductor nanocrystals. *Chemical Society Reviews* **34**, 299–312 (2005).

[176] Brütting, W. & Adachi, C. *Physics of organic semiconductors* (Wiley-VCH, Weinheim, 2012), 2nd edn.

[177] Chu, I.-H., Radulaski, M., Vukmirovic, N., Cheng, H.-P. & Wang, L.-W. Charge transport in a quantum dot supercrystal. *The Journal of Physical Chemistry C* **115**, 21409–21415 (2011).

[178] Shabaev, A., Efros, A. L. & Efros, A. L. Dark and photo-conductivity in ordered array of nanocrystals. *Nano Letters* **13**, 5454–5461 (2013).

[179] Scheele, M. To be or not to be: Band-like transport in quantum dot solids. *Zeitschrift für Physikalische Chemie* **229**, 167–178 (2015).

[180] Beenakker, C. W. J. Theory of coulomb-blockade oscillations in the conductance of a quantum dot. *Physical Review B* **44**, 1646–1656 (1991).

[181] Brust, M., Schiffrin, D. J., Bethell, D. & Kiely, C. J. Novel gold-dithiol nano-networks with non-metallic electronic properties. *Advanced Materials* **7**, 795–797 (1995).

[182] Neugebauer, C. A. & Webb, M. B. Electrical conduction mechanism in ultrathin, evaporated metal films. *Journal of Applied Physics* **33**, 74–82 (1962).

[183] Beloborodov, I. S., Lopatin, A. V., Vinokur, V. M. & Efetov, K. B. Granular electronic systems. *Reviews of Modern Physics* **79**, 469–518 (2007).

[184] Klinke, C. Electrical transport through self-assembled colloidal nanomaterials and their perspectives. *EPL (Europhysics Letters)* **119**, 36002 (2017).

[185] Prodanović, N., Vukmirović, N., Ikonić, Z., Harrison, P. & Indjin, D. Importance of polaronic effects for charge transport in CdSe quantum dot solids. *The Journal of Physical Chemistry Letters* **5**, 1335–1340 (2014).

[186] Holstein, T. Studies of polaron motion. *Annals of Physics* **8**, 325—-342 (1959).

[187] Troisi, A. Charge transport in high mobility molecular semiconductors: classical models and new theories. *Chemical Society Reviews* **40**, 2347–2358 (2011).

[188] Bozyigit, D. *et al.* Soft surfaces of nanomaterials enable strong phonon interactions. *Nature* **531**, 618–622 (2016).

[189] Yazdani, N. *et al.* Tuning electron-phonon interactions in nanocrystals through surface termination. *Nano Letters* **18**, 2233–2242 (2018).

[190] Hassinen, A. *et al.* Short-chain alcohols strip X-type ligands and quench the luminescence of PbSe and CdSe quantum dots, acetonitrile does not. *Journal of the American Chemical Society* **134**, 20705–20712 (2012).

[191] Peters, J. L. *et al.* Ligand-induced shape transformation of PbSe nanocrystals. *Chemistry of Materials* **29**, 4122–4128 (2017).

[192] Coropceanu, V. *et al.* Charge transport in organic semiconductors. *Chemical Reviews* **107**, 926–952 (2007).

[193] Li, G. *et al.* Reactivity and lability modulated by a valence electron moving in and out of 25–atom gold nanoclusters. *Angewandte Chemie* **132**, 21321–21328 (2020).

[194] Devadas, M. S. *et al.* Temperature-dependent optical absorption properties of monolayer-protected Au_{25} and Au_{38} clusters. *The Journal of Physical Chemistry Letters* **2**, 2752–2758 (2011).

[195] Hanrath, T., Choi, J. J. & Smilgies, D.-M. Structure/processing relationships of highly ordered lead salt nanocrystal superlattices. *ACS Nano* **3**, 2975–2988 (2009).

[196] Choi, J. J. *et al.* Photogenerated exciton dissociation in highly coupled lead salt nanocrystal assemblies. *Nano Letters* **10**, 1805–1811 (2010).

[197] Oh, S. J. *et al.* Engineering the surface chemistry of lead chalcogenide nanocrystal solids to enhance carrier mobility and lifetime in optoelectronic devices. *Chemical Communications* **53**, 728–731 (2017).

[198] Kovalenko, M. V., Scheele, M. & Talapin, D. V. Colloidal nanocrystals with molecular metal chalcogenide surface ligands. *Science* **324**, 1417–1420 (2009).

[199] Nag, A. *et al.* Metal-free inorganic ligands for colloidal nanocrystals: S^{2-}, HS^{-}, Se^{2-}, HSe^{-}, Te^{2-}, HTe^{-}, $TeS_3{}^{2-}$,OH^{-}, and $NH_2{}^{-}$ as surface ligands. *Journal of the American Chemical Society* **133**, 10612–10620 (2011).

[200] Chung, D. S. *et al.* Low voltage, hysteresis free, and high mobility transistors from all-inorganic colloidal nanocrystals. *Nano Letters* **12**, 1813–1820 (2012).

[201] Sayevich, V. *et al.* Hybrid n-butylamine-based ligands for switching the colloidal solubility and regimentation of inorganic-capped nanocrystals. *ACS Nano* **11**, 1559–1571 (2017).

[202] Khabibullin, A. R., Efros, A. L. & Erwin, S. C. The role of ligands in electron transport in nanocrystal solids. *Nanoscale* **12**, 23028–23035 (2020).

[203] Zhang, J. *et al.* Carrier transport in PbS and PbSe qd films measured by photoluminescence quenching. *The Journal of Physical Chemistry C* **118**, 16228–16235 (2014).

[204] Wuelfing, W. P. & Murray, R. W. Electron hopping through films of arenethiolate monolayer-protected gold clusters. *The Journal of Physical Chemistry B* **106**, 3139–3145 (2002).

[205] Zabet-Khosousi, A., Trudeau, P.-E., Suganuma, Y., Dhirani, A.-A. & Statt, B. Metal to insulator transition in films of molecularly linked gold nanoparticles. *Physical Review Letters* **96**, 156403 (2006).

[206] Brust, M. & Kiely, C. J. Some recent advances in nanostructure preparation from gold and silver particles: A short topical review. *Colloids and Surfaces A* **202**, 175–186 (2002).

[207] Whitham, K. *et al.* Charge transport and localization in atomically coherent quantum dot solids. *Nature Materials* **15**, 557–563 (2016).

[208] Whitham, K. & Hanrath, T. Formation of epitaxially connected quantum dot solids: Nucleation and coherent phase transition. *The Journal of Physical Chemistry Letters* **8**, 2623–2628 (2017).

[209] Sandeep, C. S. S. *et al.* Epitaxially connected PbSe quantum-dot films: Controlled neck formation and optoelectronic properties. *ACS Nano* **8**, 11499–11511 (2014).

[210] Choi, J.-H. *et al.* Bandlike transport in strongly coupled and doped quantum dot solids: A route to high-performance thin-film electronics. *Nano Letters* **12**, 2631–2638 (2012).

[211] Jang, J., Liu, W., Son, J. S. & Talapin, D. V. Temperature-dependent hall and field-effect mobility in strongly coupled all-inorganic nanocrystal arrays. *Nano Letters* **14**, 653–662 (2014).

[212] Lan, X. *et al.* Quantum dot solids showing state-resolved band-like transport. *Nature Materials* **19**, 323–329 (2020).

[213] Shaw, S. *et al.* Building materials from colloidal nanocrystal arrays: Preventing crack formation during ligand removal by controlling structure and solvation. *Advanced Materials* **28**, 8892–8899 (2016).

[214] Diroll, B. T., Ma, X., Wu, Y. & Murray, C. B. Anisotropic cracking of nanocrystal superlattices. *Nano Letters* **17**, 6501–6506 (2017).

[215] Mics, Z. *et al.* Charge transport and localization in nanocrystalline CdS films: A

time-resolved terahertz spectroscopy study. *Physical Review B* **83** (2011).

[216] Mentzel, T. S. *et al.* Nanopatterned electrically conductive films of semiconductor nanocrystals. *Nano Letters* **12**, 4404–4408 (2012).

[217] Agranovich, V. M., Gartstein, Y. N. & Litinskaya, M. Hybrid resonant organic-inorganic nanostructures for optoelectronic applications. *Chemical Reviews* **111**, 5179–5214 (2011).

[218] Zaumseil, J. & Sirringhaus, H. Electron and ambipolar transport in organic field-effect transistors. *Chemical Reviews* **107**, 1296–1323 (2007).

[219] Wessels, J. M. *et al.* Optical and electrical properties of three-dimensional interlinked gold nanoparticle assemblies. *Journal of the American Chemical Society* **126**, 3349–3356 (2004).

[220] Frederick, M. T., Amin, V. A., Swenson, N. K., Ho, A. Y. & Weiss, E. A. Control of exciton confinement in quantum dot-organic complexes through energetic alignment of interfacial orbitals. *Nano Letters* **13**, 287–292 (2013).

[221] Scheele, M. Bridging the gap: Where inorganic quantum dots and organic semiconductors meet. *Bunsen-Magazin* **16**, 168–175 (2014).

[222] McCold, C. E. *et al.* Ligand exchange based molecular doping in 2D hybrid molecule-nanoparticle arrays: length determines exchange efficiency and conductance. *Molecular Systems Design & Engineering* **2**, 440–448 (2017).

[223] Li, H., Zhitomirsky, D., Dave, S. & Grossman, J. C. Toward the ultimate limit of connectivity in quantum dots with high mobility and clean gaps. *ACS Nano* **10**, 606–614 (2016).

[224] André, A. *et al.* Electron-conducting PbS nanocrystal superlattices with long-range order enabled by terthiophene molecular linkers. *ACS Applied Materials & Interfaces* **10**, 24708–24714 (2018).

[225] Samadi Khoshkhoo, M. *et al.* Tunable charge transport in hybrid superlattices of indium tin oxide nanocrystals and metal phthalocyanines-toward sensing applications. *Advanced Materials Interfaces* **5**, 1701623 (2018).

[226] Maiti, S. *et al.* Dye-sensitized ternary copper chalcogenide nanocrystals: Optoelectronic properties, air stability, and photosensitivity. *Chemistry of Materials* **31**, 2443–2449 (2019).

[227] Steiner, A. M., Lissel, F., Fery, A., Lauth, J. & Scheele, M. Prospects of coupled organic–inorganic nanostructures for charge and energy transfer applications. *Angewandte Chemie International Edition* 1152 – 1175 (2020).

[228] Lauth, J. *et al.* Ultrafast charge transfer and upconversion in Zn β-tetraamino-phthalocyanine functionalized PbS nanostructures probed by transient absorption spectroscopy. *Angewandte Chemie Intrnational Edition* **129**, 14249–14253 (2017).

[229] Schedel, C., Peisert, H., Chassé, T. & Scheele, M. Evidence for photo-switchable carrier mobilities in blends of PbS nanocrystals and photochromic dithienylcyclopentene derivatives. *Zeitschrift für Physikalische Chemie* **232**, 1369–1381 (2018).

[230] Kumar, K. *et al.* Fast, infrared-active optical transistors based on dye-sensitized CdSe nanocrystals. *ACS Applied Materials & Interfaces* **11**, 48271–48280 (2019).

[231] Märker, B. *et al.* Simultaneous positive and negative optical patterning with dye-sensitized CdSe quantum dots. *The Journal of Chemical Physics* **151**, 141102 (2019).

[232] Artemyev, M. V., Bibik, A. I., Gurinovich, L. I., Gaponenko, S. V. & Woggon, U. Evolution from individual to collective electron states in a dense quantum dot ensemble. *Physical Review B* **60**, 1504–1506 (1999).

[233] M.V. Artemyev *et al.* Optical properties of dense and diluted ensembles of semiconductor quantum dots. *Physica Status Solidi B* **224**, 393–396 (2001).

[234] Mićić, O. I., Jones, K. M., Cahill, A. & Nozik, A. J. Optical, electronic, and structural properties of uncoupled and close-packed arrays of InP quantum dots. *The Journal of Physical Chemistry B* **102**, 9791–9796 (1998).

[235] Vossmeyer, T. *et al.* CdS nanoclusters: Synthesis, characterization, size dependent oscillator strength, temperature shift of the excitonic transition energy, and reversible absorbance shift. *The Journal of Physical Chemistry* **98**, 7665–7673 (1994).

[236] Collier, C. P., Saykally, R. J., Shiang, J. J., Henrichs, S. E. & Heath, J. R. Reversible tuning of silver quantum dot monolayers through the metal-insulator transition. *Science* **277**, 1978–1981 (1997).

[237] McCold, C. E., Fu, Q., Howe, J. Y. & Hihath, J. Conductance based characterization of structure and hopping site density in 2D molecule-nanoparticle arrays. *Nanoscale* **7**, 14937–14945 (2015).

[238] Parthasarathy, R., Lin, X.-M. & Jaeger, H. M. Electronic transport in metal nanocrystal arrays: The effect of structural disorder on scaling behavior. *Physical Review Letters* **87**, 1978 (2001).

[239] Akselrod, G. M. *et al.* Subdiffusive exciton transport in quantum dot solids. *Nano Letters* **14**, 3556–3562 (2014).

[240] Gilmore, R. H., Lee, E. M. Y., Weidman, M. C., Willard, A. P. & Tisdale, W. A. Charge carrier hopping dynamics in homogeneously broadened PbS quantum dot solids. *Nano Letters* **17**, 893–901 (2017).

[241] Beverly, K. C., Sampaio, J. F. & Heath, J. R. Effects of size dispersion disorder on the charge transport in self-assembled 2-D Ag nanoparticle arrays. *The Journal of Physical Chemistry B* **106**, 2131–2135 (2002).

[242] Skibinsky-Gitlin, E. S., Rodríguez-Bolívar, S., Califano, M. & Gómez-Campos, F. M. Band-like electron transport in 2D quantum dot periodic lattices: The effect of realistic size distributions. *Physical Chemistry Chemical Physics* **21**, 25872–25879 (2019).

[243] Sundar, V. C. *et al.* Elastomeric transistor stamps: reversible probing of charge transport in organic crystals. *Science* **303**, 1644–1646 (2004).

[244] Park, S. S. *et al.* Cation-dependent intrinsic electrical conductivity in isostructural tetrathiafulvalene-based microporous metal-organic frameworks. *Journal of the American Chemical Society* **137**, 1774–1777 (2015).

[245] Noriega, R. *et al.* A general relationship between disorder, aggregation and charge transport in conjugated polymers. *Nature Materials* **12**, 1038–1044 (2013).

[246] Li, T., Senesi, A. J. & Lee, B. Small angle X-ray scattering for nanoparticle research. *Chemical Reviews* **116**, 11128–11180 (2016).

[247] Egerton, R. F. *Physical principles of electron microscopy: An introduction to TEM, SEM, and AEM* (Springer, New York NY, 2005).

[248] Schroder, D. K. *Semiconductor material and device characterization* (John Wiley &

Sons, Hoboken NJ, 2006), 3rd edn.

[249] Goldstein, J. I. *et al. Scanning Electron Microscopy and X-Ray Microanalysis* (Springer, New York, NY, 2018), 4th edn.

[250] Wang, Z. L. Structural analysis of self-assembling nanocrystal superlattices. *Advanced Materials* **10**, 13–30 (1998).

[251] Massa, W. *Kristallstrukturbestimmung* (Vieweg + Teubner, Wiesbaden, 2011), 7th edn.

[252] Li, R., Bian, K., Hanrath, T., Bassett, W. A. & Wang, Z. Decoding the superlattice and interface structure of truncate PbS nanocrystal-assembled supercrystal and associated interaction forces. *Journal of the American Chemical Society* **136**, 12047–12055 (2014).

[253] Renaud, G., Lazzari, R. & Leroy, F. Probing surface and interface morphology with grazing incidence small angle X-ray scattering. *Surface Science Reports* **64**, 255–380 (2009).

[254] Meyer, A. Grazing incidence small angle X-ray scattering (2018, accessed 30th October 2020). URL http://www.gisaxs.de/gallery.html.

[255] Smilgies, D. GISAXS (2020, accessed 21st January 2021). URL https://www.classe.cornell.edu/~dms79/gisaxs/GISAXS.html.

[256] Heitsch, A. T., Patel, R. N., Goodfellow, B. W., Smilgies, D.-M. & Korgel, B. A. GISAXS characterization of order in hexagonal monolayers of FePt nanocrystals. *The Journal of Physical Chemistry C* **114**, 14427–14432 (2010).

[257] Smilgies, D.-M. & Hanrath, T. Superlattice self-assembly: Watching nanocrystals in action. *EPL (Europhysics Letters)* **119**, 1–6 (2017).

[258] Mobilio, S., Boscherini, F. & Meneghini, C. *Synchrotron Radiation: Basics, Methods and Applications* (Springer, Heidelberg, 2015).

[259] Sivia, D. S. *Elementary scattering theory: For X-Ray and neutron users* (Oxford University Press, Oxford, 2011).

[260] Bilderback, D. H., Elleaume, P. & Weckert, E. Review of third and next generation synchrotron light sources. *Journal of Physics B* **38**, S773–S797 (2005).

[261] DESY. PETRA III (2020, accessed 10th December 2020). URL https://photon-science.desy.de/facilities/petra_iii/index_eng.html.

[262] ESRF. What is a synchrotron? (2019, accessed 10th December 2020). URL https://www.esrf.eu/about/synchrotron-science/synchrotron.

[263] Kalbfleisch, S. *et al.* The Göttingen holography endstation of beamline P10 at PETRA III\DESY. *AIP Conference Proceedings* **1365**, 96–99 (2011).

[264] Salditt, T. *et al.* Compound focusing mirror and X-ray waveguide optics for coherent imaging and nano-diffraction. *Journal of Synchrotron Radiation* **22**, 867–878 (2015).

[265] Henke, B. L., Gullikson, E. M. & Davis, J. C. X-ray interactions: Photoabsorption, scattering, transmission, and reflection at E = 50-30,000 eV, Z = 1-92. *Atomic Data and Nuclear Data Tables* **54**, 181–342 (1993). URL https://henke.lbl.gov/optical_constants/filter2.html.

[266] DuPont Kapton. Summary of properties 1–20 (2020, accessed 21st Januaray 2021). URL https://www.dupont.com/content/dam/dupont/amer/us/en/products/ei-transformation/documents/EI-10142-Kapton-Summary-of-Properties.pdf.

[267] Wochner, P. *et al.* X-ray cross correlation analysis uncovers hidden local symmetries

in disordered matter. *Proceedings of the National Academy of Sciences of the United States of America* **106**, 11511–11514 (2009).

[268] Kurta, R. P. *et al.* X-ray cross-correlation analysis of liquid crystal membranes in the vicinity of the hexatic-smectic phase transition. *Physical Review E* **88**, 044501 (2013).

[269] Kurta, R. P. *et al.* Structural properties of π-π conjugated network in polymer thin films studied by X-ray cross-correlation analysis. *Journal of Physics: Conference Series* **499**, 012021 (2014).

[270] Lehmkühler, F. *et al.* Heterogeneous local order in self-assembled nanoparticle films revealed by X-ray cross-correlations. *International Union of Crystallography* **5**, 354–360 (2018).

[271] Zaluzhnyy, I. A. *et al.* Angular X-ray cross-correlation analysis (AXCCA): Basic concepts and recent applications to soft matter and nanomaterials. *Materials* **12**, 3464 (2019).

[272] Kurta, R. P., Altarelli, M. & Vartanyants, I. A. X-ray cross-correlation analysis of disordered ensembles of particles: Potentials and limitations. *Advances in Condensed Matter Physics* **2013**, 1–15 (2013).

[273] Altarelli, M., Kurta, R. P. & Vartanyants, I. A. X-ray cross-correlation analysis and local symmetries of disordered systems: General theory. *Physical Review B* **82** (2010).

[274] Mishra, U. K. & Singh, J. *Semiconductor device physics and design* (Springer, Dordrecht, 2008).

[275] Stallinga, P. *Electrical characterization of organic electronic materials and devices* (John Wiley & Sons, Chichester, 2009).

[276] Strasfeld, D. B., Dorn, A., Wanger, D. D. & Bawendi, M. G. Imaging schottky barriers and ohmic contacts in PbS quantum dot devices. *Nano Letters* **12**, 569–575 (2012).

[277] Hehenberger, P. Advanced characterization of the bias temperature instability. Dissertation, Technische Universität Wien (2011). URL https://repositum.tuwien.at/bitstream/20.500.12708/9707/2/Advanced%20characterization%20of%20the%20bias%20temperature%20instability.pdf.

[278] Madou, M. J. *Fundamentals of microfabrication: The science of miniaturization* (CRC Press, Boca Raton FL, 2002), 2nd edn.

[279] Franssila, S. *Introduction to microfabrication* (John Wiley & Sons, Chichester, 2010), 2nd edn.

[280] Thompson, L. F., Willson, C. G. & Bowden, M. J. *Introduction to Microlithography* (American Chemical Society, Washington, D.C., 1983).

[281] Laube, P. Halbleitertechnologie von A bis Z (2016, accessed 21st January 2021). URL https://www.halbleiter.org/pdf/de/halbleitertechnologie/Halbleitertechnologie%20von%20A%20bis%20Z.pdf.

[282] Chuang, Y.-J., Tseng, F.-G. & Lin, W.-K. Reduction of diffraction effect of UV exposure on SU-8 negative thick photoresist by air gap elimination. *Microsystem Technologies* **8**, 308–313 (2002).

[283] Seidel, H., Csepregi, L., Heuberger, A. & Baumgaertel, H. Anisotropic etching of crystalline silicon in alkaline solutions. *Journal of Electrochemical Society* **137**, 3612–3626 (1990).

[284] Powell, O. & Harrison, H. B. Anisotropic etching of {100} and {110} planes in (100)

silicon. *Journal of Micromechanics and Microengineering* **11** (2001).

[285] Bühler, J., Steiner, F.-P. & Baltes, H. Silicon dioxide sacrificial layer etching in surface micromachining. *Japanese Journal of Applied Physics* **7**, R1–R13 (1997).

[286] Jansen, H., Gardeniers, H., Fluitman, J., Boer, M. d. & Elwenspoek, M. A survey on the reactive ion etching of silicon in microtechnology. *Journal of Micromechanics and Microengineering* **6**, 14–28 (1996).

[287] Maradudin, A. A. *Light Scattering and Nanoscale Surface Roughness* (Springer, Boston, MA, 2007).

[288] Xia, Y. & Whitesides, G. M. Soft lithography. *Annual Review of Materials Science* **28**, 153–184 (1998).

[289] Perl, A., Reinhoudt, D. N. & Huskens, J. Microcontact printing: Limitations and achievements. *Advanced Materials* **21**, 2257–2268 (2009).

[290] Qin, D., Xia, Y. & Whitesides, G. M. Soft lithography for micro- and nanoscale patterning. *Nature Protocols* **5**, 491–502 (2010).

[291] Wisser, F. M., Schumm, B., Mondin, G., Grothe, J. & Kaskel, S. Precursor strategies for metallic nano- and micropatterns using soft lithography. *Journal of Materials Chemistry C* **3**, 2717–2731 (2015).

[292] Sharp, K. G., Blackman, G. S., Glassmaker, N. J., Jagota, A. & Hui, C.-Y. Effect of stamp deformation on the quality of microcontact printing: Theory and experiment. *Langmuir* **20**, 6430–6438 (2004).

[293] Liao, J., Bernard, L., Langer, M., Schönenberger, C. & Calame, M. Reversible formation of molecular junctions in 2D nanoparticle arrays. *Advanced Materials* **18**, 2444–2447 (2006).

[294] Kim, L. *et al.* Contact printing of quantum dot light-emitting devices. *Nano Letters* **8**, 4513–4517 (2008).

[295] Diroll, B. T. *et al.* X-ray mapping of nanoparticle superlattice thin films. *ACS Nano* **8**, 12843–12850 (2014).

[296] Williams, K. J. *et al.* Strong electronic coupling in two-dimensional assemblies of colloidal PbSe quantum dots. *ACS Nano* **3**, 1532–1538 (2009).

[297] Sanehira, E. M. *et al.* Enhanced mobility $CsPbI_3$ quantum dot arrays for record-efficiency, high-voltage photovoltaic cells. *Science Advances* **3**, eaao4204 (2017).

[298] Wilbur, J. L., Kumar, A., Biebuyck, H. A., Kim, E. & Whitesides, G. M. Microcontact printing of self-assembled monolayers: Applications in microfabrication. *Nanotechnology* **7**, 452–457 (1996).

[299] Jung, S.-H., Choi, J.-H., Yang, S.-M., Cho, W.-J. & Ha, C.-S. Syntheses and characterization of soluble phthalocyanine derivatives for organic electroluminescent devices. *Materials Science and Engineering B* **85**, 160–164 (2001).

[300] Delamarche, E., Schmid, H., Michel, B. & Biebuyck, H. Stability of molded polydimethylsiloxane microstructures. *Advanced Materials* **9**, 741–746 (1997).

[301] Himpsel F J, McFeely F R, Taleb-Ibrahimi A, Yarmoff J A and Hollinger G. Microscopic structure of the SiO_2/Si interface. *Physical Review B* **38**, 6084–6096 (1988).

[302] Beck, M. *et al.* Improving stamps for 10 nm level wafer scale nanoimprint lithography. *Microelectronic Engineering* **61-62**, 441–448 (2002).

[303] Dayen, J.-F. *et al.* Enhancing the molecular signature in molecule-nanoparticle networks via inelastic cotunneling. *Advanced Materials* **25**, 400–404 (2013).

[304] Shulga, A. G., Piveteau, L., Bisri, S. Z., Kovalenko, M. V. & Loi, M. A. Double gate PbS quantum dot field-effect transistors for tuneable electrical characteristics. *Advanced Electronic Materials* **2**, 1500467 (2016).

[305] Maier, A. *et al.* Structure-transport correlation reveals anisotropic charge transport in coupled PbS nanocrystal superlattices. *Advanced Materials* **32**, 2002254 (2020).

[306] Nagpal, P. & Klimov, V. I. Role of mid-gap states in charge transport and photoconductivity in semiconductor nanocrystal films. *Nature Communications* **2**, 486 (2011).

[307] Zhang, Y. *et al.* Molecular oxygen induced in-gap states in PbS quantum dots. *ACS Nano* **9**, 10445–10452 (2015).

[308] Tackley, D. R., Dent, G. & Ewen Smith, W. Phthalocyanines: Structure and vibrations. *Physical Chemistry Chemical Physics* **3**, 1419–1426 (2001).

[309] Voznyy, O., Sutherland, B. R., Ip, A. H., Zhitomirsky, D. & Sargent, E. H. Engineering charge transport by heterostructuring solution-processed semiconductors. *Nature Reviews Materials* **2**, 17026 (2017).

[310] Han, W. *et al.* Two-dimensional inorganic molecular crystals. *Nature Communications* **10**, 4728 (2019).

[311] Yang, P., Arfaoui, I., Cren, T., Goubet, N. & Pileni, M.-P. Unexpected electronic properties of micrometer-thick supracrystals of Au nanocrystals. *Nano Letters* **12**, 2051–2055 (2012).

[312] Roy, X. *et al.* Nanoscale atoms in solid-state chemistry. *Science* **341**, 157–160 (2013).

[313] Tulsky, E. G. & Long, J. R. Dimensional reduction: A practical formalism for manipulating solid structures. *Chemistry of Materials* **13**, 1149–1166 (2001).

[314] Baudron, S. A. *et al.* $(EDT{-}TTF{-}CONH_2)_6Re_6Se_8(CN)_6$, a metallic kagome-type organic-inorganic hybrid compound: electronic instability, molecular motion, and charge localization. *Journal of the American Chemical Society* **127**, 11785–11797 (2005).

[315] Jung, D. *et al.* A molecular cross-linking approach for hybrid metal oxides. *Nature Materials* **17**, 341–348 (2018).

[316] O'Brien, E. S. *et al.* Spontaneous electronic band formation and switchable behaviors in a phase-rich superatomic crystal. *Journal of the American Chemical Society* **140**, 15601–15605 (2018).

[317] Liu, G. *et al.* Tuning the electronic properties of hexanuclear cobalt sulfide superatoms via ligand substitution. *Chemical Science* **10**, 1760–1766 (2019).

[318] Bono, D. *et al.* Muon spin relaxation studies of superconductivity in a crystalline array of weakly coupled metal nanoparticles. *Physical Review Letters* **97**, 077601 (2006).

[319] Ong, W.-L. *et al.* Orientational order controls crystalline and amorphous thermal transport in superatomic crystals. *Nature Materials* **16**, 83–88 (2017).

[320] Torma, V., Schmid, G. & Simon, U. Structure-property relations in Au_{55} cluster layers studied by temperature-dependent impedance measurements. *ChemPhysChem* **2**, 321–325 (2001).

[321] Schmid, G. & Simon, U. Gold nanoparticles: Assembly and electrical properties in 1-3

dimensions. *Chemical Communications* 697–710 (2005).

[322] Galchenko, M. Synthese hochreiner Au_{25}-Nanocluster und Untersuchung der optoelektronischen Eigenschaften im Film. Dissertation, Universität Hamburg (2019). URL https://ediss.sub.uni-hamburg.de/bitstream/ediss/8234/1/Dissertation.pdf.

[323] Bakharev, O. N. *et al.* Superconductivity in a molecular metal cluster compound. *Physical Review Letters* **96**, 117002 (2006).

[324] Resel, R. *et al.* Multiple scattering in grazing-incidence X-ray diffraction: Impact on lattice-constant determination in thin films. *Journal of Synchrotron Radiation* **23**, 729–734 (2016).

[325] Shibu, E. S. & Pradeep, T. Photoluminescence and temperature dependent emission studies of Au_{25} clusters in the solid state. *International Journal of Nanoscience* **8**, 223–226 (2009).

[326] Roest, A. L., Kelly, J. J., Vanmaekelbergh, D. & Meulenkamp, E. A. Staircase in the electron mobility of a ZnO quantum dot assembly due to shell filling. *Physical Review Letters* **89**, 036801–036804 (2002).

[327] Kwak, K., Thanthirige, V. D., Pyo, K., Lee, D. & Ramakrishna, G. Energy gap law for exciton dynamics in gold cluster molecules. *The Journal of Physical Chemistry Letters* **8**, 4898–4905 (2017).

[328] Negishi, Y., Nobusada, K. & Tsukuda, T. Glutathione-protected gold clusters revisited: Bridging the gap between gold(I)-thiolate complexes and thiolate-protected gold nanocrystals. *Journal of the American Chemical Society* **127**, 5261–5270 (2005).

[329] Pyo, K. *et al.* Ultrabright luminescence from gold nanoclusters: Rigidifying the Au(I)-thiolate shell. *Journal of the American Chemical Society* **137**, 8244–8250 (2015).

[330] Zheng, J., Zhou, C., Yu, M. & Liu, J. Different sized luminescent gold nanoparticles. *Nanoscale* **4**, 4073–4083 (2012).

[331] Link, S. *et al.* Visible to infrared luminescence from a 28-atom gold cluster. *The Journal of Physical Chemistry B* **106**, 3410–3415 (2002).

[332] Devadas, M. S. *et al.* Unique ultrafast visible luminescence in monolayer-protected Au_{25} clusters. *The Journal of Physical Chemistry C* **114**, 22417–22423 (2010).

[333] Kang, X. & Zhu, M. Tailoring the photoluminescence of atomically precise nanoclusters. *Chemical Society Reviews* **48**, 2422–2457 (2019).

[334] Weerawardene, K. L. D. M. & Aikens, C. M. Theoretical insights into the origin of photoluminescence of $Au_{25}(SR)_{18}^{-}$ nanoparticles. *Journal of the American Chemical Society* **138**, 11202–11210 (2016).

[335] Goswami, N. *et al.* Luminescent metal nanoclusters with aggregation-induced emission. *The Journal of Physical Chemistry Letters* **7**, 962–975 (2016).

[336] Liu, X. *et al.* Crystal and solution photoluminescence of $MAg_{24}(SR)_{18}$ (M = Ag/Pd/Pt/Au) nanoclusters and some implications for the photoluminescence mechanisms. *The Journal of Physical Chemistry C* **121**, 13848–13853 (2017).

[337] Qian, H., Eckenhoff, W. T., Bier, M. E., Pintauer, T. & Jin, R. Crystal structures of Au_2 complex and Au_{25} nanocluster and mechanistic insight into the conversion of polydisperse nanoparticles into monodisperse Au_{25} nanoclusters. *Inorganic Chemistry* **50**, 10735–10739 (2011).

[338] Choi, J.-P. & Murray, R. W. Electron self-exchange between $Au_{140}^{+/0}$ nanoparticles is faster than that between $Au_{38}^{+/0}$ in solid-state, mixed-valent films. *Journal of the American Chemical Society* **128**, 10496–10502 (2006).

[339] Zabet-Khosousi, A. & Dhirani, A.-A. Charge transport in nanoparticle assemblies. *Chemical Reviews* **108**, 4072–4124 (2008).

[340] Jiang, Z. GIXSGUI: A MATLAB toolbox for grazing-incidence X-ray scattering data visualization and reduction, and indexing of buried three-dimensional periodic nanostructured films. *Journal of Applied Crystallography* **48**, 917–926 (2015).

[341] Mooney, J. & Kambhampati, P. Get the basics right: Jacobian conversion of wavelength and energy scales for quantitative analysis of emission spectra. *The Journal of Physical Chemistry Letters* **4**, 3316–3318 (2013).

[342] Ghibaudo, G. New method for the extraction of MOSFET parameters. *Electronics Letters* **24**, 543 (1988).

[343] Xu, Y. *et al.* Modified transmission-line method for contact resistance extraction in organic field-effect transistors. *Applied Physics Letters* **97**, 063302 (2010).

[344] Liu, C., Xu, Y. & Noh, Y.-Y. Contact engineering in organic field-effect transistors. *Materials Today* **18**, 79–96 (2015).

[345] Black, C. T. Spin-dependent tunneling in self-assembled cobalt-nanocrystal superlattices. *Science* **290**, 1131–1134 (2000).

List of publications & scholarly contributions

Peer-reviewed publications

This thesis is largely based on the following publications:

1. **Andre Maier**, Ronny Löffler & Marcus Scheele.
   Fabrication of nanocrystal superlattice microchannels by soft-lithography for electronic measurements of single-crystalline domains.
   Nanotechnology **31**, 405302 (2020).
   https://doi.org/10.1088/1361-6528/ab9c52

2. **Andre Maier**, Dmitry Lapkin, Nastasia Mukharamova, Philipp Frech, Dameli Assalauova, Alexandr Ignatenko, Ruslan Khubbutdinov, Sergey Lazarev, Michael Sprung, Florian Laible, Ronny Löffler, Nicolas Previdi, Annika Bräuer, Thomas Günkel, Monika Fleischer, Frank Schreiber, Ivan A. Vartanyants & Marcus Scheele.
   Structure-transport correlation reveals anisotropic charge transport in coupled PbS nanocrystal superlattices.
   Advanced Materials **32**, 2002254 (2020).
   https://doi.org/10.1002/adma.202002254

3. Florian Fetzer*, **Andre Maier***, Martin Hodas, Olympia Geladari, Kai Braun, Alfred J. Meixner, Frank Schreiber, Andreas Schnepf & Marcus Scheele.
   Structural order enhances electronic coupling in self-assembled micro-crystals of Au nanoclusters.
   Nature Communications **11**, 6188 (2020).
   https://doi.org/10.1038/s41467-020-19461-x
   (* Equal contribution.)

Other scholarly publications with the author of this thesis:

1. Santanu Maiti, Sonam Maiti, **Andre Maier**, Jan Hagenlocher, Andrei Chumakov, Frank Schreiber, Marcus Scheele.
   Understanding the formation of conductive mesocrystalline superlattices with cubic PbS nanocrystals at the liquid/air interface.
   Journal of Physical Chemistry C **123**, 1519-1526 (2019).
   https://pubs.acs.org/doi/10.1021/acs.jpcc.8b11518

2. Sonam Maiti, Santanu Maiti, **Andre Maier**, Rupak Banerjee, Chen Shen, Bridget M. Murphy, Marcus Scheele, Frank Schreiber.
   In-situ formation of electronically coupled superlattice of $Cu_{1.1}S$ nanodiscs at the liquid/air interface.
   Chemical Communications **55**, 4805-4808 (2019).
   https://pubs.rsc.org/en/content/articlehtml/2019/CC/C9CC01758E

3. Krishan Kumar, Quan Liu, Jonas Hiller, Christine Schedel, **Andre Maier**, Alfred J. Meixner, Kai Braun, Jannika Lauth, Marcus Scheele.
   Infrared-active optical transistor based on dye-sensitized CdSe nanocrystals.
   ACS Applied Materials & Interfaces **11**, 48271 (2019).
   https://pubs.acs.org/doi/10.1021/acsami.9b18236

4. Christine Schedel, Fabian Strauß, Krishan Kumar, **Andre Maier**, Kai Wurst, Patrick Michel, Marcus Scheele.
   Substrate effects on the bandwidth of CdSe quantum dot photodetectors.
   Submitted (2021).

5. Dmitry Lapkin, Christopher Kirsch, Jonas Hiller, Denis Andrienko, Dameli Assalauova, Kai Braun, Jerome Carnis, Young Yong Kim, Mukunda Mandal, **Andre Maier**, Alfred Meixner, Nastasia Mukharamova, Marcus Scheele, Frank Schreiber, Michael Sprung, Jan Wahl, Sophia Westendorf, Ivan Zaluzhnyy, Ivan A. Vartanyants.
   Supercrystals of Caesium Lead Halide Perovskite nanocrystals as model systems for the analogy between atoms and nanoparticles.
   In preparation (2021).

6. Olympia Geladari*, Martin Eberle*, **Andre Maier***, Florian Fetzer, Thomas Chassé, Alfred J. Meixner, Marcus Scheele, Andreas Schnepf, Kai Braun.
   Direct laser-induced gold printing with sub-µm resolution for (opto-)electronic device fabrication.
   In preparation (2021). (* Equal contribution.)

Conference talks

During this thesis, the following conference talks were given:

1. Andre Maier. The effect of long-range order on charge transport in self-assembled nanocrystal and nanocluster superlattices.
   Bunsen-Tagung "Multi-Scale Modelling & Physical Chemistry of Colloids", Virtual, Keynote Speaker (May 2021).

2. Andre Maier. The effect of long-range order on charge transport in self-assembled nanocrystal superlattices.
   nanoGe Spring Meeting, Virtual, (March 2021).

3. Andre Maier. Correlation of structural and electronic properties of coupled PbS nanocrystal superlattices.
   Bunsen-Tagung "Functional Materials", Jena, Germany (May 2019).

Supervision of theses and practical courses

During this thesis, the following students were supervised:

1. Nicolas Previdi, Bachelor Thesis, Nano-Science (2018)
   "Microfabrication of gold electrodes and patterned PbS-Cu4APc films to probe charge carrier transport in µm-scaled COIN domains."

2. Nils Rieger, Bachelor Thesis, Nano-Science (2019)
   "Correlation of thickness and conductivity in hybrid PbS-Cu4APc thin films."

3. Angelika Rein, Practical course, Chemistry (2019)
   "Temperaturabhängige Leitfähigkeit von amorphen $Au_{32}(^{n}Bu_3P)_{12}Cl_8$-Cluster-filmen."

4. Pia Kohlschreiber, Bachelor Thesis, Nano-Science (2020)
   "Electronic properties of metalloid gold cluster $Au_{32}(R_3P)_{12}Cl_8$ thin films and micro-crystals."

5. Mario Martin, Bachelor Thesis, Nano-Science (2021)
   "The diversity of gold: Transport measurements of Au nanocluster thin films."

Contribution to other theses

During this thesis, the author contributed to the following other theses, mainly by performing scanning electron microscopy and photolithography:

1. Sonam Maiti, PhD Thesis
2. Krishan Kumar, PhD Thesis
3. Björn Märker, PhD Thesis
4. Christine Schedel, PhD Thesis
5. Jan Wahl, PhD Thesis
6. Christopher Kirsch, PhD Thesis
7. Philipp Haizmann, PhD Thesis
8. Florian Fetzer, PhD Thesis
9. Olympia Geladari, PhD Thesis
10. Theresa Zelger, Master Thesis
11. Christoph Steve Conrad, Master Thesis

12. Philipp Frech, Bachelor Thesis
13. Sophia Westendorf, Bachelor Thesis
14. Nicolas Bader, Bachelor Thesis
15. Matthias Benz, Bachelor Thesis
16. Katharina Gruber, Bachelor Thesis
17. Clemens Weig, Bachelor Thesis
18. Benedikt Jäger, Bachelor Thesis
19. Fabian Strauß, Practical course
20. Patrick Tim Michel, Practical course
21. Leah Schynowski, Practical course

Declaration of contribution

In this Chapter I declare my own contribution and those of collaboration partners to the publications of this cumulative thesis.

Publication I

"Fabrication of nanocrystal superlattice microchannels by soft-lithography for electronic measurements of single crystalline domains", published in Nanotechnology:
Here, all the fabrication steps as well as data generation, analysis and interpretation was performed by me. The scientific ideas were theoretically developed with Ronny Löffler. Marcus Scheele supervised the project. The manuscript was entirely written by me, supported by a critical review of Ronny Löffler and Marcus Scheele. I am the corresponding author of this publication.
Estimated contribution of my own: $\sim 90\%$.

Publication II

"Structure-transport correlation reveals anisotropic charge transport in coupled PbS nanocrystal superlattices", published in Advanced Materials:
I performed the device fabrication, sample preparation, SEM, AFM, Raman and electrical measurements, analysed and interpreted the results and wrote most parts of the manuscript. Dmitry Lapkin and Nastasia Mukharamova performed the X-ray nano-diffraction experiment, analysed the results and wrote parts of the manuscript. Philipp Frech supported the sample preparation and electrical measurements. Damelie Assalauova, Alexandr Ignatenko, Ruslan Khubbutdinov, Sergey Lazarev and Michael Sprung performed and supported the X-ray nano-diffraction experiment. Florian Laible, Ronny Löffler, Nicolas Previdi, Annika Bräuer, Thomas Günkel and Monika Fleischer supported the device fabrication. Frank Schreiber, Ivan A. Vartanyants and Marcus Scheele conceived and supervised the project, together with a revision of the manuscript.
Estimated contribution of my own: $\sim 60\%$.

Publication III

"Structural order enhances charge carrier transport in self-assembled Au nanoclusters", published in Nature Communications:

I performed the device fabrication, SEM measurements and analyzed the electrical measurements. Florian Fetzer and I conducted optical absorbance measurements, electrical measurements, interpreted the results and wrote the manuscript. Florian Fetzer synthesized the nanoclusters and performed the micro-crystal fabrication. Martin Hodas performed the GISAXS measurements and analysis. Olympia Geladari, Kai Braun and Alfred Meixner conducted the luminescence measurements. Frank Schreiber, Andreas Schnepf and Marcus Scheele conceived and supervised the project.

Estimated contribution of my own: $\sim 40\%$.

Acknowledgements

Even though this thesis bears my name, I would like to note that it would have been difficult, if not impossible, to accomplish this without the support of many great and helpful people.

First of all I would like to thank my supervisor and the head of the group Marcus Scheele. Thank you for your strong support and guidance, the financial support as well as the large degree of freedom during the last years. Thank you for being always available somehow no matter how tough your schedule was. I really have learned a lot – scientifically and far beyond.

I would particularly like to thank Frank Schreiber for the strong and vital support during our numerous projects, beam times and paper writing procedures as well as for being part of the board of examiners. I thank Monika Fleischer for the access to the clean room facilities and the support in terms of microfabrication as well as for being part of the board of examiners. I also thank Reinhold Fink for being the second reviewer of this thesis and being part of the board of examiners. Special thanks goes to Alexander Eychmüller as the third supervisor for preparing the external expert review.

I wish to thank Andreas Schnepf for the successful collaboration and I gratefully acknowledge the close teamwork with Flo Fetzer, which has not only been proven to be scientifically fruitful but also a lot of fun.

Special thanks goes to our partners from Hamburg for the fruitful collaboration and great science: Dmitry Lapkin, Nastya Mukharamova and Ivan Vartanyants. Further I wish to thank the entire team which led our DESY beam time to success: Dameli Assalauova, Alexandr Ignatenko, Ruslan Khubbutdinov, Sergey Lazarev, Michael Sprung and the group of Tim Salditt.

I thank Alfred Meixner and especially Kai Braun for providing access to all the optical instruments and the AFM as well as for the rich discussions.

Grateful thanks goes to the people who supported this scientific work:
Ronny Löffler for the teaching in microfabrication, without which this thesis would not have come so far, Elke Nadler for the profound introduction to electron microscopy, the enjoyable teaching to catch the perfect image and the excellent cooperation, Alexander André for introducing me to the wonderful world of nanoparticle self-assembly and the synthesis of Cu4APc, Martin Hodas for the great collaboration and the tremendous

amount of GISAXS measurements, Florian Laible for the dedication and excellent support in microfabrication, Markus Turad for all the support regarding instruments and techniques, Olympia Geladari for the luminescence measurements and the great cooperation, Michelle Weber for providing their high-quality nanoparticles, Christoph Dreser, Annika Bräuer and Simon Dickreuter for the assistance with the home-built optical setup for measuring single micro-crystal spectra, Benedikt Fischer for the assistance during the interference reflection microscopy measurements, and especially Philipp Frech for the continuous and magnificent support before and during the DESY beamtime.

A very special thanks goes to the brilliant people that I had pleasure working with and enjoying our memorable activities. Thank you: Christine Schedel, Philipp Frech, Kai Wurst, Krishan Kumar, Björn Märker, Sonam Maiti, Jan Wahl, Chris Kirsch, Philipp Heizmann and Sophia Westendorf.

I would also like to thank my students Nicolas Previdi, Nils Rieger, Angelika Rein and Pia Kohlschreiber – teaching is always a give and take.

I also would like to acknowledge Karsten Stampke for the always reliable technical assistance and access to the workshop, Alexander Schnapper and the crew from the mechanical workshop for all the detailed technical realization of my drawings, and the secretary office, especially Bettina Kappler, Brigitte Doez and Heike Alexa, for all the red tape that comes up during a doctorate and the daily work routine.

Furthermore, my special thanks goes to Florian Fetzer, Philipp Frech, Ronny Löffler, Olympia Geladari and Viola Sottru for diligently proofreading this thesis.

Last but not least I wish to thank my whole family for the continuous support and particularly Viola Sottru for the ongoing support, patience and encouragement.